Title
Amphiphilic and Bio-Inspired Adhesive Interactions at Hydrophobic and Hydrophilic Surfaces

Permalink
https://escholarship.org/uc/item/6688t4m8

Author
Rapp, Michael V.

Publication Date
2016

UNIVERSITY OF CALIFORNIA

Santa Barbara

Amphiphilic and Bio-Inspired Adhesive Interactions at Hydrophobic and Hydrophilic Surfaces

A dissertation submitted in partial satisfaction of the
requirements for the degree Doctor of Philosophy
in Chemical Engineering

by

Michael Vincent Rapp

Committee in charge:

Professor Jacob N. Israelachvili, Chair

Professor Michael J. Gordon

Professor Todd M. Squires

Professor J. Herbert Waite

June 2016

The dissertation of Michael Vincent Rapp is approved.

Professor Michael J. Gordon

Professor Todd M. Squires

Professor J. Herbert Waite

Professor Jacob N. Israelachvili, Committee Chair

April 2016

Amphiphilic and Bio-Inspired Adhesive Interactions

at Hydrophobic and Hydrophilic Surfaces

by

Michael Vincent Rapp

ACKNOWLEDGEMENTS

Truthfully, this section should be longer, and more intricate, than all the rest of this dissertation. Both this research and my own personality have been profoundly influenced by such wonderful teachers and friends, and I am hopelessly in debt to all of you.

With the utmost gratitude, I thank my advisor, Prof. Jacob Israelachvili. While most scientists will know you as the brilliant pioneer of interfacial phenomena, your students will always know you as the magnanimous jokester that has made our education such a treat. To my “unofficial” advisor, Prof. Herb Waite, I likewise extend my sincerest thanks; without your sage-like wisdom, I would have been as adrift as a mussel without its plaque. Equally, I thank the remaining members of my committee, Prof. Mike Gordon and Prof. Todd Squires, for years of guidance and inspiration in my research.

I am humbled to have worked with an exceptional group of collaborators throughout my graduate studies. A tremendous thanks is due to my predecessors in the Israelachvili lab—Dr. Jing Yu, Dr. Steve Donaldson, and Dr. Dong-Woog Lee—for both your mentorship and your friendship. Similarly, thank you to my contemporaries in the lab—Dr. Kai Kristiansen, Dr. Yair Kaufman, Dr. Matt Gebbie, Nick Cadirov, Alex Schrader, Howie Dobbs, Tom Cristiani, and Sandy Chen—for making my days endlessly entertaining. Ardently, I thank the true hero of the Israelachvili lab: Nancy Emerson, the oil that keeps the machine running. Outside of my own lab, I thank the entire Interdisciplinary Research Group (IRG-1) of the Materials Research Lab for years of stimulating discussions, and particularly to my collaborators Prof. Alison Butler, Prof. Joan-Emma Shea, Dr. Zach Levine, Dr. Wei Wei, and Greg Maier.

Mom, Dad, and Juju—thank you for every bug that you helped me chase, every Lego you helped me build, every wound you helped me heal. Thank you for every resisted push that you gave me along the way, every phone call, and every hug. Thank you for every moment of your wonderful lives that you have spent with me.

Finally and emphatically, I thank my friends—from Santa Barbara and afar—for your boundless love and support: Harry, Carol, Cov, Settle, Molly, Matt, Michelle, Chris, Ed, and many others who have enlivened this adventure. If you parse closely enough, you will find your own influence written into each page of this book—making this dissertation as much yours as it is my own.

VITAE OF MICHEAL VINCENT RAPP

June 2016

EDUCATION

University of California-Santa Barbara (UCSB), Santa Barbara, California
Ph. D. in Chemical Engineering, 2011-2016
Specialization: Interfacial Phenomena, Biomolecular Adhesion, Surface Forces

Virginia Polytechnic Institute and State University (Virginia Tech), Blacksburg, Virginia
B.S. in Chemical Engineering, Magna Cum Laude, 2006-2011

RESEARCH EXPERIENCE

NSF Graduate Research Fellow: Dept. of Chemical Engineering, UCSB, 2012-2016
Advisor: Prof. Jacob N. Israelachvili

- Understanding the fundamentals of protein, peptide, and biomolecular interactions at organic and inorganic surfaces
- Translating the fundamentals of wet bio-adhesion into synthetic adhesives across multiple length scales, for marine and physiological applications
- Managed a collaboration with Procter & Gamble to study solvation (hydrophobic and hydrophilic), electrostatic, and non-equilibrium forces within complex polymer, surfactant, and polyelectrolyte systems.

Undergraduate Research: Department of Chemical Engineering, Virginia Tech, 2008-2011
Advisor: Prof. William A. Ducker

- Complex wetting phenomena at thin organic films
- Development of electro-responsive peptide films capable of selective antibody binding

FELLOWSHIPS & AWARDS

NSF Graduate Student Fellowship Program, 2012-2016
UC-Santa Barbara Doctoral Student Travel Grant, 2015
Dow-Materials Research Lab Travel Fellowship, 2014
Clorox-Amgen Graduate Student Symposium Best Poster Award, 2014
Denmark Technical University Scholarship (Kgs. Lyngby, Denmark), 2010

PUBLICATIONS (Lead Author)

(1) *Defining the Catechol-Cation Synergy for Enhanced Wet Adhesion to Mineral Surfaces*. **Rapp, MV* (co-1st author)**; Maier, GP*; H.A. Dobbs; Higdon, NJ; Waite, JH; Israelachvili, JN; Butler, A. (2016) ***Submitted to J. Am. Chem. Soc.***

(2) *Electrochemical Switching Reversibly Modulates Adhesion in Nanoscale Peptide Films*. Gebbie, MA*; **Rapp, MV* (co-1st author)**; Yu, J; Wei, W; Waite, JH; Israelachvili, JN. (2016) ***In Preparation for ACS Nano***

(3) *Surface Force Measurements and Simulations of Mussel-Derived Peptide Adhesives on Wet Organic Surfaces.* Levine, ZA*; **Rapp, MV* (co-1st author)**; Wei, W; Mullen, RG; Wu, C; Zerze, GH; Mittal, J; Waite, JH; Israelachvili, JN; Shea, JE. (2016) ***Proc. Natl. Acad. Sci. USA***, DOI:10.1073/pnas.1603065113

(4) *Adaptive Synergy between Catechol and Lysine Promotes Wet Adhesion by Surface Salt Displacement*. Maier, GP*; **Rapp, MV* (co-1st author)**; Waite, JH; Israelachvili, JN; Butler, A. (2015) ***Science***, 349 (6248):628-632

(5) *Effects of Surfactants and Polyelectrolytes on the Interaction Between a Negatively Charged Surface and a Hydrophobic Polymer Surface*. **Rapp, MV**; Donaldson, SH; Gebbie, MA; Y; Gizaw, Y; Koenig, P; Roiter, Y; Israelachvili, JN (2015) ***Langmuir***, 31 (29):8013-8021

(6) *Hydrophobic, Electrostatic, and Dynamic Polymer Forces at Silicone Surfaces Modified with Long-Chain Bolaform Surfactants.* **Rapp, MV**; Donaldson, SH; Gebbie, MA; Das, S; Kaufman, Y; Gizaw, Y; Koenig, P; Roiter, Y; Israelachvili, JN (2015) ***Small***, 11 (17):2058-2068

(7) *Enantiospecific Wetting.* **Rapp, M**; Ducker, WA (2010) ***J. Am. Chem. Soc.***, 132 (51):18051-18053

PUBLICATIONS (Co-Author)

(1) *Measuring Concentration Fields in Microfluidic Channels In Situ with a Fabry-Perot Interferometer.* Vogus, DR; Mansard, V; **Rapp, MV**; Squires, TM (2015) ***Lab on a Chip***, 15 (7):1689-1696

(2) *Developing a General Interaction Potential for Hydrophobic and Hydrophilic Interactions*. Donaldson, SH; Royne, A; Kristiansen, K; **Rapp, MV**; Das, S; Gebbie, MA; Lee, DW; Chmelka, B; Valtiner, M; Israelachvili, JN (2014) ***Langmuir (Feature Article)***, 31, (7):2051-2064

(3) *The Intersection of Interfacial Forces and Electrochemical Reactions*. Israelachvili, JN; Kristiansen, K; Gebbie, MA; Lee, DW; Donaldson, SH; Das, S; **Rapp, MV**; Banquy, X; Valtiner, M; Yu, J (2013) ***J. Phys. Chem. B (Feature Article)***, 117 (51):16369-16387

(4) *Adaptive Hydrophobic and Hydrophilic Interactions of Mussel Foot Proteins with Organic Thin Films*. Yu, J; Kan, Y; **Rapp, M**; Danner, E; Wei, W; Das, S; Miller, DR; Chen, Y; Waite, JH; Israelachvili, J.N. (2013) ***Proc. Natl. Acad. Sci. USA***, 110 (39):15680-15685

(5) *Asymmetric Electrostatic and Hydrophobic-Hydrophilic Interaction Forces Between Mica Surfaces and Silicone Polymer Thin Films*. Donaldson, SH; Das, S; Gebbie, M; **Rapp, M**; Jones L; Roiter, Y; Koenig, P; Gizaw, Y; Israelachvili JN (2013) ***ACS Nano***, 7 (11):10094-10104

(6) *The Formation of Hydrophobic Films on Silica with Alcohols*. Dion, M; **Rapp, M**; Rorrer, N; Shin, DH; Martin, S; Ducker, WA (2010) ***Colloids and Surfaces A***, 362 (1-3):65-70

NEWS & PRESS

(1) *Positive Charges and Underwater Adhesion*. Wilker, JJ. (2015) ***Science***, 349 (6248):582-583

(2) *One Mystery of How Mussels Stick to Rocks, Boats Solved*. Everts, S (Aug 6, 2015) ***Chemical & Engineering News***. (http://cen.acs.org/articles/93/web/2015/08/One-Mystery-Mussels-Stick-Rocks.html)

(3) *A Sticky Situation*. Cohen, J (Aug 6, 2015) ***The UC-Santa Barbara Current***. (http://www.news.ucsb.edu/2015/015797/sticky-situation). Republished by: (Aug 10, 2015) ***Materialsgate*** (http://www.materialsgate.de/de/mnews/26853/A+sticky+situation.html?cc=bco93w); (Aug 10, 2015) ***Futurity*** (http://www.futurity.org/molecules-mussels-adhesion-978552/); (Aug 7, 2015) ***Lab Manager*** (http://www.labmanager.com/news/2015/08/a-sticky-situation?fw1pk=2%23.VcTILqjQTSg#.VcjynPlViko); (Aug 11, 2015) ***Chem Europe*** (http://www.chemeurope.com/en/news/154059/a-sticky-situation.html)

(4) *UCSB Researchers Create Underwater Super Glue.* (Aug 6, 2015) ***Pacific Coast Business Times***. (http://www.pacbiztimes.com/2015/08/06/ucsb-researchers-create-underwater-super-glue/)

(5) *Improved CTC Molecule Shows Excellent Adhesive Strength in Aqueous Environments*. Ellison, B (Aug 10, 2015). ***AZO Materials***. (http://www.azom.com/news.aspx?newsID=44288)

(6) *A New Underwater Glue Inspired by Mussels*. Richter, V. (Aug 17, 2015) ***Cosmos*** (https://cosmosmagazine.com/life-sciences/new-underwater-glue-inspired-mussels)

(7) *Ça y est, on sait enfin pourquoi la moule colle* (Aug 25, 2015) ***Ouest France*** (http://www.ouest-france.fr/leditiondusoir/index.html)

CONFERENCE PRESENTATIONS

(1) **Rapp, MV**; et al. Adaptive and Synergistic Interactions of Amino Acids in Underwater Bio-Adhesives. *UCSB Amgen-Clorox Graduate Student Symposium*, Santa Barbara, CA, September 29, 2015 (Oral)

(2) **Rapp, MV**; et al. The Effects of Surfactant and Polyelectrolyte Self-Assembly on the Interaction between a Negatively-Charged Surface and a Hydrophobic Polymer Surface. *ACS Colloid & Surface Science Symposium*, Pittsburgh, PA, June 15-17, 2015 (Oral)

(3) **Rapp, MV**; et al. Siderophores Mediate Robust Adhesion in Harsh, Wet Environments. *Clorox-Amgen Graduate Student Symposium*, Santa Barbara, California, Oct 10, 2014 (Best Poster Award)

(4) **Rapp, MV**; et al. Hydrophobic, Electrostatic, and Dynamic Polymer Forces at Surfactant-Modified Silicone Surfaces. *International Workshop in CAI-STEM*, Cancun, Mexico, Aug 24-29, 2014 (Oral)

(5) **Rapp, MV**; et al. Bio-Inspired Wet Adhesion. *NSF MRSEC Summer Student Symposium*, Santa Barbara, California, Aug 6, 2014 (Oral)

(6) **Rapp, MV**; et al. Adaptive Hydrophobic and Hydrophilic Interactions of Mussel Foot Proteins with Organic Thin Films. *Materials Research Outreach Program Symposium*, University of California-Santa Barbara, Feb 4-5, 2014 (Poster)

(7) **Rapp, MV**; et al. Hydrophobic, Electrostatic, and Polymer Bridging Forces at Surfactant-Modified Silicone Surfaces. *AIChE Annual Meeting*, San Francisco, California, Nov 3-8, 2013 (Oral)

(8) **Rapp, MV**; et al. Hydrophobic, Electrostatic, and Polymer Bridging Forces at Surfactant-Modified Silicone Surfaces. *Clorox-Amgen Graduate Student Symposium*, Santa Barbara, California, Oct 4, 2013 (Poster)

(9) **Rapp, MV**; et al. Adaptive Hydrophobic and Hydrophilic Interactions of Mussel Foot Proteins with Organic Thin Films. *International UCSB/KAIST Workshop on Biologically-Inspired Soft Matter*, Santa Barbara, California, Sept 23-25, 2013 (Poster)

INDUSTRIAL EXPERIENCE

Process Engineering Co-op: ExxonMobil, Beaumont, Texas, 2008-2009

- Two-term summer co-op working in the Process Safety and Technical divisions of the Beaumont chemical plant and oil refinery

TEACHING & MENTORSHIP

Research Mentor:	Cooperative International Science & Engineering Internships (CISEI), UCSB, 2015
Teaching Assistant:	Chemical Engineering Colloids and Interfaces, UCSB, 2015
Teaching Assistant:	Chemical Engineering Thermodynamics, UCSB, 2014
Teaching Assistant:	Analytical Methods in Chemical Engineering, UCSB, 2012
Teaching Assistant:	Unit Operations Laboratory, Denmark Technical University (Kgs. Lyngby), 2011
Teaching Assistant:	Chemical Engineering Thermodynamics, Virginia Tech, 2010

OUTREACH

Graduate Students for Diversity in Science (GSDS)-Student Contact Chair: Materials Research Lab, UCSB, 2013-2015

- The GSDS is an interdisciplinary group of young scientists that aims to foster peer-to-peer mentorship, promote research excellence, and provide networking opportunities in academia and industry. At UCSB, the GSDS organizes a Distinguished Lecture series for renowned scientists from under-represented groups. The GSDS hosts top-performing undergraduate STEM students from California State Universities at our campus (~20/yr, primarily female and minority), to introduce them to the opportunities of graduate school and diversity-focused organizations.

ScienceLine "Ask a Scientist": Materials Research Lab, UCSB, 2013-2015

- Answer weekly questions on broad science and engineering topics submitted on-line by local K-12 students and teachers

Outreach Volunteer: Materials Research Lab, UCSB, 2014

- National NanoDays volunteer scientist for local K-8 students

Outreach Volunteer: Materials Research Lab, UCSB, 2013

- Santa Barbara Natural History Museum "Tinker Festival" volunteer scientist

ABSTRACT

Amphiphilic and Bio-Inspired Adhesive Interactions at Hydrophobic and Hydrophilic Surfaces

by

Michael Vincent Rapp

In aqueous solutions—such as physiological fluids, seawater, or detergent solutions—both adhesion and cohesion between surfaces are severely limited by high salt concentrations, oxidizing pH levels, and bound hydration layers at the solid-liquid interface. While problematic, these limitations do not entirely prohibit adhesion: certain synthetic polymers and biological molecules exhibit adaptive amphiphilic interactions that strongly bind to wet surfaces and lead to robust adhesion. Identifying the intra- and inter-molecular interactions between adhesive molecules and surfaces—including hydrogen bonding, electrostatic interactions, solvation interactions, polymer dynamics, and synergistic interactions—is imperative for the future design of high-performance wet adhesives and materials. In the following thesis, a surface forces apparatus (SFA) and other surface characterization techniques are used to study how unique molecules display concurrent adhesive mechanisms, adapt, self-assemble, and partition between chemically heterogeneous surfaces (either hydrophobic or hydrophilic) to achieve durable wet adhesion.

This thesis is divided into chapters on surfactant and polyelectrolyte self-assembly and adhesion (Chapter 2) and bio-inspired peptidyl adhesion (Chapters 3 and 4). Chapter 2 explores the behaviors of aliphatic surfactants and silicone polyelectrolytes as they self-assemble at hydrophobic interfaces and mediate strong adhesion to mineral surfaces. In this section, the molecular geometries of surfactants and polyelectrolytes are shown to control the self-assembled structures that form at aqueous surfaces, as well as the overall adhesion between surfaces in solution.

Chapters 3 and 4 investigate the molecular origins of peptide-based wet adhesion. Certain sessile marine organisms, particularly mussels, robustly attach to wet and chemically heterogeneous surfaces through protein adhesive plaques that contain high concentrations of the catecholic amino acid 3,4-dihydroxyphenylalanine (Dopa). In Chapter 3, SFA measurements and molecular dynamics simulations reveal how Dopa and other amino acids in mussel foot proteins (Mfps) or peptides partition between hydrophobic or hydrophilic organic surfaces, leading to an adaptive adhesion mechanism. Chapter 4 explores the synergistic interaction between catechol and cationic amino acids (such as lysine and arginine) in surface adhesion. Through SFA measurements with siderophores—bacterial iron-chelators that consist of paired catechol and cationic moieties—it is shown that adjacent catechol-cation placement provides a “1-2 punch”, whereby cationic amino acids evict hydrated salt ions from a mineral surface, allowing catechol binding to underlying oxides. Overall, these results provide a compelling rationale for the >20 mole% of cationic residues in Dopa-rich Mfps and establish a set of design parameters for future bio-inspired synthetic polymers.

TABLE OF CONTENTS

CHAPTER 1

Intermolecular and Surface Forces in Aqueous Systems

1.1 Introduction and Motivation

> *"There are therefore Agents in Nature able to make the Particles of Bodies stick together by very strong Attractions. And it is the Business of experimental Philosophy to find them out."* –Isaac Newton (1704)[1]

Some 2500 years ago, the Greek philosopher Empedocles proposed the embryonic concept of interaction forces: all matter was composed of four elements—earth, air, fire, water—and the powers of Love and Strife wove through these elements to create life or disorder.[2,3] Within this philosophy, Empedocles concealed the notion that the universe is a balance between *attractions* (Love) and *repulsions* (Strife). Leaping forward two millennia, a similar postulate emerged. In 1662, Robert Boyle proposed a law of gasses that suggested gas "corpuscles"—the antecedents to the atom—*repel* each other.[2,3] Yet several years later (1687), after allegedly contemplating a hanging apple, Isaac Newton deduced that two bodies *attract* each other through gravity, with an inverse-squared distance dependence in the force law. In order to rectify this apparent contradiction, Newton and others concluded that the interaction force between particles must change from attractive to repulsive, or vice versa, at varying distances.[1,4] These early scientists believed that particles first attract each other at large separations (gravity), then repel at shorter distances (gas pressure), then attract (to account for gas condensation into liquids and solids), and then ultimately repel at the smallest distances (because particles do not vanish into nothingness). As our understanding of matter has progressed, energy and the quantum nature of atoms have replaced corpuscles, yet the basic concept remains the same: the properties of ordinary matter are a delicate balance between the *attractive* and *repulsive* interactions of molecules.

In this dissertation, we use direct experimental measurements with the Surface Forces Apparatus (SFA) to quantify these attractive and repulsive intermolecular interactions between polymer or bio-inspired molecules and surfaces in solution. We develop a catalog of the intermolecular interactions that either enhance or reduce the adhesion of molecules to underwater surfaces—including hydrogen bonding, Coulomb interactions, solvation interactions, polymer dynamics, and synergistic interactions between chemical moieties. Furthermore, we use this fundamental understanding of intermolecular forces to outline the molecular design criteria for the development of high performance underwater adhesives, coatings, emulsions, lubricants, and anti-fouling films.

Water proves particularly quarrelsome when designing adhesives or coatings for aqueous applications. Water molecules are small, distinctly polar, and form dynamic hydrogen bonded networks with ~ 3.5 hydrogen bonds per molecule; these characteristics lead to water's unique properties of high latent heat, high surface tension (energy), and the ability to dissolve most solutes.[2] Yet for these same reasons, water is the nemesis of adhesion; water strongly hydrogen bonds to hydrophilic ("water loving", polar) surfaces—such as minerals, metals, oxides, fabrics, and biological interfaces—and forms a barrier to attachments at surfaces that is known as the hydration layer.[2,5,6] As discussed in Sections 1.4 and 1.5, the high dielectric constant of water, $\varepsilon = 80$, dramatically reduces the strength of non-covalent intermolecular interactions, further weakening adhesion. Moreover, water deteriorates the bulk of adhesives through swelling, oxidation, hydrolysis, erosion, and crazing.[6]

On the other hand, the inability of water to hydrogen bond near hydrophobic ("water fearing", non-polar) molecules drives the attraction and self-assembly of lipids, proteins, and polymers.[2,7] Water *enhances* the adhesion and attachments between hydrophobic surfaces, or between a hydrophobic surface and non-polar molecules. Thus, the key to the design of multifunctional wet adhesives—that robustly attach to a broad spectrum of surfaces—is in the control of the amphiphilic nature of the adhesive molecules, i.e. the balance between hydrophobic and hydrophilic chemistries. Throughout this dissertation, we demonstrate how amphiphilic molecules subvert the effects of water in their adhesion to surfaces. The unique molecules described herein display concurrent adhesive mechanisms, adapt, self-assemble, and partition between chemically heterogeneous surfaces (either hydrophobic or hydrophilic) to achieve durable wet adhesion.

1.2 Organization of Dissertation

The remainder of Chapter 1 outlines the fundamental interaction energies, forces, concepts and techniques that are discussed in the later chapters of this dissertation. We primarily restrict the discussion to the intermolecular (non-covalent) interactions between molecules, as these are the forces which lead to reversible (physical) adhesion in wet environments. Additionally, we introduce the concept of surface forces, where the cumulative intermolecular forces at an interface manifest into qualitatively and quantitatively different forces than those experienced by individual molecules. We conclude Chapter 1 with a summary of the major experimental techniques that are used in the ensuing chapters.

Chapter 2 explores the behaviors of different classes of surfactants and polyelectrolytes as they self-assemble at a silicone-water interface and mediate strong adhesion to mineral surfaces. We begin by developing a molecularly-smooth and hydrophobic silicone surface, and characterizing the surface forces at the silicone-water interface. We then provide a broad overview of how chemical and structural properties of surfactant molecules result in different self-assembled structures at silicone and mineral surfaces, by studying three classes of surfactants: (1) anionic aliphatic surfactants, (2) cationic aliphatic surfactants, and (3) silicone polyelectrolytes with silicone mid-blocks and cationic end groups. Lastly, we demonstrate how the head-group charge density of silicone polyelectrolytes controls the adhesion of silicone films to mineral surfaces.

Chapters 3 and 4 investigate the molecular origins of peptide-based wet adhesion. The need for bio-inspired wet adhesives has skyrocketed in the past few decades (e.g. for dental and medical transplants, coronary artery coatings, cell encapsulants, etc.).[8] Despite this, the molecular basis behind protein-mediated adhesion to surfaces remains unclear, thus hindering synthesis and optimization of novel underwater adhesives. Certain sessile marine organisms, particularly mussels, robustly attach to wet and chemically heterogeneous surfaces through protein adhesive plaques that contain high concentrations of the catecholic amino acid 3,4-dihydroxyphenylalanine (Dopa). In Chapter 3, we combine direct force measurements of native mussel proteins and mussel-inspired peptides with all-atom molecular dynamics simulations to yield a comprehensive framework that explicitly identifies the basis for mussel adhesion to hydrophobic and hydrophilic surfaces. We demonstrate how Dopa and other amino acids partition between chemically dissimilar surfaces and lead to an adaptive adhesion mechanism.

Chapter 4 explores the synergistic interactions between catechols and cationic residues in adhesion to mineral surfaces in salty solutions. To isolate interactions between catechols and cations, we perform SFA adhesion measurements with siderophores—bacterial iron-chelating small molecules that consist of paired catechol and cation functionalities—or synthetic siderophore analogs at mineral surfaces. We reveal that catechols and cationic molecules—such as arginine, lysine, or other primary amines—work together to promote adhesion at mineral surfaces; the cationic groups in the adhesive molecules evict the native hydrated cations from a mineral surface, allowing catechols to bind to the underlying interface. Overall, these results provide a compelling rationale for the >20 mole % of cationic residues in Dopa-rich mussel proteins and establish a set of design parameters for future bio-inspired synthetic polymers.

1.3 Interaction Energies and Surface Forces

At the molecular length scale, the *electromagnetic* interaction dominates the phenomena between molecules and atoms, surpassing in magnitude the three other fundamental interactions: *strong nuclear*, *weak nuclear*, and *gravitational* interactions. The total electromagnetic interaction between two molecules is known as the pair potential—or the potential of mean force—and is represented as $w(r)$, where r is the separation distance between the interacting molecules. The interaction force, f, between two molecules is related to the pair potential through a derivative:[2]

$$f = -\frac{\partial}{\partial r}(w(r)) \tag{1.1}$$

In a condensed medium—such as in a liquid or at a solid surface—the pair potential between two molecules becomes exceedingly complex, as every pair potential involves "many-body interactions" between the surrounding molecules in the medium. In a solution, the pair potential between two solute molecules involves: solute-solute interactions, solute-solvent interactions, solvent-solvent interactions, distance-dependent structural perturbations to the solvent ordering, and solvent-induced polarization changes to the solutes. Currently, the complete analysis of the total intermolecular forces between molecules in solution is intractable, even for small systems, and it would require the explicit solution to the Schrödinger equation[9] for many interacting atoms. In order to simplify the analysis, we generally divide the *total* intermolecular interactions into constituent interactions—such as dispersion, electrostatic, or hydrophobic interactions—and discuss each of these interactions individually.

Throughout this dissertation, we consider how varying aspects of intermolecular interactions manifest into unique phenomena at surfaces in solution. We used direct force measurements between macroscopic surfaces to determine how the intervening molecules assemble and adhere at these surfaces. Similar to the force and pair potential between individual molecules, the interaction force (*F*) between two macroscopic surfaces is related to the interaction energy (*W*) as a function of the surface separation distance (*D*) by:

$$F = -\frac{\partial}{\partial D}(W(D)) \tag{1.2}$$

Experimentally, it is more practical to measure the interaction force between curved surfaces, rather than flat surfaces. The measured force between curved surfaces is related to the thermodynamic interaction energy of planar surfaces via the well-known Derjaguin approximation.[2] By integrating the interaction energy over the surface area, the force of a macroscopic sphere (of radius R) approaching a surface is related to the interaction energy between two planar surfaces with Equation 1.3; this treatment is identical to the situation of two crossed cylinders (each or radius R) interacting at a distance, D.

$$F(D) = 2\pi R W(D) \tag{1.3}$$

The Derjagiun approximation is also used to relate the adhesion force (F_{ad}) to the work of adhesion (W_{ad}) required to separate two non-deforming crossed cylinders in solution, with a solid-liquid interfacial energy γ:[2]

$$\frac{F_{ad}}{R} = 2\pi W_{ad} = 4\pi\gamma \tag{1.4}$$

However, when elastic surfaces adhere together with a strong attractive force, the contact area between the surfaces may deform or flatten. For this case of deforming surfaces, the adhesive force is related to the work of adhesion via the Johnson, Kendall, and Roberts theory (JKR theory) for elastic surfaces:[10]

$$\frac{F_{ad}}{R} = \frac{3}{2}\pi W_{ad} = 3\pi\gamma \tag{1.5}$$

In the study of surface forces, also known as colloidal forces, the total interaction force between the surfaces is generally described as a sum of distinct constituent forces—such as dispersion, electrostatic, or solvation forces. While all of these forces are manifestations of the fundamental electromagnetic interaction, these forces have different thermodynamic origins, and are thus classified as different phenomena. The range (distance dependence), magnitude, and sign (attractive or repulsive) of colloidal forces vary considerably, and a general comparison of the force-distance profiles of several canonical forces is shown in Figure 1.1. The next several sections of Chapter 1 outline the theoretical basis for the colloidal forces that are discussed throughout this dissertation.

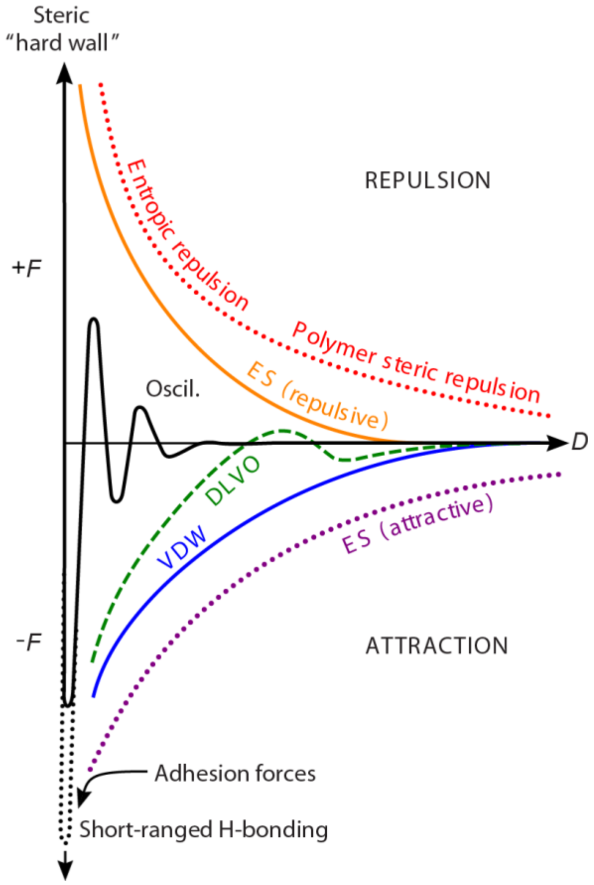

Figure 1.1: Comparison of the contributions from several colloidal forces (*F*) to the total interaction force between two surfaces as a function of distance, *D*. General colloidal forces include: electrostatic double layer forces (ES), van der Waals forces (VDW), Derjaguin-Landau-Verwey-Overbeek forces (DLVO = ES + VDW), steric repulsions, entropic repulsions, oscillatory structural forces, and short-ranged hydrogen bonding. Figure reproduced from Leckband and Israelachvili.[11]

1.4 Coulomb (Charge-Charge) Interactions

The Coulomb interaction between two electrically charged species is the strongest and longest-ranged physical interaction that is considered in this dissertation. In soft matter systems, Coulomb interactions are generally much greater than the thermal energy, k*T*, and regulate phenomena such as ion solubility,[2] protein-surface adsorption,[12] surfactant or biological self-assembly,[2] and coacervation.[13] Coulomb's Law gives the force between two charges, Q_1 and Q_2, at a separation distance, r, as:[2]

$$f(r) = \frac{Q_1 Q_2}{4\pi\varepsilon_0 \varepsilon r^2} \tag{1.6}$$

where ε_0 is the permittivity of free space and ε is the dielectric constant of the medium. Integrating the Coulomb force from r to $r = \infty$ (the zero energy reference state) provides the Coulomb free energy, $w(r)$:

$$w(r) = \int_{\infty}^{r} -f(r)dr = \frac{Q_1 Q_2}{4\pi\varepsilon_0 \varepsilon r} \tag{1.7}$$

In the ensuing chapters, repulsive or attractive Coulomb interactions dominate a variety of phenomena at aqueous surfaces. The repulsive forces between similarly-charged surfactant headgroups govern the equilibrium geometry and density of ionic surfactants adsorbing at surfaces. Conversely, the attractive forces between ionic moieties and charged surfaces are capable of driving strong and stable aqueous adhesion that is appreciably larger than the thermal energy.

1.5 Van der Waals Interactions

Dispersion (or London) forces are quantum mechanical in origin and exist between all matter. Dispersion forces arise from the instantaneous dipole moments that occur in all molecules: while a non-polar molecule may have a time-averaged dipole moment of zero, at any given instant, there exist small fluctuations in the atom's electron cloud which give rise to an instantaneous dipole moment. The instantaneous dipole moment of one molecule polarizes local molecules, resulting in induced instantaneous dipole moments in the surrounding molecules. This induced-dipole/induced-dipole effect gives rise to a finite attractive force between all molecules. Although less dominant than dispersion forces, Keesom orientation forces (permanent dipole interactions) and Debye induction forces (dipole/induced-dipole interactions) are also pervasive in polar compounds. Together, the dispersion, orientation, and induction forces make up the van der Waals force. The van der Waals free energy between two molecules has an inverse sixth-power distance dependence and is expressed as:

$$w_{VDW}(r) = \frac{-C_{VDW}}{r^6} \tag{1.8}$$

where C_{VDW} is the van der Waals energy coefficient, and it is a function of the individual atom's electronic polarizability, permanent dipole moment, and ionization potential.[2,14,15]

The total van der Waals interaction energy for two macroscopic interacting bodies is found by integrating the two-body potential over all molecules in the surfaces. The resulting interaction potential for the van der Waals energy between two planar surfaces is:

$$W_{VDW}(r) = -\frac{A}{12D^2} \tag{1.9}$$

where A is the Hamaker constant, which is a function of the number densities of the molecules in the respective surfaces, ρ_1 and ρ_2:

$$A = \pi^2 C_{VDW} \rho_1 \rho_2 \tag{1.10}$$

While useful, the preceding analysis operates under the false assumption of pairwise-additive interactions between molecules. In reality, dispersion forces are heavily influenced by the presence of surrounding media, and the interactions of bodies in a medium are not simply additive. The Lifshitz theory amends this issue by applying a continuum theory to the interaction—single molecules are ignored and interactions are based upon bulk physical properties of the surrounding media, particularly how the dielectric permittivity varies with frequency.[16,17] In Lifshitz theory, the form of the interaction potential is left unchanged, and the Hamaker constant for two bodies (1 and 2) interacting across a medium (3) is given by Equation 1.11.

$$\begin{aligned} A_{total} &= A_{v=0} + A_{v>0} = \frac{3}{4}kT\left(\frac{\varepsilon_1-\varepsilon_3}{\varepsilon_1+\varepsilon_3}\right)\left(\frac{\varepsilon_2-\varepsilon_3}{\varepsilon_2+\varepsilon_3}\right) \\ &+\frac{3h\nu_e}{8\sqrt{2}}\frac{\left(n_1{}^2-n_3{}^2\right)\left(n_2{}^2-n_3{}^2\right)}{\left(n_1{}^2+n_3{}^2\right)^{1/2}\left(n_2{}^2+n_3{}^2\right)^{1/2}\left\{\left(n_1{}^2+n_3{}^2\right)^{1/2}+\left(n_2{}^2+n_3{}^2\right)^{1/2}\right\}} \end{aligned} \tag{1.11}$$

Here, the Hamaker constant accounts for the static zero-frequency ($A_{\mathrm{v=0}}$, Keesom and Debye dipolar interactions) and the electronic dispersion ($A_{\mathrm{v>0}}$, London interactions) energy contributions to the total van der Waals interaction. In Equation 1.11, h is Planck's constant,

k is the Boltzmann's constant, T is temperature, ν_e is the electronic adsorption frequency, and n and ε are the bulk refractive index and dielectric constant of the respective bodies.

1.6 Electrostatic Double Layer Interactions

When solid bodies interact in aqueous solution, their surfaces frequently incur an electric charge through either the dissociation of surface groups, the adsorption of ions from solution, or through inter-surface charge transfer (acid-base interactions). In aqueous solutions, the dissolved salt ions will arrange to form ion clouds—termed the diffuse electric double layer—around each surface that screen the magnitude of the electrostatic force between the two surfaces with a characteristic decay length (double-layer "thickness") known as the Debye length (shown here for a monovalent salt):[2]

$$\kappa^{-1} = \sqrt{\frac{\varepsilon_0 \varepsilon kT}{2\rho_\infty e^2}} \tag{1.12}$$

where κ^{-1} is the Debye length, ρ_∞ is the number density of the bulk salt, and e is the electronic charge. Between similarly charged surfaces, the confined ions of the diffuse double-layer will give rise to an osmotic pressure that seeks to drive the surfaces apart.

In order to calculate the osmotic pressure (or force) between the two double layers, we first determine the distance dependence of the electric potential, ψ, as it decays away from the surface. The Guoy-Chapman model of the electric double layer is applied to the Poisson-Boltzmann equation to give Equation 1.13, where c is the salt concentration and z is the valence.

$$\frac{d^2\psi}{dx^2} = \frac{8\pi cez}{\varepsilon_0\varepsilon}\sinh\left(\frac{ze\psi}{kT}\right) \tag{1.13}$$

Using the Deybe-Hückle theory at low potentials (< ±25 mV) for a 1:1 electrolyte, Equation 1.13 reduces to:

$$\frac{d^2\psi}{dx^2} = \kappa^2\psi \tag{1.14}$$

When two charged surfaces interact, inevitably some charge regulation will occur, particularly at small separations, and both the surface charge and surface potential will vary as the surfaces are approached or separated. However, wieldy solutions to Equation 1.14 require the application of boundary conditions at the surfaces, leading to the limits of constant potential and constant charge that provide the lower and upper bounds, respectively, on the magnitude of the electrostatic interaction. Generally, all electrostatic interactions between surfaces will fall between the bounds of constant charge and constant potential. Applying the method of Hogg, Healy, and Fuerstenau,[18] the interaction energy between two planar surfaces with asymmetric constant potentials (ψ_1 and ψ_2) is:

$$W(D) = \varepsilon_0\varepsilon\kappa\left\{\frac{2\psi_1\psi_2\exp[-\kappa D] - (\psi_1{}^2 + \psi_2{}^2)\exp[-2\kappa D]}{1 - \exp[-2\kappa D]}\right\} \tag{1.15}$$

Collectively, the summation of the van der Waals and electrostatic double layer interactions between surfaces is known as the Derjaguin-Landau-Verwey-Overbeek (DLVO) theory. While complex numerical solutions are needed to solve for the full electrostatic interactions of charge-regulating surfaces, the DLVO theory has been shown to satisfactorily describe the aqueous interactions of many practical surfaces, such as mica,[19,20] silica,[21–23] surfactant and lipid films,[24–27] metals,[28–30] or metal oxides.[29–31] The findings presented in Chapter 2 of this dissertation also indicate that constant potential electrostatic double layers accurately describe the interaction of mica with silicone—and surfactant-decorated silicone—surfaces.

1.7 Hydrogen Bonds

With the increasing sophistication of experimental observations in recent decades, the definition of the hydrogen bond—and conceivably all bonds in general[32]—has grown quite nebulous. The nascent concept of the hydrogen bond (H-bond) was first proposed in the early 1900s to describe the weakly basic behavior of ammonium salts[33,34] and the physical properties of highly associated liquids (such as water and hydrogen fluoride),[35,36] and later expanded upon by Pauling.[37] Initially, the H-bond was believed to be a primarily electrostatic interaction—"no more than a particularly strong type of dipole-dipole interaction"[2]—between a donor and acceptor, X—H···X', where X and X' are electronegative atoms with lone pair electrons (O, F, or N). However, over the ensuing decades, it has been accepted that H-bonding may occur when X or X' are any atoms that are more electronegative that H (X or X' = F, Cl, Br, I, O, S, Se, N, P, C). Furthermore, extensive research has shown that the theory of an H-bond as a rigid dipole-dipole interaction is incomplete; in addition to the London interactions, H-bonds contain significant contributions from charge-transfer-induced covalency and exchange correlation effects.[38,39] These findings led the International Union of Pure and Applied Chemistry (IUPAC) to recently renew and broaden the definition of the hydrogen bond:

> *“The hydrogen bond is an attractive interaction between a hydrogen atom from a molecule or a molecular fragment X–H in which X is more electronegative than H, and an atom or a group of atoms in the same or a different molecule, in which there is evidence of bond formation.”*[38]

Throughout this dissertation, hydrogen bonding—or lack thereof—plays a critical role in the aqueous phenomena at surfaces. We primarily discuss the O—H···O hydrogen bond in interfacial water, or between hydroxyl-containing organic molecules and surfaces. The properties of the O—H···O bond vary tremendously, ranging in energy from < 1 to ~30 kcal/mol with a corresponding inter-oxygen distance ranging from 3 to 2.38 Å.[39] In the ensuing chapters, H-bonds between water and polar surfaces lead to strongly bound hydration layers, while the inability of water to H-bond around hydrophobes drives the self-assembly of surfactants and proteins at surfaces. Additionally, bidentate hydrogen bonds between catechols and surfaces are shown to be particularly strong—owing to a significantly increased bond lifetime over single H-bonds—and provide robust adhesion in wet environments.

1.8 Solvation Interactions

Reproduced in part from: Donaldson, S. H.; Røyne, A.; Kristiansen, K.; Rapp, M. V; Das, S.; Gebbie, M. A.; Lee, D. W.; Stock, P.; Valtiner, M.; Israelachvili, J. Developing a General Interaction Potential for Hydrophobic and Hydrophilic Interactions. *Langmuir* **2015**, *31*, 2051–2064

1.8.1 Hydrophobic Interactions

Hydrophobic interactions are ubiquitous in water-based biological and technological systems, and are directly implicated in everyday phenomena such as the separation of salad dressing, the gripping ability of surfers' feet on a freshly waxed surfboard, and the cleaning action of shampoos and detergents. At the molecular level, biological membranes and proteins organize into highly specific structures that determine their functions, driven by the arrangement of hydrophobic units within the macromolecules. The self-assembly process of proteins, in which hydrophobic groups bury within the macromolecular interior and hydrophilic groups are exposed to aqueous solution, was understood already in simple terms in the 1950s and 1960s in seminal works by Kauzmann and Tanford.[40,41] More recent theoretical work indicates that there is a general length-scale dependence for hydrophobic interactions: for small hydrophobes, the hydration free energy scales with volume, while for large hydrophobic surfaces, the hydration free energy scales with surface area, with the crossover occurring at hydrophobic length scale of ~ 1 nm.[7,42–44] Therefore, near an extended hydrophobic surface, water cannot orient into the preferred hydrogen bonding network, resulting in a fluctuating vapor-liquid like interface.[7,45] As two such hydrophobic interfaces approach each other, liquid water becomes metastable compared to the vapor and a drying transition induces evaporation between the two hydrophobic surfaces.[46,47]

A drying transition should occur between macroscopic hydrophobic interfaces at separation distance D_c ~ 100 nm, according to the Kelvin equation.[46–48] However, evaporation between two static hydrophobic surfaces approaching to close distances is generally not observed experimentally. A large energy barrier prevents evaporation even at nanoscopic distances D ~ 5-10 nm,[49,50] and a strongly attractive surface interaction acts to pull the surfaces into contact at these same distances.[51–54] Although a vapor bridge between the surfaces is the thermodynamic equilibrium state below D_c ~ 100 nm, liquid water remains metastable throughout, so this attractive interaction occurs on a metastable branch of the free energy landscape. The attractive interaction between hydrophobic surfaces has become known as the hydrophobic interaction or hydrophobic force.

The hydrophobic force is longer ranged and stronger than van der Waals interactions, with an effective range of $D \leq 20$ nm.[51–53] Even for partially hydrophobic surfaces with contact angles smaller than 90°, a significant contribution from hydrophobicity is found. The exact physical mechanism of this force remains in question, although it should have some fundamental relationship to the physics of hydrophobicity discussed above, based on the loss of water's hydrogen bonding network at the mutually approaching hydrophobic interfaces. Since the first direct force measurements between two hydrophobic surfaces in 1982 using the surface forces apparatus (SFA),[53] there have been many attempts to quantify the distance dependence of the attractive hydrophobic force.[51–58] The original experimental study by Israelachvili and Pashley concluded that the hydrophobic attraction decayed approximately exponentially with a decay length of about 1 nm and effective range of 10 nm.[53] Subsequent studies provided wildly varying accounts of the range and magnitude of the hydrophobic attraction, with some work reporting an effective range of up to several μm.[51] Within the past ten years, Israelachvili and coworkers have shown that long-range artifacts can arise due to preparation techniques and experimental conditions,[51,52,59] as discussed below, but pure hydrophobic interactions are found to be shorter ranged, and in fact close to the original study,[53] with a decay length of ~1 nm.[51,52] The wide variation of reported data can be attributed to the inherent difficulty of studying hydrophobic interactions. This difficulty lies in reproducible production of stable, impurity-free hydrophobic surfaces.

In many of the early experiments, the surfaces were made hydrophobic by physically adsorbing cationic surfactant or lipid monolayers on an anionic mica surface. It was later found that these monolayers can overturn with immersion time in aqueous solution, leaving behind a patchy surface of bilayer regions and bare mica regions.[59,60] The interaction between two such surfaces is fully attractive, although due to the slow overturning of molecules, this attraction arises from electrostatic forces rather than hydrophobic interactions.[59–62] Alternately, individual molecules can overturn, leading to a partially hydrophilic monolayer. Other longer-range (i.e., effective from $D > 300$ nm in some cases) attractive forces were shown to arise from bridging nanobubbles, revealing the importance of degassing the aqueous medium.[56,63–65] Current understanding is that the effective range of the hydrophobic interaction that is inherently due to the hydrophobicity of the surfaces, i.e., the distance at which the purely hydrophobic force becomes measureable, is about 10-20 nm with decay length of about 1 nm.[51] Adding further intrigue is that a shorter-ranged, attractive 0.3 nm exponential decay has been measured in dynamic SFA[51,52] and very recent dynamic atomic force microscope (AFM) measurements[55] between hydrophobic surfaces. Similar characteristic decay lengths, in fact, have also been measured between *hydrophilic* surfaces.

1.8.2 Hydrophilic Interactions

Interestingly, around the same time as the original studies between hydrophobic surfaces were being done, the interactions between hydrophilic surfaces were also under heavy investigation.[20,25,66–69] Many of the early studies between hydrated surfaces were performed between rigid mica surfaces in aqueous salt solution and found an exponential repulsion with distance, with a decay length of about 1 nm.[20,66,67] Further work between hydrophilic surfaces with thermally mobile groups (e.g., lipid bilayers) also showed an exponential repulsion, albeit with a significantly shorter decay length of about 0.3 nm.[25,69] At the time, no qualitative or quantitative connection was made between the exponentially decaying forces that exhibited identical decay lengths albeit opposite signs (repulsive/attractive).

These similar decay lengths, in the range of ~0.3 nm to ~1 nm for both hydrophobic and hydrophilic forces, indicate that perhaps there is a unifying mechanism for hydrophobic and hydrophilic interactions related to the degree of hydrogen bonding at a given interface. Indeed, some authors have referred to both attractive and repulsive hydration forces,[70,71] but these interactions have not been fully unified theoretically, for example, in terms of a generalized potential function. The approximate ranges of previously measured forces as a function of distance, between both hydrophobic and hydrophilic surfaces, are shown in Figure 1.2A. The attractive hydrophobic and repulsive hydrophilic forces tend to dominate over typical van der Waals forces at most distances, for very hydrophobic surfaces and very hydrophilic surfaces respectively. Oscillatory solvation forces that arise between smooth, crystalline surfaces with water layers in between also manifest an exponentially decaying (oscillatory) force with a periodicity of about 0.3 nm, as shown in the inset of Figure 1.2A. Recently, work by Donaldson and colleagues[27,72,73] has led to the development of an interaction potential that accounts for both the attractive hydrophobic and repulsive hydrophilic forces. The interaction potential is introduced fully below in Equations 1.16 and 1.17.

We recently derived an interaction potential to account for the hydrophobic attraction in surfactant membrane fusion[27,74] and hydrophobic polymer coatings,[72,75] shown in Equation 1.16, which can be used to calculate the interaction energy per unit area, W_{H}, as a function of the separation distance, D, between two hydrophobic interfaces. The interaction potential depends on the hydrophobic-water interfacial tension, γ_i (γ_i = 50 mJ/m^2 for hydrocarbon interfaces in water), the Hydra parameter Hy, and decay length D_H ~ 1 nm (but can be as small as 0.3 nm).[55] $Hy \equiv 1 - a_0/a$, where a_0 is the hydrophilic area and a is the hydrophobic area at a given interface. Defined in this way, Hy can be considered the effective fraction of hydrophobic area at a given interface or the fractional area covered by hydrophobic groups. For $a >> a_0$, $Hy = 1$, which corresponds to the maximum hydrophobic interaction, while for $0 < Hy < 1$ the surface is partially hydrophobic.

This interaction potential also naturally accounts for repulsive interactions between hydrophilic surfaces, generally known as hydration forces, which exhibit decay lengths D_H in the same range as hydrophobic interactions. When $a_0 > a$, $Hy < 0$ (i.e., the interfacial surface coverage is dominated by hydrophilic groups) and the overall interaction potential becomes repulsive instead of attractive. Hydrophilic surfaces repel each other due to water's ability to hydrogen bond and hydrate the surface, resulting in a repulsive osmotic pressure.[5] Hydrophilic interactions are certainly ubiquitous in nature as well, providing stabilizing structural forces for self-assembled vesicles, micelles, and proteins. Equation 1.16 can be reformulated as shown in Equation 1.17, where $\gamma_{eff} \equiv \gamma_{i,} \cdot Hy$, reducing the number of unknown variables in situations where γ_i is not well-defined, for example in hydrophilic systems. A negative effective interfacial tension (i.e., $Hy < 0$ and $\gamma_{eff} < 0$) indicates that work needs to be done to bring the surfaces into contact. While there is a well-defined maximum for hydrophobic interactions ($Hy = 1$), there is no practical analog for an "ideal" or maximum hydrophilic interaction. The theoretical limit is perhaps γ_{eff} = -72 mJ/m^2, i.e., the suface tension of water and describing in this case the interaction of two water films, but observed hydrophilic interactions are generally in the range of -0.5 to -15 mJ/m^2 for the observed γ_{eff}.

$$W_{\text{H}} = -2\gamma_{\text{i}} Hy \cdot \exp\left[-D / D_H\right] \tag{1.16}$$

$$W_{\text{H}} = -2\gamma_{\text{eff}} \cdot \exp[-D / D_H] \tag{1.17}$$

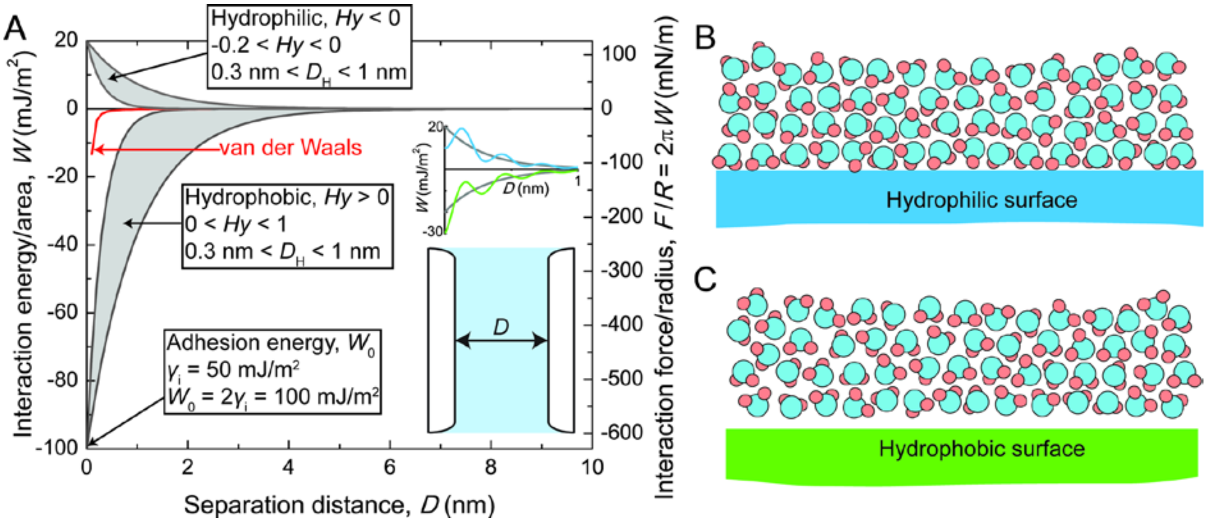

Figure 1.2: (A) An approximate summary of previously measured repulsive forces between hydrophilic surfaces and attractive forces between hydrophobic surfaces. These forces can be monotonic or oscillatory as shown in the inset, with the approximate periodicity of the diameter of water molecules (0.3 nm). Oscillatory forces are only observed between rigid surfaces; these oscillations are often smeared out between real surfaces, resulting in the monotonic force envelope shown in grey in the inset. As shown schematically in (B), hydrophilic surfaces have one (or more) hydration layers that result in repulsive osmotic forces when two such surfaces approach and interact. At hydrophobic surfaces, as shown in (C), water cannot hydrogen bond, and thus are fluctuating, soft interfaces that result in dewetting or attractive hydrophobic forces when two hydrophobic surfaces approach and interact. The measured interactions between such surfaces due to hydrophobicity/philicity can be described by Equations 1.16 and 1.17 using the parameter values displayed in (A).

1.9 Experimental Techniques

1.9.1 The Surface Forces Apparatus

The Surface Forces Apparatus (SFA)—specifically the SFA 2000 (manufactured by SurForce LLC, shown in Figure 1.3)—was the primary tool used in this dissertation for identifying and quantifying intermolecular and adhesive interactions. The SFA measures both equilibrium and dynamic (time-dependent) forces, F, between two macroscopic surfaces as a function of distance, D, with distance accuracy of 0.1 nm and a force sensitivity of ~10 nN. From 1969 to 1973, Tabor, Wennerstrom, and Israelachvili developed the original SFA technique to measure and confirm the Lifshitz theory of van der Waals forces between smooth mica surfaces in air.[76–78] Later, the SFA technique was further refined to measure the normal[19,79] and lateral (frictional)[80] forces between surfaces immersed in liquids. Over the ensuing decades—and many design iterations of the SFA later—the SFA technique measured and characterized most of the intermolecular and colloidal forces that occur between surfaces in solution, including: DLVO forces,[19,79] oscillatory structural forces,[81] hydrophobic forces,[53,73] steric hydration forces,[67,82] steric polymer forces,[83] biological forces (including ligand-receptor binding),[11,84] friction and lubrication forces,[80,85] forces at surfaces under imposed electric fields,[29,30] and non-equilibrium (dynamic) interactions.[80,86,87]

In a typical experiment, two molecularly smooth surfaces, with reflecting back layers, were first glued onto small cylindrical glass discs. The radii of the glass discs, R, were generally ~ 2 cm. Two types of reflecting surfaces were used in this dissertation: (1) cleaved mica surfaces (2-5 μm thick) that were back-coated with a 55 nm layer of silver using thermal evaporation and (2) 44 nm-thick gold surfaces that were templated to mica using electron-beam deposition (see Chapter 2). In each Chapter of this dissertation, different types of adsorbates or films were deposited onto either the mica or gold surfaces prior to the force measurements [please refer to the Materials section of each Chapter for a complete description of each specific preparation technique]. Following the film or surface preparation, the cylindrical surfaces were mounted inside the SFA, facing each other with their long axes perpendicular. One surface was fixed to a set of double-cantilever springs with a known spring constant, K_s, while the other surface was attached to a linear piezoelectric actuator. Aqueous solution was either injected in between the two surfaces, or used to fill the entire SFA chamber. Coarse and differential micrometers were used to bring the surfaces close together, and the entire system was then allowed to equilibrate until the mechanical and thermal drift between the surfaces became negligible.

Equilibrium force-distance measurements were performed by moving the top surface normally toward or away from the lower surface, with the piezoelectric actuator, at a slow and constant velocity (usually ~ 1 nm/s). At these velocities, the hydrodynamic forces between the surfaces are negligible. In certain measurements at slowly-equilibrating polymer surfaces (Chapter 2), “quasi-static” approach and separations were used: the surfaces were stepped toward or away from one another (~ 5 nm/step), and the system was allowed to re-equilibrate for >30 seconds before another movement was performed. In either case, the normal force between the surfaces was calculated with Hooke’s law (Equation 1.18), where the cantilever spring deflection, ΔD, is the difference between the applied movement distance, D_{applied} (calibrated), and the measured movement distance, D_{measured}.

$$F(D) = K_s \Delta D = K_s (D_{applied} - D_{measured}) \tag{1.18}$$

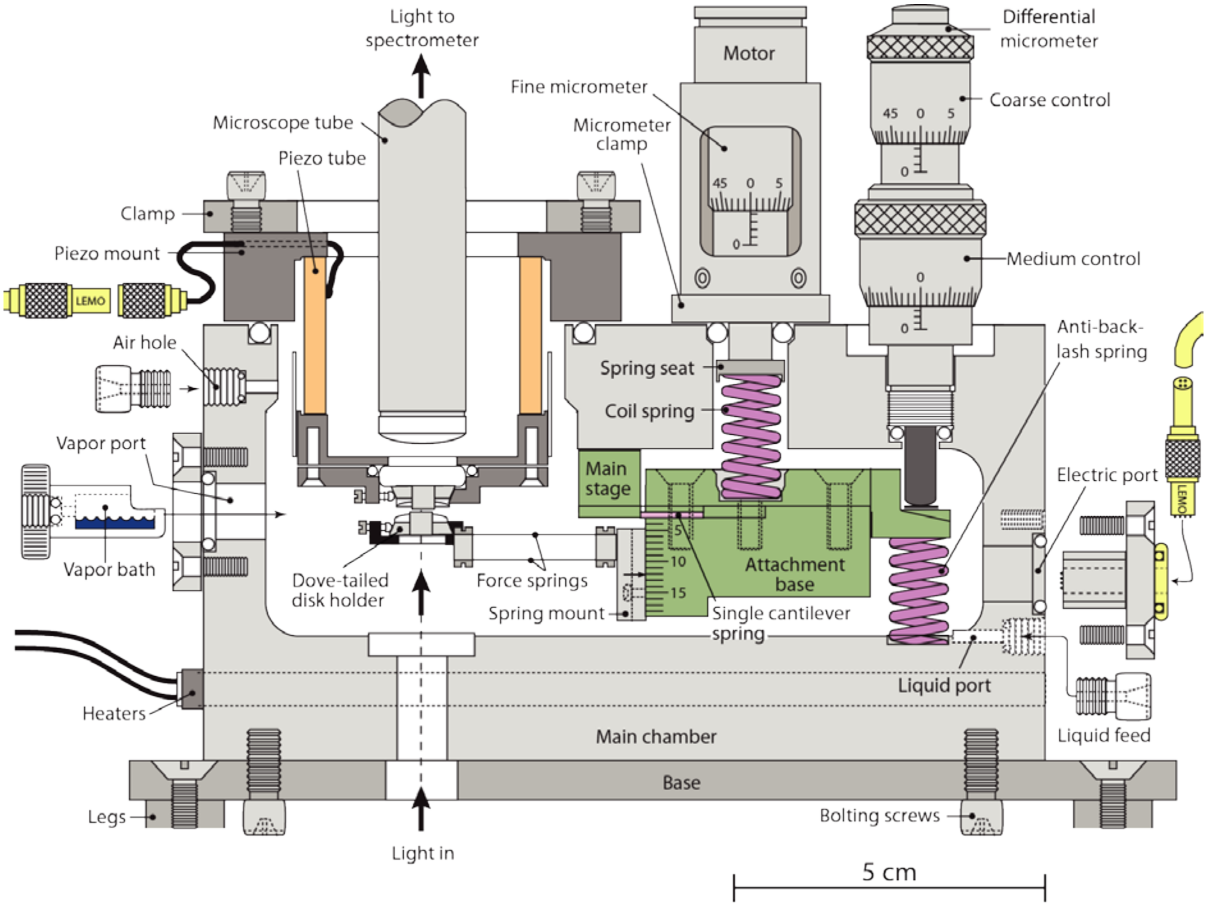

Figure 1.3: A cross-section schematic diagram of the Surface Forces Apparatus 2000. Image reprinted from Israelachvili et al. (2010).[88]

The absolute separation distance between the two surfaces and the interacting geometry of the surfaces is measured at all times during an SFA experiment using Multiple Beam Interferometry (MBI, shown in Figure 1.4). Collimated white light is passed orthogonally up through the lower surface in the SFA and some light transmits through the lower reflecting layer. Once between the two surfaces, the light constructively and destructively interferes between the reflecting layers. The resulting radiation that transmits through the upper surface is an interference pattern, known as Fringes of Equal Chromatic Order (FECO), that has intensity peaks at discrete wavelengths of constructive interference. The interference pattern is passed through a spectrometer, and the distinct wavelengths of the

FECO pattern are monitored throughout the experiment. Figure 1.4 displays a representative FECO profile of two back-silvered mica surfaces as well as a schematic of the MBI light path through the SFA.

In a typical experiment between two mica surfaces, such as in Chapter 4, the FECO profile appears as a series of “odd and even” bright fringes that trace the geometry of the interacting surfaces—a visualization of Newton’s interference rings along a single line (Figure 1.4a and b). Odd fringes represent the standing wave solutions for symmetric interferometers that have an anti-node at the center between the two reflecting layers; conversely, even fringes represent the standing wave solutions that have a node at the center (Figure 1.4c). At the start of an experiment, the pristine surfaces are brought into contact in a dry atmosphere in the SFA, and the wavelengths of an adjacent odd (λ_n^0) and even fringe (λ_{n-1}^0) are measured; these wavelengths correspond to a surface separation distance of $D = 0$. After these surfaces are separated, the new wavelength of the odd-ordered fringe, λ_n^D, is measured and converted to an absolute separation distance via Equation 1.19, where μ is the refractive index of the medium and $\bar{\mu} = \mu_{mica}/\mu$. In Chapters 2 and 3, forces are measured between one back-silvered mica surface and one thin gold surface, rather than between two symmetric mica surfaces. In this asymmetric interferometer, all FECO fringes are even as all of the standing wave solutions have nodes at the center between the gold and silver layers. Equation 1.19 is still valid for asymmetric interferometers, and the wavelengths λ_n^0 and λ_{n-1}^0 are measured for adjacent even fringes.

$$\tan\left(\frac{2\pi\mu D}{\lambda_n^D}\right)=\frac{2\bar{\mu}\sin\left(\dfrac{1-\lambda_n^0/\lambda_n^D}{1-\lambda_n^0/\lambda_{n-1}^0}\pi\right)}{\left(1+\bar{\mu}^2\right)\cos\left(\dfrac{1-\lambda_n^0/\lambda_n^D}{1-\lambda_n^0/\lambda_{n-1}^0}\pi\right)\pm\left(\bar{\mu}^2-1\right)} \tag{1.19}$$

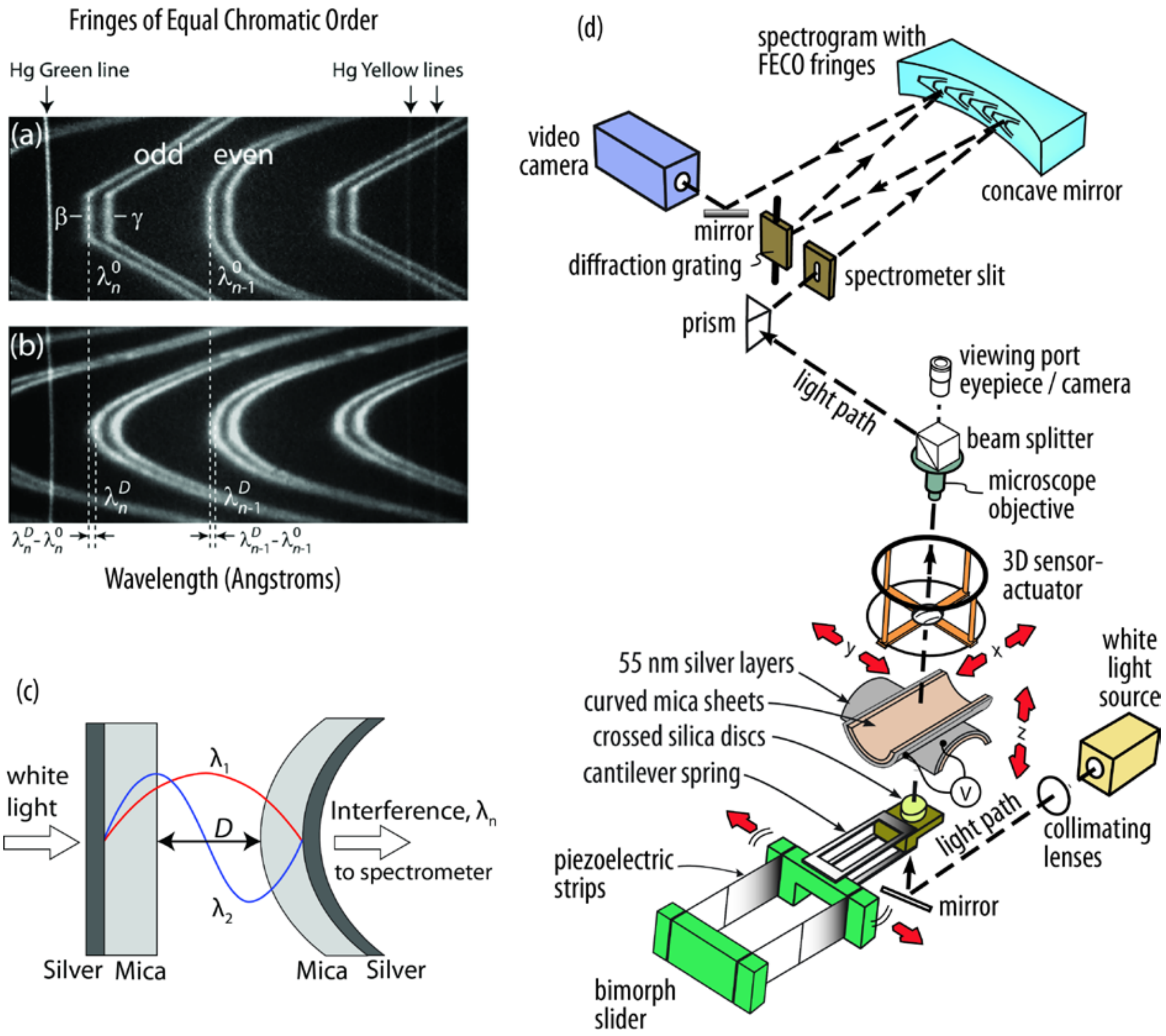

Figure 1.4: Multiple beam interferometry in the surface forces apparatus. (a) Fringes of Equal Chromatic Order (FECO) pattern for two symmetric back-silvered mica surfaces in contact. The FECO fringes appear as doublets because mica is birefringent, with refractive indices β and γ. The flattened area in the middle of the frame represents the deformed contact area between the surfaces that is in strong adhesive contact. The vertical spectral mercury (Hg) lines provide reference wavelengths to calibrate the absolute wavelength of the fringes. (b) FECO pattern when the mica surfaces are separated by ~10 nm. (c) Schematic of the mica surfaces. (d) The path of light through the SFA.[88]

1.9.2 Replica Exchange Molecular Dynamics Simulations

The SFA provides direct and quantitative measurements of the total intermolecular forces at surfaces; however, the specific interactions and orientations of molecules must be *inferred* from the forms of the measured force profiles or confirmed with complementary techniques. In Chapter 3, we compliment SFA measurements of adhesive proteins and peptides at organic surfaces with a computational technique known as Replica Exchange Molecular Dynamics (REMD), which we use to simulate the conformations and energetics of peptides at surfaces. An extension of Markov-Chain Monte-Carlo simulations, REMD is a technique in the canonical thermodynamic ensemble that enhances the sampling of systems that tend to get trapped in local—rather than global—energetic minima.[89] REMD is particularly well-suited for simulating the conformational space of proteins at surfaces, where the protein length and the array of amino acid chemistries lead to complex and stubborn energy landscapes.[90]

REMD utilizes the concept of "parallel tempering." To begin, *N* replicas of a system are initialized at different temperatures, T_n (n = 1,…, N). Molecular dynamics trajectories are used within each replica, where the Hamiltonian is composed of potentials such as parameterized Lennard-Jones and Coulomb interactions.[89,90] At regular time intervals in the simulation, replicas at adjacent temperatures, T_i and T_j, may be swapped based on Metropolis-Hastings criterion:[91,92]

$$\Delta = (\beta_i - \beta_j)(E_i - E_j) \tag{1.20}$$

$$P^{acc}(T_i \leftrightarrow T_j) = \min(1, \exp[-\Delta]) \tag{1.21}$$

where $\beta_i = 1/k_B T_i$ is the reciprocal thermodynamic temperature, E_i is the potential energy of replica *i*, and P^{acc} is the probability of accepting the switch between replicas *i* and *j*. When $\Delta \leq 0$, the switch is always performed; when $\Delta > 0$, the switch is performed with the probability $P = \exp[-\Delta]$. Running the replicas at many elevated temperatures, and allowing switching between the replicas, ensures that the final replica trajectory at room temperature has traversed the entire energy landscape.

1.10 References

(1) Newton, I. *Opticks: Or a Treatise of the Reflections, Refractions, Inflections, and Colours of Light*; London, 1704.

(2) Israelachvili, J. N. *Intermolecular and Surface Forces: Revised Third Edition*; Academic Press, 2011.

(3) Israelachvili, J.; Ruths, M. Brief History of Intermolecular and Intersurface Forces in Complex Fluid Systems. *Langmuir* **2013**, *29*, 9605–9619.

(4) Boscovich, R. J. *Philosophiae Naturalis Theoria*, English Tr.; Vienna, 1758.

(5) Israelachvili, J.; Wennerström, H. Role of Hydration and Water Structure in Biological and Colloidal Interactions. *Nature* **1996**, *379*, 219–225.

(6) Lee, B. P.; Messersmith, P. B.; Israelachvili, J. N.; Waite, J. H. Mussel-Inspired Adhesives and Coatings. *Annu. Rev. Mater. Res.* **2011**, *41*, 99–132.

(7) Chandler, D. Interfaces and the Driving Force of Hydrophobic Assembly. *Nature* **2005**, *437*, 640–647.

(8) Dolgin, E. The Sticking Point. *Nat. Med.* **2013**, *19*, 124–125.

(9) Schrödinger, E. An Undulatory Theory of the Mechanics of Atoms and Molecules. *Phys. Rev.* **1926**, *28*, 1049–1070.

(10) Johnson, K. L.; Kendall, K.; Roberts, A. D. Surface Energy and the Contact of Elastic Solids. *Proc. R. Soc. A Math. Phys. Eng. Sci.* **1971**, *324*, 301–313.

(11) Leckband, D.; Israelachvili, J. Intermolecular Forces in Biology. *Q. Rev. Biophys.* **2001**, *34*, 105.

(12) Zeng, H. *Polymer Adhesion, Friction, and Lubrication*; John Wiley & Sons, 2013.

(13) Jong, H. B. de; Kruyt, H. Coacervation (partial Miscibility in Colloid Systems). *Proc K. Ned. Akad.* **1929**.

(14) Derjaguin, B.; Landau, L. Theory of the Stability of Strongly Charged Lyophobic Sols and of the Adhesion of Strongly Charged Particles in Solutions of Electrolytes. *Prog. Surf. Sci.* **1993**, *43*, 30–59.

(15) Verwey, E. J. W.; Overbeek, J. T. G.; Overbeek, J. T. G. *Theory of the Stability of Lyophobic Colloids*; Courier Corporation, 1948.

(16) Lifshitz, E. M. The Theory of Molecular Attractive Forces between Solids. *Sov. Phys. Jetp-USSR* **1956**, *2*, 73–83.

(17) Dzyaloshinskii, I. E.; Lifshitz, E. M.; Pitaevskii, L. P. General Theory of Van Der Waals Forces. *Sov. Phys. Uspekhi* **1961**, *4*, 153–176.

(18) Hogg, R.; Healy, T. W.; Fuerstenau, D. W. Mutual Coagulation of Colloidal Dispersions. *Trans. Faraday Soc.* **1966**, *62*, 1638.

(19) Israelachvili, J. N.; Adams, G. E. Measurement of Forces between Two Mica Surfaces in Aqueous Electrolyte Solutions in the Range 0–100 Nm. *J. Chem. Soc. Faraday Trans. 1 Phys. Chem. Condens. Phases* **1978**, *74*, 975.

(20) Pashley, R. .; Israelachvili, J. . Dlvo and Hydration Forces between Mica Surfaces in Mg2+, Ca2+, Sr2+, and Ba2+ Chloride Solutions. *J. Colloid Interface Sci.* **1984**, *97*, 446–455.

(21) Ducker, W. A.; Senden, T. J.; Pashley, R. M. Direct Measurement of Colloidal Forces Using an Atomic Force Microscope. *Nature* **1991**, *353*, 239–241.

(22) Horn, R. G.; Smith, D. T.; Haller, W. Surface Forces and Viscosity of Water Measured between Silica Sheets. *Chem. Phys. Lett.* **1989**, *162*, 404–408.

(23) Grabbe, A.; Horn, R. G. Double-Layer and Hydration Forces Measured between Silica Sheets Subjected to Various Surface Treatments. *J. Colloid Interface Sci.* **1993**, *157*, 375–383.

(24) Pashley, R. M.; Israelachvili, J. N. A Comparison of Surface Forces and Interfacial Properties of Mica in Purified Surfactant Solutions. *Colloids and Surfaces* **1981**, *2*, 169–187.

(25) Marra, J.; Israelachvili, J. Direct Measurements of Forces between Phosphatidylcholine and Phosphatidylethanolamine Bilayers in Aqueous Electrolyte Solutions. *Biochemistry* **1985**, *24*, 4608–4618.

(26) Anderson, T. H.; Donaldson, S. H.; Zeng, H.; Israelachvili, J. N. Direct Measurement of Double-Layer, van Der Waals, and Polymer Depletion Attraction Forces between Supported Cationic Bilayers. *Langmuir* **2010**, *26*, 14458–14465.

(27) Donaldson, S. H.; Lee, C. T.; Chmelka, B. F.; Israelachvili, J. N. General Hydrophobic Interaction Potential for Surfactant/lipid Bilayers from Direct Force Measurements between Light-Modulated Bilayers. *Proceedings of the National Academy of Sciences*, 2011, *108*, 15699–15704.

(28) Smith, C. P.; Maeda, M.; Atanasoska, L.; White, H. S.; McClure, D. J. Ultrathin Platinum Films on Mica and the Measurement of Forces at the Platinum/water Interface. *J. Phys. Chem.* **1988**, *92*, 199–205.

(29) Valtiner, M.; Kristiansen, K.; Greene, G. W.; Israelachvili, J. N. Effect of Surface Roughness and Electrostatic Surface Potentials on Forces between Dissimilar Surfaces in Aqueous Solution. *Adv. Mater.* **2011**, *23*, 2294–2299.

(30) Valtiner, M.; Banquy, X.; Kristiansen, K.; Greene, G. W.; Israelachvili, J. N. The Electrochemical Surface Forces Apparatus: The Effect of Surface Roughness, Electrostatic Surface Potentials, and Anodic Oxide Growth on Interaction Forces, and Friction between Dissimilar Surfaces in Aqueous Solutions. *Langmuir* **2012**, *28*, 13080–13093.

(31) Larson, I.; Drummond, C. J.; Chan, D. Y. C.; Grieser, F. Direct Force Measurements between Titanium Dioxide Surfaces. *J. Am. Chem. Soc.* **1993**, *115*, 11885–11890.

(32) Ball, P. Beyond the Bond. *Nature* **2011**, *469*, 26–28.

(33) Werner, A. Ueber Haupt- Und Nebenvalenzen Und Die Constitution Der Ammoniumverbindungen. *Justus Liebig's Ann. der Chemie* **1902**, *322*, 261–296.

(34) Moore, T. S.; Winmill, T. F. The State of Amines in Aqueous Solution. *J. Chem. Soc. Trans.* **1912**, *101*, 1635.

(35) Latimer, W. M.; Rodebush, W. H. Polarity and Ionization from the Standpoint of the Lewis Theory of Valence. *J. Am. Chem. Soc.* **1920**, *42*, 1419–1433.

(36) Huggins, M. L. Hydrogen Bridges in Organic Compounds. *J. Org. Chem.* **1936**, *01*, 407–456.

(37) Pauling, L. *The Nature of the Chemical Bond*, Third Edit.; Cornell University Press, 1960.

(38) Arunan, E.; Desiraju, G. R.; Klein, R. A.; Sadlej, J.; Scheiner, S.; Alkorta, I.; Clary, D. C.; Crabtree, R. H.; Dannenberg, J. J.; Hobza, P.; et al. Defining the Hydrogen Bond: An Account (IUPAC Technical Report). *Pure Appl. Chem.* **2011**, *83*, 1619–1636.

(39) Gilli, G.; Gilli, P. *The Nature of the Hydrogen Bond: Outline of a Comprehensive Hydrogen Bond Theory*; OUP Oxford, 2009.

(40) Kauzmann, W. Some Factors in the Interpretation of Protein Denaturation. *Adv. Protein Chem.* **1959**, *14*, 1–63.

(41) Tanford, C. Contribution of Hydrophobic Interactions to the Stability of the Globular Conformation of Proteins. *J. Am. Chem. Soc.* **1962**, *84*, 4240–4247.

(42) Rajamani, S.; Truskett, T. M.; Garde, S. Hydrophobic Hydration from Small to Large Lengthscales: Understanding and Manipulating the Crossover. *Proc. Natl. Acad. Sci. U. S. A.* **2005**, *102*, 9475–9480.

(43) Davis, J. G.; Gierszal, K. P.; Wang, P.; Ben-Amotz, D. Water Structural Transformation at Molecular Hydrophobic Interfaces. *Nature* **2012**, *491*, 582–585.

(44) Chaimovich, A.; Shell, M. S. Length-Scale Crossover of the Hydrophobic Interaction in a Coarse-Grained Water Model. *Phys. Rev. E. Stat. Nonlin. Soft Matter Phys.* **2013**, *88*, 052313.

(45) Jamadagni, S. N.; Godawat, R.; Garde, S. Hydrophobicity of Proteins and Interfaces: Insights from Density Fluctuations. *Annu. Rev. Chem. Biomol. Eng.* **2011**, *2*, 147–171.

(46) Lum, K.; Chandler, D.; Weeks, J. D. Hydrophobicity at Small and Large Length Scales. *J. Phys. Chem. B* **1999**, *103*, 4570–4577.

(47) Lum, K.; Luzar, A. Pathway to Surface-Induced Phase Transition of a Confined Fluid. *Phys. Rev. E* **1997**, *56*, R6283–R6286.

(48) Cerdeiriña, C. A.; Debenedetti, P. G.; Rossky, P. J.; Giovambattista, N. Evaporation Length Scales of Confined Water and Some Common Organic Liquids. *J. Phys. Chem. Lett.* **2011**, *2*, 1000–1003.

(49) Sharma, S.; Debenedetti, P. G. Free Energy Barriers to Evaporation of Water in Hydrophobic Confinement. *J. Phys. Chem. B* **2012**, *116*, 13282–13289.

(50) Leung, K.; Luzar, A.; Bratko, D. Dynamics of Capillary Drying in Water. *Phys. Rev. Lett.* **2003**, *90*, 065502.

(51) Hammer, M. U.; Anderson, T. H.; Chaimovich, A.; Shell, M. S.; Israelachvili, J. The Search for the Hydrophobic Force Law. *Faraday Discuss.* **2010**, *146*, 299.

(52) Meyer, E. E.; Rosenberg, K. J.; Israelachvili, J. Recent Progress in Understanding Hydrophobic Interactions. *Proc. Natl. Acad. Sci.* **2006**, *103*, 15739–15746.

(53) Israelachvili, J.; Pashley, R. The Hydrophobic Interaction Is Long Range, Decaying Exponentially with Distance. *Nature* **1982**, *300*, 341–342.

(54) Christenson, H. K.; Claesson, P. M. Direct Measurements of the Force between Hydrophobic Surfaces in Water. *Adv. Colloid Interface Sci.* **2001**, *91*, 391–436.

(55) Tabor, R. F.; Wu, C.; Grieser, F.; Dagastine, R. R.; Chan, D. Y. C. Measurement of the Hydrophobic Force in a Soft Matter System. *J. Phys. Chem. Lett.* **2013**, *4*, 3872–3877.

(56) Faghihnejad, A.; Zeng, H. Hydrophobic Interactions between Polymer Surfaces: Using Polystyrene as a Model System. *Soft Matter* **2012**, *8*, 2746.

(57) Pashley, R.; McGuiggan, P.; Ninham, B.; Evans, D. Attractive Forces between Uncharged Hydrophobic Surfaces: Direct Measurements in Aqueous Solution. *Science (80-.).* **1985**, *229*, 1088–1089.

(58) Mastropietro, D. J.; Ducker, W. A. Forces between Hydrophobic Solids in Concentrated Aqueous Salt Solution. *Phys. Rev. Lett.* **2012**, *108*, 106101.

(59) Meyer, E. E.; Lin, Q.; Hassenkam, T.; Oroudjev, E.; Israelachvili, J. N. Origin of the Long-Range Attraction between Surfactant-Coated Surfaces. *Proc. Natl. Acad. Sci.* **2005**, *102*, 6839–6842.

(60) Perkin, S.; Kampf, N.; Klein, J. Long-Range Attraction between Charge-Mosaic Surfaces across Water. *Phys. Rev. Lett.* **2006**, *96*, 038301.

(61) Silbert, G.; Ben-Yaakov, D.; Dror, Y.; Perkin, S.; Kampf, N.; Klein, J. Long-Ranged Attraction between Disordered Heterogeneous Surfaces. *Phys. Rev. Lett.* **2012**, *109*, 168305.

(62) Jho, Y. S.; Brewster, R.; Safran, S. A.; Pincus, P. A. Long-Range Interaction between Heterogeneously Charged Membranes. *Langmuir* **2011**, *27*, 4439–4446.

(63) Attard, P. Nanobubbles and the Hydrophobic Attraction. *Adv. Colloid Interface Sci.* **2003**, *104*, 75–91.

(64) Parker, J. L.; Claesson, P. M.; Attard, P. Bubbles, Cavities, and the Long-Ranged Attraction between Hydrophobic Surfaces. *J. Phys. Chem.* **1994**, *98*, 8468–8480.

(65) Stevens, H.; Considine, R. F.; Drummond, C. J.; Hayes, R. A.; Attard, P. Effects of Degassing on the Long-Range Attractive Force between Hydrophobic Surfaces in Water. *Langmuir* **2005**, *21*, 6399–6405.

(66) Pashley, R. . DLVO and Hydration Forces between Mica Surfaces in Li+, Na+, K+, and Cs+ Electrolyte Solutions: A Correlation of Double-Layer and Hydration Forces with Surface Cation Exchange Properties. *J. Colloid Interface Sci.* **1981**, *83*, 531–546.

(67) Pashley, R. M. Hydration Forces between Mica Surfaces in Electrolyte Solutions. *Adv. Colloid Interface Sci.* **1982**, *16*, 57–62.

(68) Israelachvili, J. N.; Pashley, R. M. Molecular Layering of Water at Surfaces and Origin of Repulsive Hydration Forces. *Nature* **1983**, *306*, 249–250.

(69) Rau, D. C.; Lee, B.; Parsegian, V. A. Measurement of the Repulsive Force between Polyelectrolyte Molecules in Ionic Solution: Hydration Forces between Parallel DNA Double Helices. *Proc. Natl. Acad. Sci.* **1984**, *81*, 2621–2625.

(70) Rand, R. P.; Fuller, N.; Parsegian, V. A.; Rau, D. C. Variation in Hydration Forces between Neutral Phospholipid Bilayers: Evidence for Hydration Attraction. *Biochemistry* **1988**, *27*, 7711–7722.

(71) Israelachvili, J. N.; McGuiggan, P. M. Forces Between Surfaces in Liquids. *Science (80-.).* **1988**, *241*, 795–800.

(72) Donaldson, S. H.; Das, S.; Gebbie, M. A.; Rapp, M.; Jones, L. C.; Roiter, Y.; Koenig, P. H.; Gizaw, Y.; Israelachvili, J. N. Asymmetric Electrostatic and Hydrophobic-Hydrophilic Interaction Forces between Mica Surfaces and Silicone Polymer Thin Films. *ACS Nano* **2013**, *7*, 10094–10104.

(73) Donaldson, S. H.; Røyne, A.; Kristiansen, K.; Rapp, M. V; Das, S.; Gebbie, M. A.; Lee, D. W.; Stock, P.; Valtiner, M.; Israelachvili, J. Developing a General Interaction Potential for Hydrophobic and Hydrophilic Interactions. *Langmuir* **2015**, *31*, 2051–2064.

(74) Banquy, X.; Kristiansen, K.; Lee, D. W.; Israelachvili, J. N. Adhesion and Hemifusion of Cytoplasmic Myelin Lipid Membranes Are Highly Dependent on the Lipid Composition. *Biochim. Biophys. Acta* **2012**, *1818*, 402–410.

(75) Sánchez-Iglesias, A.; Grzelczak, M.; Altantzis, T.; Goris, B.; Pérez-Juste, J.; Bals, S.; Van Tendeloo, G.; Donaldson, S. H.; Chmelka, B. F.; Israelachvili, J. N.; et al. Hydrophobic Interactions Modulate Self-Assembly of Nanoparticles. *ACS Nano* **2012**, *6*, 11059–11065.

(76) Tabor, D.; Winterton, R. The Direct Measurement of Normal and Retarded van Der Waals Forces. *Proc. R. Soc. London. Ser. A* **1969**, *312*, 435–450.

(77) Israelachvili, J. N.; Tabor, D. The Measurement of Van Der Waals Dispersion Forces in the Range 1.5 to 130 Nm. *Proc. R. Soc. A Math. Phys. Eng. Sci.* **1972**, *331*, 19–38.

(78) Israelachvili, J.; Tabor, D. Van Der Waals Forces: Theory and Experiment. *Prog. Surf. Membr. Sci.* **1973**, *7*, 1–55.

(79) Israelachvili, J. N.; Adams, G. E. Direct Measurement of Long Range Forces between Two Mica Surfaces in Aqueous KNO3 Solutions. *Nature* **1976**, *262*, 774–776.

(80) Israelachvili, J. N.; McGuiggan, P. M.; Homola, A. M. Dynamic Properties of Molecularly Thin Liquid Films. *Science* **1988**, *240*, 189–191.

(81) Horn, R. G. Direct Measurement of Structural Forces between Two Surfaces in a Nonpolar Liquid. *J. Chem. Phys.* **1981**, *75*, 1400.

(82) Pashley, R. M.; Israelachvili, J. N. Molecular Layering of Water in Thin Films between Mica Surfaces and Its Relation to Hydration Forces. *J. Colloid Interface Sci.* **1984**, *101*, 511–523.

(83) Klein, J.; Kamiyama, Y.; Yoshizawa, H.; Israelachvili, J. N.; Fredrickson, G. H.; Pincus, P.; Fetters, L. J. Lubrication Forces between Surfaces Bearing Polymer Brushes. *Macromolecules* **1993**, *26*, 5552–5560.

(84) Wong, J. Y. Direct Measurement of a Tethered Ligand-Receptor Interaction Potential. *Science (80-.).* **1997**, *275*, 820–822.

(85) Bhushan, B.; Israelachvili, J.; Landman, U. Nanotribology: Friction, Wear and Lubrication at the Atomic Scale. *Nature* **1995**.

(86) Yoshizawa, H.; McGuiggan, P.; Israelachvili, J. Identification of a Second Dynamic State during Stick-Slip Motion. *Science* **1993**, *259*, 1305–1308.

(87) Rapp, M. V; Donaldson, S. H.; Gebbie, M. A.; Das, S.; Kaufman, Y.; Gizaw, Y.; Koenig, P.; Roiter, Y.; Israelachvili, J. N. Hydrophobic, Electrostatic, and Dynamic Polymer Forces at Silicone Surfaces Modified with Long-Chain Bolaform Surfactants. *Small* **2015**, *11*, 2058–2068.

(88) Israelachvili, J.; Min, Y.; Akbulut, M.; Alig, A.; Carver, G.; Greene, W.; Kristiansen, K.; Meyer, E.; Pesika, N.; Rosenberg, K.; et al. Recent Advances in the Surface Forces Apparatus (SFA) Technique. *Reports Prog. Phys.* **2010**, *73*, 036601.

(89) Sugita, Y.; Okamoto, Y. Replica-Exchange Molecular Dynamics Method for Protein Folding. *Chem. Phys. Lett.* **1999**, *314*, 141–151.

(90) Shea, J.-E.; Levine, Z. A. Studying the Early Stages of Protein Aggregation Using Replica Exchange Molecular Dynamics Simulations. *Methods Mol. Biol.* **2016**, *1345*, 225–250.

(91) Metropolis, N.; Rosenbluth, A. W.; Rosenbluth, M. N.; Teller, A. H.; Teller, E. Equation of State Calculations by Fast Computing Machines. *J. Chem. Phys.* **1953**, *21*, 1087.

(92) Hastings, W. K. Monte Carlo Sampling Methods Using Markov Chains and Their Applications. *Biometrika* **1970**, *57*, 97–109.

CHAPTER 2

The Self-Assembly and Adhesive Interactions of Surfactants and Polyelectrolytes at Hydrophobic Silicone Surfaces

2.1 Hydrophobic, Electrostatic, and Dynamic Polymer Forces at Silicone Surfaces Modified with Long-Chain Bolaform Surfactants

Rapp, M. V.; Donaldson, S. H.; Gebbie, M. A.; Das, S.; Kaufman, Y.; Gizaw, Y.; Koenig, P.; Roiter, Y.; Israelachvili, J. N. (2015) ***Small***, 11 (17):2058-2068

2.1.1 Abstract

Surfactant self-assembly on surfaces is an effective way to tailor the complex forces at and between hydrophobic-water interfaces. Here, we demonstrate the range of structures and forces that are possible at surfactant-adsorbed hydrophobic surfaces: certain long-chain bolaform surfactants—containing a polydimethylsiloxane (PDMS) mid-block domain and two cationic α, ω-quarternary ammonium end-groups—readily adsorb onto thin PDMS films and form dynamically fluctuating nanostructures. Through measurements with the surface forces apparatus (SFA), we find that these soft protruding nanostructures display polymer-like exploration behavior at the PDMS surface and give rise to a long-ranged, temperature- and rate-dependent attractive bridging force (*not* due to viscous forces) on approach to a hydrophilic bare mica surface. Coulombic interactions between the cationic surfactant end-groups and negatively-charged mica result in a rate-dependent polymer bridging force during separation as the hydrophobic surfactant mid-blocks are pulled out from the PDMS interface, yielding strong adhesion energies. Thus, (i) we highlight the versatile array of surfactant

structures that may form at hydrophobic surfaces, (ii) emphasize the need to consider the interaction *dynamics* of such self-assembled polymer layers, and (iii) show that long-chain surfactants can promote robust adhesion in aqueous solutions.

2.1.2 Introduction

Silicone products are ubiquitous in modern life, spanning from cosmetic products at home to designer surfaces in the laboratory. Boasting a favorable set of material properties—including hydrophobicity, biocompatibility, optical transparency, low chemical reactivity, low surface tension, and unique tribological properties—viscoelastic silicones are widely used in applications such as biomedical implants,[1,2] contact lenses,[3] scaffolds for tissue engineering,[4] and lubricating films.[5,6] Polydimethylsiloxane (PDMS) is the most commonly used silicone compound in research, industrial, and consumer product applications. In the lab, PDMS can be (i) molded into microfluidic channels for lab-on-a-chip diagnostic experiments,[7] (ii) patterned with lithography to form micron-scale surface features that control adhesion, friction, and wettability,[8,9] or (iii) functionalized and dispersed in water to form stimuli-responsive hydrogels[10,11] and emulsions.[12] In consumer products such as fabric softeners and cosmetic creams, PDMS is used to form thin lubricating films that impart a favorable tactile sensation onto clothes or skin.[13]

In many of these practical applications, the desired functionality of the PDMS material—*in situ* wet adhesion, lubrication, or colloidal stabilization—is based upon the aqueous interfacial properties of either a plain or a functionalized PDMS surface. To understand the interfacial forces that exist at PDMS surfaces, a method to reliably prepare thin (6-10 nm), smooth (~0.3 nm rms roughness), and covalently-grafted collapsed-brush PDMS films on extended gold or mica substrates was developed previously.[14] These PDMS films serve as nano-thin templates to explore the interfacial forces at plain or functionalized silicone surfaces. When exposed to water, the hydrophobic surface of PDMS dewets, and water forms large contact angles on the surface (advancing contact angle, θ_A = 113° ± 2°, and receding contact angle, θ_R = 103° ± 2°). Through measurements with the surface forces apparatus (SFA), the PDMS surface was found to display a negative surface charge in solution at pH > 3 (~ -100 ± 20 mV at pH 10 in 1 mM NaCl), a characteristic of most hydrophobic surfaces.[15–18] The interaction between the negatively charged PDMS surface and a negatively charged mica surface at pH 10 results in a monotonic repulsion between the surfaces that is due to the repulsive osmotic pressure between the surface's overlapping electric double layers at large distances (> ~1 Debye screening length) and due to the steric hydration forces between the surfaces at small separation distances (< ~2 nm).

The negative charge on the PDMS surface can be problematic for certain applications. In a wet environment, attractive van der Waals forces are not strong enough to overcome the repulsive electrostatic and hydration forces that exist between a PDMS surface and another negatively charged surface (such as a mineral, metal, cotton, or keratin). In applications that require strong binding of a PDMS interface to a negatively charged surface in solution—say, securing a prosthetic silicone implant onto bone, or binding lubricating thin films of silicone onto hair—PDMS surface functionalization is required for robust adhesion. The hydrophobicity of the PDMS surface can be exploited by adsorbing amphiphilic molecules onto the surface, leading to non-destructive physisorbed surface modifications that enhance the adhesive potential of PDMS. Amphiphilic polymers[19,20] and polyelectrolytes[21–

[23] are frequently adsorbed onto hydrophobic surfaces to reduce friction or wear at hydrophobic polymer surfaces. Intrinsically unstructured proteins extracted from the adhesive plaques of marine mussels adsorb to hydrophobic surfaces via hydrophobic amino acid residues, and mediate adhesion to a hydrophilic mineral surface.[24–26] Quaternary ammonium polyelectrolytes function as biofunctional coatings when adsorbed onto PDMS and facilitate the attachment and growth of bone marrow cells.[27] However, the physisorption of polymeric surfactants has not been explicitly used to promote adhesion between hydrophobic and hydrophilic surfaces.

The adsorption of adhesion-promoting amphiphiles or surfactants onto a hydrophobic surface is fundamentally interesting when considering the intermolecular forces that determine the equilibrium geometry of the surface aggregates. In bulk solution above the critical micelle concentration (CMC), the self-assembly of ionic surfactants depends on a balance of forces between the hydrophobic attractions between surfactant tails, the electrostatic repulsion between surfactant head-groups, and geometric packing constraints.[28] Comparatively, ionic surfactants self-assemble at hydrophobic surfaces above a critical aggregation concentration (CAC, where CAC < CMC). The balance of forces that govern surface assembly becomes more complex as additional parameters are introduced, namely the hydrophobic attraction between the surfactant tails and the surface, and the geometric constraints of the surface. Previous research has shown that short-chain aliphatic surfactants (cetyl trimethylammonium halides, sodium dodecyl sulfate, alkylpoly[ethylene oxide], C_{12} zwitterionic surfactants) adsorb onto solid hydrophobic surfaces (crystalline graphite, methylated silica) and may form a variety of aggregate morphologies (monolayers, flat discs, hemimicelles, hemicylinders) that are dependent upon surfactant geometry, headgroup type, the surfactant concentration, and the type of hydrophobic surface.[29–34] Force measurements with the atomic force microscope (AFM) indicate that these adsorbed ionic layers give rise to time-invariant and exponentially decaying double layer forces between an AFM probe and the surfactant-adsorbed substrate.[31,35] While there is undoubtedly a constant exchange of surfactant monomers between the surface aggregates and solution, the previous reports on these aggregates indicate that their shapes do not dynamically change or fluctuate in a significant way over the timescale of an AFM measurement (with typical AFM line scan rates of 0.1 to 1 μm/s). The static nature and relatively simple geometries of these surface aggregates perhaps are not surprising, as the majority of the studied surfactants adsorb from small spherical micelles in solution to form surface features that are similar in dimension to the size of their bulk micelles (~2-5 nm). We hypothesize that increasing the complexity of the system—including adding long polymer chains and multiple headgroups to the adsorbing surfactants, altering the structure of the bulk surfactant aggregates, and using grafted chains of soft polymers as the hydrophobic surface—may result in more complex morphologies and dynamic (time-dependent) behaviors at self-assembled surfaces.

In this work, we investigate the self-assembly phenomenon of a long-chain bolaform surfactant as it adsorbs onto a grafted PDMS brush film. The bolaform surfactant (bolaquat-PDMS or bq-PDMS, Figure 2.1A) contains a linear PDMS mid-block domain and cationic α, ω-quarternary ammonium headgroups. As shown schematically in Figure 2.1B, bq-PDMS forms vesicles in solution; both cryogenic transmission electron microscopy (TEM) images (Figure 2.1C) and dynamic light scattering (DLS) confirmed that the vesicles are spherical with an average diameter of ~100 nm. In the following experiments, we adsorbed vesicles of bq-PDMS onto gold-grafted PDMS brush films (Au-PDMS, Figure 2.1D) to obtain a bq-

PDMS functionalized interface. Using the SFA, we measured the normal interaction forces in aqueous solution between (i) a negatively-charged mica surface and an adsorbed bq-PDMS film and (ii) two symmetric bq-PDMS films. The results show that bq-PDMS self-assembles into soft, fluctuating nanostructures on the grafted-PDMS surface that give rise to dynamic polymer bridging forces between extended surfaces. Furthermore, a sparingly low concentration of bq-PDMS mediates exceptionally strong adhesion between mineral (mica) and polymer (PDMS) surfaces.

2.1.3 Materials and Methods

Grafted PDMS film preparation: The full details of the Au-PDMS and mica-PDMS film preparation are described in our previous work.[14] To prepare Au-PDMS films for SFA measurements, cylindrical disks (area ~ 1 cm^2) of molecularly smooth gold are produced through a mica-templating technique. These clean gold surfaces are immersed in a 1 mM solution of 11-amino-1-undecanethiol hydrochloride (Sigma-Aldrich) for 2 hours and then rinsed with ethanol, forming an amine-functionalized self-assembled monolayer (SAM). The SAM surfaces are submerged and heated in neat monoglycidyl ether-terminated polydimethylsiloxane (MW = 5,000 g mol^{-1}, Sigma-Aldrich) at 130°C for 1 hour. A click-chemistry reaction proceeds between the PDMS epoxide ring and the SAM amine group, to produce a covalently grafted PDMS film. Non-grafted PDMS is removed from the surface with cycles of rinsing and sonicating in toluene and ethanol.

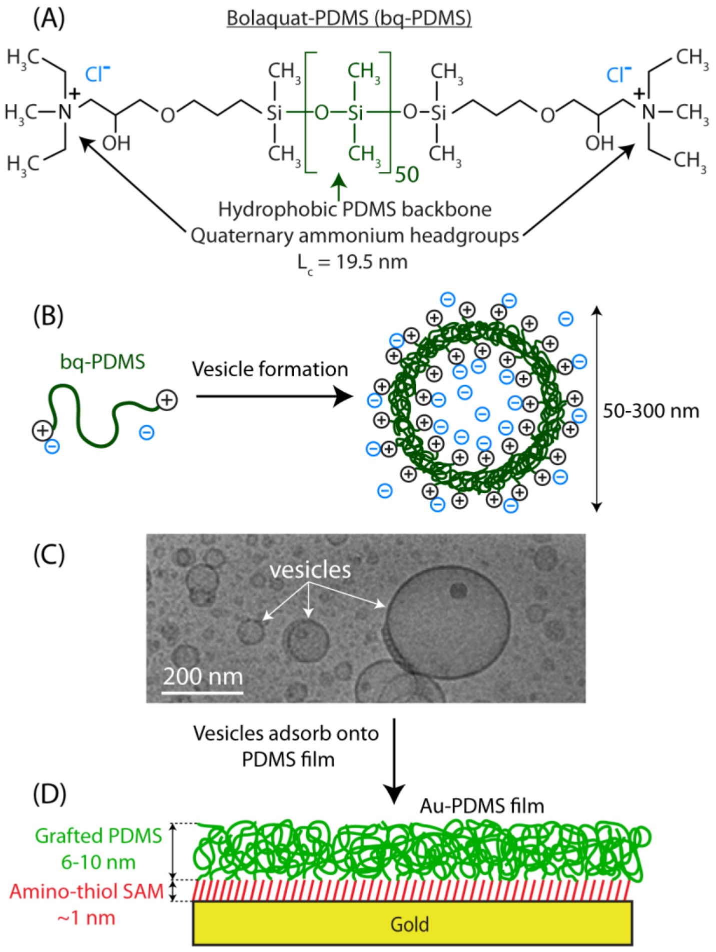

Figure 2.1: The bolaform polysurfactant vesicles and grafted silicone surfaces used in this study. (A) The chemical structure of bolaquat-PDMS (bq-PDMS). (B) A schematic representation of bq-PDMS vesicles. (C) A representative cryo-TEM image of 1% v/v bq-PDMS dispersed in water. The bq-PDMS typically forms spherical single unilamellar vesicles from ~50 nm up to ~300 nm in diameter. Some small bq-PDMS aggregates (~10-20 nm diameter) are also observed. (D) A schematic representation of the thin, covalently-grafted PDMS films on gold that are used in this study.

In the symmetric experiment between two bq-PDMS surfaces, one mica-PDMS surface and one Au-PDMS surface were used instead of two Au-PDMS surfaces, because an insufficient amount of light transmits between two Au-PDMS surfaces and FECO is not observed. To prepare a mica-PDMS film,[51] a clean mica surface is treated with ozone for 20 minutes to activate the surface hydroxyl groups. The mica surface is amine-functionalized through immersion in a 1 vol% solution of (3-trimethoxysilylpropyl)diethylenetriamine (DETAS, Gelest Inc., Morrisville, PA) in methyl ethyl ketone (MEK, Sigma-Aldrich) for 2 hours. Next the surface is rinsed with ethanol, dried, immersed in monoglycidyl ether-terminated polydimethylsiloxane and then placed into a vacuum oven at 80°C for 60 hours. The remaining preparation steps are exactly the same on mica-PDMS as they are on Au-PDMS.

Bq-PDMS vesicle preparation and adsorption: Bq-PDMS (formally, α,ω-[diethylmethyl{isopropoxypropanol}ammonium chloride]-polydimethylsiloxane, MW = 4238 g mol^{-1}) was provided by the Proctor & Gamble Company (Cincinnati, Ohio). Bq-PDMS was mixed in hexylene glycol (~ 6.4*10^{-7} moles bq-PDMS/L hexylene glycol) to form stable bq-PDMS vesicles. Au- or mica-PDMS surfaces were immersed in a small vial (~2 mL) filled with the bq-PDMS/hexylene glycol mixture, and bq-PDMS vesicles were allowed to adsorb onto the surface for 1.5 hours. Varying the adsorption time from 1-3.5 hours did not alter the measured forces. Following the adsorption step, the reservoir of bq-PDMS/hexylene glycol surrounding the surface was replaced with a 1 mM NaCl pH ~ 10 solution through a solvent exchange procedure. The small vial (2 mL), containing the surface and bq-PDMS/hexylene glycol solution, was submerged in a larger vial (~30 mL) of 1 mM NaCl pH ~ 10 solution and was gently mixed for 1 minute. The small vial—containing a bq-PDMS/hexylene glycol mixture diluted 15x with aqueous solution—was then removed from the larger vial. This dilution procedure was performed 10 times (using a fresh 1 mM NaCl solution during each dilution) to ensure that only negligible amounts of non-adsorbed bq-PDMS and hexylene glycol could exist in the reservoir surrounding the target surface. The bq-PDMS surface, resting in the small vial, was then transferred under solution into the SFA for force measurements. During the adsorption, dilution, and transfer process, the bq-PDMS surface was kept continually under solution; if the bq-PDMS surfaces were exposed to air at any point in the preparation, the subsequent force measurements would return non-reproducible results, and the long-ranged attractive forces to mica (attributed to the bq-PDMS nanostructures) were not observed. This result is not surprising, as exposure to air collapses the self-assembled bq-PDMS aggregates, and most likely washes a significant portion of bq-PDMS from the Au-PDMS surface with the receding air-water interface.

SFA: SFA measurements were performed with an SFA 2000 (manufactured by SurForce Llc., Santa Barbara, California). The SFA results presented here are representative of force measurements performed over more than 10 separate experimental set-ups. Prior to all SFA experiments, the SFA system was allowed to fully equilibrate at a given temperature, until no thermal or mechanical drift was observed.

Cryo-TEM: Cryo-TEM images were performed with a Tecnai TEM at Proctor & Gamble's facilities in Cincinnati, Ohio. Bq-PDMS/hexylene glycol vesicle mixtures ($6.4*10^{-7}$ moles bq-PDMS/L hexylene glycol) were dispersed in water at a 1% v/v ratio. The introduction of the bq-PDMS vesicles into water did not alter the vesicle size, as confirmed with DLS. The samples were prepared for analysis by placing ~2 µl of sample onto a lacey carbon grid, blotting away the excess and plunging the specimen rapidly into liquid ethane using a controlled environment vitrification system. The frozen samples were stored under liquid nitrogen until being loaded into a Gatan model 626 cryo-stage. The specimens were then loaded into the TEM and imaged at 120 KV in low dose mode.

2.1.4 Dynamic vs Quasi-Static SFA Measurements

The SFA was used in this work to examine the interaction forces primarily between a bq-PDMS functionalized surface and a mica surface. The SFA provides distinct advantages in accuracy, visualization, and versatility for measuring force-distance curves between extended soft matter surfaces and structures.[36] The SFA utilizes a technique known as fringes of equal chromatic order (FECO), in which the wavelengths of light interference fringes are used to measure the absolute separation distance, D, between two extended cross-cylinder surfaces with an accuracy of ~ 1 Å.[37] The radius of the macroscopic interacting surfaces, $R \sim 2$ cm, is also measured by FECO. The interaction force between the two surfaces, F, is measured by the deflection of a double-cantilevered spring with a known spring constant, k. When measuring forces between attractive or adhesive surfaces, mechanical instabilities occur when the slope of the interaction force between the two surfaces equals the spring constant ($\mathrm{d}F/\mathrm{d}D = k$), and the surfaces rapidly jump into an adhesive contact on approach, or jump out of adhesive contact as the surfaces are separated. The FECO provide a real-time virtual image of the interacting surfaces during the force measurement, through which the separation distance (D), contact mechanics, adhesion, and deformations of the interacting surfaces can be determined. The SFA technique measures the absolute separation distance between the surfaces at all times, which allows for the accurate measurements of time-dependent forces (ranging from transient to long-equilibrating forces) that are frequently found in polymer or biological systems.

A typical force-distance curve plots the force scaled by radius (F/R) versus the surface separation distance (D). Typically the force, F, is normalized by the radius, R, to allow for comparison with separate experiments and techniques because interaction forces scale with *R*. An advantage of the SFA—which is important especially for the interactions examined in this work—is the ability to explore a wide range of surface approach and separation rates, *v*, which ranges from $v \sim 0.1$ to 10 nm/s. Two measurement techniques were used in the present study: (1) a "dynamic" technique and (2) a "quasi-static" technique. In a dynamic measurement, the surfaces are driven towards each other at a constant rate, $v \sim 2$-10 nm/s, while measuring the force instantaneously at each separation distance in the force curve. In a quasi-static measurement, the equilibrium force between the surfaces is measured after the surfaces are equilibrated for 30 seconds at a given separation distance. The surfaces are then moved to a new separation distance (step size ~ 5 nm) and allowed to equilibrate again for 30 s before measuring the equilibrium force ($v_{\text{average}} \sim 0.2$ nm/s). The quasi-static technique provides the most accurate equilibrium force measurements and can detect forces that may take tens of seconds to equilibrate, such as polymer bridging forces.[38] In both dynamic and quasi-static SFA measurements, the approach and separation rates are so slow that hydrodynamic (viscous) forces between the surfaces are negligible, and the measured forces are incontrovertibly due to interaction of a bq-PDMS film with a mica surface. The differences between quasi-static and dynamic measurements, and their implications on the physical interactions and structures of bq-PDMS, will be discussed in detail below.

To determine the interactions of the bq-PDMS film with a mica surface, the bq-PDMS was initially adsorbed, via vesicles, onto an Au-PDMS grafted layer. This bq-PDMS-coated surface was then mounted in the SFA opposite a clean mica surface for the force measurement while immersed in 1 mM NaCl, pH ~ 10 solution. As discussed below, the interactions during both approach and separation of the bq-PDMS at the target mica surface are strongly attractive. The approach and separation curves are both very complex and appear to be governed by somewhat different physical mechanisms, so we first discuss the approach in Section 2.1.

2.1.5 Asymmetric Interactions Between Bq-PDMS and Mica Surfaces During Approach

The interactions during approach of a bq-PDMS film and mica exhibit a long-range attractive jump-in to contact that depends sensitively on the rate of approach of the two surfaces, as shown in Figure 2.2A. At room temperature (T = 22°C), when a bq-PDMS film and mica are driven towards each other at a rate v ~ 6 nm/s (dynamic), an attractive force is first measured at D ~ 33 nm, and is followed by a jump into adhesive contact to the contact distance, D_0 = 10 nm (red points, Figure 2.2A). When the surface approach is quasi-static, the onset of attraction increases dramatically to D ~ 49 nm, and the surfaces subsequently jump into contact from a much greater distance (blue points, Figure 2.2A). Raising the temperature, from room temperature to T = 28 °C, results in the onset of attraction increasing further, to D ~ 58 nm (green points, Figure 2.2A). For comparison, the interaction of a clean Au-PDMS surface (i.e., in the absence of bq-PDMS) with a mica surface is also shown (black points, Figure 2.2A). As described previously,[14] the interaction is fully repulsive (in 1 mM NaCl solution at pH ~10). The maximum attractive electric double layer interaction between negatively charged mica and a fully-charged cationic surface (as might be expected for an adsorbed monolayer of bq-PDMS) is also shown for comparison (dashed black line, Figure 2.2A).

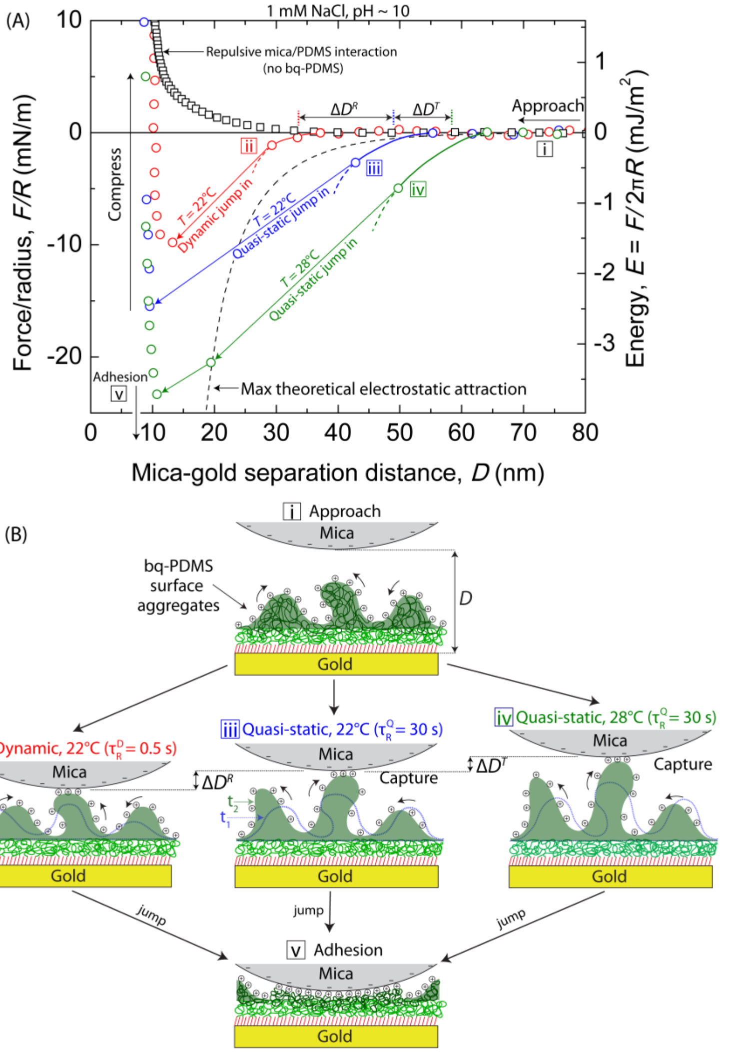

Figure 2.2: The interactions of a mica surface approaching a film of adsorbed bq-PDMS. (A) Comparative SFA force-distance measurements of the interaction between mica and an adsorbed bq-PDMS film, performed either dynamically (red circles, approach speed of v~6 nm/s) or quasi-statically (30 second equilibration periods were allowed after each approach step of ~5 nm). Quasi-static measurements are shown for T = 22°C (blue circles) and T = 28°C (green circles). The solid colored lines (red, blue, green) show the probable interaction potentials for each measurement, and these curves continue as dashed colored lines in the unstable regions after the points where the surfaces abruptly jump into adhesive contact. The black dashed curve indicates the theoretical maximum attractive electrostatic double-layer force between a mica surface and a fully ionized cationic surface. The monotonically repulsive PDMS/mica interaction in the absence of adsorbed bq-PDMS is shown for reference (black squares). (B) Schematic representations of the hypothesized interacting structures. The images are intended as visual aids and are not drawn to scale. (i) The mica surface approaches the bq-PDMS film. The bq-PDMS 'micelle-like' aggregates contact the mica surface at a smaller separation distance when the approach is performed dynamically (ii) than if the approach is performed quasi-statically (iii). As the temperature is increased (iv), the bq-PDMS aggregates contact the mica surface at an even greater separation distance due to their faster dynamics. In schematics (ii), (iii), and (iv), the blue dashed line indicates the outline of the bq-PDMS aggregates at an initial time t_1 and the green shaded region indicates the position of the aggregates when they contact (capture) the incoming mica surface at time t_2 ($t_2 > t_1$). (v) The mica surface jumps into a strong adhesive contact with the underlying PDMS layer.

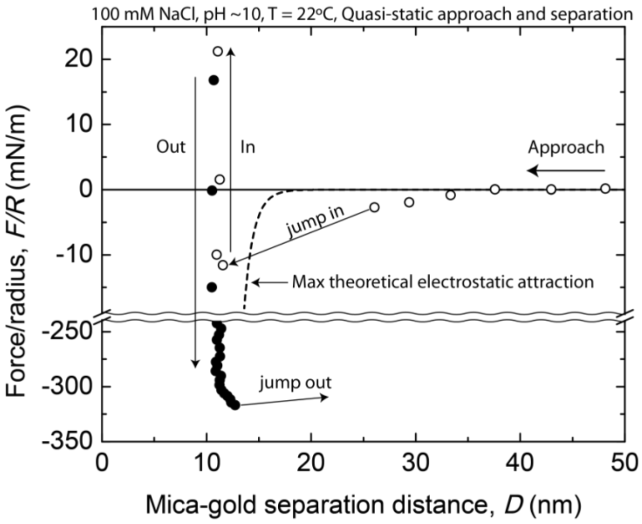

Figure 2.3: A quasi-static force-distance measurement of a mica surface interacting with a film of adsorbed bq-PDMS in a 100 mM NaCl pH ~ 10 solution at room temperature (22°C). Data points that are measured on the first approach of the mica to the bq-PDMS film are shown as open circles, and data points measured during separation of the two surfaces are shown as filled black circles. The dashed black line represents the theoretical maximum (constant potential) attractive electrostatic force that could occur at 100 mM ionic strength, between a mica surface and another surface composed of fully ionized cations spaced ~0.7 nm apart on a lattice (the Bjerrum length). On approach, the range and magnitude of the attraction and jump-in are far too large to be described by an electrostatic double layer model. While the attraction at 100 mM is slightly shoter-ranged than at 1 mM, these measured forces are still consistent with the hypothesis of fluctuating nanostructures. At higher salt concentrations, the decreased electrostatic repulsion between headgroups may alter the structure's aggregation number, size, and periodicity[29] —collectively changing the aggregate geometry or dynamics—which leads to a small decrease in the overall attractive force. Sufficient waiting times were not performed on during the separation of the two surfaces to observe the fully equilibrated bridging interaction at constant force.

The measured attractive forces for both the room temperature and elevated temperature quasi-static measurements are much stronger and longer-ranged than the maximum electrostatic force, so a simple electrostatic double layer attraction between the cationic bq-PDMS and negatively-charged mica can be ruled out. The attraction is also longer-ranged than the fully extended length of the bq-PDMS molecule (contour length, L_C ~ 20 nm), indicating that a molecular extension event cannot explain the measured attraction. Molecular bridging can be further ruled out because there would be a large energy penalty for extending the hydrophobic central block of the bq-PDMS molecules into the aqueous solution, which would be necessary for a molecular bridging between bq-PDMS headgroups and mica. Quasi-static SFA measurements between a bq-PDMS film and mica in 100 mM NaCl show a slightly shorter-ranged attraction and jump-in distance, but the interaction is still much stronger and longer-ranged than any expected electrostatic attraction between the oppositely charged interfaces (Figure 2.3).

The rate dependence, temperature dependence, and ionic strength dependence of the bq-PDMS and mica SFA measurements lead to the hypothesis that nanoscale, micelle-like, and dynamically fluctuating aggregates of bq-PDMS protrude from the bq-PDMS/Au-PDMS interface, leading to the observed capture and subsequent strong adhesion between the two interacting surfaces (shown schematically in Figure 2.2B). These nanoscale aggregates likely behave similarly to grafted polymers or cylindrical micelles, with similar relaxation times and temperature effects, as they fluctuate near the PDMS surface due to constrained Brownian motion (Figure 2.2B-i). At the surface, the aggregates diffuse within a given configuration space and statistically explore all of their possible configurations. The onsets of the attractions in the measured force profiles correspond to rare events when an aggregate samples an extended configuration and binds to the approaching mica surface with the quaternary ammonium headgroups (referred to as “capture” events). At a fixed separation distance, the probability of a capture event increases with time. Accordingly, during a quasi-static approach (Figure 2.2B-ii), the longer equilibration time (30 s) at each separation distance results in a capture event that occurs at a much larger separation distance than when the approach is performed dynamically (0.5 s between each measurement point, Figure 2.2B-iii). The additional energy provided by increasing the temperature leads to an increase in the rate, size, and exploration space of the fluctuating bq-PDMS aggregates, leading to a greater onset of attraction at the elevated temperature (Figure 2.2B-iv). Quaternary ammonium groups are known to form a strong ionic bond with binding energy of ~5-9 kT at mica surface sites in aqueous solution.[39,40] The specific Coulombic bond between the quaternary ammonium headgroups and the mica surface allows for the capture of the mica surface, while the hydrophobic interaction between the bq-PDMS surfactant chains and Au-PDMS chains leads to the ultimate collapse of the layer (Figure 2.2B-v).

The dynamics of the surface aggregates as they explore space and bind to the mica can be analyzed in terms of mean-field theories, similar to the scaling theories originally developed for end-grafted polymer chains by de Gennes.[41] As described by Wong *et al* for tethered ligand-receptor interactions,[42] in this case the analogous aggregates diffuse within a given configuration space, exploring all possible configurations, with the range of the attraction depending on the equilibration time at each separation distance. The typical time for an aggregate to sample a configuration at an extended distance, D_E, is known as the exploration time, τ_R, and is given by $\tau_R(D_E) = \tau_0 \cdot \exp[E_{ext}(D_E)/k_B T]$, where $E_{ext}(D_E)$ is an external potential, τ_0 is the intrinsic relaxation rate of a single polymeric aggregate, k_B is Boltzmann's constant and T is the temperature. The intrinsic relaxation rate of a single aggregate is known as the Zimm time,[43] $\tau_0 \approx \eta R_F^3/k_B T$, where η is the viscosity of water, and R_F is the effective Flory radius of the polymer aggregate. The external potential can be approximated as a parabolic potential, $E_{ext}(D_E) = D_E^2 k_B T/2R_F^2$, where $D_E > R_F$. Taking τ_R to be the sampling period between measurement points ($\tau_R^D = 0.5$ s for dynamic measurements and $\tau_R^Q = 30$ s for quasi-static measurements) and D_E to be the difference between the measured onset of attraction and the Au-PDMS film thickness ($D_E = D_A - D_0$), the Flory radius of the aggregate protrusions is estimated as 4.0 nm < R_F < 6.1 nm. This polymer-like behavior suggests that even longer-ranged attractive forces would be observed if the equilibration time is increased beyond 30 seconds; however, to observe a meaningful increase in the onset of attraction beyond the 30 second waiting time case, the waiting time must increase to experimentally-impractical intervals (on the order of 10 minutes), due to the exponential function of the exploration time. The timescale over which these aggregates fluctuate resembles the range for the “slow” characteristic relaxation times of whole micelles in solution, generally called τ_2. In surfactant micellar solutions, τ_2 corresponds to the timescale of the micellization-dissolution process—or the micelle stability—and it generally falls in the range of hundreds of microseconds to tens of seconds for short aliphatic surfactants (in contrast to the much shorter lifetimes of the individual surfactant molecules in the micelles).[44,45] This rough analysis demonstrates that the ‘fluctuating micelle’ hypothesis is a viable possibility. After the capture event and collapse of the layer, the bq-PDMS headgroups are strongly attached to the mica, and a very strong adhesion is measured upon separating the surfaces, as discussed in the following section.

2.1.6 Asymmetric Interactions Between Bq-PDMS and Mica Surfaces During Separation

The separation of bq-PDMS/mica surfaces leads to very large adhesion, which exhibit highly rate-dependent interactions, similar to the approach interactions shown above. Figure 2.4A shows a comparison between a dynamic separation (red points), and a quasi-static separation (blue points). In a dynamic separation, a tensile load is applied to the surfaces at a constant rate ($\dot{F}/R$ ~ 8.5 mN m^{-1} s^{-1}); in a quasi-static separation, the tensile load is applied in increments (F/R ~ 5-15 mN m^{-1}) and the system is allowed to equilibrate for 30 seconds after each increase in load (average $\dot{F}/R$ ~ 0.3 mN m^{-1} s^{-1}). Additionally, under certain tensile loads during the quasi-static run, the surfaces were allowed to fully equilibrate for longer time periods (~10-50 minutes), indicated by the blue squares during the quasi-static separation run. These two different modes of separating the surfaces allow for observation of differences in the rate-dependent polymer chain behavior between the surfaces as they are separated. The dynamic separation exhibits an extremely strong adhesion energy of E_{ad} = -240 mJ m^{-2}. This adhesion is dramatically smaller, E_{ad} = -72 mJ m^{-2}, when the separation is performed quasi-statically. Interestingly, when the surfaces are allowed to equilibrate under a strong tensile load, the surfaces slowly creep apart, observed as an increase in separation distance while the applied force remains constant (labeled as “constant force bridging”, Figure 2.4A). At a tensile load of E = -55 mJ m^{-2}, the surfaces extend from D = 7 nm to D = 10 nm. Increasing the tensile load to E = -62 mJ m^{-2} causes the surfaces to extend further from D = 10 nm to D = 11 nm. Increasing the adhesive load to E = -68 mJ m^{-2} leads to extension from D = 11 nm to D = 12 nm. Ultimately, when the negative tensile load reaches the measured adhesion energy, E_{ad} = -72 mJ m^{-2}, the surfaces bridge dramatically before the jump-out, from D = 12 nm to D = 22 nm. The average quasi-static adhesion energy measured over multiple experiments is E_{avg} = -77 ± 8 mJ m^{-2}. The extension of the force curve before the jump-out indicates that the polymer chains of the bq-PDMS molecules relax and untangle from the Au-PDMS chains that are attached to the anchoring gold surface.

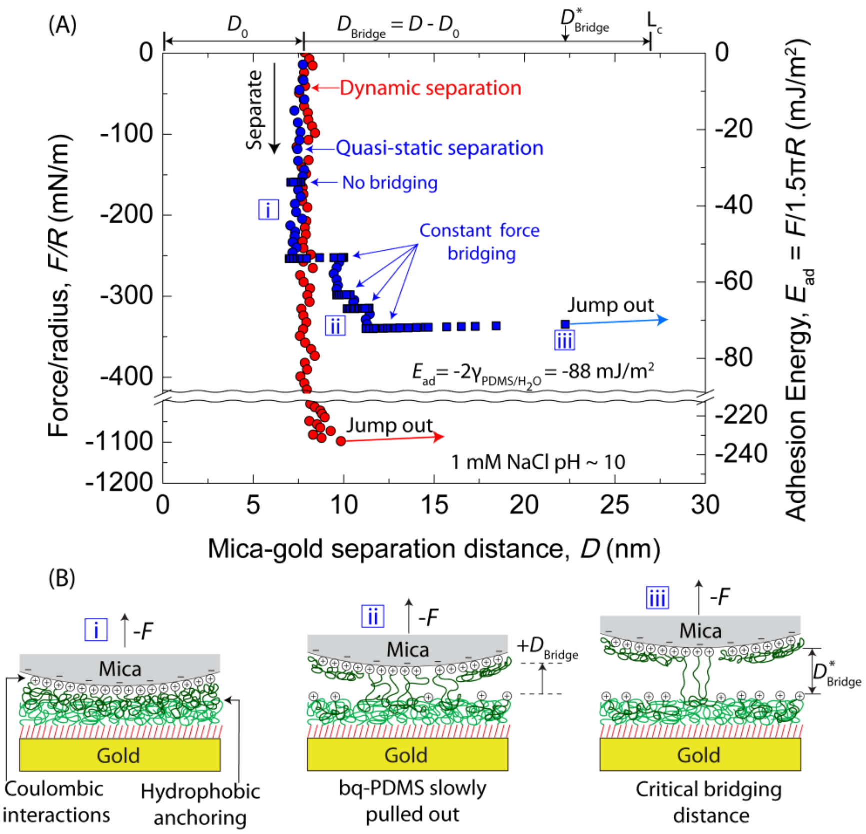

Figure 2.4: The adhesive interactions of a mica surface separating from a film of adsorbed bq-PDMS. (A) Dynamic (red circles) and quasi-static (blue circles/squares) force-distance measurements for the separation of a mica surface from the PDMS/bq-PDMS interface. At certain times during the quasi-static separation (marked with blue squares) the surfaces were allowed to fully equilibrate while under constant tensile load. In this particular quasi-static separation, constant force bridging between the surfaces is first observed at a tensile load of ~-250 mN/m, as bq-PDMS molecules are pulled out from the grafted PDMS film. (B) A schematic representation of the interaction potential during the quasi-static separation of the surfaces. (i) Coulombic (headgroup-mica) interactions strongly bind the mica surface to the bq-PDMS film, while the polymer mid-block of the bq-PDMS strongly anchor into the grafted PDMS film by hydrophobic interactions. (ii) When given sufficient relaxation times under high tensile load, bq-PDMS molecules around the contact area perimeter are pulled out from the PDMS film, transferring to the mica surface. (iii) Bridging adhesion continues until the bq-PDMS molecules at the apex of the surface are pulled out from the PDMS film at $D_{Bridge} = D^*_{Bridge}$, a mica-PDMS separation distance near the fully extended length of bq-PDMS.

The characteristic “L” shape of the force curve during a quasi-static separation has been previously observed for separating tethered ligand-receptor bonds,[42] peeling polymers from a hydrophobic interface,[46] and specific interactions of tethered polymers with a target surface.[46,47] This kind of force-distance profile is observed when the specific endgroup-target surface attraction is stronger than the anchoring interaction.[42] In the present case, within the contact area between the bq-PDMS and mica surfaces, the bq-PDMS headgroups attach strongly and specifically to the mica surface, while the polymer mid-blocks anchor into the grafted Au-PDMS layer through hydrophobic interactions (Figure 2.4B-i). When the two surfaces are slowly separated from molecular contact, the bq-PDMS polymer chains are provided enough time to slowly rearrange, untangle, and extend out from the grafted Au-PDMS layer (Figure 2.4B-ii). Due to the surface curvature, bq-PDMS molecules around the perimeter of the given contact area are the first molecules to fully extend and are plucked from the Au-PDMS surface, breaking contact between the hydrophobic segments of the bq-PDMS and Au-PDMS chains. Bq-PDMS molecules around the contact area perimeter are continually extended and removed from the Au-PDMS surface, causing the contact area to shrink, until eventually only the chains at the apex bridge between the two surfaces (Figure 2.4B-iii). The bridging molecules at the apex extend all the way to $D^*_{\mathrm{Bridge}} = 15$ nm—nearly the fully extended length of the bq-PDMS molecules, $L_{\mathrm{C}} \sim 20$ nm. For two curved surfaces, the force-law for the molecular pullout is independent of D,[42] and the force is therefore constant as D increases from D_0 to D^*_{Bridge}, at which point the rupture occurs. After the last bridging bq-PDMS molecule is plucked from the Au-PDMS, the two surfaces rapidly jump apart.

The strength of the specific Coulombic attraction between the bq-PDMS headgroup and the mica surface is stronger than the equilibrium hydrophobic interaction between the bq-PDMS and Au-PDMS chains, so bq-PDMS molecules are pulled out of the Au-PDMS film and transferred onto the mica surface. Material transfer of bq-PDMS onto the mica surface was confirmed by FECO and by a repeated force run at the same contact position, as shown in Figure 2.5. The measured adhesion is thus effectively due to separation of the two PDMS interfaces (bq-PDMS and Au-PDMS), and the average adhesion energy E_{avg} = -77 ± 8 mJ m^{-2} approaches the thermodynamically expected adhesion between two hydrophobic PDMS films or surfaces, $E_0 = -2\gamma_{\mathrm{i}} = -88$ mJ m^{-2}, where $\gamma_{\mathrm{i}} = 44$ mJ m^{-2} is the PDMS-water interfacial tension. E_{avg} is slightly less than E_0 due to the presence of cationic headgroups and excess surfactants near the hydrophobic failure interface. While the adhesion energy between extended hydrophobic surfaces decreases with moderate increases in temperature,[48] no significant change in the adhesion energy was measured over the small range of temperatures used in this study (22 - 26°C).

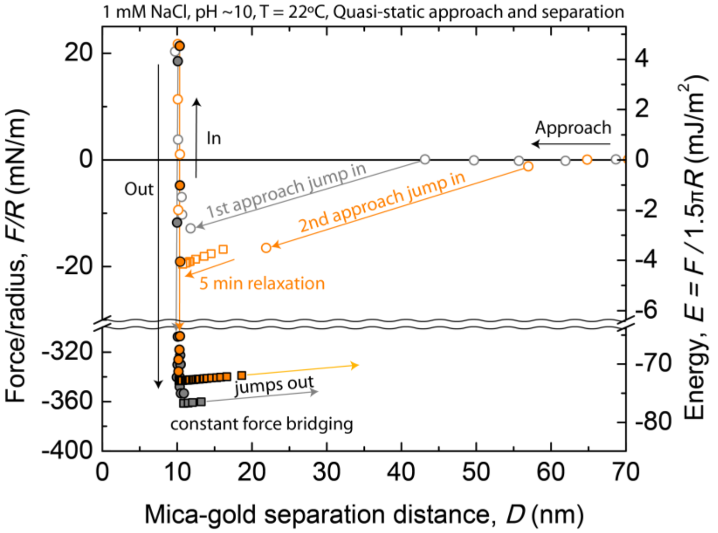

Figure 2.5: Quasi-static force-distance measurements of the 1st (grey circles/squares) and 2nd (orange circles/squares) approach and separation of a mica surface to a film of adsorbed bq-PDMS. The approach and separation are performed consecutively at the same contact location between the surfaces. As the surfaces are separated for the 1st time, bq-PDMS molecules are pulled out of the Au-PDMS interface and are transferred to the mica surface. As the surfaces approach for the 2nd time, the bq-PDMS surface aggregates will interact strongly and attractively with the adsorbed mass of bq-PDMS on the mica surface, leading to a longer ranged jump-in to adhesive contact. After the jump in to adhesive contact during the 2nd approach, the system was allowed to equilibrate for 5 minutes without further applying any compressive force (open orange squares); during this period, the mass of confined bq-PDMS relaxes and interdiffuses, pulling the surfaces into closer separation distance. During both the 1st and 2nd separation, near the adhesive minimum, the system was allowed to equilibrate under constant tensile load (filled squares), and bridging adhesion was observed.

Particularly noteworthy is the large difference in the adhesions of quasi-static and dynamic separations: E_{ad} = -72 mJ m^{-2} *vs* E_{ad} = -240 mJ m^{-2} respectively. In the quasi-static case, the polymer chains re-arrange and reach preferred low-energy configurations, allowing the bq-PDMS molecules to be progressively pulled out of the Au-PDMS through a low-energy pathway. Thus, slow and quasi-static separations provide the lower bound and equilibrium adhesion energy between soft polymer surfaces. In contrast, during dynamic separations, the polymers do not have time to relax and rearrange, and the detachment or 'pull-off' between the bq-PDMS and Au-PDMS chains occurs simultaneously over the entire contact region, leading to energy dissipation in the entangled polymer film and much larger measured adhesion (see also Bell's theory on bond lifetimes).[49] To gain further physical insights into the proposed fluctuating aggregates and bridging forces, we also measured the forces between two bq-PDMS coated surfaces, to compare with the asymmetric bq-PDMS/mica interactions.

2.1.7 Symmetric Interaction Between Bq-PDMS Interfaces

A thin PDMS film can also be supported on mica surfaces, using similar click chemistry with an amine-terminated silane monolayer on the mica surface (rather than the amine-terminated thiol monolayer used on gold).[48] A symmetric experiment between bq-PDMS layers was performed, in which a bq-PDMS layer supported on Au-PDMS interacts with a similar bq-PDMS layer supported on mica-PDMS. Figure 2.6 shows a comparison of the asymmetric interaction of bq-PDMS and mica surfaces with the symmetric interaction of two bq-PDMS interfaces. The same data discussed above for the asymmetric quasi-static separation (Figure 2.4A, blue points) and its corresponding approach measurement are shown also in Figure 2.6 for comparison to the symmetric experiment. The symmetric experiment (Figure 2.6, green points) exhibits several qualitative similarities to the asymmetric experiment: during the approach, a very long-ranged attraction is observed, and during separation, the characteristic "L" shaped polymer-bridging force-distance profile is observed (filled green points). However, important differences between the symmetric and asymmetric experiments are detected, which can help explain and confirm the proposed mechanisms discussed above.

The major difference between the symmetric and asymmetric experiments is the range of interaction, for both the approach and separation force-distance curves. During the approach in the asymmetric experiment, the attractive force onsets near D = 49 nm and jumps-in to a contact distance of D_0 = 10 nm, with an approximate range of interaction of 39 nm. The range of interaction increases for the symmetric system, with an attractive force onset near D = 105 nm, eventually jumping-in to a contact distance of D = 28 nm, corresponding to a range of interaction of about 77 nm. The range of interaction has therefore doubled for the symmetric interaction compared to the asymmetric one. This is consistent with the protruding aggregates model, now adsorbed on *both* surfaces as shown in Figure 2.6B, approaching each other (Figure 2.6B-i), then encountering each other and coalescing (Figure 2.6B-ii), leading to the observed longer-ranged attraction. The large increase in the range of attraction further suggests that the protrusions are intrinsically dynamic and fluctuating structures; the nanostructures are not "activated" by the approach of another negatively charged surface, such as mica. No repulsive force was measured between the symmetric surfaces during a quasi-static approach, indicating that the attractive hydrophobic force between critically extended bq-PDMS aggregates overwhelms any repulsive electrostatic force between the similarly charged aggregates. A simple energy balance between the electrostatic, van der Waals, and hydrophobic pair potentials between two model nano-aggregates (*R* ~ 4 nm) indicates that these aggregates will coalesce even at moderate-to-high surface charge densities.

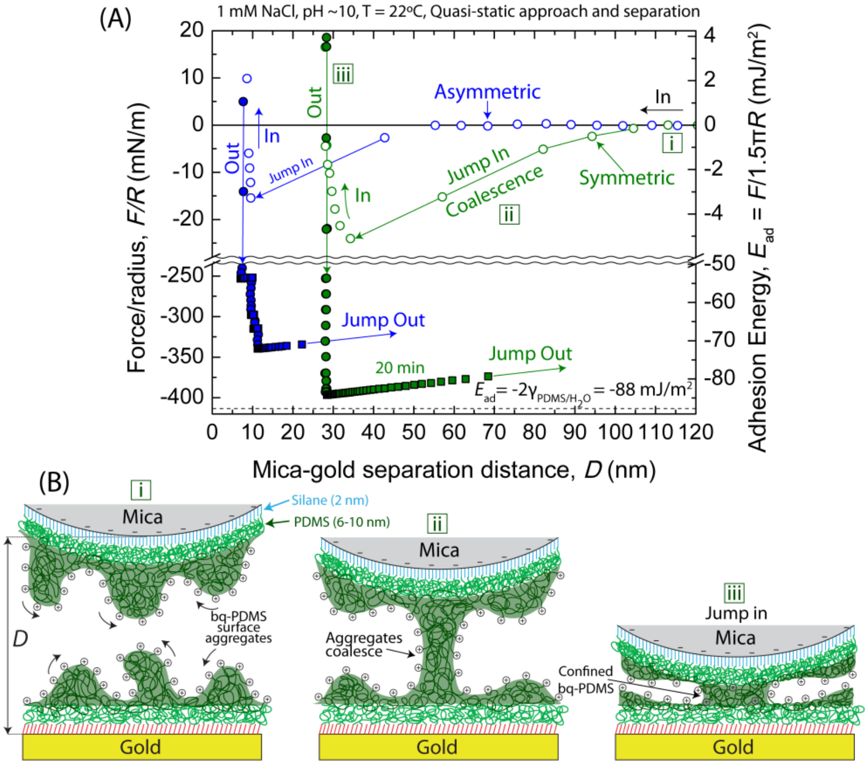

Figure 2.6: The forces between two symmetric bq-PDMS films. (A) Quasi-static force-distance measurements for the approach and separation of two symmetric bq-PDMS films (green circles/squares). Near the adhesive minimum, the system was allowed to equilibrate under a constant tensile load, and bridging adhesion was observed over 20 minutes (closed green squares). The asymmetric interaction between mica and one adsorbed bq-PDMS film on approach and separation is shown as blue circles/squares (same data as the quasi-static measurements shown in Figure 2.4, for comparison). (B) A schematic representation of the hypothesized interaction potential on approach of two symmetric bq-PDMS films. (i) The undulating bq-PDMS films approach one another. (ii) At large separation distances, the bq-PDMS aggregates coalesce and bridge the two surfaces. (iii) The coalesced bridge collapses, pulling the surfaces into a strong adhesive contact. Some bq-PDMS is confined between the grafted PDMS films.

Interestingly, the attractive force leads to collapse of the protruding aggregates, although a significant amount of bq-PDMS appears to be trapped in the gap between the surfaces, as indicated by the hard-wall distance for the asymmetric (D = 8 nm) *vs* symmetric (D = 28 nm) cases. A naïve expectation would be that the hard-wall distance should double in this case; however, the hard-wall distance has increased by 3.5 times for the symmetric experiment. In the case of bq-PDMS approaching a bare mica surface, the bq-PDMS headgroups can spread on the mica surface, leading to a full collapse of the bq-PDMS layer. For two bq-PDMS surfaces, both surfaces already are fully saturated (if not over-saturated) with bq-PDMS and therefore cannot spread, and a significant amount is trapped between the surfaces, leading to the larger than expected hard-wall distance for the symmetric case. This result also suggests that the protruding aggregates are possibly formed due to an excess of bq-PDMS material at the PDMS thin film surface. Micron-sized lipid "worms" have previously been found to dynamically form and protrude at overpacked phospholipid bilayer-covered interfaces by fluorescence imaging,[50] however the proposed bq-PDMS nanostructures are too small to image with fluorescence, and too dynamic and soft to image with atomic force microscopy[51,52] (AFM images produced only smeared-out and featureless images of the bq-PDMS surface, Figure 2.7).

The separation curve for two bq-PDMS surfaces also exhibits a larger range of interaction compared to the bq-PDMS/mica separation curve. The bridging distance increases from D^*_{Bridge} = 15 nm for the asymmetric case to D^*_{Bridge} = 40 nm for pulling apart two bq-PDMS surfaces. The dramatic increase in the polymer bridging distance indicates that bq-PDMS molecules, perhaps some in the form of bq-PDMS aggregates, extend between the two surfaces and lead to the measured bridging force. Only a single step-wise bridging event occurs for the symmetric separation in Figure 2.6A, as only one extended equilibration time was permitted past the bridging threshold load in this particular experiment. The average adhesion energy between two bq-PDMS coated surfaces E_{avg} = -79 ± 9 mJ m^{-2} is slightly less than the expected thermodynamic adhesion for two PDMS interfaces, E_0 = -88 mJ m^{-2}, similar to the adhesion between bq-PDMS and mica, further confirming that the strong adhesion (in both the asymmetric and symmetric cases) arises from the energy of cohesion between PDMS surfaces.

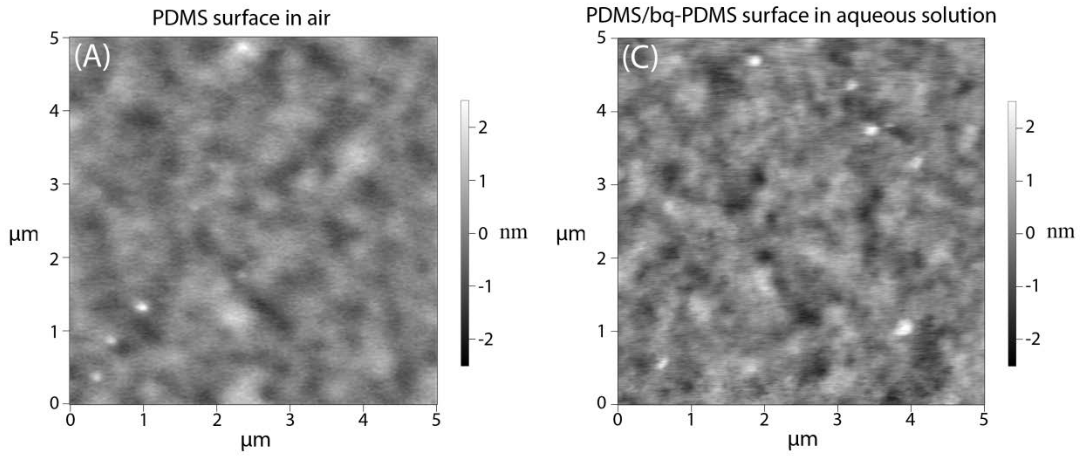

(B) PDMS surface in air

(D) PDMS/bq-PDMS surface in aqueous solution

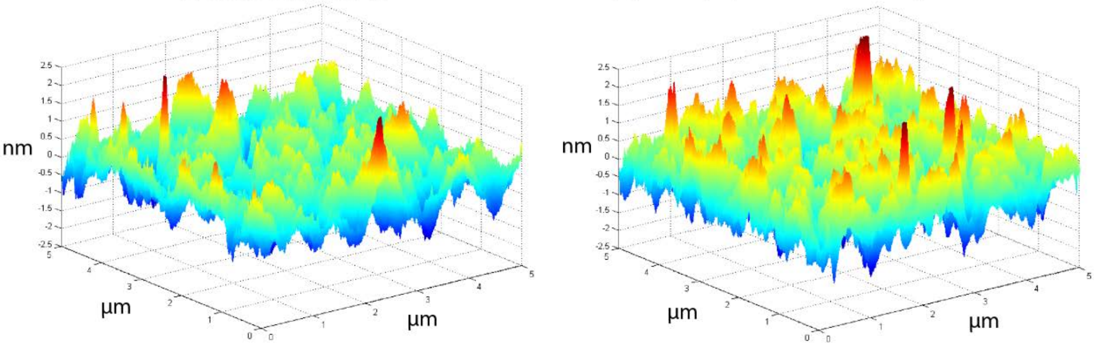

Figure 2.7: Representative tapping-mode AFM images of the surfaces used in this study. The images were generated using a MFP-3D standard system (Asylum Research, Santa Barbara, CA). (A, B) 2D and 3D image of a grafted Au-PDMS surface (without adsorbed bq-PDMS) measured in air with a silicon nitride-tipped probe. The plain PDMS surface is smooth and featureless, with rms roughness ~ 0.4 nm. (C, D) 2D and 3D image of a bq-PDMS film adsorbed onto an Au-PDMS surface through vesicle deposition. The imaging was performed in a 1 mM NaCl pH=10 solution. The image was generated with a charge-neutral (3-aminopropyl)triethoxysilane-

coated silicon nitride cantilever tip (Novascan Technologies, Ames, Iowa) to eliminate strong electrostatic bq-PDMS adsorption onto the tip. The bq-PDMS films appear smeared-out and featureless as the rapid motion of the rigid cantilever tip is too coarse and disruptive to adequately image the soft and dynamically fluctuating bq-PDMS nanostructures. The bq-PDMS surface does show a small increase in the surface roughness (rms ~ 0.5 nm), which may suggest the existence of the nanostructures, although the imaged features are small. The AFM scans on their own are insufficient to confirm the nanostructural size and shape of the bq-PDMS features, as this small change in roughness may still be due to either: (1) the bq-PDMS surfaces have an additional processing step compared to the plain PDMS surface, and (2) the bq-PDMS surface is imaged in solution rather than air. Images taken on bq-PDMS surfaces using a negatively-charged silicon nitride cantilever tip result in both the significant adsorption of bq-PDMS molecules onto the tip and the disruption of the bq-PDMS surface (not shown).

2.1.8 Conclusions

We have shown that long-chain bolaform surfactants self-assemble at hydrophobic interfaces and form more complicated and dynamic morphologies than previously reported for short-chain aliphatic surfactants. Short-chain aliphatic surfactants are known to adsorb to solid hydrophobic surfaces, form small structures (monolayers, hemicylinders, hemimicelles) similar in dimension to their bulk micelle size, and give rise to primarily electrostatic double layer forces when interacting with another surface in solution. By adsorbing a long-chain bolaform surfactant (bq-PDMS) onto a hydrophobic polymer brush film—drastically increasing the complexity of the system—we have found that dynamically fluctuating nanoscale surfactant aggregates form on the surface and persist for many hours. These bq-PDMS aggregates behave analogously to grafted polymer chains, as they fluctuate and explore their full configuration space. In measurements with the SFA, these aggregates induce an attractive force with an approaching mica surface as the aggregates contact the mica surface and the cationic surfactant headgroups bind to mica. The range of this attractive force (and the range of the abrupt jump in to adhesive contact) depends significantly on the rate of approach; decreasing the approach speed allows the aggregates to sample larger extended configurations, re-organize, and contact the mica surface at larger separation distances. The range of the attractive force and jump-in also increases with increasing temperature. When two similar surfaces of adsorbed bq-PDMS film approach in solution, the surface aggregates on opposite surfaces coalesce and give rise to a long-ranged bridging force.

These particular surface structures presumably exist only for specific combinations of surfactant geometries and surface types. Small changes to the surfactant molecule—such as changing the backbone composition, the backbone length, or the headgroup charge (changing the surfactant "packing factor")—or small changes to the surface structure—such as changing the surface hydrophobicity, degree of cross-linking, or polymer brush length—are all expected to affect the adsorbed surfactant structures and colloidal forces in complex ways. We are currently investigating this phenomenon with follow-up work.

The results presented in this study suggest that careful consideration should always be given to the rates at which measurements are performed at soft polymer interfaces. By varying the rate and method by which we separate a mica surface from the adsorbed bq-PDMS films, we find large differences in the separation mechanism and in the measured adhesion energy. When the separation is performed quickly, the polymer chains are not allowed enough time to relax and untangle, and consequently a massive—mostly dissipative—adhesion energy is measured. However, when the separation is performed slowly with sufficient waiting times, the mica-bound bq-PDMS surfactants untangle and are pulled out from the underlying polymer layer, which manifests as slowly equilibrating molecular bridging force that extends nearly to the stretched length of the bq-PDMS molecules. This slow pull-out effect produces an adhesive energy that approaches the equilibrium adhesion energy between PDMS surfaces. These rate- and time-dependent effects should also arise when soft polymer surfaces, polymer-coated colloidal particles, or emulsions are sheared, mixed, or agitated, as these movements also involve two surfaces or particles approaching, and then separating, in a suspending liquid.

These cationic long-chain surfactants mediate remarkably strong adhesion between a polymer and a mineral surface, with adhesive forces that are significantly greater than those observed between hydrophobic and hydrophilic surfaces bridged by adhesive proteins.[24–26] The adhesive mechanisms displayed by these surfactants lend themselves well to applications such as binding lubricating films to anionic surfaces or securing polymer devices onto mineral or oxide films. The polymer mid-blocks of the surfactants entangle within a non- or partially-crosslinked polymer surface; the entangled polymer interface can dissipate energy during unloading or shearing events, leading to exceptionally large non-equilibrium adhesion energies. During separation of the mica and bq-PDMS surfaces, the specific Coulombic interactions between the quaternary ammonium surfactant headgroups and the mica surface are strong enough to shift the interface of failure to the hydrophobic PDMS-PDMS interface between the surfactant tails and the grafted polymer layer. This constitutes an important strategy for the design of robust adhesives in wet environments: whenever possible, shift the failure interface between the surfaces to a cohesive hydrophobic interface, as this results in an equilibrium adhesive energy that approaches a thermodynamic value of $E_{\mathrm{ad}} = -2\gamma \sim -2(50\ \mathrm{mJ\ m^{-2}}) \sim -100\ \mathrm{mJ\ m^{-2}}$.

2.2 Effects of Surfactants and Polyelectrolytes on the Interaction Between a Negatively Charged Surface and a Hydrophobic Polymer Surface

Rapp, M. V.; Donaldson, S. H.; Gebbie, M. A.; Gizaw, Y.; Koenig, P.; Roiter, Y.; Israelachvili, J. N. (2015) ***Langmuir***, 31 (29):8013-8021

2.2.1 Abstract

We have measured and characterized how three classes of surface active molecules self-assemble at, and modulate the interfacial forces between, a negatively charged mica surface and a hydrophobic end-grafted polydimethylsiloxane (PDMS) polymer surface in solution. We provide a broad overview of how chemical and structural properties of surfactant molecules result in different self-assembled structures at polymer and mineral surfaces, by studying three characteristic surfactants: (1) an anionic aliphatic surfactant, sodium dodecyl sulfate (SDS), (2) a cationic aliphatic surfactant, myristyltrimethylammonium bromide (MTAB), and (3) a silicone polyelectrolyte with a long-chain PDMS mid-block and multiple cationic endgroups. Through surface forces apparatus measurements, we show that the separate addition of three surfactants can result in interaction energies ranging from fully attractive to fully repulsive. Specifically, SDS adsorbs at the PDMS surface as a monolayer and modifies the monotonic electrostatic repulsion to a mica surface. MTAB adsorbs at both the PDMS (monolayer) and the mica surface (monolayer or bilayer), resulting in concentration dependent interactions, including: a long-range electrostatic repulsion, a short-range steric hydration repulsion, and a short-range hydrophobic attraction. The cationic polyelectrolyte adsorbs as a monolayer on the PDMS and causes a long-range electrostatic attraction to mica, which can be modulated to a monotonic repulsion upon further addition of SDS. Therefore, through judicious selection of

surfactants, we show how to modify the magnitude and sign of the interaction energy at different separation distances between hydrophobic and hydrophilic surfaces, which govern the static and kinetic stability of colloidal dispersions. Additionally, we demonstrate how the charge density of silicone polyelectrolytes modifies both their self-assembly at polymer interfaces and the robust adhesion of thin PDMS films to target surfaces.

2.2.2 Introduction

Surfactant adsorption is the most prevalent method to control the aqueous interfacial energy of both mineral and soft polymer surfaces.[53] Amphiphilic ionic surfactants have the versatility to adsorb and self-assemble at either a charged surface through electrostatic interactions with their polar headgroups, or at a hydrophobic surface through interactions with their non-polar tails. In industrial separation and recovery processes—such as froth flotation, flocculation, and hydraulic fracturing—surfactants are vital additives that regulate the wettability and friction at mineral-water interfaces. In addition to their abundant use as grease-cleaning detergents, surfactants stabilize hydrophobic oil droplets in emulsions and cosmetics.[10,12,54,55] Frequently, consumer products and industrial separation techniques employ a mixture of surfactants, polymers, and polyelectrolytes in synergy to achieve a desired behavior of an end product.[9–12,27,55–60]

A tremendous variety of useful surfactants exist. The properties of specific classes of surfactants, and the resultant engineering functions of these surfactants, depend on differences in the surfactant structure (lipid, gemini, or bolaform surfactants), the size and number of the non-polar tails (ranging from short aliphatic chains to long polymer chains), or the headgroup charge (anionic, cationic, non-ionic, zwitterionic, polymeric, or polyelectrolyte surfactants).[28] At a surface, surfactants self-assemble into different interfacial structures—such as monolayers, bilayers, hemicylinders, or hemimicelles—based on the innate chemical and physical characteristics of both the surfactant and the surface, as well as the solution concentration.[29,30,32,35,39,61,62] Correspondingly, the self-assembled structures modulate the interaction forces between surfaces in solution, controlling the stabilization, flocculation, viscosity, lubrication, or adhesion of colloidal suspensions and macroscopic surfaces.

In a previous study using the surface forces apparatus (SFA), we demonstrated that a long-chain polydimethylsiloxane (PDMS) bolaform surfactant (bq-PDMS) adsorbs onto grafted-PDMS polymer brush surfaces and forms dynamically fluctuating nanostructures that protrude tens of nanometers into solution.[63] These soft nanostructures behave analogously to surface-tethered polymers exposed to bulk solution and give rise to rate-dependent attractive and adhesive forces on the approach and separation of another surface. These nanostructures represent a unique subset of self-assembled films that presumably exist for only certain surfactant-surface combinations; small changes to the surfactant length or charge are expected to result in different self-assembly and force profiles at polymer surfaces.

In this study, we extend our previous work to explore how three classes of surfactants self-assemble at, and modulate the surface forces between, a negatively charged mineral surface (mica) and a hydrophobic polymer surface (PDMS) in aqueous solution (Figure 2.8). The three surfactants used in this study were selected for their wide range of chemical and structural properties: (1) sodium dodecyl sulfate (SDS), a characteristic anionic aliphatic surfactant, (2) myristyltrimethylammonium bromide (MTAB), a characteristic cationic aliphatic surfactant, and (3) bq5x-PDMS, a polyelectrolyte similar in structure to the previously-studied bq-PDMS, but with a five-fold increase in the endgroup charge density. Measurements were performed in single component surfactant solutions, as well as a binary mixture of SDS and bq5x-PDMS. Overall, the resulting self-assembled structures and measured forces between these interfaces provide a broad overview of surfactant behavior at polymer and mineral surfaces. This comprehensive understanding of surfactant-polymer-surface interactions establishes design parameters for functionalized interfaces in consumer products and industrial applications.

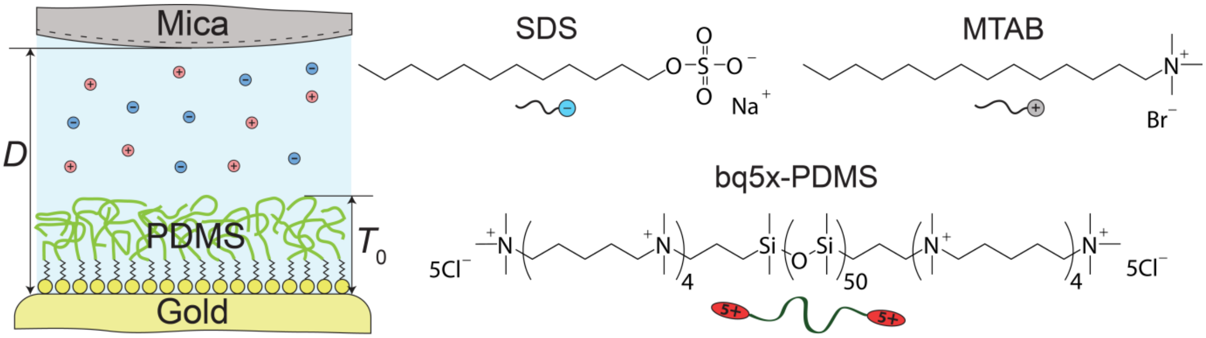

Figure 2.8: A schematic of the experimental setup in the SFA and the surfactant molecules used in this study. In an aqueous solution, a mica surface approaches and separates normal to a covalently-grafted PDMS surface on gold. In separate experiments, these surfaces are subsequently modified by the addition of anionic SDS surfactants, cationic MTAB surfactants, or cationic bq5x-PDMS polyelectrolytes.

2.2.3 Materials and Methods

Surface forces measurements were performed with the SFA 2000, manufactured by SurForce LLC., Santa Barbara, California. The full details of the SFA technique may be found elsewhere.[36] Briefly, the interaction force (F) between two crossed-cylinder surfaces (radius, R ~ 2 cm) is measured as a function of separation distance (D) between two surfaces.

The two surfaces used in this study are (1) a freshly-cleaved, back-silvered mica surface, and (2) a molecularly smooth gold surface that has been covalently grafted with a hydrophobic PDMS brush film. The absolute separation distance between the surfaces is measured with multiple beam interferometry between the reflecting gold and silver layer on mica.

At the start of an experiment, a pristine mica and gold surface (without a grafted film) were installed in the SFA and brought into molecular contact in dry N_2; this separation distance was assigned $D = 0$. The pristine gold surface was then replaced in the SFA with a gold surface that had been grafted with a PDMS film, and the chamber of the SFA was filled with degassed aqueous solution (typically 1 or 5 mM NaCl). The presence of interfacial nanobubbles was never observed at the PDMS surface. The system was allowed to equilibrate until thermal and mechanical drift in the SFA were negligible, and force measurements were performed by the normal approach and separation of the mica and PDMS surfaces at a rate of ~ 2 nm/s. The interaction forces between the surfaces at all distances are calculated from the deflection of a double-cantilevered spring that holds one of the two surfaces. For comparison between differing experiments, all forces in this study are normalized by the radius (F/R), and when appropriate, the measured interaction force is converted into an interaction energy using the Derjaguin approximation ($W=F/2\pi R$) or an adhesion energy using the Johnson-Kendal-Roberts theory ($W_{ad}=F_{ad}/1.5\pi R$).[64] All force measurements in this study were reproduced over multiple experiments, and represent the quasi-equilibrium interaction forces between the surfaces.

PDMS films were prepared as previously described.[14] Briefly, molecularly smooth gold surfaces were prepared via a mica templating technique.[65,66] An amine-functionalized self-assembled monolayer (SAM) was adsorbed onto the gold surface through immersion in a

1 mM solution of 11-amino-1-undecanethiol hydrochloride (Sigma-Aldrich) in ethanol for 2 hours. The SAM surfaces were rinsed in ethanol, dried in N_2, and then submerged in neat monoglycidyl ether-terminated polydimethlsiloxane (Sigma-Aldrich, MW = 5,000 g/mol) at 130°C for 1 hour. In this step, the PDMS polymers are covalently grafted to the SAM layer through a click reaction between the PDMS epoxide ring and the SAM terminal amine. At 130°C, some fraction of the SAM film may desorb from the gold surface; however, the PDMS length and grafting density are large enough to ensure uniformly-dense brush films that are free from holes. The click reaction may also be performed at lower temperatures with longer reaction times.[48] Following the reaction, unbound PDMS was removed from the gold surface through a cycle of rinsing and sonicating in toluene. Slight variations in the PDMS grafting density between sample preparations result in a total SAM+PDMS film thickness (T_0) that varies from ~6-10 nm between separate experiments; while the thickness of the film varies slightly between separate surfaces, the thickness of a film on a single surface was uniform.

Sodium dodecyl sulfate (SDS) and myristyltrimethylammonium bromide (MTAB) were purchased from Sigma-Aldrich. In experiments with SDS or MTAB, force measurements were first performed between the PDMS and mica surface at a specific contact point in a surfactant-free solution, to ascertain a baseline film thickness and interaction in aqueous solution. The aqueous reservoir between the two surfaces was then exchanged with a particular solution of SDS or MTAB, the system was allowed to equilibrate for ~ 1 hour, and force runs were performed between the surfaces at the same contact position as in the surfactant-free measurements.

Bq5x-PDMS (MW = 4842 g/mol) was provided by the Procter & Gamble Company (Cincinnati, Ohio). Bq5x-PDMS was dispersed in aqueous solution (1 NaCl, pH ~ 9) at a concentration of ~ 6 x 10^{-5} moles bq5x-PDMS/L; at this concentration, bq5x-PDMS forms aggregates of ~400 nm in diameter, as measured by Dynamic Light Scattering (DLS). In the SFA experiments presented in this study, bq5x-PDMS was adsorbed onto only the PDMS surface. First, freshly-prepared PDMS surfaces on gold were immersed in a small vial (~2 mL) of the bq5x-PDMS solution for 1.5 hours. A solvent exchange procedure was then performed to deplete any non-adsorbed bq5x-PDMS aggregates from the reservoir, without ever exposing the PDMS surface to air and perturbing the adsorbed state of the bq5x-PDMS film. After the adsorption step, the entire small vial was: (1) submerged within a larger vial (30 mL) of 1 mM NaCl, (2) gently mixed for 1 minute, and (3) removed from the larger vial with a 15x diluted reservoir surrounding the PDMS surface. This solvent exchange procedure was repeated 7 times for each surface. The PDMS surface was then transferred under solution into the SFA for force measurements.

2.2.4 Anionic Surfactant Monolayers

The headgroups of anionic surfactants, such as SDS, are repelled from the negatively charged mica surface, so little to no adsorption occurs on mica regardless of the bulk surfactant concentration. On a PDMS surface, the hydrophobic chains of SDS adsorb into the hydrophobic polymer layer of the PDMS thin film, resulting in a negatively charged SDS surface. Generally, hydrophobic surfaces display a negative surface charge at basic pH in aqueous solution,[15,18] and their interactions are repulsive with a likewise negatively charged mica surface. As shown in Figure 2.9, the addition of SDS above the critical micelle concentration (CMC_{SDS} = 8.2 mM) modifies the magnitude, the decay length, and the plane of origin of the repulsion between mica and PDMS thin films. Without SDS (blue points), the interaction is mainly an electrostatic double-layer repulsion, with a steric-hydration component at small separations. As described in our previous work, these forces can be modeled as a combination of van der Waals, asymmetric electrostatic double-layer, and steric-hydration using the model shown in Equation 2.1.[14]

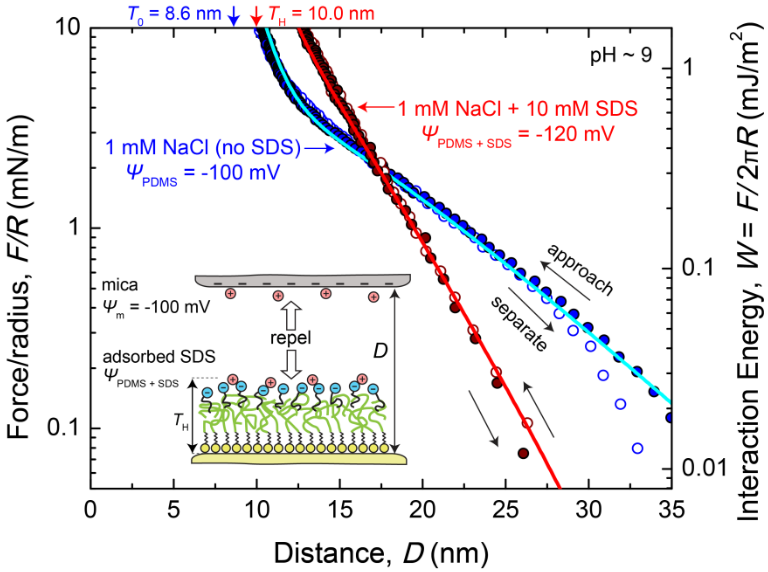

Figure 2.9: Interaction forces between a PDMS surface and a mica surface in a solution of SDS. SFA measurements were performed in a 1 mM NaCl solution at pH = 9, both before (blue data points) and after (red data points) 10 mM SDS was injected into the gap solution between the surfaces. Closed and open circles represent data measured on the approach and separation of the two surfaces, respectively. The corresponding solid curves passing through the data represent the fits with Equation 2.1 using the surface potentials shown in the figure. Arrows at the top of the figure indicate the “hardwall” film thicknesses measured at maximum compression (T_H).

$$W(D) = -\frac{1}{12\pi}\left(\frac{A_{\mathrm{mPg}}}{D^2} + \frac{A_{\mathrm{mwP}}}{(D-T_{\mathrm{H}})^2}\right)$$
$$+\varepsilon\varepsilon_0\kappa\left\{\frac{2\psi_{\mathrm{m}}\psi_{\mathrm{P}}\exp[-\kappa(D-T_{\mathrm{H}})] - (\psi_{\mathrm{m}}^2+\psi_{\mathrm{P}}^2)\exp[-2\kappa(D-T_H)]}{1-\exp[-2\kappa(D-T_H)]}\right\} \quad (2.1)$$
$$-2\gamma_i \cdot Hy \cdot \exp\left[\frac{-(D-T_H)}{D_H}\right]$$

For consistency, the equations presented herein are reported as the interaction energy, W, as a function of separation distance, D. T_{H} is the measured film thickness under maximum compression, *i.e.*, the "hardwall" thickness. The first term in Equation 2.1 is the van der Waals term; the Hamaker constants, A, were calculated according to Lifshitz theory[28] as previously described for mica (m) and gold (g) interacting across PDMS (P), $A_{\mathrm{mPg}} = 3.4\mathrm{x}10^{-20}$ J, and mica and PDMS interacting across water (w), $A_{\mathrm{mwP}} = 7.1\mathrm{x}10^{-21}$ J. The second term is the electrostatic term for asymmetric double-layers interacting at constant potential[67,68] with surface potentials ψ_{m} and ψ_{P} for the mica and PDMS surfaces, respectively. The Debye length κ^{-1} was calculated from Equation 2.2:

$$\kappa^{-1} = \left(\frac{\varepsilon_0\varepsilon kT}{2N_{\mathrm{A}}[\mathrm{NaCl}]e^2}\right)^{1/2} \quad (2.2)$$

where ε is the dielectric constant of water, ε_0 is the vacuum permittivity, N_{A} is Avogadro's number, e is the fundamental charge, k is Boltzmann's constant, and T is the absolute temperature. The third term in Equation 2.1 is the steric-hydration term. As described in our previous work, the Hydra parameter Hy is used to quantify the relative hydrophilicity ($Hy < 0$) or hydrophobicity ($Hy > 0$) of interfaces.[14,48]. The Hydra parameter Hy is a measure of the excess hydrophobic or hydrophilic area at an interface: $Hy \equiv 1\text{-}a_0/a$, where a is the hydrophobic area and a_0 is the hydrophilic area, with $Hy = 1$ corresponding to the maximum hydrophobic interaction, $Hy = 0$ corresponding to no additional hydrophobic or hydrophilic force, and $Hy < 0$ corresponding to a hydrophilic interaction.[48,69] D_H is the decay length of the hydrophobic/hydrophilic interaction (generally D_H is between 0.3 – 2 nm depending on the system). In this case, $Hy < 0$ models the observed repulsive steric-hydration force, with a hydration decay length of $D_H \sim 1$ nm and a hydrocarbon-water interfacial tension of $\gamma_i = 50$ mJ/m^2.

In the absence of SDS, the interaction between mica and PDMS is described with a Hydra parameter of $Hy = -0.2 \pm 0.06$, a PDMS surface potential of $\psi_P = -100 \pm 20$ mV, and a mica surface potential of $\psi_m = -100 \pm 10$ mV, with a fitted screening length of $\kappa_{fit}^{-1} = 7.0 \pm 0.5$ nm (theoretical $\kappa^{-1} = 9.6$ nm). Increasing the NaCl concentration from 1 to 10 mM does not significantly alter ψ_m, however ψ_P decreases to -40 ±10 mV at 10 mM NaCl.[14] The addition of 10 mM SDS modifies the PDMS surface potential and the electrostatic decay length (red points, Fig. 2), to $\psi_P = -120 \pm 20$ mV and $\kappa^{-1} = 3.1$ nm (with $Hy = -0.24 \pm 0.1$). Thus, SDS adsorption preserves a high surface potential at the PDMS interface even in solutions of increased ionic strength. The self-assembly of SDS also shifts the hardwall distance from $T_H = 8.6$ nm in the absence of SDS, to $T_H = 10$ nm in the presence of SDS. The difference of 1.4 nm is the approximate length of a SDS molecule; however, from the force measurements, we are unable to determine if this shift out in the hardwall is due to a SDS monolayer that lies on top of the PDMS film, or due to a partially interdigitated SDS monolayer that swells the PDMS film. The overall analysis indicates that the addition of SDS results in SDS adsorption—either monolayer or interdigitated monolayer—to the PDMS film, primarily inducing a modification to the electrostatic double-layer force between the mica and PDMS surface.

2.2.5 Cationic Surfactant Monolayers and Bilayers

Cationic surfactants modify both the mica and the PDMS surface. The cationic headgroups of the surfactants adsorb to the negatively charged mica surface, resulting in a monolayer or an incomplete bilayer on the mica at C ≪ CMC, and a complete fluid bilayer at C ≳ CMC (CMC_{MTAB} = 3.7 mM).[39,53,70] On the PDMS surface, the hydrophobic surfactant tails adsorb, either into or onto, the hydrophobic PDMS chains, with a dilute monolayer forming at C ≪ CMC and a dense monolayer at C ≳ CMC.[29,32,53] Accordingly, the forces between a PDMS surface and a mica surface modified by adsorbed layers of cationic surfactant are dependent on the solution concentration of the cationic surfactant, as shown in Figure 2.10.

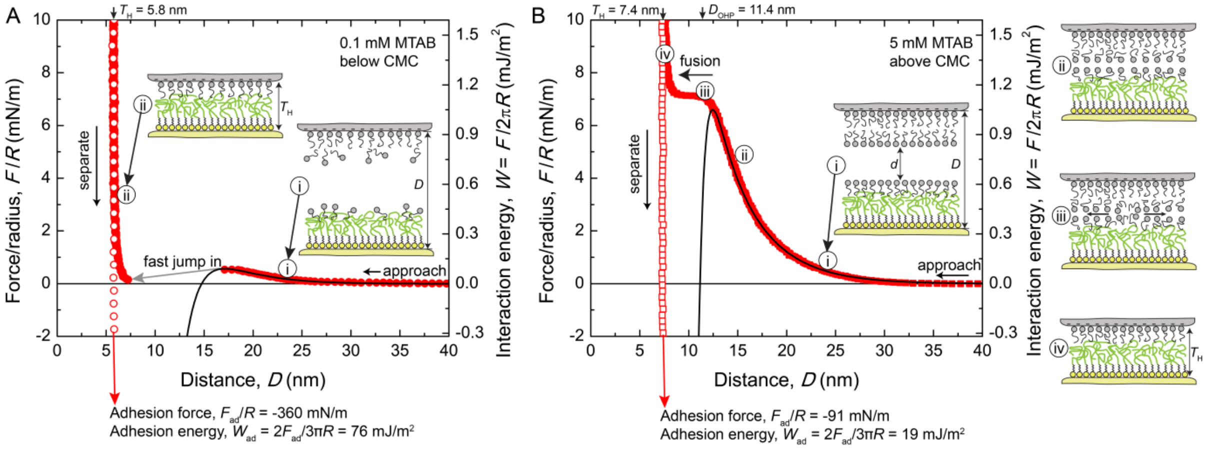

Figure 2.10: Interaction forces between a PDMS surface and a mica surface in a solution of cationic MTAB surfactants. The MTAB adsorbs to both the mica and PDMS surfaces. (A) 0.1 mM MTAB (C < CMC_{MTAB}). The interactions and mechanisms are shown in the schematic drawings i and ii and described in detail in the text. (B) 5 mM MTAB (C > CMC_{MTAB}). The structural transformations of the adsorbed layers are shown in the schematic drawings i, ii, iii, and iv and described in detail in the text. In A and B, the solid black curves passing through the data represent the fits with Equations 2.3 and 2.5, respectively.

When C < CMC (Figure 2.10A), a long-range repulsion is measured during approach of the surfaces, followed by an instability jump-in to contact. The surfaces adhere strongly, with an adhesion energy of $W_{\mathrm{ad}} = 76$ mJ/m^2 measured upon separation. The repulsion on approach can be described by the electrostatic double-layer interaction. There are two potential explanations for the attractive (adhesion) force, which is much stronger than the van der Waals force: hydrophobic interactions between the adsorbed monolayer on the mica and the PDMS film,[71] and/or a subtle charge regulation mechanism in which surfactants exchange during approach and result in an attractive electrostatic force.[72,73] The adhesion, however, appears to be primarily due to a hydrophobic interaction, as the strong measured adhesion energy of $W_{\mathrm{ad}} = 76$ mJ/m^2 is close to the theoretical adhesion energy between two hydrophobic surfaces, $W_0 = 2\gamma_{\mathrm{i}} = 80\text{-}100$ mJ/m^2.[28] Without further evidence of the charge regulation mechanism, the attractive force is quantitatively described with the recently proposed Hydra model for hydrophobic interactions.[14,48]

The theoretical model (black line, Figure 2.10A) includes contributions from van der Waals, electrostatics, and hydrophobic interactions, as described by Equation 2.3:

$$W_{\mathrm{tot}}(D) = -\frac{1}{12\pi}\left(\frac{A_{\mathrm{mPg}}}{D^2} + \frac{A_{\mathrm{swP}}}{(D-T_H)^2}\right) + \frac{\kappa Z}{2\pi}\exp[-\kappa D] - 2\gamma_i \cdot Hy \cdot \exp\left[\frac{-(D-T_H)}{D_H}\right] \qquad (2.3)$$

The double-layer interaction is treated as a constant potential interaction with symmetric potentials. The Hamaker constant for mica-bound surfactant and PDMS interacting across water, $A_{\mathrm{swP}} = 4.4\mathrm{x}10^{-21}$ J, was calculated as previously described.[28] The Debye length κ^{-1} was calculated from Equation 2.2, and the interaction constant Z is calculated from Equation 2.4:

$$Z = 64\pi\varepsilon_0\varepsilon\left(\frac{kT}{e}\right)^2 \tanh^2\left(\frac{ze\psi_0}{4kT}\right) \tag{2.4}$$

where ψ_0 is the symmetric surface potential, $z = 1$ is the ion valency, and all other variables are given above. $T_H = 5.7$ nm is the hardwall thickness. The salt concentration is 5.1 mM (5 mM NaCl plus 0.1 mM MTAB), giving a theoretical Debye length of $\kappa^{-1} = 4.3$ nm. The long-range repulsion can be fitted by using the theoretical Deybe length and adjusting ψ_0 to find $\psi_0 = 78$ mV. Fitting the short-range attraction to the jump-in distance and adhesion shows that $D_H = 1.5$ nm and $Hy = 0.8$. Since $Hy = 1$ corresponds to two fully hydrophobic surfaces (maximum hydrophobic attraction), the measured value of $Hy = 0.8$ indicates that there could be some degree of overturned surfactants on the cationic monolayer or trapped surfactants upon adhesion.

For surfactant concentrations above the CMC, a fluid MTAB bilayer adsorbs on the mica and a densely packed MTAB monolayer adsorbs into the PDMS layer. The interaction forces now resemble the interactions measured between two fusing lipid bilayers,[69,74,75] as shown in Figure 2.10B. The adsorbed layers first approach each other and interact through a long-range electrostatic interaction (Figure 2.10B-i). As the approach continues and additional force is applied, the layers experience an additional repulsion due to steric-hydration forces, resulting in large normal stresses on the layers, which begin to squeeze and spread (Figure 2.10B-ii). This spreading exposes the hydrophobic interior, eventually leading to an instability where the hydrophobic attraction overwhelms the strong steric and electrostatic repulsions, causing the outer surfactant layers to be pushed out (Figure 2.10B-iii). This squeeze-out event leads to adhesive contact between the hydrophobic inner layers (monolayer of MTAB in contact with PDMS) (Figure 2.10B-iv).

The fusion process was modeled previously for surfactant bilayers, and a similar analysis is applied here, as the physics appears to be nearly identical.[69,76] The model is similar to Equation 2.3 above, with extra terms for the bilayer stretching energy and steric-hydration repulsion. As shown in Equation 2.5, the total interaction energy $W(d)$ for bilayer fusion is quantitatively described as a sum of bilayer stretching, hydrophobic interactions, electrostatic interactions, and steric hydration repulsion. Note that the theoretical model $W(d)$ is calculated as a function of the bilayer-bilayer distance, d, while the forces are plotted as a function of the mica-gold separation distance, D. The constant thickness of the PDMS and inner monolayer on mica, $T_{\mathrm{H}} = 6$ nm, must be added to the variable thickness of the two outer layers that stress during the experiment, $T(d) = a(d)/v_0$, where v_0 was found from $a_0 l_0$ ($l_0 = 2$ nm is the surfactant chain length), such that $D = d + T_{\mathrm{H}} + 2T(d)$. The calculated $W(d)$ is plotted vs. D to compare with the measurements. In this case, the Hydra parameter is a function of distance as the surfactant layers are stressed: $Hy(d) \equiv 1 - a_0/a(d)$, where $a_0 = 45$ Å^2 is the equilibrium surfactant headgroup area and $a(d)$ is the stressed headgroup area, calculated as shown in Equation 2.6. The hydrophobic force acts at the plane just beneath the surfactant headgroups, so the plane of origin for the hydrophobic force is shifted in by a total of 2δ, where $\delta = 0.2$ nm is the approximate thickness of the headgroup. As the layers are stressed, $a(d)$ increases from a_0 and the hydrophobic interaction becomes dominant at small separations.

$$W(d) = \left(2\gamma_i \frac{a_0^{\,2}}{a(d)^2} - 2\gamma_i \right) - 2\gamma_i \cdot Hy(d) \cdot \exp\left[\frac{-(d + 2\delta)}{D_H} \right] + \frac{C_{\mathrm{ES}}}{a(d)} \exp[-\kappa d] + \frac{C_{\mathrm{SHR}}}{a(d)} \exp\left[\frac{-d}{D_{SHR}} \right] \tag{2.5}$$

$$a(d) = a_0 \left(1 - \exp\left[\frac{-(d+2\delta)}{D_H}\right]\right)^{-1/2} \tag{2.6}$$

The electrostatics are determined in the limit of large d, such that $C_{\mathrm{ES}}/a_0 = \kappa Z/2\pi$, allowing for calculation of the surface potential ψ_0 as shown in Equation 2.4. The steric hydration pre-exponential term, C_{SHR}, and steric-hydration decay length, D_{SHR}, are fitted in the steep repulsion regime. Here, the total salt concentration is 5 mM MTAB (no background electrolyte), so κ^{-1} = 4.3 nm, and the fitted C_{ES} = 1x10^{-21} J, corresponding to ψ_0 = 110 mV. The remaining parameters are D_{H} = 1 nm, γ_{i} = 50 mJ/m^2, C_{SHR} = 3.1x10^{-20} J with D_{SHR} = 1 nm.

As shown, the model captures the long-range forces, the short-range forces, and the force magnitude of the breakthrough event (instability). The predicted adhesion energy is ~ 42 mJ/m^2, much larger than the measured adhesion of 19 mJ/m^2. This discrepancy occurs because there is a surfactant reservoir in solution, thus surfactants can re-assemble in the contact region during the separation, decreasing the interfacial energy γ_{i} of the hydrophobic interface. Nonetheless, the model is robust and captures most of the quantitative details of the measured interaction forces.

The effects of cationic surfactants are observed to be significantly more complicated than those of anionic surfactants, due to the fact that MTAB can actively adsorb to both surfaces and modify their corresponding surface properties accordingly.

2.2.6 Polycationic Surfactant Monolayers and Multicomponent Films

For the sake of simplicity, the polyelectrolyte surfactant bq5x-PDMS was only adsorbed onto the PDMS film, where the PDMS chain of the surfactant can entangle with the PDMS chains that are grafted to the gold surface. Thus, the mica remains negatively charged, while the PDMS surface adopts a positive charge due to the adsorption of the cationic bq5x-PDMS. The interaction between the mica and the bq5x-PDMS functionalized surface is fully attractive, as shown in Figure 2.11A. The interaction becomes significantly shorter-ranged when increasing the salt concentration from 1 mM NaCl (blue points and curve, Figure 2.11A) to 5 mM NaCl (green points and curve, Figure 2.11A), a signature behavior of electrostatic double layer interactions. The interactions in this case are analyzed with a simple DLVO model that includes contributions from van der Waals and asymmetric electrostatic double layer interactions, as shown in Equation 2.7, where all parameters have been previously described in the previous sections.

Since ψ_{m} is measured in a separate experiment, and the Debye length is calculated from Equation 2.2 above, the only fitting parameter in Equation 2.7 is ψ_{bq5x}, the surface potential of the bq5x-PDMS functionalized surface. The data is described quantitatively by Equation 2.7 for both 1 mM NaCl and 5 mM NaCl, indicating that the measured attraction is due to an attractive electrostatic double-layer force between the asymmetric double layers. The fitting reveals that ψ_{bq5x} decreases from 60 mV at 1 mM NaCl to 40 mV at 5 mM NaCl, which is the expected trend for the surface potential as a function of increasing salt concentration. Repeat experiments on completely different experimental set-ups and days resulted in a wide range of ψ_{bq5x}, as shown in Figure 2.12. This variance likely comes from variance in the prepared layers, due to slight differences in the adsorption structure and coverage of the bq5x-PDMS layer on the grafted PDMS layer.

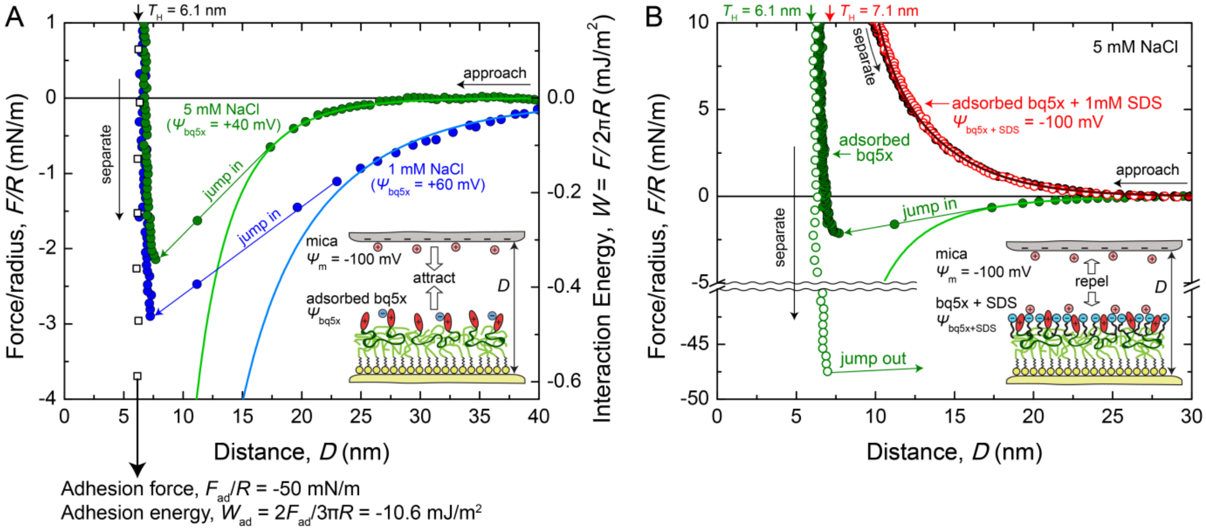

Figure 2.11: (A) Interaction forces between a PDMS surface pre-adsorbed with cationic bq5x-PDMS surfactant and a mica surface. SFA measurements were performed in 1 mM (closed blue circles) and 5 mM (closed green circles) NaCl solutions. As the surfaces approach, an electric double-layer attraction is measured until the gradient of the interaction becomes larger than the SFA spring constant, and the surfaces jump into adhesive contact (indicated with arrows). Strong adhesion is measured between the surfaces as they are separated (open black squares). (B) Addition of 1 mM SDS (red data points) reverses the charge at the bq5x-PDMS interface, and a monotonic repulsion is measured. The green data points (5 mM NaCl, no SDS) are repeated from A, for comparison. Closed and open circles represent data measured on the approach and separation of the two surfaces, respectively. In both A and B, the corresponding solid curves passing through the data represent the fits with Equation 2.7 using the surface potentials show in the figure.

$$W(D) = -\frac{1}{12\pi}\left(\frac{A_{\mathrm{mPg}}}{D^2} + \frac{A_{\mathrm{mwP}}}{(D-T_{\mathrm{H}})^2}\right) + \varepsilon\varepsilon_0\kappa\left[\frac{2\psi_{\mathrm{m}}\psi_{\mathrm{P}}\exp[-\kappa(D-T_H)] - (\psi_{\mathrm{m}}^2+\psi_{\mathrm{P}}^2)\exp[-2\kappa(D-T_H)]}{1-\exp[-2\kappa(D-T_H)]}\right] \qquad (2.7)$$

The strong measured adhesion energy, W_{ad} = -10.6 mJ/m^2, is possibly due to specific interactions of the bq5x-PDMS headgroups with mica. Quaternary ammonium groups are known to strongly interact with negatively charged mica surface sites.[39,40,63] It is unclear if the asymmetric double layer force can be extrapolated to contact or if the adhesion is purely due to this specific amine-mica interaction. Interestingly, these force runs are fully reproducible, i.e., subsequent approach/separation cycles at the same position result in identical data, indicating that no bq5x-PDMS molecules are being pulled out from the layers during the force runs. This is a notable difference from our previous experiments with bq-PDMS surfaces, as discussed below.

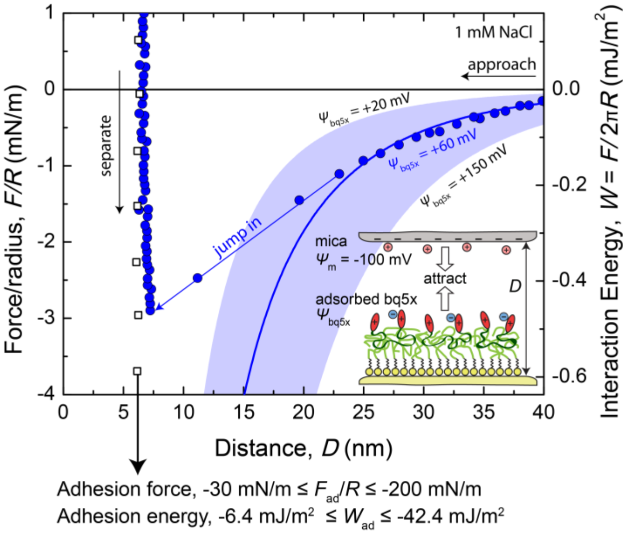

Figure 2.12: Force-distance interaction between a PDMS surface pre-adsorbed with cationic bq5x-PDMS surfactant and a mica surface in 1 mM NaCl solution. The blue data points and curve are repeated from Figure 2.11 in the main text. The shaded blue band indicates the range of electrostatic attractions that were measured over many experiments. The range of attractions is presumably due to variance in the density of adsorbed bq5x surfactant at the PDMS surface between separate experiments—leading to variation in the surface potential at the PDMS-surfactant interface. This variance in bq5x surface density also results in a variation in the measured adhesion forces, with attractions of larger or smaller magnitudes corresponding to adhesion forces of larger or smaller magnitudes, respectively. This range of adhesion forces (and corresponding adhesion energies) is indicated at the bottom of the figure. The attractive interactions and adhesive forces are reproducible over multiple measurements at each unique contact point between the surfaces; however the magnitudes will vary between different contact points within a single experiment, likely indicating non-uniform bq5x adsorption.

Lastly, the effect of adding an SDS co-surfactant to the system with adsorbed bq5x-PDMS was examined, as shown in Figure 2.11B. Addition of SDS results in a monotonic repulsion during both approach and separation of the surfaces. Once again, these forces are analyzed with a DLVO model (Equation 2.7), which indicates that the positive charge on the bq5x-PDMS surface has been reversed and is now strongly negative, resulting in the fitted value of $\psi_{\text{bq5x+SDS}}$ = -100 mV. The SDS appears to have strongly adsorbed into the PDMS layer, reversing the cationic charge of the bq5x-PDMS surface, perhaps removing some bq5x-PDMS, and resulting in an overall strong electrostatic repulsion with the mica.

2.2.7 Discussion

Self-assembled surface structures are varied and complex.[35,53,61–63] At an interface, surfactant equilibrium structure depends on the chemistry and structure of the surface, the chemistry and structure of the surfactant, and the concentration of surfactants in the solution. By measuring the interactions between a hydrophobic polymer surface and a mineral surface in surfactant solutions, we have explored a diverse range of self-assembly phenomena and forces.

At the PDMS-water interface, both anionic and cationic surfactants, polyelectrolytes, and multicomponent mixtures of polyelectrolytes and surfactants adsorb through hydrophobic interactions to form monolayers, or slightly interdigitated monolayers, at the surface. At the mica-water interface, anionic surfactants do not adsorb, while cationic surfactants form monolayers (C<CMC) or fluid bilayers (C ~ CMC). Despite the variety and complexity of self-assembled surface structures, the well-known theories of electrostatic double layers, hydrophobicity, hydration, and van der Waals energies combine to describe the interactions between these self-assembled films in solution. These fundamental potentials quantitatively account for the interactions described in this study, including monotonic repulsions, monotonic attractions, non-monotonic interactions, bilayer fusion events, and strong adhesion forces due to Coulombic or hydrophobic interactions.

The insights gained through force measurements at the PDMS-surfactant interface translate to physical properties that are relevant for colloidal stability and wetting phenomena. SDS preserves a high surface charge on PDMS, even at increased salt concentrations, and should maintain the stability of silicone emulsions. MTAB reverses the surface charge at the PDMS surface. The concentration of MTAB (above or below the CMC) should result in markedly different flocculation and stability of mineral slurries: below the CMC, monolayers of the cationic surfactant adsorb and hydrophobize the mineral surface, leading to rapid flocculation of a suspension; above the CMC, fluid bilayers on the mineral surface result in metastable suspensions that resist flocculation due to repulsive electrostatic, headgroup hydration, and bilayer stress energies. The concentration of the surfactant in solution also regulates the viscosity and frictional losses near an interface; below the CMC, the exposed hydrophobic MTAB tails may result in a finite hydrodynamic slip plane (reducing friction), while above the CMC, the exposed hydrated surfactant headgroups result in a zero-slip boundary condition and increased interfacial water viscosity.[77,78]

The silicone-based bq5x-PDMS surfactant is dispersible in water—despite a large hydrophobic polymer domain—and functions as a practical adhesive in the interface between hydrophobic silicone films and negatively charged hydrophilic surfaces. Unlike short-chain aliphatic surfactants, long-chain PDMS surfactants do not rapidly desorb from a hydrophobic PDMS interface—due to increased hydrophobic interactions and interdigitation (entanglements) with the polymer midblock—resulting in a functionalized PDMS surface that maintains adhesive ability in surfactant-depleted solutions. In the interactions with MTAB solutions, bq5x-PDMS, and the previously-studied bq-PDMS, the mechanism that supports adhesion between the mica and PDMS surfaces is initially the same: electrostatic interactions bind the surfactant headgroups to the mica surface, while hydrophobic interactions between the surfactant tail (or mid-block) maintain the adhesive bridge to the PDMS surface. Yet interestingly, the adhesive bridge fails along different planes for these surfactants. For MTAB and bq-PDMS, the adhesion breaks along the hydrophobic interface (MTAB tail/PDMS interface, or bq-PDMS midblock/PDMS interface) and corresponds to a large adhesion energy that approaches the expected thermodynamic adhesion between 2 hydrophobic surfaces ($2\gamma_{\mathrm{i}}$ ~ 80-100 $\mathrm{mJ/m^2}$). However, in bq5x-PDMS experiments, the adhesion fails at the interface between the bq5x-PDMS quaternary ammonium headgroups and the mica surface, constituting a break in interfacial electrostatic (Coulombic) bonds that result in a lower overall adhesion energy and zero mass transfer of the bq5x-PDMS surfactant onto the mica surface.

Thus, increasing the number of endgroup cations in silicone surfactants actually reduces their overall adhesion to negatively charged surfaces. This type of “bond saturation” has been previously observed to reduce the adhesive performance in other systems,[79] and we speculate that it is either caused by adverse competition for binding sites between mobile neighboring headgroups, a subtle geometry constraint of the endgroup structure, or counter-ion condensation. In applications that require robust adhesion of silicones to negatively charged surfaces, such as the adsorption of lubricating PDMS films to natural polymers, minerals, or fabrics, the “less is more” philosophy of reducing the number of cationic endgroups can thus promote a strongly-bound and longer film lifetime.

Increasing the endgroup size and charge from bq-PDMS to bq5x-PDMS radically alters how the molecules self-assemble at a silicone film, and correspondingly, the surface forces at the silicone interface. At the PDMS surface, bq-PDMS self-assembles into dynamically fluctuating nanostructures that extend into solution. The surface forces of the bq-PDMS film are long-ranged (extending over tens of nm), time- and temperature-dependent, principally due to bridging interactions that occur between the extended bq-PDMS structures and other approaching surfaces. A fivefold increase in the endgroup charge density results in bq5x-PDMS molecules that adsorb to the silicone film as a monolayer, lacking any obvious dynamic fluctuations in the monolayer structure. The bq5x-PDMS monolayers behave as a smeared-out layer of cations and their attractive interactions on approach to mica (for $D > 1$ Debye length) are described by the asymmetric theory of electrostatic double layers. While bq-PDMS films exhibit a rate-dependent bridging force during separation from mica, the higher-charged bq5x-PDMS films do not exhibit a rate-dependent adhesion force as the Coulombic bonds between the headgroups and mica break before the surfactant polymer segments are pulled out from underlying PDMS surface.

While the PDMS polyelectrolytes reverse the surface charge at PDMS and mediate strong adhesion energy to negatively charged surfaces, low concentrations of anionic surfactants can completely eliminate this adhesive functionality. At a concentration of ~1/8th CMC, SDS molecules over-adsorb to the PDMS-polyelectrolyte interface, resulting in charge-reversal behavior that causes the PDMS-polyelectrolyte-SDS structure to carry an overall negative surface charge. Presumably, conscious control over both the headgroup charge density of the PDMS polyelectrolyte and the anionic surfactant concentration would result in the precise control over the PDMS surface charge, with intermediate surface charges between “maximally negative” and “maximally positive.”

The activity and phase stability of emulsions depend on both inter- and intra-aggregate interactions. Inter-aggregate surface interactions, e.g., between an emulsion droplet and a surface or between two emulsion droplets, include electrostatic double layer, hydrophobic, steric, and van der Waals forces as shown above. Intra-aggregate molecular interactions within emulsion droplets are also highly significant, e.g., hydrophobic interactions of a surfactant molecule within the oil droplet, or Coulombic interactions between oppositely charged surfactant species. In practice, the SFA measurements presented here primarily measure the inter-aggregate interaction energy per unit area. Indeed, accurate values of the surfactant adsorption free energies and adsorption profiles to hydrophobic and hydrophilic surfaces,[80–82] combined with surface forces studies, would account for both the intra- and inter-aggregate interactions to fully characterize an emulsion's phase behavior. Given the hydrophobic backbone of bq5x-PDMS, we hypothesize that the polyelectrolyte adsorbs to oil-water interfaces with an adsorption free energy that is larger (more favorable) than the adsorption of more hydrophilic polyelectrolytes.[80–82]

2.2.8 Conclusions

Overall, the charge and self-assembled structure of ionic surfactants can be used to control the sign, magnitude, and range of the interaction energy between hydrophobic and hydrophilic surfaces in solution. The adsorption of charged species to surfaces modulates the strength and sign of the long-range electrostatic double-layer interaction between the surfaces, and can produce monotonic attractions or repulsions. However, non-monotonic interactions—and accordingly, finite energy barriers to adhesion—are also possible by adsorbing surfactants that give rise to total interaction energies between two surfaces that are of opposite sign at small and large separation distances. At smaller separation distances, ionic surfactants can modify repulsions through the steric-hydration energy of polar headgroups or through the unfavorable elastic spreading energy between adjacent surfactants in a bilayer; conversely, attractive and adhesive energies are tuned through hydrophobic interactions between surfactant tails and non-polar surfaces, or from Coulombic interactions between headgroups and charged surfaces.

In any case, the results show how one can rationally design anionic, cationic, polyelectrolyte, and mixed surfactant systems to predict and control the desired static or kinetic stability of various emulsions, dispersions, lubricating thin films, or polymeric adhesives. The self-assembly of silicone polyelectrolytes offers an additional level of control over the surface forces and energies: by modifying the endgroup charge density of the polyelectrolyte, we can incorporate dynamic (rate-dependent) behavior into a system via soft nanostructures,[63] and we can control the equilibrium adhesion energy of a PDMS-polyelectrolyte-mica junction. Thus, these silicone polyelectrolytes can serve as tunable adhesives to directly deposit thin silicone films at target surfaces for lubrication and controlled wetting applications.

2.3 References

(1) Ratner, B. D.; Hoffman, A. S.; Schoen, F. J.; Lemons, J. E. *Biomaterials Science: An Introduction to Materials in Medicine*; Academic Press, 2004.

(2) Williams, D. On the Mechanisms of Biocompatibility. *Biomaterials* **2008**.

(3) Stapleton, F.; Stretton, S.; Papas, E.; Skotnitsky, C.; Sweeney, D. F. Silicone Hydrogel Contact Lenses and the Ocular Surface. *Ocul. Surf.* **2006**, *4*, 24–43.

(4) Khademhosseini, A.; Langer, R.; Borenstein, J.; Vacanti, J. P. Microscale Technologies for Tissue Engineering and Biology. *Proc. Natl. Acad. Sci. U. S. A.* **2006**, *103*, 2480–2487.

(5) Bongaerts, J. H. H.; Fourtouni, K.; Stokes, J. R. Soft-Tribology: Lubrication in a Compliant PDMS–PDMS Contact. *Tribol. Int.* **2007**, *40*, 1531–1542.

(6) Dyson, A.; Wilson, A. R. Film Thicknesses in Elastohydrodynamic Lubrication by Silicone Fluids. *Arch. Proc. Inst. Mech. Eng. Conf. Proc. 1964-1970 (vols 178-184), Var. titles Label. Vol. A to S* **1965**, *180*, 97–112.

(7) Sia, S.; Whitesides, G. Microfluidic Devices Fabricated in Poly (dimethylsiloxane) for Biological Studies. *Electrophoresis* **2003**.

(8) Yu, J.; Chary, S.; Das, S.; Tamelier, J.; Pesika, N. S.; Turner, K. L.; Israelachvili, J. N. Gecko-Inspired Dry Adhesive for Robotic Applications. *Adv. Funct. Mater.* **2011**, *21*, 3010–3018.

(9) Murarash, B.; Itovich, Y.; Varenberg, M. Tuning Elastomer Friction by Hexagonal Surface Patterning. *Soft Matter* **2011**, *7*, 5553.

(10) Kim, J.; Gao, Y.; Hebebrand, C.; Peirtsegaele, E.; Helgeson, M. E. Polymer–surfactant Complexation as a Generic Route to Responsive Viscoelastic Nanoemulsions. *Soft Matter* **2013**, *9*, 6897.

(11) Helgeson, M. E.; Moran, S. E.; An, H. Z.; Doyle, P. S. Mesoporous Organohydrogels from Thermogelling Photocrosslinkable Nanoemulsions. *Nat. Mater.* **2012**, *11*, 344–352.

(12) Somasundaran, P.; Mehta, S. C.; Purohit, P. Silicone Emulsions. *Adv. Colloid Interface Sci.* **2006**, *128-130*, 103–109.

(13) La Torre, C.; Bhushan, B. Nanotribological Effects of Silicone Type, Silicone Deposition Level, and Surfactant Type on Human Hair Using Atomic Force Microscopy. *J. Cosmet. Sci. 57*, 37–56.

(14) Donaldson, S. H.; Das, S.; Gebbie, M. A.; Rapp, M.; Jones, L. C.; Roiter, Y.; Koenig, P. H.; Gizaw, Y.; Israelachvili, J. N. Asymmetric Electrostatic and Hydrophobic-Hydrophilic Interaction Forces between Mica Surfaces and Silicone Polymer Thin Films. *ACS Nano* **2013**, *7*, 10094–10104.

(15) Tian, C. S.; Shen, Y. R. Structure and Charging of Hydrophobic Material/water Interfaces Studied by Phase-Sensitive Sum-Frequency Vibrational Spectroscopy. *Proc. Natl. Acad. Sci. U. S. A.* **2009**, *106*, 15148–15153.

(16) Mishra, H.; Enami, S.; Nielsen, R. J.; Stewart, L. A.; Hoffmann, M. R.; Goddard, W. A.; Colussi, A. J. Brønsted Basicity of the Air-Water Interface. *Proc. Natl. Acad. Sci. U. S. A.* **2012**, *109*, 18679–18683.

(17) Gray-Weale, A.; Beattie, J. K. An Explanation for the Charge on Water's Surface. *Phys. Chem. Chem. Phys.* **2009**, *11*, 10994–11005.

(18) Creux, P.; Lachaise, J.; Graciaa, A.; Beattie, J. K.; Djerdjev, A. M. Strong Specific Hydroxide Ion Binding at the Pristine Oil/water and Air/water Interfaces. *J. Phys. Chem. B* **2009**, *113*, 14146–14150.

(19) Fontani, G.; Gaspari, R.; Spencer, N. D.; Passerone, D.; Crockett, R. Adsorption and Friction Behavior of Amphiphilic Polymers on Hydrophobic Surfaces. *Langmuir* **2013**, *29*, 4760–4771.

(20) Lee, S.; Spencer, N. D. Aqueous Lubrication of Polymers: Influence of Surface Modification. *Tribol. Int.* **2005**, *38*, 922–930.

(21) Argillier, J.-F.; Tirrell, M. Adsorption of Water Soluble Ionic/hydrophobic Diblock Copolymer on a Hydrophobic Surface. *Theor. Chim. Acta* **1992**, *82*, 343–350.

(22) Liberelle, B.; Giasson, S. Friction and Normal Interaction Forces between Irreversibly Attached Weakly Charged Polymer Brushes. *Langmuir* **2008**, *24*, 1550–1559.

(23) Raviv, U.; Giasson, S.; Kampf, N.; Gohy, J.-F.; Jérôme, R.; Klein, J. Normal and Frictional Forces between Surfaces Bearing Polyelectrolyte Brushes. *Langmuir* **2008**, *24*, 8678–8687.

(24) Yu, J.; Kan, Y.; Rapp, M.; Danner, E.; Wei, W.; Das, S.; Miller, D. R.; Chen, Y.; Waite, J. H.; Israelachvili, J. N. Adaptive Hydrophobic and Hydrophilic Interactions of Mussel Foot Proteins with Organic Thin Films. *Proc. Natl. Acad. Sci. U. S. A.* **2013**, *110*, 15680–15685.

(25) Lee, H.; Lee, B. P.; Messersmith, P. B. A Reversible Wet/dry Adhesive Inspired by Mussels and Geckos. *Nature* **2007**, *448*, 338–341.

(26) Lu, Q.; Danner, E.; Waite, J. H.; Israelachvili, J. N.; Zeng, H.; Hwang, D. S. Adhesion of Mussel Foot Proteins to Different Substrate Surfaces. *J. R. Soc. Interface* **2013**, *10*, 20120759.

(27) Mehta, G.; Kiel, M. J.; Lee, J. W.; Kotov, N.; Linderman, J. J.; Takayama, S. Polyelectrolyte-Clay-Protein Layer Films on Microfluidic PDMS Bioreactor Surfaces for Primary Murine Bone Marrow Culture. *Adv. Funct. Mater.* **2007**, *17*, 2701–2709.

(28) Israelachvili, J. N. *Intermolecular and Surface Forces: Revised Third Edition*; Academic Press, 2011.

(29) Wanless, E. J.; Ducker, W. A. Organization of Sodium Dodecyl Sulfate at the Graphite−Solution Interface. *J. Phys. Chem.* **1996**, *100*, 3207–3214.

(30) Ducker, W. A.; Grant, L. M. Effect of Substrate Hydrophobicity on Surfactant Surface−Aggregate Geometry. *J. Phys. Chem.* **1996**, *100*, 11507–11511.

(31) Liu, J.-F.; Ducker, W. A. Surface-Induced Phase Behavior of Alkyltrimethylammonium Bromide Surfactants Adsorbed to Mica, Silica, and Graphite. *J. Phys. Chem. B* **1999**, *103*, 8558–8567.

(32) Grant, L. M.; Tiberg, F.; Ducker, W. A. Nanometer-Scale Organization of Ethylene Oxide Surfactants on Graphite, Hydrophilic Silica, and Hydrophobic Silica. *J. Phys. Chem. B* **1998**, *102*, 4288–4294.

(33) Tiberg, F.; Brinck, J.; Grant, L. Adsorption and Surface-Induced Self-Assembly of Surfactants at the Solid–aqueous Interface. *Curr. Opin. Colloid Interface Sci.* **1999**, *4*, 411–419.

(34) Johnson, R. A.; Nagarajan, R. Modeling Self-Assembly of Surfactants at Solid/liquid Interfaces. I. Hydrophobic Surfaces. *Colloids Surfaces A Physicochem. Eng. Asp.* **2000**, *167*, 31–46.

(35) Manne, S.; Cleveland, J. P.; Gaub, H. E.; Stucky, G. D.; Hansma, P. K. Direct Visualization of Surfactant Hemimicelles by Force Microscopy of the Electrical Double Layer. *Langmuir* **1994**, *10*, 4409–4413.

(36) Israelachvili, J.; Min, Y.; Akbulut, M.; Alig, A.; Carver, G.; Greene, W.; Kristiansen, K.; Meyer, E.; Pesika, N.; Rosenberg, K.; et al. Recent Advances in the Surface Forces Apparatus (SFA) Technique. *Reports Prog. Phys.* **2010**, *73*, 036601.

(37) Israelachvili, J. . Thin Film Studies Using Multiple-Beam Interferometry. *J. Colloid Interface Sci.* **1973**, *44*, 259–272.

(38) Ruths, M.; Israelachvili, J. N.; Ploehn, H. J. Effects of Time and Compression on the Interactions of Adsorbed Polystyrene Layers in a Near-ϑ Solvent. *Macromolecules* **1997**, *30*, 3329–3339.

(39) Chen, Y. L.; Chen, S.; Frank, C.; Israelachvili, J. Molecular Mechanisms and Kinetics during the Self-Assembly of Surfactant Layers. *J. Colloid Interface Sci.* **1992**, *153*, 244–265.

(40) Claesson, P.; Horn, R. G.; Pashley, R. M. Measurement of Surface Forces between Mica Sheets Immersed in Aqueous Quaternary Ammonium Ion Solutions. *J. Colloid Interface Sci.* **1984**, *100*, 250–263.

(41) Gennes, P.-G. de. *Scaling Concepts in Polymer Physics*; Cornell University Press, 1979.

(42) Wong, J. Y. Direct Measurement of a Tethered Ligand-Receptor Interaction Potential. *Science (80-.).* **1997**, *275*, 820–822.

(43) Zimm, B. H. Dynamics of Polymer Molecules in Dilute Solution: Viscoelasticity, Flow Birefringence and Dielectric Loss. *J. Chem. Phys.* **1956**, *24*, 269.

(44) Aniansson, E. A. G.; Wall, S. N.; Almgren, M.; Hoffmann, H.; Kielmann, I.; Ulbricht, W.; Zana, R.; Lang, J.; Tondre, C. Theory of the Kinetics of Micellar Equilibria and Quantitative Interpretation of Chemical Relaxation Studies of Micellar Solutions of Ionic Surfactants. *J. Phys. Chem.* **1976**, *80*, 905–922.

(45) Patist, A.; Axelberd, T.; Shah, D. Effect of Long Chain Alcohols on Micellar Relaxation Time and Foaming Properties of Sodium Dodecyl Sulfate Solutions. *J. Colloid Interface Sci.* **1998**, *208*, 259–265.

(46) Valtiner, M.; Donaldson, S. H.; Gebbie, M. A.; Israelachvili, J. N. Hydrophobic Forces, Electrostatic Steering, and Acid-Base Bridging between Atomically Smooth Self-Assembled Monolayers and End-Functionalized PEGolated Lipid Bilayers. *J. Am. Chem. Soc.* **2012**, *134*, 1746–1753.

(47) Donaldson, S. H.; Valtiner, M.; Gebbie, M. A.; Harada, J.; Israelachvili, J. N. Interactions and Visualization of Bio-Mimetic Membrane Detachment at Smooth and Nano-Rough Gold Electrode Surfaces. *Soft Matter* **2013**, *9*, 5231.

(48) Donaldson, S. H.; Røyne, A.; Kristiansen, K.; Rapp, M. V; Das, S.; Gebbie, M. A.; Lee, D. W.; Stock, P.; Valtiner, M.; Israelachvili, J. Developing a General Interaction Potential for Hydrophobic and Hydrophilic Interactions. *Langmuir* **2015**, *31*, 2051–2064.

(49) Bell, G. Models for the Specific Adhesion of Cells to Cells. *Science (80-.).* **1978**, *200*, 618–627.

(50) Weirich, K. Membrane Deformations: Quantitative Investigations with Lipid Worms and Supported Bilayers, University of California-Santa Barbara, 2012.

(51) O’Shea, S. J.; Welland, M. E.; Rayment, T. An Atomic Force Microscope Study of Grafted Polymers on Mica. *Langmuir* **1993**, *9*, 1826–1835.

(52) Huang, H.; Rankin, S. E.; Penn, L. S.; Quirk, R. P.; Cheong, T. H. Transition from Mushroom to Brush during Formation of a Tethered Layer. *Langmuir* **2004**, *20*, 5770–5775.

(53) Zhang, R.; Somasundaran, P. Advances in Adsorption of Surfactants and Their Mixtures at Solid/solution Interfaces. *Adv. Colloid Interface Sci.* **2006**, *123-126*, 213–229.

(54) De Gennes, P. G.; Taupin, C. Microemulsions and the Flexibility of Oil/water Interfaces. *J. Phys. Chem.* **1982**, *86*, 2294–2304.

(55) Hunter, T. N.; Pugh, R. J.; Franks, G. V; Jameson, G. J. The Role of Particles in Stabilising Foams and Emulsions. *Adv. Colloid Interface Sci.* **2008**, *137*, 57–81.

(56) Antonietti, M.; Conrad, J.; Thuenemann, A. Polyelectrolyte-Surfactant Complexes: A New Type of Solid, Mesomorphous Material. *Macromolecules* **1994**, *27*, 6007–6011.

(57) Banerjee, S.; Cazeneuve, C.; Baghdadli, N.; Ringeissen, S.; Leermakers, F. A. M.; Luengo, G. S. Surfactant-Polymer Interactions: Molecular Architecture Does Matter. *Soft Matter* **2015**, DOI: 10.1039/C5SM00117J.

(58) Faul, C. F. J.; Antonietti, M. Ionic Self-Assembly: Facile Synthesis of Supramolecular Materials. *Adv. Mater.* **2003**, *15*, 673–683.

(59) Gonzenbach, U. T.; Studart, A. R.; Tervoort, E.; Gauckler, L. J. Ultrastable Particle-Stabilized Foams. *Angew. Chem. Int. Ed. Engl.* **2006**, *45*, 3526–3530.

(60) Noro, A.; Hayashi, M.; Matsushita, Y. Design and Properties of Supramolecular Polymer Gels. *Soft Matter* **2012**, *8*, 6416.

(61) Ducker, W. A.; Wanless, E. J. Surface-Aggregate Shape Transformation. *Langmuir* **1996**, *12*, 5915–5920.

(62) Manne, S.; Gaub, H. E. Molecular Organization of Surfactants at Solid-Liquid Interfaces. *Science (80-.).* **1995**, *270*, 1480–1482.

(63) Rapp, M. V; Donaldson, S. H.; Gebbie, M. A.; Das, S.; Kaufman, Y.; Gizaw, Y.; Koenig, P.; Roiter, Y.; Israelachvili, J. N. Hydrophobic, Electrostatic, and Dynamic Polymer Forces at Silicone Surfaces Modified with Long-Chain Bolaform Surfactants. *Small* **2015**, *11*, 2058–2068.

(64) Johnson, K. L.; Kendall, K.; Roberts, A. D. Surface Energy and the Contact of Elastic Solids. *Proc. R. Soc. A Math. Phys. Eng. Sci.* **1971**, *324*, 301–313.

(65) Hegner, M.; Wagner, P.; Semenza, G. Ultralarge Atomically Flat Template-Stripped Au Surfaces for Scanning Probe Microscopy. *Surf. Sci.* **1993**, *291*, 39–46.

(66) Chai, L.; Klein, J. Large Area, Molecularly Smooth (0.2 Nm Rms) Gold Films for Surface Forces and Other Studies. *Langmuir* **2007**, *23*, 7777–7783.

(67) Hogg, R.; Healy, T. W.; Fuerstenau, D. W. Mutual Coagulation of Colloidal Dispersions. *Trans. Faraday Soc.* **1966**, *62*, 1638.

(68) Parsegian, V. A.; Gingell, D. On the Electrostatic Interaction across a Salt Solution between Two Bodies Bearing Unequal Charges. *Biophys. J.* **1972**, *12*, 1192–1204.

(69) Donaldson, S. H.; Lee, C. T.; Chmelka, B. F.; Israelachvili, J. N. General Hydrophobic Interaction Potential for Surfactant/lipid Bilayers from Direct Force Measurements between Light-Modulated Bilayers. *Proceedings of the National Academy of Sciences*, 2011, *108*, 15699–15704.

(70) Mittal, K. L.; Bothorel, P. *Surfactants in Solution*; Mittal, K. L., Bothorel, P., Eds.; Springer US: Boston, MA, 1987.

(71) Israelachvili, J.; Pashley, R. The Hydrophobic Interaction Is Long Range, Decaying Exponentially with Distance. *Nature* **1982**, *300*, 341–342.

(72) Subramanian, V.; Ducker, W. Proximal Adsorption of Cationic Surfactant on Silica at Equilibrium. *J. Phys. Chem. B* **2001**, *105*, 1389–1402.

(73) Lokar, W. J.; Ducker, W. A. Proximal Adsorption at Glass Surfaces: Ionic Strength, pH, Chain Length Effects. *Langmuir* **2004**, *20*, 378–388.

(74) Evans, E.; Metcalfe, M. Free Energy Potential for Aggregation of Giant, Neutral Lipid Bilayer Vesicles by Van Der Waals Attraction. *Biophys. J.* **1984**, *46*, 423–426.

(75) Servuss, R. M.; Helfrich, W. Mutual Adhesion of Lecithin Membranes at Ultralow Tensions. *J. Phys.* **1989**, *50*, 809–827.

(76) Banquy, X.; Kristiansen, K.; Lee, D. W.; Israelachvili, J. N. Adhesion and Hemifusion of Cytoplasmic Myelin Lipid Membranes Are Highly Dependent on the Lipid Composition. *Biochim. Biophys. Acta* **2012**, *1818*, 402–410.

(77) Audry, M.-C.; Piednoir, A.; Joseph, P.; Charlaix, E. Amplification of Electro-Osmotic Flows by Wall Slippage: Direct Measurements on OTS-Surfaces. *Faraday Discuss.* **2010**, *146*, 113.

(78) Honig, C. D. F.; Ducker, W. A. Squeeze Film Lubrication in Silicone Oil: Experimental Test of the No-Slip Boundary Condition at Solid−Liquid Interfaces. *J. Phys. Chem. C* **2008**, *112*, 17324–17330.

(79) Wang, J.; Tahir, M. N.; Kappl, M.; Tremel, W.; Metz, N.; Barz, M.; Theato, P.; Butt, H.-J. Influence of Binding-Site Density in Wet Bioadhesion. *Adv. Mater.* **2008**, *20*, 3872–3876.

(80) Li, D.; Schubert, B.; Wagner, N. J. Characterization of Cationic Polyelectrolytes Adsorption to an Anionic Emulsion via Zeta-Potential and Microcalorimetry. *J. Surfactants Deterg.* **2013**, *17*, 655–667.

(81) Li, D.; Kelkar, M. S.; Wagner, N. J. Phase Behavior and Molecular Thermodynamics of Coacervation in Oppositely Charged Polyelectrolyte/surfactant Systems: A Cationic Polymer JR 400 and Anionic Surfactant SDS Mixture. *Langmuir* **2012**, *28*, 10348–10362.

(82) Seng, W. P.; Tam, K. C.; Jenkins, R. D.; Bassett, D. R. Calorimetric Studies of Model Hydrophobically Modified Alkali-Soluble Emulsion Polymers with Varying Spacer Chain Length in Ionic Surfactant Solutions. *Macromolecules* **2000**, *33*, 1727–1733.

CHAPTER 3

Adaptive Interactions of Mussel Foot Proteins and Peptides on Wet Organic Films

3.1 Adaptive Hydrophobic and Hydrophilic Interactions of Mussel Foot Proteins with Organic Thin Films

Yu, J.; Kan, Y.; Rapp, M. V.; Danner, E.; Wei, W.; Das, S.; Miller, D. R.; Chen, Y.; Waite, J. H.; Israelachvili, J. N. (2013) ***Proc. Natl. Acad. Sci. U. S. A.***, 110 (39):15680–15685.

3.1.1 Abstract

The adhesion of mussel foot proteins (Mfps) to a variety of specially engineered mineral and metal oxide surfaces has previously been extensively investigated, but the relevance of these studies to adhesion in biological environments remains unknown. Most solid surfaces exposed to seawater or physiological fluids become fouled by organic conditioning films and biofilms within minutes. Understanding the binding mechanisms of Mfps to organic films of known chemical and physical properties is therefore of considerable theoretical and practical interest. Using self-assembled monolayers (SAMs) on atomically smooth gold substrates and the surface forces apparatus, we explored the force-distance profiles and adhesion energies of three different Mfps: Mfp-1, Mfp-3, and Mfp-5, on (a) hydrophobic methyl- (CH_3-) and (b) hydrophilic alcohol- (OH-) terminated SAM surfaces between pH 3-7.5. At acidic pH, all three Mfps adhered strongly to the CH_3-terminated SAM surfaces via hydrophobic interactions (range of E_{ad} = -4 to -9 mJ/m^2), but only weakly to the OH-terminated SAM surfaces through hydrogen bonding ($E_{ad} \leq$ -0.5 mJ/m^2). 3, 4-

Dihydroxyphenylalanine (Dopa) residues in Mfps mediate binding to both SAM surface types, but through different interactions: typical bidentate H-bonding by Dopa is frustrated by the longer spacing of OH-SAMs; in contrast, on CH_3-SAMs, Dopa in synergy with other nonpolar residues, partitions to the hydrophobic surface. Asymmetry in the distribution of hydrophobic residues in intrinsically unstructured proteins, the distortion of bond geometry between H-bonding surfaces, and the manipulation of physisorbed binding lifetimes represent important new concepts for the design of adhesive, as well as non-fouling, surfaces.

3.1.2 Introduction

Marine mussels are experts at wet adhesion, achieving strong and durable attachments to a variety of surfaces in their chemically heterogeneous habitat. Adhesion is mediated by a byssus, essentially a bundle of leathery threads that emerge from the living mussel tissue at one end, and tipped by flat adhesive plaques at the other. Byssal plaques consist of a complex array of proteins (mostly *mussel foot proteins*, Mfps), each of which has a distinct localization and function in the structure, but all share the unusual modified amino acid 3,4-dihydroxyphenylalanine (Dopa, see Figure 3.1).

Of the dozen or so known mussel foot proteins, Mfp-1, Mfp-3, and Mfp-5 have been shown to exhibit remarkable binding to mineral surfaces such as mica and TiO_2.[1] The versatility of mussel adhesion to surfaces with wide-ranging chemical and physical properties has inspired much research dedicated to understanding the mechanism of mussel adhesion as well as developing biomimetic coatings and adhesives for wide-ranging industrial and biomedical applications, the latter including paints for coronary arteries,[2] fetal membrane sealants,[3] cell encapsulants,[4] bone glues,[5] and for securing transplants for diabetics.[6]

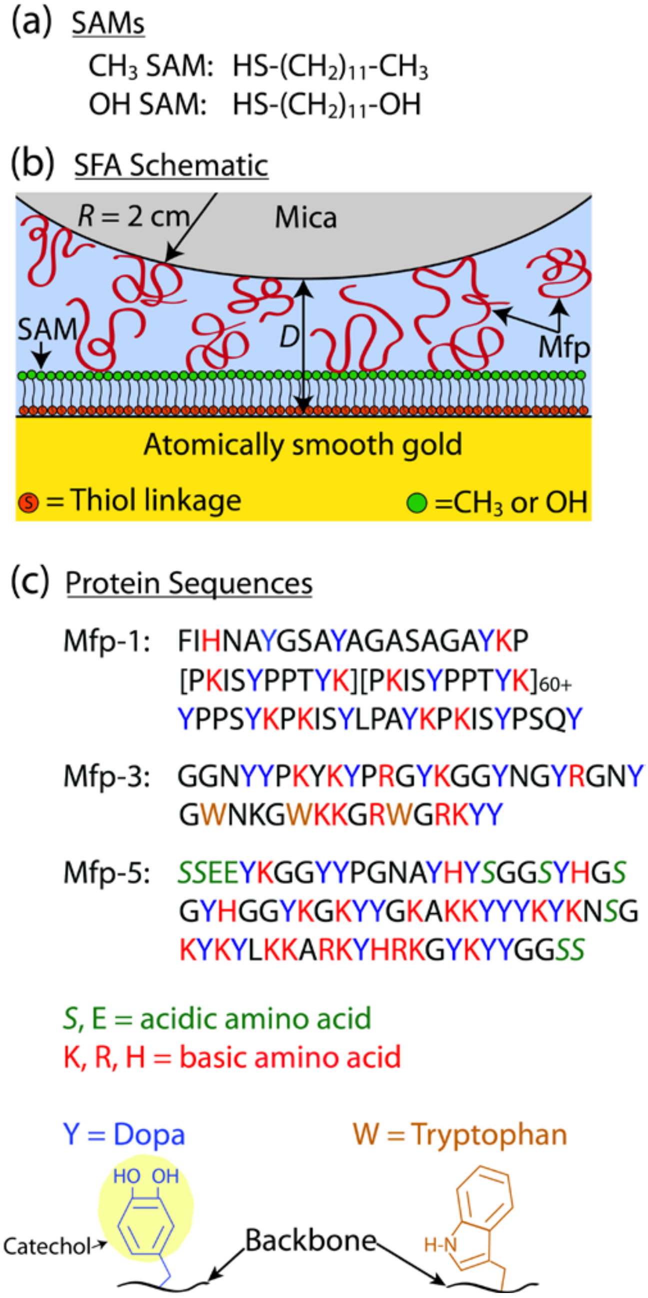

Figure 3.1: Adhesive Mytilus foot proteins (Mfp) and self-assembled monolayers. (a) The hydrophobic CH_3-SAM (1-undecanethiol) and the hydrophilic OH-SAM (11-mercapto-1-undecanol). (b) Experimental setup of the asymmetric surfaces used in the surface forces apparatus experiments in this study. (c) The amino acid sequences of Mfp-1 (sequence shown is Mcfp-1), Mfp-3 (Mcfp-3F), and Mfp-5 (Mefp-5). Italicized S residues in Mfp-5 represent phosphoserines. The Dopa catechol moiety is highlighted in light yellow.

The catecholic moiety of Dopa (Figure 3.1) binds strongly to a variety of metal oxide surfaces by forming stable bidentate modes of H-bonding and metal coordination. Therefore, Dopa-containing proteins and polymers have considerable appeal as molecular coatings and glues for metal oxide surfaces. The coordination chemistry of Dopa/catecholic ligands has been studied extensively, particularly with transition metal ions,[7] and is in general agreement with nanomechanical studies of tethered catechols binding to well-characterized solid surfaces. For example, AFM tests have shown that the pull-off (adhesion) force of a single Dopa residue chemisorbed to a wet titania surface is about 1 nN (corresponding to a bond energy of ~ 30 kcal/mol), and is completely reversible, as expected for a coordination complex.[8] Strong adhesion forces have also been reported by recent SFA tests of Mfp-3 and Mfp-1 on TiO_2 substrates.[9,10]

A significant oversight of many current investigations of the mechanisms of wet adhesion is the observation that, in the natural world, surfaces, such as titania and mica, are not necessarily available for adhesion because they are covered by thick (often > 1 μm) organic films of various types.[11] How mussels contrive to adhere to such fouled surfaces is of fundamental importance, perhaps more so than to the metal oxide itself. We report here on the adhesion of three Mfps to thin films (known as self-assembled monolayers, SAMs) deposited onto gold surfaces. The results suggest that in some cases Mfp-SAM adhesion is stronger than the Mfp adhesion to mica; in others, it is much weaker. These differences reveal potential strategies for promoting or inhibiting wet adhesion.

3.1.3 Materials and Methods

Protein purification: Purifications of Mfp-1, 3F and 5 were achieved as previously described.[12,13] The purified proteins were suspended in a pH 3 buffer (0.1 M acetic acid (EMD Chemicals, Gibbstown, NJ), and 0.25 M potassium nitrate (Sigma Aldrich, St. Louis, MO)). The protein solutions were divided into small aliquots and stored at -50°C before experiments.

Surface preparation: Atomically smooth gold surfaces were prepared using a mica templating technique. A 45 nm thick gold layer was first deposited on a freshly cleaved mica sheet. The mica sheet was then glued onto a cylindrical glass disk using a UV-curable glue with the gold layer facing down to the UV glue, after which the glue was fully cured by exposing to UV light for 3 hours. The mica sheet was peeled off in ethanol to reveal the atomically smooth gold surface that is predominantly <111>.[14] Freshly cleaved gold surfaces were immediately immersed into 1mM ethanolic solutions of the respective alkane thiols (11-mercaptoundecanol or 1-Undecanethiol). The surface was kept in the thiol solution for 12 hours, allowing for the SAM deposition, and then rinsed thoroughly with ethanol to remove the excess alkane thiols. This technique has been previously shown to produce uniform monolayers on <111> gold surfaces with a headgroup spacing of 0.5 nm.[14,15]

Surface forces apparatus (SFA): The adhesion of Mfp-1, Mfp-3, and Mfp-5 on SAM surfaces was studied using a surface forces apparatus 2000 (SFA 2000) with a reported geometry.[16,17] Following buffers were used in the experiments: 0.1 M acetic acid, 0.25 M potassium nitride (pH 3); 0.016 M potassium phosphate monobasic (Mallinckrodt, Hazelwood, MO) and 0.084 M potassium phosphate dibasic (EMD Chemicals, Gibbstown, NJ) (pH 7.5). Milli-Q water (Millipore, Bedford, MA) was used for all the glassware cleaning and solution preparation.

3.1.4 Adhesion Measurements

Molecularly smooth gold surfaces were prepared with a mica templating technique.[16] The gold surfaces were then modified with self-assembled alkanethiol monolayers. The SAM termination directly affects the surface energy, surface chemistry, and wettability of the surfaces. To assess the adhesive versatility of the three Mfps (Mfp-1, Mfp-3, and Mfp-5, see Figure 3.1) on the SAM surfaces, two different SAMs, a hydrophobic methyl-terminated SAM (CH_3-SAM) and an alcohol-terminated SAM (OH-SAM), were used in this study, giving distinctly different surface chemistries: CH_3-SAM gives a very hydrophobic surface (advancing contact angle $\theta_a \sim 110°$), whereas OH-SAM gives a hydrophilic surface ($\theta_a < 10°$).[18] These two SAMs provide two very disparate surface conditions that mussels might encounter in their natural environment, a very hydrophobic surface and a relatively hydrophilic surface.

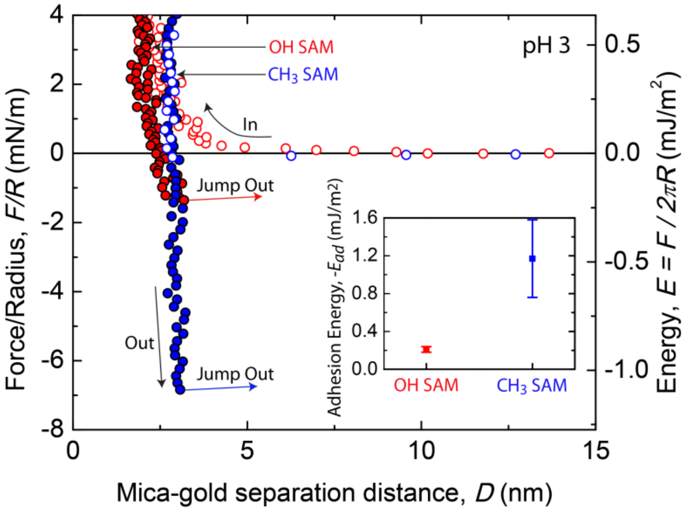

Figure 3.2: Force-distance profiles of a bare mica surface against CH_3- and OH-SAM surfaces in pH 3 buffer. The insert shows the adhesion energies measured by the SFA.

Only weak adhesion forces were measured when separating a bare mica surface and a SAM modified gold surface for both the methyl terminated CH_3-SAM and the alcohol terminated OH-SAM (Figure 3.2). This weak interaction is likely to arise from (the relatively weak) van der Waals interactions between the SAMs and mica.[16] After determining the reference of the interaction between CH_3-SAM and bare mica, picomlar amounts of Mfp-1, 3 or 5 were then added to the gap solution between the two surfaces, allowing the protein to adsorb to the mica or SAM surfaces for 20 min. Strong adhesion forces were measured upon separation after bringing two surfaces into contact, with the adhesion energies E_{adh} of -3.5 ± 1.0, -8.9 ± 0.2, and - 6.7 ± 0.2 mJ/m^2 for Mfp-1, 3, and 5, respectively (Figure 3.3a). Increasing the pH of the solution from 3 to 7 totally abolished the adhesion forces of the three Mfps between the CH_3-SAM and mica surfaces (Figure 3.3b and 3.4a). This loss of adhesion is expected given that the auto-oxidation of Dopa to Dopa-quinone at pH 7 deprives Dopa of its bidentate H-bonding anchor to the mica surface.

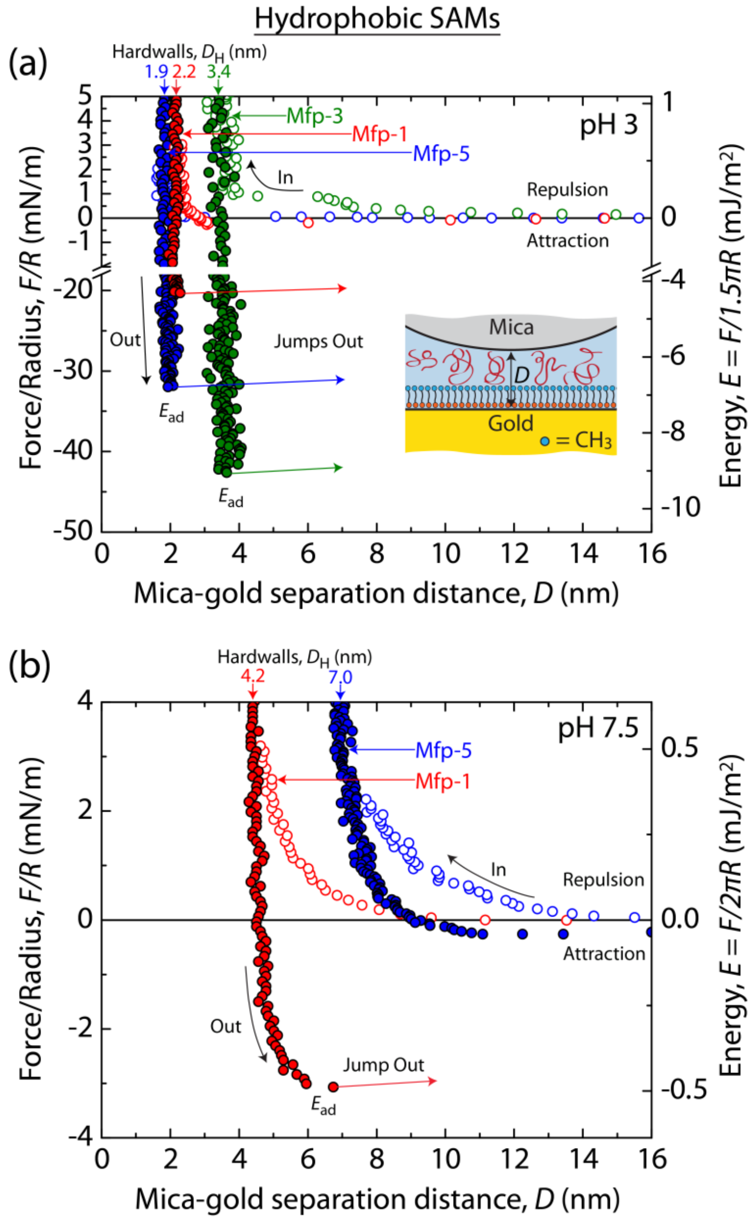

Figure 3.3: Measured force-distance curves of Mfps between a hydrophobic CH_3-SAM surface and a mica surface. The measured curves correspond to either ~3 picomoles (~0.3 μg) of Mfp-1, ~200 picomoles (~1.0 μg) of Mfp-3, or ~27 picomoles (0.24 μg) of Mfp-5 injected into the gap solution between the surfaces. (a) Mfp-1, Mfp-3, and Mfp-5 all exhibit strong adhesion between the hydrophobic SAM and the mica surface at pH 3, and significant flattening of the contact area is observed (with Fringes of Equal Chromatic Order, or FECO, in the SFA). Accordingly, the adhesion energy is related to the measured force via the Johnson, Kendall, and Roberts theory for the adhesion of elastic surfaces, $E_{ad} = F_{ad}/1.5\pi R$.[19] (b) Increasing the pH from 3 to 7.5 significantly reduces the adhesion, and increases the intervening film thickness, of Mfp-1 and Mfp-5. Significant flattening of the contact area was not observed for any Mfp at pH 7.5, and the adhesion energy is related to the measured force via the Derjaguin approximation.[20] Data for Mfp-3 are not included because of pH-dependent protein precipitation (see Figure 3.6).

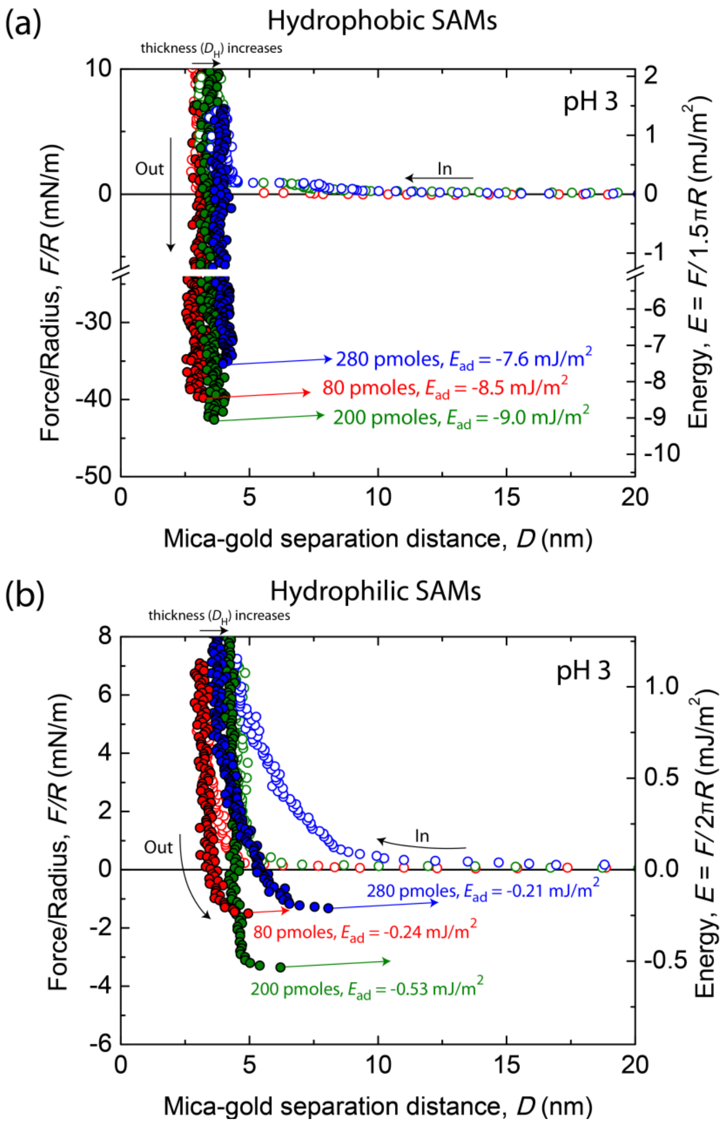

Figure 3.4: Force-distance profiles between mica and SAM surfaces with increasing amounts of Mfp-3 added to the gap solution between the surfaces. (a) Mfp-3 mediated interactions between mica and CH_3-SAMs. The total film thickness increases with increasing added amount of Mfp-3, and the adhesion goes through a maximum at ~200 pmoles of added Mfp-3. (b) Mfp-3 mediated interactions between mica and OH-SAMs. The total film thickness increases with increasing added amount of Mfp-3, and the adhesion goes through a maximum at ~200 pmoles of added Mfp-3. The onset of repulsion increases with increasing amounts of added protein.

The bridging adhesions of the three Mfps between OH-SAM/mica surfaces were much weaker at pH 3 in comparison to the CH_3-SAM/Mfp/mica configuration, with adhesion energies of -0.25 ± 0.07, -0.37 ± 0.15, and -0.31 ± 0.02 mJ/m^2 measured for Mfp-1, 3, and 5, respectively (Figure 3.5a). Similarly, all three Mfps lost the ability to bridge the two surfaces after oxidation by increasing the solution pH to 7 (Figure 3.5b).

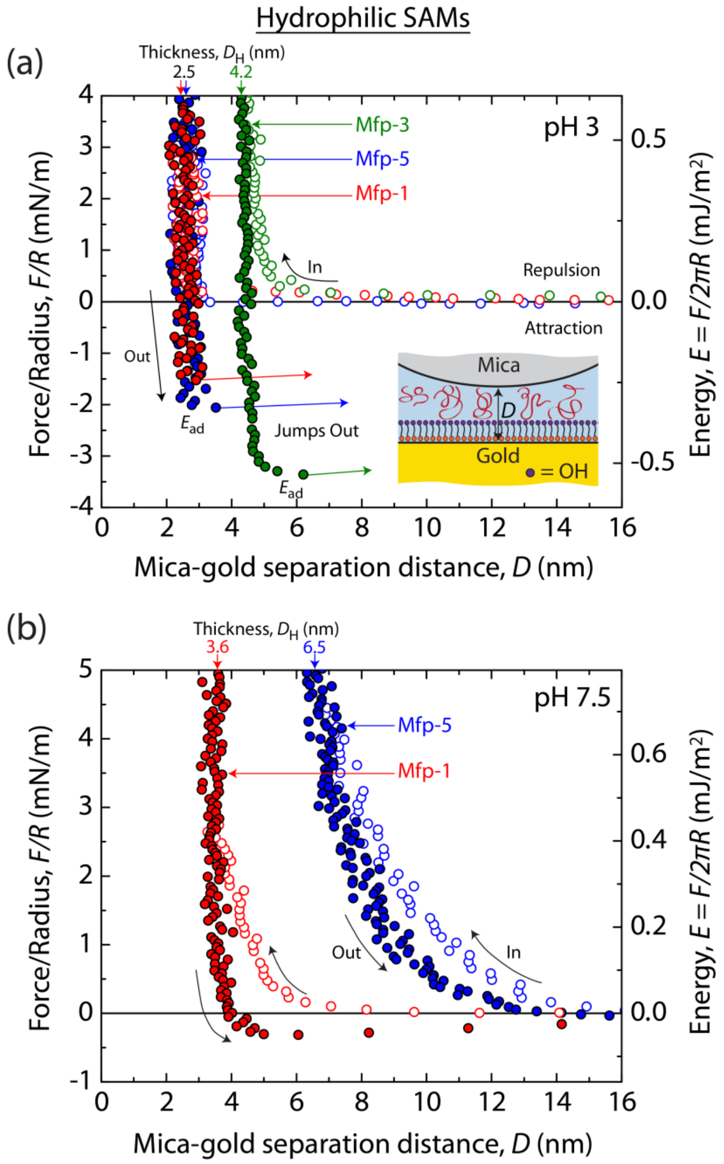

Figure 3.5: Measured force-distance curves of Mfps between a hydrophilic OH-SAM surface and a mica surface. The measured curves correspond to either ~3 picomoles (~0.3 μg) of Mfp-1, ~200 picomoles (~1.0 μg) of Mfp-3, or ~27 picomoles (0.24 μg) of Mfp-5 injected into the gap solution between the surfaces. (a) Mfp-1, Mfp-3, and Mfp-5 all exhibit weak adhesion between the hydrophilic SAM and the mica surface at pH 3. Significant flattening of the contact area was not observed for any Mfp at pH 3, and the adhesion energy is related to the measured force via the Derjaguin approximation. (b) Increasing the pH from 3 to 7.5 reduces or eliminates the adhesion, and increases the intervening film thickness, of Mfp-1 and Mfp-5. Data for Mfp-3 are not included because of pH-dependent protein precipitation (see Figure 3.6).

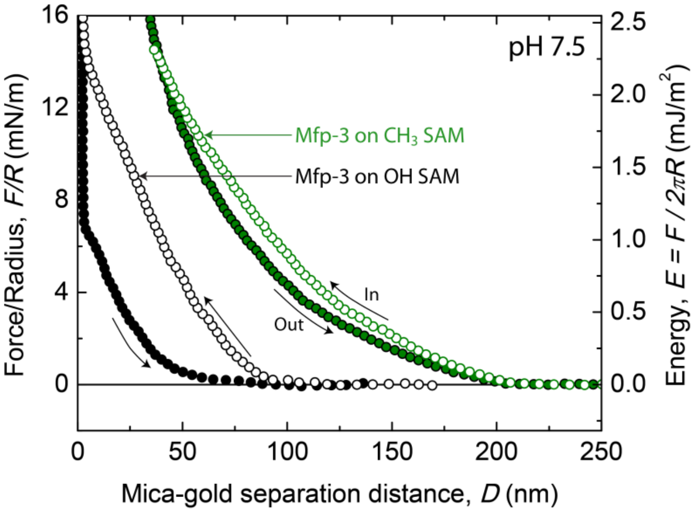

Figure 3.6: Force-distance curves of Mfp-3 between a mica surface and a SAM surface at pH 7.5.

A strong correlation was observed between the amount of Mfp-3 added into the gap solution between two surfaces and the measured adhesion (Figures 3.4 and 3.7). On CH_3-SAM/mica surfaces, 80 pmole Mfp-3 was first injected into the solution, resulting in an E_{ad} of -8.8 ± 1.4 mJ/m^2. Adding 120 pmole more Mfp-3 slightly increased the adhesion to –8.9 ± 0.2 mJ/m^2. Interestingly, injecting more Mfp-3 didn't further enhance the adhesion, instead, the adhesion energy leveled off to –7.3 ± 0.2 mJ/m^2 after a total of 280 pmole Mfp-3 was injected into the solution between CH_3-SAM and mica surfaces. A very similar correlation between the Mfp-3 added and the adhesion strength was measured for the bridging adhesion of Mfp-3 across OH-SAM/mica surfaces. An adhesion energy of -0.24 ± 0.03 mJ/m^2 was measured with 80 pmole injected in the gap solution between OH-SAM and mica surfaces. The adhesion energy increased to -0.37 ± 0.13 mJ/m^2 after a total amount of 200 pmole Mfp-3 was added in the gap solution and decreased to only -0.23 ± 0.03 mJ/m^2 with further addition of 280 pmole Mfp-3.

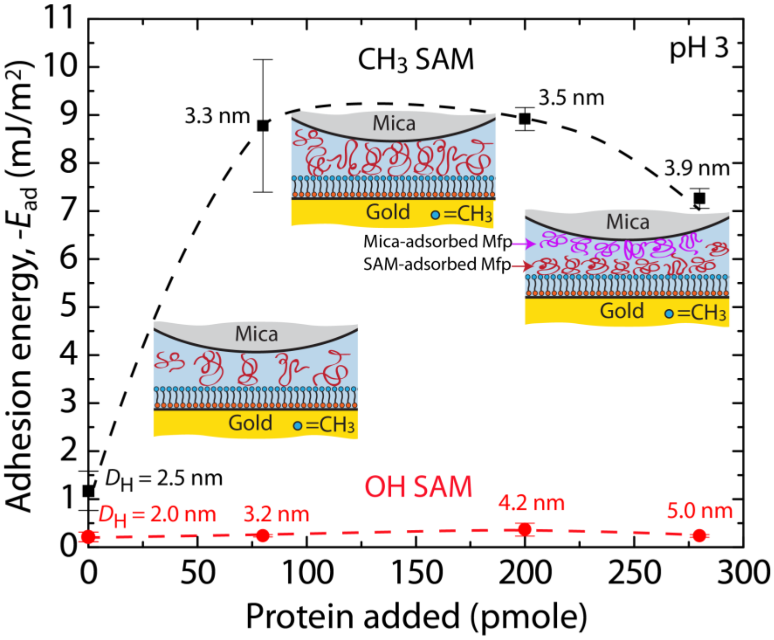

Figure 3.7: The correlation between the added amount of Mfp-3 and the measured adhesion energy. The values of D_H represent the total thickness of the adsorbed protein film and the SAM between the mica and gold surface at the corresponding amount of protein added. The dashed lines are provided as guides for the observed trends in adhesion energy.

3.1.5 Mfp Crowding Effect

The correlation between the amount of Mfp-3 added into the gap solution between two surfaces and the adhesion energies measured upon separation suggests that the structure of the adsorbed Mfp-3 layers on the SAM and mica surfaces is Mfp-3 concentration dependent. Without protein adsorption, the interaction between the SAM surface (either CH_3- or OH-) is mainly van der Waals (Figure 3.2). When 80 pmole Mfp-3 is added into the solution between two surfaces, the surfaces are not fully covered by Mfp-3, with large spaces between protein molecules. Every Mfp-3 molecule therefore can attach to both SAM and mica surfaces, giving rise to bridging adhesion. Further increasing the amount of Mfp-3 to

200 pmole increases the density of the adsorbed protein, however, two surfaces are still not fully covered, and therefore all the Mfp-3 molecules can still bridge across two surfaces, leading to an increase of the binding density and stronger adhesion energy. Adding 280 pmole Mfp-3, however, starts to saturate both surfaces with adsorbed proteins, which introduces the steric repulsion between two adsorbed Mfp-3 layers. Under such conditions, some absorbed Mfp-3 molecules on one surface can repel the Mfp-3 molecules adsorbed on the other surface, reducing the chance to make bridging contact with all the protein molecules. This steric effect therefore reduces the adhesion force despite the higher protein coverage on the surfaces. This effect is analogous to the concentration-induced microphase ordering—and corresponding steric repulsion—that has been predicted in simulations of random block copolymers that have adsorbed onto two approaching surfaces.[21] Additional evidence for the increasing film coverage can be seen in the increasing thickness, D_H, of the confined film (SAM + Mfp-3) as more Mfp-3 is added between the surfaces (Figures 3.4 and 3.7). D_H was taken as the absolute separation distance between the mica and gold surface at an applied load of 5 mN/m for all SAM-protein combinations

3.1.6 Mfp Interactions at a CH_3-SAM Surface

At pH 3, the strong adhesive bridging of the Mfps between a mineral (mica) surface and a hydrophobic surface indicates that the Mfps are capable of (at least) two distinct and concurrent adhesion mechanisms (Figure 3.8a). At the mica interface, the commensurate spacing of the inter-oxygen distance of mica (0.28 nm) and the two dopa *o*-hydroxyl groups (0.29 nm) leads to bidentate hydrogen bonding, with the dopa *o*-hydroxyls as hydrogen donors and the mica surface-oxygens as hydrogen acceptors. At the CH_3-SAM interface, the uniformly hydrophobic surface does not offer the opportunity for hydrogen bonding, covalent, or coulombic interactions to promote adhesion; in the absence of these forces, the strong adhesion at the CH_3-SAM interface must arise due to hydrophobic interactions between the methyl SAM headgroups and the side chains of hydrophobic amino acid residues, as illustrated in Figure 3.8a.

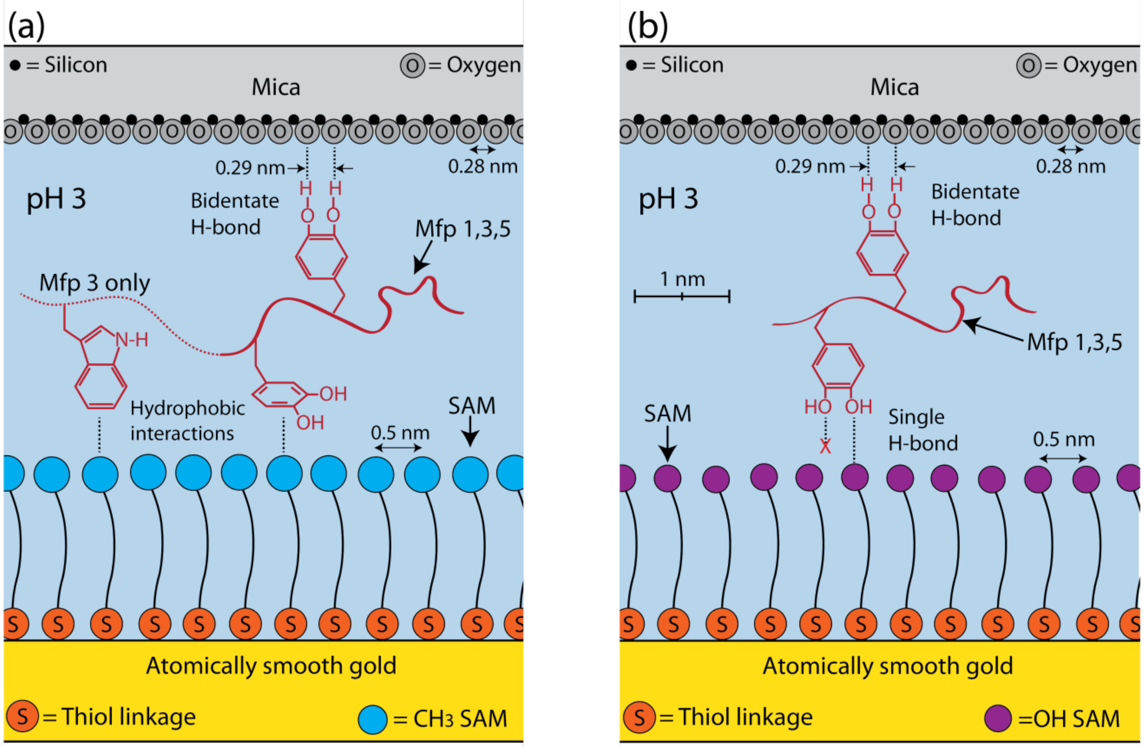

Figure 3.8: The adhesion mechanisms of Mfps between mica and SAM surfaces. The sizes of the SAM molecules are drawn to scale (including headgroup size, thiol group size, chain height, and molecular spacing). The radii of the SAM headgroups and thiol groups represent the van der Waals radii of the moiety. The size of the dopa molecules and catechol spacing is drawn to scale. The spacing of the mica atoms is drawn to scale and the radii of the atoms represent the ionic radii. The Mfp chains are represented schematically and are not drawn to scale. (a) The adhesion mechanism of mfps between a mica surface and a CH_3-SAM surface. While only Dopa (the most prevalent hydrophobic residue common to all 3 proteins) is represented interacting at the CH_3-SAM interface for all 3 proteins, other contributions from hydrophobic residues certainly occur. The tryptophan-rich C-terminus of Mfp-3 is represented with a continued-dotted line. (b) The adhesion mechanism of Mfps between a mica surface and an OH-SAM surface. Bidentate hydrogen bonding is not possible at the OH-SAM interface due to mismatched molecular spacing between H-bond donors and acceptors.

Each protein examined in this study has a unique array of hydrophobic amino acid residues that can—individually or synergistically—contribute to the hydrophobic adhesion to the CH_3 SAM surface. Interestingly, the most prevalent hydrophobic amino acid common to all three proteins is Dopa. With hydrophobic qualities similar to tyrosine ($\Delta G_{\text{t-Dopa}}$ = 1.8 kcal/mol vs $\Delta G_{\text{t-Tyrosine}}$ = 2.3 kcal/mol in transfer from 100% organic to water at 25˚C from),[22] Dopa is capable of hydrophobically interacting with the alkyl surface through its aromatic ring. Thus, Dopa can display Janus-like adhesive properties—forming bidentate bonds to hydrophilic mineral surfaces through its catechol group, or through hydrophobic interactions at alkyl surfaces with its aromatic ring—dependent on the chemistry of its neighboring surface (Figure 3.8).

Other amino acid residues may contribute to hydrophobic adhesion as well. Mfp-1 contains leucine, isoleucine, and phenylalanine residues that may partition to the alkyl interface. Lysine, common to all three proteins, contains a $(CH_2)_4$ block that may contribute to the hydrophobic interaction.[23] Perhaps most significantly, Mfp-3 contains three tryptophan residues—the strongest partitioning amino acid ($\Delta G_{\text{t-Tryptophan}}$ = 3.2 kcal/mol)[22]—all located toward the protein's C-terminus. It is hypothesized that Mfp-3's increased adhesion over both Mfp-1 and Mfp-5 is a result of the marked asymmetric distribution of hydrophobic tryptophans along the protein length; with the predominantly hydrophobic C-terminus of Mfp-3 adsorbed at the CH_3-SAM interface, the remainder of the molecule is more mobile to scavenge Dopa-mediated binding sites at the mica interface. This effect may be enhanced by Mfp-3's high degree of chain flexibility.[24] Preferential distribution of hydrophobic moieties toward either terminus of a peptide sequence is believed to be a favorable criterion for designing proteins with maximum adhesion between chemically heterogeneous interfaces, worthy of further investigation, and may be further generalized to include the preferential distribution of any chemically specific moieties towards the end of any polymer adhesive.

The adhesion of Mfps between surfaces is adaptive. When confined between chemically asymmetric surfaces, Mfps are capable of partitioning domains of chemically specific residues to their strongest interacting surface, in a strategy that lowers the protein total free energy and increases the adhesion energy.[25] This is shown through the increased adhesion energy of both Mfp-1 and Mfp-3 when confined to an asymmetric hydrophobic-mica geometry, compared with the lower adhesion energies observed for these proteins between two symmetric mica surfaces or between two symmetric hydrophobic surfaces. Mfp-1 is a large (~108 kDa) coating protein found in the byssal cuticle and has a comparatively low Dopa concentration (15 mol %). It has been shown that Mfp-1 will coat the surface of mica, however, in doing so, it will expose its unbound—and Dopa-free—segments into solution, and is incapable of bridging adhesion between two symmetric mica surfaces ($E_{ad} < 0.1$ mJ/m^2). Thus between symmetric mineral surfaces, Mfp-1 displays its protective coating qualities, rather than bridging adhesive qualities. Likewise, when confined between two hydrophobic polystyrene surfaces, Mfp-1 is unable to bridge the surfaces and offers little adhesive potential ($E_{ad} = 0.33$ mJ/m^2 after 1 hour of contact time).[10] However, when confined between the CH_3-SAM and mica interfaces, Mfp-1 displays a remarkably increased adhesion energy ($E_{ad} = -3.5 \pm 1.0$ mJ/m^2). The interfacial adhesive protein Mfp-3 also displays this same trend of increased adhesion energy between a CH_3-SAM and mica surface ($E_{ad} = 8.9 \pm 0.2$ mJ/m^2) compared to the adhesion energy between two symmetric mica surfaces ($E_{ad} = 1.2 – 1.4$ mJ/m^2)[26] or between two symmetric polystyrene surfaces ($E_{ad} = 2.7$ mJ/m^2).[10]

3.1.7 Mfp Interactions at an OH-SAM Surface

The minimal adhesion observed between films of both Mfp-3 and Mfp-5 to the OH-SAM surface highlights the importance of molecular geometry in bidentate-mediated surface interactions. When Mfp-3 and Mfp-5 are confined between 2 symmetric mica surfaces, the spacing between the catechol *o*-hydroxyl groups is commensurate with the mica surface oxygen spacing, which allows for the formation of dopa-mediated bidentate bonds on each surface that lead to strong adhesion energies ($E_{\text{ad, Mfp-3}}$ = -1.2 to -1.4 mJ/m^2, $E_{\text{ad, Mfp-5}}$ = -9.0 to -13.7 mJ/m^2).[1] Strong Dopa-mediated adhesion has also been shown with Mfps on other oxide surfaces—such as titania and silica—that possess hydrogen bond acceptors that lie within the reach of both dopa *o*-hydroxyl arms.[8,9,27] However, when the spacing between the surface hydrogen bonding groups is increased to 0.5 nm—the equilibrium headgroup spacing of the OH-SAM[20] (Figure 3.8b)—the catechol hydroxyls are unable to stretch to form a bidentate bond, and consequently the adhesion is significantly reduced. At the OH-SAM surface, each Dopa is presumably able to form only a single hydrogen bond with the OH-SAM headgroup. Bond lifetimes, τ, are predicted by the Bell theory, $\tau = \tau_0 e^{-E/kT}$, where E is the bond-dissociation energy, T is temperature, k is Boltzmann's constant, and τ_0 is the average time of molecular vibrations.[19,28] At the OH-SAM surface in aqueous solution, Dopa's single phenolic O-H---O hydrogen bond ($E_{\text{monodentate}} \approx -14\ kT$)[29] will exist for only ~10^2 times longer than the fleeting and promiscuous hydrogen bonding of water to the OH-SAM surface ($E_{\text{water-SAM}} \approx -9\ kT$).[30] The transient lifetime of the monodentate hydrogen bond results in minimal Mfp adhesion observed on the OH-SAM surface in SFA force measurements, where measurements are performed over time scales much greater than the bond lifetime. This poor performance of a monodentate hydrogen bond in wet adhesion compared to bidentate hydrogen bond ($E_{\text{bidentate}} \approx 2E_{\text{monodentate}} \approx$ -28 kT, or $\tau_{\text{bidentate}} \approx 10^6 \tau_{\text{monodentate}}$) indicates the importance of the interfacial geometry in the design of strong and robust wet adhesion to hydrophilic surfaces.

The spontaneous formation of films on surfaces, including biosurfaces, is generally reckoned to compromise good practical adhesion. Our results with Mfp adhesion to SAMs suggest that this conventional wisdom is no longer warranted. Adhesion that is either stronger or weaker than the adhesion between Mfps and clean substrate surfaces can be achieved by subtle adjustments to film chemistry. This has important implications for improving environmental and medical adhesives and coatings that erroneously assume clean substrate surfaces but actually encounter surfaces already covered by various natural and man-made films.

3.2 Surface Force Measurements and Simulations of Mussel-Derived Peptide Adhesives on Wet Organic Surfaces

*Levine, Z. A.; *Rapp, M. V.; Wei, W.; Mullen, R. G.; Wu, C.; Zerze, G. H.; Mittal, J.; Israelachvili, J. N.; Waite, J. H.; Shea, J. E. (2016) ***Proc. Natl. Acad. Sci. U. S. A.***, DOI:10.1073/pnas.1603065113

3.2.1 Abstract

Translating sticky biological molecules—such as mussel foot proteins (MFPs)—into synthetic, cost-effective underwater adhesives with adjustable nano- and macro-scale characteristics requires an intimate understanding of the glue's molecular interactions. To help facilitate the next-generation of aqueous adhesives, we performed a combination of surface forces apparatus (SFA) measurements and replica-exchange molecular dynamics (REMD) simulations on a synthetic, easy to prepare, Dopa-containing peptide (MFP-3s peptide), which adheres to organic surfaces just as effectively as its wild-type protein analog. Experiments and simulations both show significant differences in peptide adsorption on CH_3-terminated (hydrophobic) and OH-terminated (hydrophilic) self-assembled monolayers (SAMs), where adsorption is strongest on hydrophobic SAMs due to orientationally-specific interactions with Dopa. Additional umbrella-sampling simulations yield free energy profiles that quantitatively agree with SFA measurements, and are used to extract the adhesive properties of individual amino acids within the context of MFP-3s peptide adhesion, revealing a delicate balance between van der Waals, hydrophobic, and electrostatic forces.

3.2.2 Introduction

Demand for biologically-inspired underwater adhesives, such as those secreted by marine mussels to adhere to a wide variety of hard and soft surfaces,[1] have seen tremendous growth over the past decade, with applications to bone sealing,[5] dental and medical transplants,[31] coronary artery coatings,[2] cell encapsulants,[4] and other systems. To facilitate the construction of next-generation underwater adhesives, we can mimic existing biological glues—such as those containing mussel foot proteins (MFPs)—and translate the glues' structures in order to create biologically inspired synthetic adhesives.[32] Doing so requires detailed knowledge of the molecular interactions that take place, many of which occur on length- and time-scales that are, at present, too small to be accurately characterized by experiments. Therefore, more sophisticated studies that combine theoretical modeling with state-of-the-art experiments are necessary for advancing the development of novel underwater adhesives.

Although the mussel's talent for wet adhesion has been known for centuries, the true molecular understanding of adhesion began in 1952 with Brown's hypothesis that the mussel's byssus thread and adhesive plaques are comprised of intrinsically disordered proteins rich in the catecholic amino acid 3,4-dihydroxyphenylalanine (Dopa).[33] With knowledge of Dopa's binding ability, an abundance of Dopa-containing polymers were synthesized that displayed impressive adhesive,[34,35] coating,[1,2] structural,[36,37] and self-healing [38,39] properties. The surface forces apparatus (SFA) has been used to measure the adhesion of MFP-containing glues,[1,26,32,40–42] however it remains difficult to unambiguously identify individual or cooperative interactions of amino acids that facilitate adhesion since few theoretical models are available for comparison.[43,44]

The majority of MFP-inspired adhesives have been investigated on pristine surfaces in solution;[43–47] however under more realistic conditions, surfaces targeted for adhesion are rarely free from contaminants and are fouled with organic films that impede robust adhesion. Yu *et al*.[42] demonstrated that certain MFPs promote strong adhesion to hydrophobic self-assembled monolayers (SAMs), presumably through direct interactions with the surface, while exhibiting weak adhesion to hydrophilic SAMs.

Here we study a peptide mimic of the full-length 45-residue MFP-3s protein[48] (termed MFP-3s peptide), which consists of only 25 residues (seq: N-GYDGYNWPYGYNGYRYGWNKGWNGY-C). The peptide (shown in Figure 3.9) retains 7 out of 11 Dopa (denoted here as Y) and 3 out of 4 tryptophan (W) residues found in the full-length protein, in addition to 3 charged residues, which play a dominant role in the adhesion of MFPs to hydrophobic and hydrophilic organic surfaces.[42] Short, MFP-derived peptides such as the MFP-3s peptide are overwhelmingly appealing alternatives to full proteins[32] because (*i*) the shorter length allows more tractable theoretical and experimental analysis of surface interactions, (*ii*) peptides are significantly cheaper and easier to produce compared to extracting and purifying biological proteins, and (*iii*) Dopa-containing peptides can be engineered and optimized to retain or enhance the adhesive properties of full-length proteins. We show using a combination of SFA measurements and molecular dynamics simulations that MFP-3s peptides exhibit strong adhesion energies to organic hydrophobic (CH_3-terminated) surfaces through direct, catechol-mediated interactions with surface methyl groups, where the underlying mechanisms of adhesion are elucidated. Alternatively, these peptides exhibit weak binding affinities to hydrophilic (OH-terminated) surfaces. Results from both experiments and simulations show excellent agreement with one another.

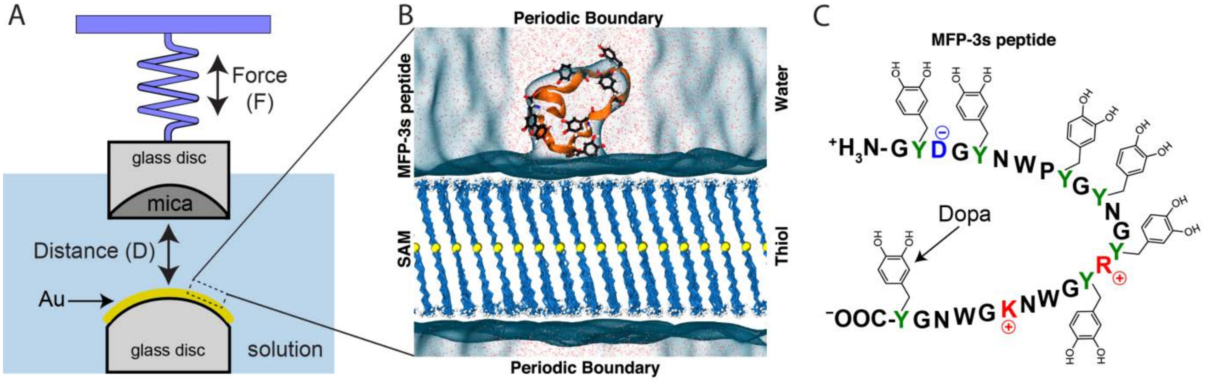

Figure 3.9: [*A*] Schematic of the mica and gold surfaces used in SFA measurements. CH_3 or OH self-assembled monolayers are adsorbed onto the gold surface. [*B*] Configuration of a typical MD simulation containing an MFP-3s peptide and a self-assembled monolayer. [*C*] The amino acid sequence for the MFP-3s peptide containing Dopa (post-translationally modified from tyrosine).

3.2.3 Materials and Methods

Simulation Structures: Self-assembled monolayers were constructed by creating a fixed two-dimensional grid of sulfur atoms in a diamond geometry in the middle of a unit cell.[49] Then, a ten-atom alkane chain $(CH_2)_{10}$ was attached to both the top and bottom of each sulfur anchor, terminated by either a CH_3 group (for hydrophobic interfaces) or an OH group (for hydrophilic interfaces). SAM chains were left unfrozen in order to observe if fluctuations in surface spacing would promote bidentate bonding between MFP Dopa residues and surface groups. Parameterization of SAMs were performed by Garde *et al.*[49] The net charge of each SAM was kept neutral. Box dimensions were on the order of 8 x 8 x 10 nm^3, and periodic boundary conditions were implemented to mitigate system size effects and reduce computation. The system was then hydrated at room temperature with a semi-isotropic barostat that froze the XY box dimensions, while the Z dimension was allowed to fluctuate in order to establish 1 bar of pressure. An unfolded MFP-3s peptide (with +1e net charge) was then added to the bulk solution above the SAM, alongside a chloride counter ion. The Z box dimension was subsequently fixed after bulk water density was re-established at 1 bar of pressure in Z, where the system was ready to be simulated under a canonical (constant volume) ensemble.

Replica Exchange Molecular Dynamics Simulations: Simulations were carried out using GROMACS 4.6.1[50] on the Stampede supercomputer at the Texas Advanced Computing Cluster. REMD[51] simulations utilized 70 replicas at increasingly higher temperatures that (after a number of preliminary values were tested) yielded an average exchange rate of 25% between adjacent replicas during the initial 10 ns, ranging in temperature from 288 to 506 K. Exchanges between replicas were attempted every 3 ps to allow an adequate mixing of states to occur. Replicas were initially heated for 20 ns followed by a 200 ns production run at constant temperature, however only the final 100 ns was analyzed and summarized here. Peptide topologies were derived from the AMBER03* force fields.[49,52,53] Partial charges for 3,4-dihydroxyphenylalanine residues (Dopa) were parameterized by fitting quantum gas-phase potentials of each atom using the restrained electrostatic potential (RESP) method,[54] while other parameters (bond, angle, torsion and Lennard-Jones constants) were taken from AMBER03*. The use of idealized Lennard-Jones and Coulomb potentials in simulations allowed for the reproduction of a number of interactions between molecules such as van der Waals forces, dispersion, hydrogen-bonding, hydrophobicity, and dielectric responses. While more complex Hamiltonians can be implemented in MD that incorporate additional terms, the Hamiltonian in the AMBER03* force field is sufficient for capturing the most dominant molecular interactions. TIP3P rigid water molecules[55] were used to hydrate each system, where up to 15000 explicit water molecules were used per simulation box. Simulations were initially equilibrated with a weakly coupled, semi-isotropic Berendsen barostat[56] at 1 bar, with an isothermal compressibility of 4.5×10^{-5} bar^{-1}, and a velocity-rescaled thermostat[57] that maintained temperature at 300 K. After the box-dimensions converged, the unit-cell volume was fixed, and switched over to a canonical NVT ensemble under a Nosé-Hoover thermostat[58] for the remainder of the study. A leapfrog algorithm was utilized in order to integrate Newton's equations of motion with an integration time step of 2 fs. Peptide and SAM molecular bonds were constrained using the LINCS algorithm,[59] while water bonds were constrained using the SETTLE algorithm.[60] Short-range electrostatic and Lennard-Jones forces were truncated at 1 nm, where long-range interactions took over using a Particle Mesh Ewald (PME) algorithm.[61]

Adhesive Force Calculations: Additional simulations were carried out to ascertain the potentials of mean force (PMF) on MFP-3s peptides, Dopa, Lys, and Dopa-Gly-Lys peptides on hydrophobic and hydrophilic SAMs. PMFs were extracted by umbrella sampling[62] molecules along a reaction coordinate normal to the SAM surface (in 1 Å bins) for a total of 10 ns per bin. A spring with a constant of 8000 kJ mol^{-1} nm^{-2} was used to sample each reaction coordinate, and the weighted histogram analysis method (WHAM)[62] was used to extract free energy profiles from normalized probability measurements. Bayesian bootstrapping was used (in conjunction with WHAM) to generate PMF error bars.

Simulation Analysis and Tools: Molecular graphics were generated with Visual Molecular Dynamics (VMD) 1.9.1.[63] The GROMACS tools g_hbond, g_traj, g_gyration, and g_cluster were used to measure the probabilities of intramolecular hydrogen bonding, peptide end-to-end distance (R_{ee}), the radius of gyration (R_g), and clusters of dominant peptide morphologies at room temperature. Hydrogen bonds were defined with an O-H spacing of 0.25 nm or smaller, and O-H-N angles of 30 degrees or less. R_{ee} was measured from the N-Gly center of mass to the C-Dopa center of mass. MFP-3s peptide conformations were clustered according to the Daura criteria,[64] which compares protein backbones (excluding terminal amino acids) and groups them together based on a root mean square cutoff of 0.14 nm or less. Secondary structures were extracted using the DSSP tool.[65]

MFP-3s Peptide Synthesis: Peptides were commercially synthesized using solid-phase peptide synthesis (GenScript Inc.). Tyr residues in the peptides were then hydroxylated in-house to Dopa by using commercially available mushroom tyrosinase (Sigma Aldrich), where the yield of Dopa conversion was controlled by fine-tuning the enzyme/substrate ratios and reaction times. The resulting MFP-3s peptides contained, on average, seven Dopa units per molecule, which was confirmed by amino acid analysis and mass spectrometry.

SAM Surface Preparation: Self-assembled CH_3- and OH-monolayers were prepared on molecularly smooth gold surfaces using a previously described technique.[14,42] First, a 42.5 nm layer of gold was deposited onto a freshly cleaved mica surface using electron beam deposition. Individual pieces of gold-coated mica were glued, with the gold side down, onto cylindrical glass SFA discs (radius, R ~ 2 cm) using a UV-curable adhesive. After the glue had set, the discs were immersed in ethanol, and the mica back-sheets were carefully peeled away from the underlying gold layers. The templating procedure results in cylindrically-shaped and molecularly-smooth gold surfaces with 0.2 nm rms roughness. This templating procedure results in cylindrically shaped and molecularly smooth gold surfaces. After cleaving, the pristine gold surfaces were immersed in 1 mM solutions of either 1-undecanethiol (CH_3-SAM, Sigma Aldrich) or 11-mercapto-1-undecanol (OH-SAM, Sigma

Aldrich) in ethanol for 18 hours to adsorb the respective monolayer. Following the adsorption, the surfaces were rinsed with ethanol for 30 seconds to remove excess SAM molecules, dried under N_2, and installed in the SFA for force measurements.

Surface Forces Apparatus (SFA): SFA measurements were performed with a SFA 2000 (SurForce Llc., Santa Barbara, CA), and the full details of the SFA technique may be found elsewhere.[17] Briefly, a freshly cleaved, back-silvered mica surface was glued to a cylindrical glass disc, and installed in the SFA with the mica surface facing the SAM surface. Droplets of pH = 3 buffer solution [0.1 M acetic acid + 0.25 M KNO_3 (Sigma Aldrich)] were injected into the gap between the mica and SAM surfaces (~50 μL total volume), and force measurements were performed between the surfaces in buffer solution. Picomolar amounts of MFP-3s peptide—suspended in the same buffer solution—were then injected into the gap solution between the two surfaces, and allowed to adsorb and equilibrate for 30 minutes. Force measurements were then performed between the surfaces at an approach/separation rate of ~1 nm/s, with the interactions mediated by the adsorbed layers of MFP-3s peptide. The absolute separation distance between the two surfaces was measured with fringes of equal chromatic order (FECO) assuming a two-layer interferometer between the gold and silver layers.[66,67] After multiple force measurements were performed and found to be reproducible with a given amount of injected peptide, an additional picomolar aliquot of MFP-3s peptide was injected between surfaces. The peptides were again allowed to adsorb for 30 minutes, where additional force measurements were performed. Within a single experiment, this process was repeated until the adhesion between the surfaces either plateaued or began to decrease with greater amounts of injected MFP-3s peptide. The force measurements presented in this work are representative of at least 4 separate experimental set-ups for each SAM type.

3.2.4 Peptides Strongly Adhere to Hydrophobic, but Not Hydrophilic, Underwater Surfaces

Using the surface forces apparatus (SFA) (Figure 3.10) we determined the interaction force (F) as a function of distance (D) between mica (with radius R) and either a CH_3-terminated (hydrophobic) SAM surface or an OH-terminated (hydrophilic) SAM surface in a solution of MFP-3s peptide. In agreement with our previous full-length MFP measurements on SAMs,[42] MFP-3s peptides exhibit strong adhesion forces between hydrophobic surfaces, and moderate-to-weak adhesion forces between hydrophilic surfaces. Firstly, SAMs were adsorbed onto smooth (rms roughness 0.2 nm) gold surfaces, and then mounted in the SFA opposite from a mica surface. Control force-distance measurements between mica and the SAMs are shown in Figure 3.11. In each experiment, increasing aliquots of MFP-3s peptides were injected between the two surfaces before force measurements were performed, until the surfaces were saturated with bound peptides. At saturation, the surfaces are fully covered with a single layer of peptide. Further injection of the peptide beyond the saturation point resulted in both a decrease in adhesion, and an increase in the peptide film thickness (Figure 3.12), due to stacking of multiple peptide layers. Using the Johnson-Kendall-Roberts theory[68] for adhering surfaces, the measured interaction force per unit radius is converted into an adhesion energy per unit area ($E_{\mathrm{ad}} = F_{\mathrm{ad}}/1.5\pi R$). The average adhesion energy required to separate a peptide film from a hydrophobic and hydrophilic SAM (E_{ad}) was -7.7 ± 1.9 mJ/m^2 and -0.4 ± 0.3 mJ/m^2, respectively. Energy minima for each system were observed at distances (r_{min}) of 2.5 ± 0.2 nm and 2.7 ± 0.3 nm from the gold SFA surface for hydrophobic and hydrophilic systems.

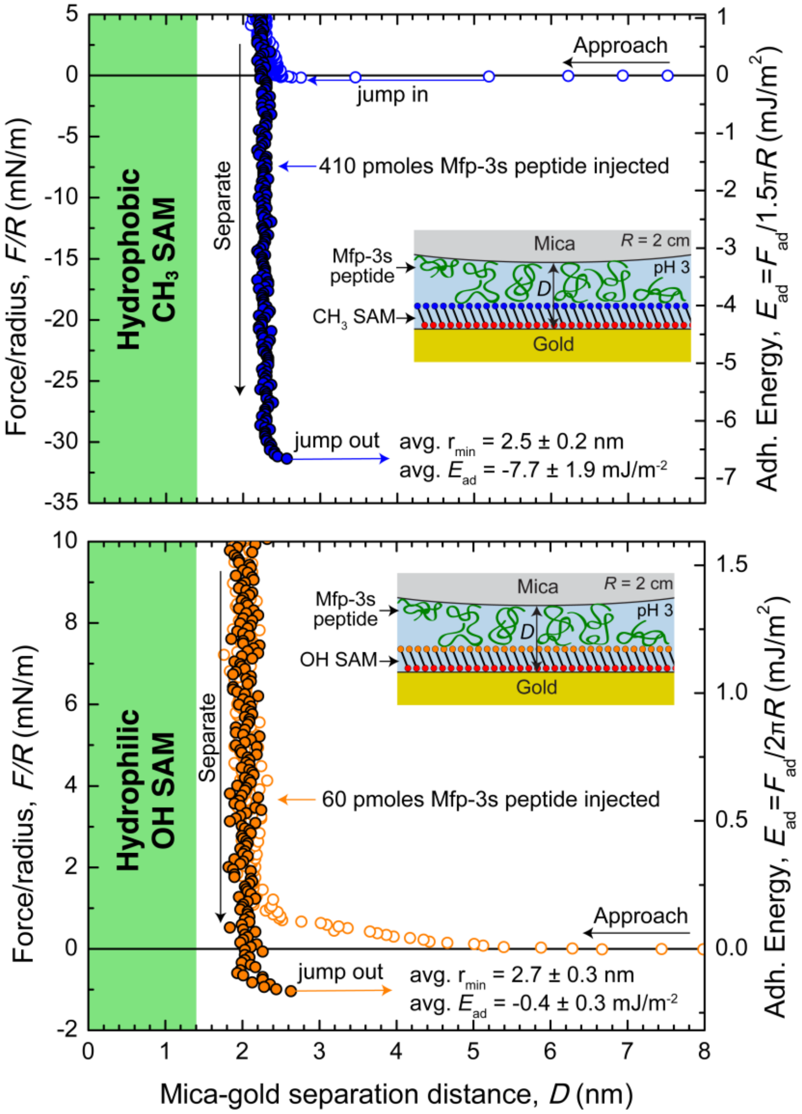

Figure 3.10: Representative force-distance profiles for MFP-3s peptides adsorbed at full saturation between either a hydrophobic CH_3-SAM film (*top*) or a hydrophilic OH-SAM film (*bottom*), and mica, in a solution of 0.1 M acetic acid and 0.25 M KNO_3 (pH = 3). Data points on approach are shown as open circles, while data points measured during separation are shown as closed circles. The inset presents a schematic diagram of the interacting surfaces.

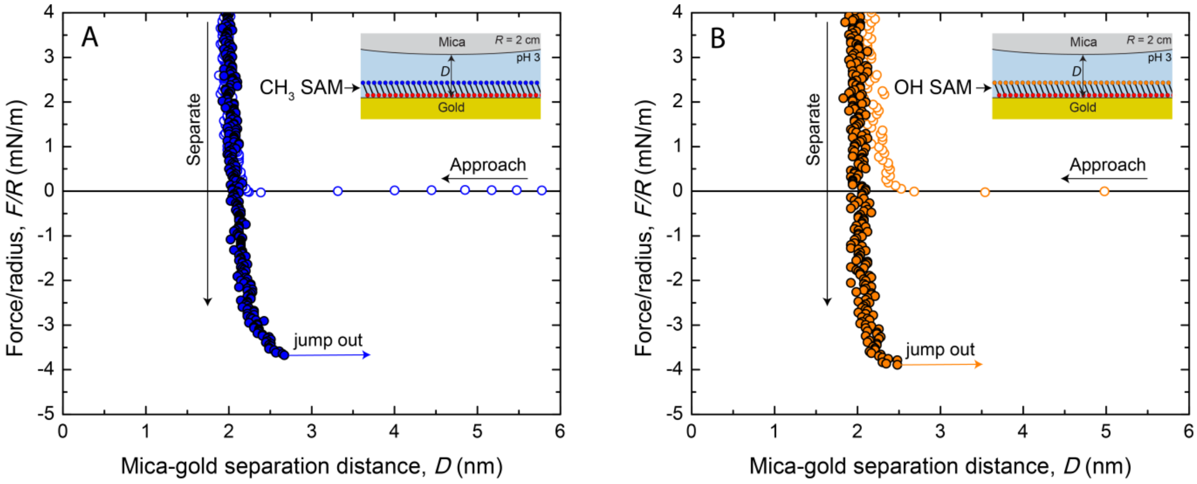

Figure 3.11: Representative SFA force-distance profiles for mica interacting with either a CH_3-SAM (*A*) or an OH-SAM (*B*) before adsorption of the MFP-3s peptide. The forces were measured in a solution of 0.1 M acetic acid and 0.25 M KNO_3 (pH 3).

To gain further insight into the adhesion mechanisms of this peptide we performed umbrella sampling simulations to estimate free energy (or potential of mean force) as a function of distance.[62] PMF simulations yielded one-dimensional free energy profiles of MFP-3s peptide adhesion as a function of the peptide's center-of-mass distance from the SAM substrate, where attractive and repulsive regions can be seen in Figure 3.13. These results show a large -34.7 *k*T energy minimum for the peptide at 1.9 nm above the hydrophobic SAM. In contrast, the peptide is only bound with -6.2 *k*T of energy on hydrophilic SAMs at an equilibrium distance (r_{min}) of 2.1 nm, almost six times weaker than on hydrophobic surfaces. These energies were then converted to an adhesion per unit area (Figure 3.13, *secondary axis*) by dividing the adhesion energy by the average peptide contact area of about 8-9 nm^2. The simulated adhesion strengths for the MFP-3s peptide on hydrophobic and hydrophilic SAMs were 15.9 mJ/m^2 and 2.9 mJ/m^2, respectively.

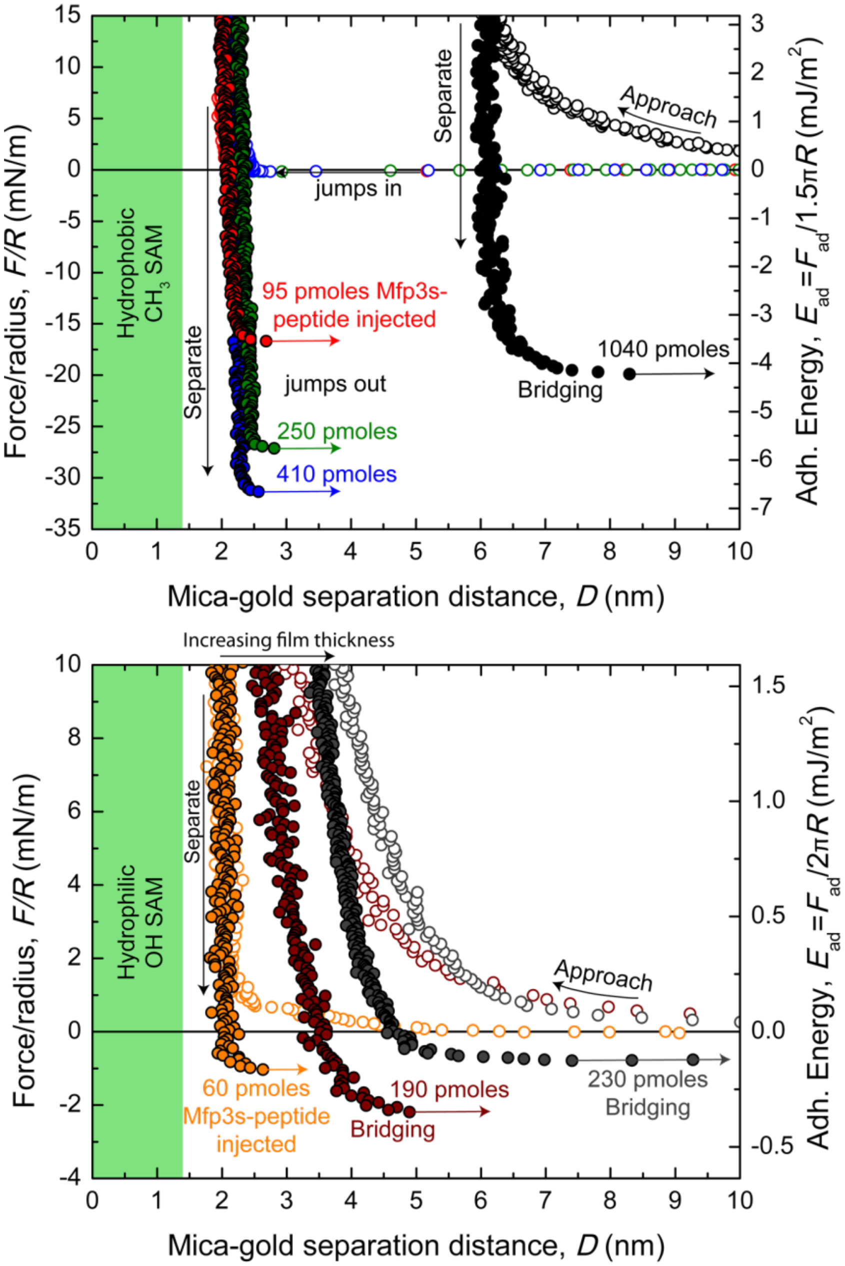

Figure 3.12: SFA force-distance profiles for MFP-3s peptides adsorbed at various saturations between either a hydrophobic CH_3-SAM film (*top*) or a hydrophilic OH-SAM film (*bottom*), and mica, in conditions similar to Figure 3.10. As increasing quantities of peptide are injected into the system, adhesion increases until saturation occurs. Adhesion then decreases as a result of the formation of multiple peptide layers at the surface. Data points on approach are shown as open circles, while data points measured during separation are shown as closed circles.

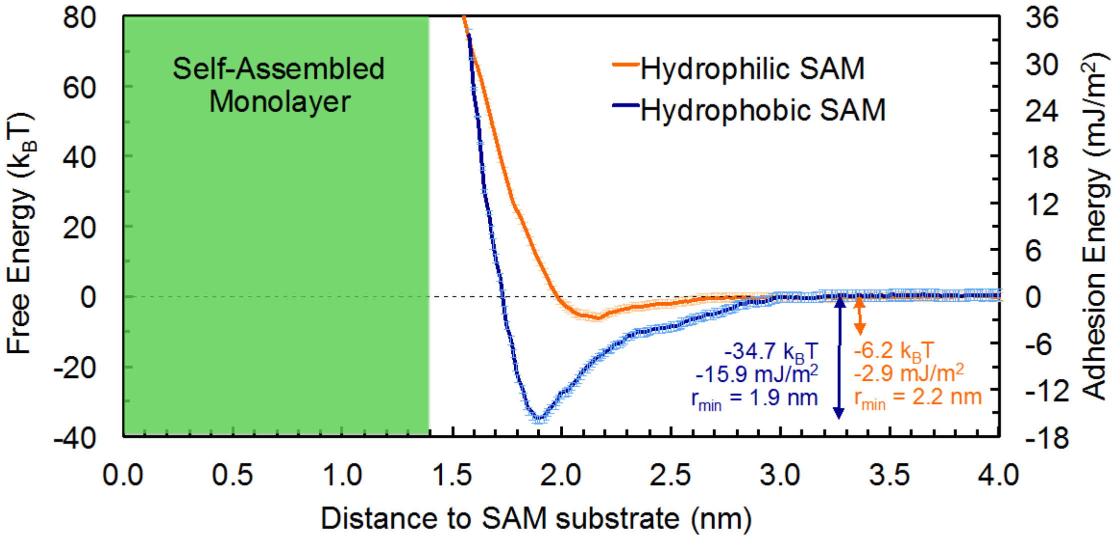

Figure 3.13: Simulated potentials of mean force for the MFP-3s peptide on organic surfaces, plotted as a function of distance from the SAM substrate. Free energies [*primary axis*] are also converted to adhesion energies per unit area [*secondary axis*] by dividing by the peptide's convergent contact area with the surface (on order of 9 nm^2). Peptides strongly adhere to hydrophobic SAMs (colored blue), and weakly to hydrophilic SAMs (colored orange).

If we compare the ratios of the energy minima (at $r_{\min}$) between simulations (Figure 3.13) and experiments (Figure 3.10, E_{ad}), we find that on hydrophobic SAMs E_{sim}/E_{exp} = (-15.9 mJ/m^2) / (-7.7 mJ/m^2) = 2.1, and on hydrophilic SAMs (-2.9 mJ/m^2) / (-0.4 mJ/m^2) = 7.2. These ratios are approximate, and are subject to change if the SFA error bars are strictly applied; however, adhesion from the simulations was always stronger than what was measured in experiments. Simulations exhibit increased peptide adhesion because only one surface is present, where all adhering residues must detach for separation to occur. However, in SFA experiments there are two opposing surfaces, and peptides can remain bound to the upper mica surface as the mica separates from the opposing SAM surface. On average, if symmetric adhesion occurs in the SFA, where half the Dopa residues bind to opposite surfaces, we would expect to measure approximately half the adhesive force in SFA experiments compared to simulation. However, if non-symmetric binding of Dopa to lower

SAM surfaces (compared to upper mica surfaces) occurs, this discrepancy can vary considerably, as observed on hydrophilic surfaces. Despite these factors, both methods agree that MFP-3s peptides bind more weakly to, and at slightly further distances from, OH-terminated SAMs.

Overall, the experimental and computational measurements are in good agreement with one another. In the simulations, the peptide's distance is measured from the SAM substrate to the peptide center-of-mass. In the SFA experiments, distance is measured from the SAM substrate to the opposing mica surface. The length of the SAMs' alkane chains in both experiment and simulation were also the same. Therefore, we obtain a similar r_{min} by offsetting the simulated value by the peptide's radius of gyration (R_{g}), which was around 0.8 nm (Figure 3.14). From simulations we find that ($r_{\mathrm{min}} + R_{\mathrm{g}}$) = 2.7 nm on hydrophobic SAMs, and 2.9 nm on hydrophilic SAMs, precisely within the uncertainty observed in SFA experiments (2.5 ± 0.2 nm and 2.7 ± 0.3 nm, respectively). Even the difference in $\mathrm{r_{min}}$ between hydrophobic and hydrophilic surfaces (0.2 nm) was accurately reproduced in the simulations.

3.2.5 Dopa Binds Parallel to Hydrophobic Organic Interfaces, and Perpendicular to Hydrophilic Organic Interfaces

At crystalline oxide or mineral surfaces—such as mica or TiO_2—MFPs adhere in solution via coordination or bidentate bonds with Dopa's hydroxyls, and electrostatic interactions with charged residues.[69,70] However, at organic surfaces with varying polarities and thermally mobile surface groups, the adhesive interactions are expected to differ. To probe the atomic binding behaviors and orientations of MFP-3s peptides to the two surfaces, we performed replica-exchange molecular dynamics (REMD) simulations, as described in the Materials and Methods (Section 3.2.3). Figure 3.14 highlights the most dominant peptide conformations found from REMD on each surface, where Dopa tends to be oriented parallel ($\leq 45°$ from the plane of the surface) near hydrophobic SAMs, and perpendicular ($> 45°$ from the plane of the surface) near hydrophilic SAMs. This observation confirms our earlier hypothesis[42] that Dopa will take on parallel and perpendicular orientations on hydrophobic and hydrophilic surfaces, respectively, in order to minimize Dopa's free energy. In contrast to the bidentate interactions observed at crystalline surfaces, only monodentate hydrogen bonds were observed between Dopa and the thermally mobile OH-SAM surface. The bond lifetimes of monodentate interactions are significantly shorter than bidentate interactions, which dramatically reduces the peptide's adhesion to the OH-SAM surface compared with mineral or oxide surfaces. These results also reveal that Dopa, which is amphiphilic, sometimes orients outward towards the bulk solution with its hydroxyls hydrated, while tryptophan (which is purely hydrophobic) orients toward the hydrophobic interior of the peptide's globular core. Peptide secondary structures are also highlighted in Figure 3.14, where hydrophobic SAMs promote extended, flatter hairpin conformations, while hydrophilic surfaces reinforce more globular bulk states, similar to other small proteins on organic surfaces.[71] Detailed secondary structural information is presented in Figure 3.15 as a function of the peptide's amino acid sequence, where a small but noticeable increase in β-bridging occurs on the surface of hydrophobic SAMs. However, because the MFP-3s peptide is intrinsically disordered, no major secondary structures persist.

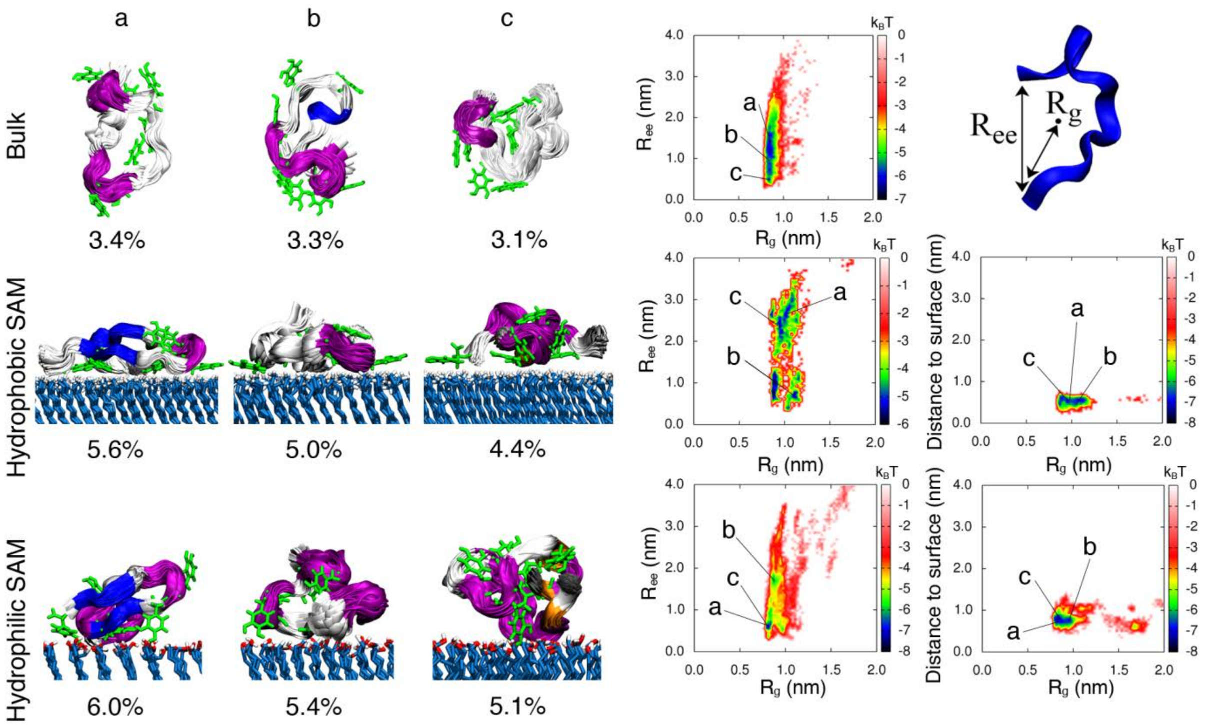

Figure 3.14: The top three dominant MFP-3s peptide morphologies (clusters a-c) are shown in the bulk or on SAM surfaces [*left*], grouped in descending order, with corresponding percentages of time spent in each configuration. Free energy landscapes for each of these systems are also displayed [*right*], as a function of the peptide end-to-end distance (R_{ee}) and radius of gyration (R_g). Favorable low energy basins are colored in black and blue, whereas less-favorable energy states are colored in red and white.

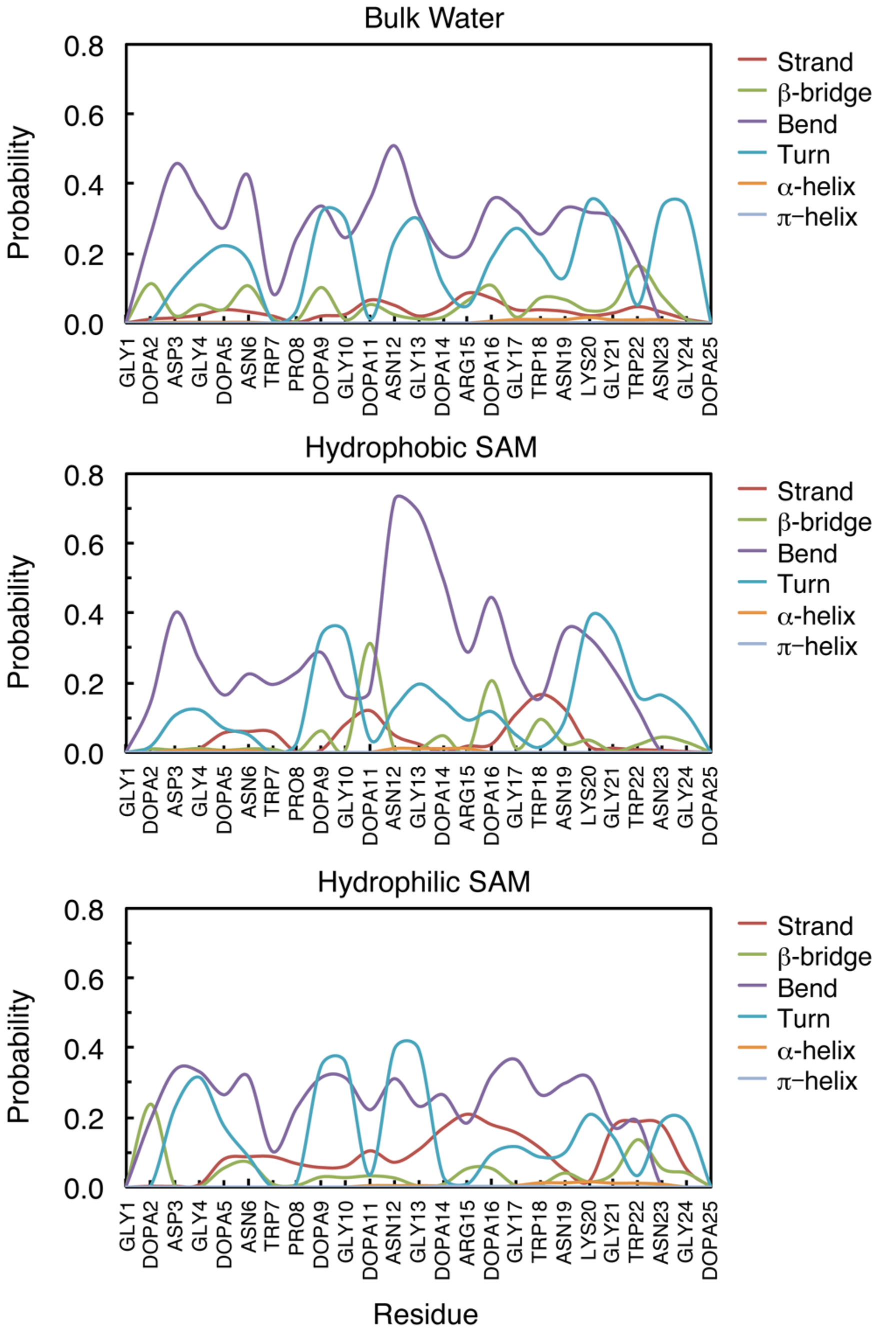

Figure 3.15: Peptide secondary structural probabilities are displayed from simulations as a function of the MFP-3s peptide sequence, and for each surface they interact with.

3.2.6 Hydrophobic Surfaces Unfold MFP-3s Peptides, Whereas Hydrophilic Surfaces Stabilize MFP-3s Peptides

From simulations we extract the top three MFP-3s peptide conformations found in bulk solution, and on hydrophobic and hydrophilic SAMs (Figure 3.14, *left*). We find that while the peptide spends little time in any single conformation (where every cluster persists ≤ 6% of the total simulation time), the top three dominant structures (labeled clusters a, b, and c) exhibit similar morphologies. These trends were not limited to the top three peptide conformations, as can be seen in Figure 3.16. However, for clarity, only the top three peptide clusters were presented in detail, since the remaining structures were variants of the first three conformations. To better characterize the energetics of peptide folding, we plot complimentary two-dimensional free energy surfaces (FES) to the right of each set (Figure 3.14, *right*), as a function of the peptide's end-to-end distance (R_{ee}) and radius of gyration (R_{g}). In bulk water, MFP-3s peptides can traverse across multiple FES minima by increasing their end-to-end distance from 0.5 nm to 2 nm, however this movement always occurs at constant R_{g} (0.8 nm). Higher R_{g} are only accessible to MFP-3s peptides under energy penalties of 5-7 kT, however surfaces significantly modify these barriers. For clarity, each cluster is explicitly identified on the FES, typically residing at free-energy minima.

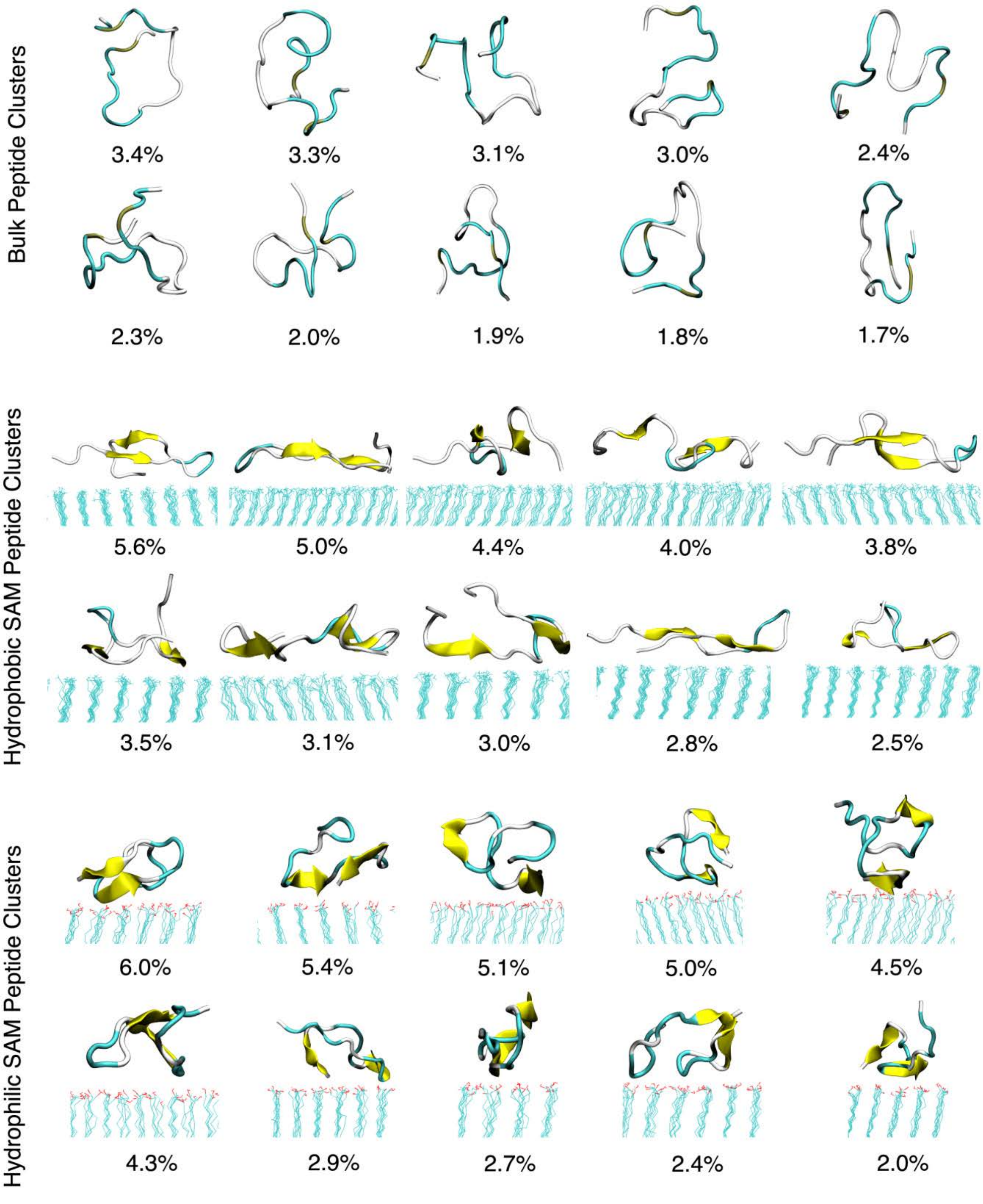

Figure 3.16: The top ten MFP-3s peptide conformations exhibit similar characteristics to the top three peptide conformations. Population percentages for intrinsically disordered peptides are much smaller than for globular proteins, and often exhibit cluster populations that lack a significant drop off.

On hydrophobic and hydrophilic SAMs, peptide adhesion is observed in all three of the most dominant peptide clusters, where Dopa facilitates peptide binding in parallel and perpendicular orientations on CH_3- and OH-terminated SAMs, respectively. Additional free energy basins appear near hydrophobic SAMs, where MFP-3s peptides take on either comparable (0.8 nm) or larger (1.1 nm) radii of gyration compared to bulk. Similarly, larger end-to-end distances are observed near hydrophobic SAMs (up to 3.2 nm, as shown in clusters a and c), but these states are separated from other states (e.g. cluster b) by about 6 *k*T. However, peptides may change their radii of gyration (through extension or contraction) without leaving the SAM surface, as shown in Figure 3.14 (*far right*). Conversely, hydrophilic surfaces stabilize bulk peptide conformations, though peptides remain bound to the surface by polar interactions between the interface and Dopa hydroxyls. The reduction in the number of free energy basins near hydrophilic SAMs is also striking, with peptides primarily taking on compact (small R_{ee}, small R_g) conformations near the SAM surface. Multiple end-to-end peptide distances are also observed on hydrophilic SAMs, though clusters a and c are only separated from cluster b by about 2-3 *k*T, due to the persistence of the bulk state.

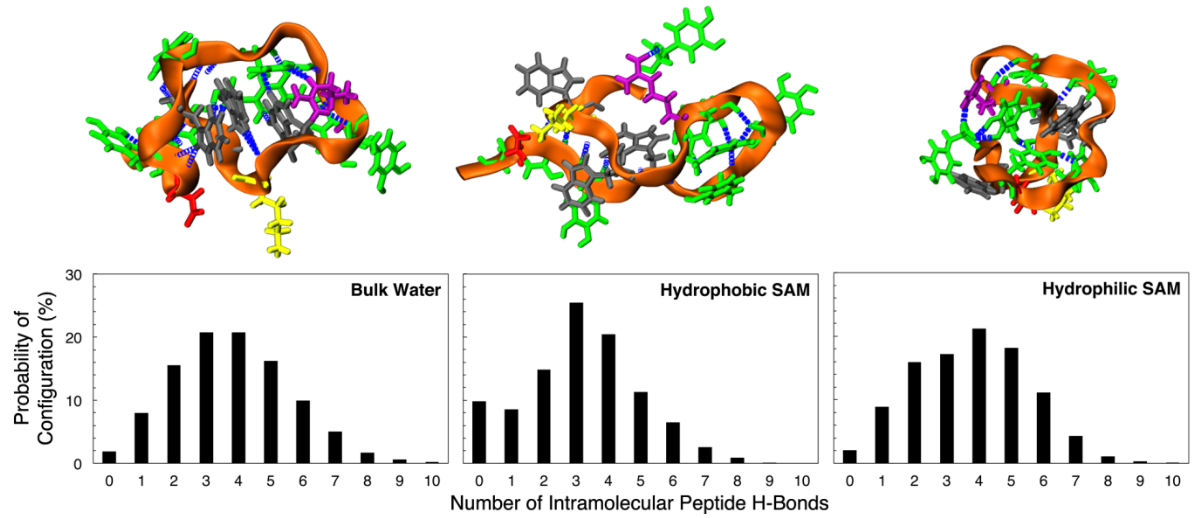

Figure 3.17: Probabilities of encountering MFP-3s peptides with varying amounts of intramolecular backbone hydrogen bonds, in bulk and on organic SAMs [*bottom*]. Distributions shifted to the left indicate more extended peptide structures that contain few backbone hydrogen bonds, whereas distributions that are shifted to the right indicate more compact structures with multiple hydrogen bonds. Representative snapshots for the most dominant (highest probability) structures are also shown [*top*] to illustrate where hydrogen bonds (colored blue) are typically encountered. Dopa is colored green, Trp is colored grey, Asp is colored red, Arg is colored yellow, and Lys is colored purple.

We also observed a decrease in the number of intramolecular hydrogen bonds formed between MFP-3s peptide backbones (C=O and N-H groups) near hydrophobic SAM surfaces. Figure 3.17 shows the emergence of a number of new peptide structures on hydrophobic surfaces that contain very few hydrogen bonds, thereby reinforcing more extended peptide conformations with high-contact surface areas. This is consistent with our observation of multiple hairpin structures (containing few intramolecular hydrogen bonds) on the surface of hydrophobic SAMs. Hydrophilic surfaces, however, do not strongly perturb the distribution of peptide hydrogen bonds from bulk, thereby encouraging peptide conformations with smaller surface contact areas.

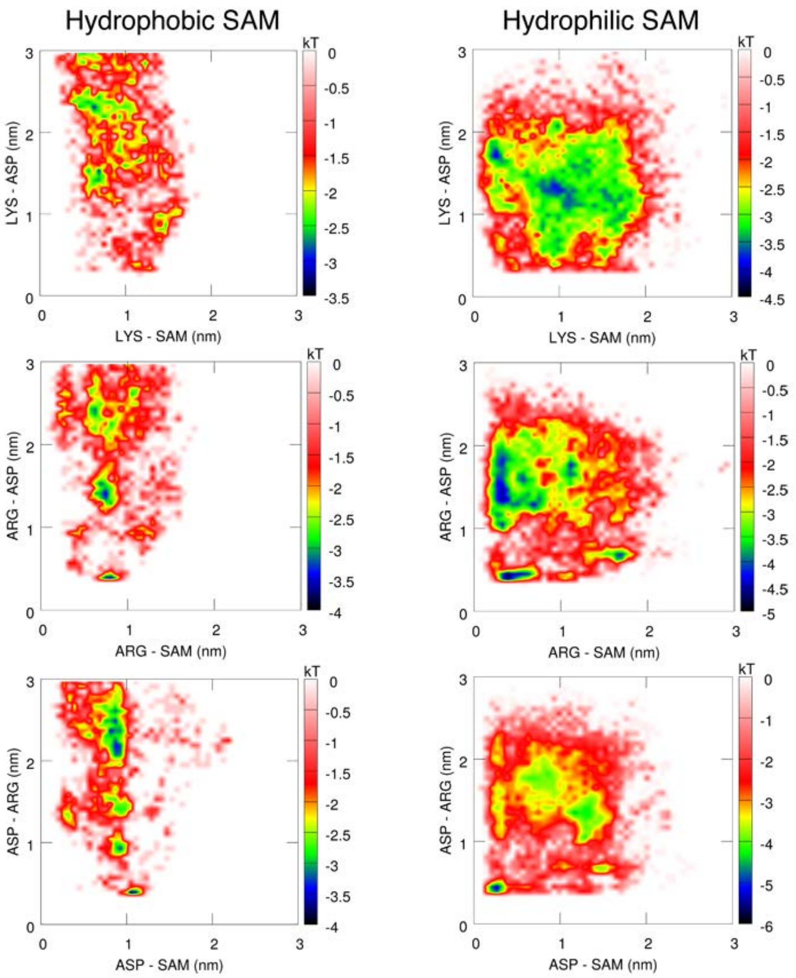

Figure 3.18: Free energy surfaces for MFP-3s peptides on hydrophobic [*left*] and hydrophilic [*right*] SAMs, as a function of various amino acid proximities. Smaller values indicate a higher propensity for pair interactions, while colors correspond to the relative free energies encountered in each of these states.

A number of Arg-Asp salt-bridges are also observed in MFP-3s peptides on the surface of hydrophobic SAMs. Figure 3.18 shows multiple FES plotted as a function of the proximities between charged Asp, Arg and Lys residues, in addition to their positions relative to the SAM surface. Energy minima at small distances (e.g. ≤ 0.3 nm) indicate strong electrostatic interactions between oppositely charged residues. Asp-Arg salt-bridges persist on hydrophobic SAMs, though Lys-Asp salt-brides are not often observed because Lys favors the SAM surface instead, despite the reduction of hydrating water molecules at the interface. On hydrophilic SAMs, both Arg-Asp and Lys-Asp salt bridges are observed, though Lys and Arg maintain contact with the OH SAM surface. Interestingly, Arg is bound so tightly to Asp that it sometimes pulls the negatively charged residue with it upon binding to the surface.

We also plot FES for individual Dopa and Trp residues in the MFP-3s peptide (Figure 3.19), to extract the per-residue energetics of Dopa/Trp rotation at organic interfaces, as a function of their distances to the surface. We observed that almost all Dopa residues were oriented perpendicular (90°) to organic surfaces far above the interface (or in random orientations that averaged to 90°), but subsequently rotated parallel (0° or 180°) on hydrophobic surfaces during approach. The energy required for Dopa to transition from perpendicular to parallel orientations ranges from 4-4.5 kT, however, Trp is more freely able to rotate on hydrophobic organic surfaces with an energy penalty of only 1-2 kT. Results were quite different on hydrophilic surfaces, where multiple Dopa and Trp orientations were observed close to 45° from the surface.

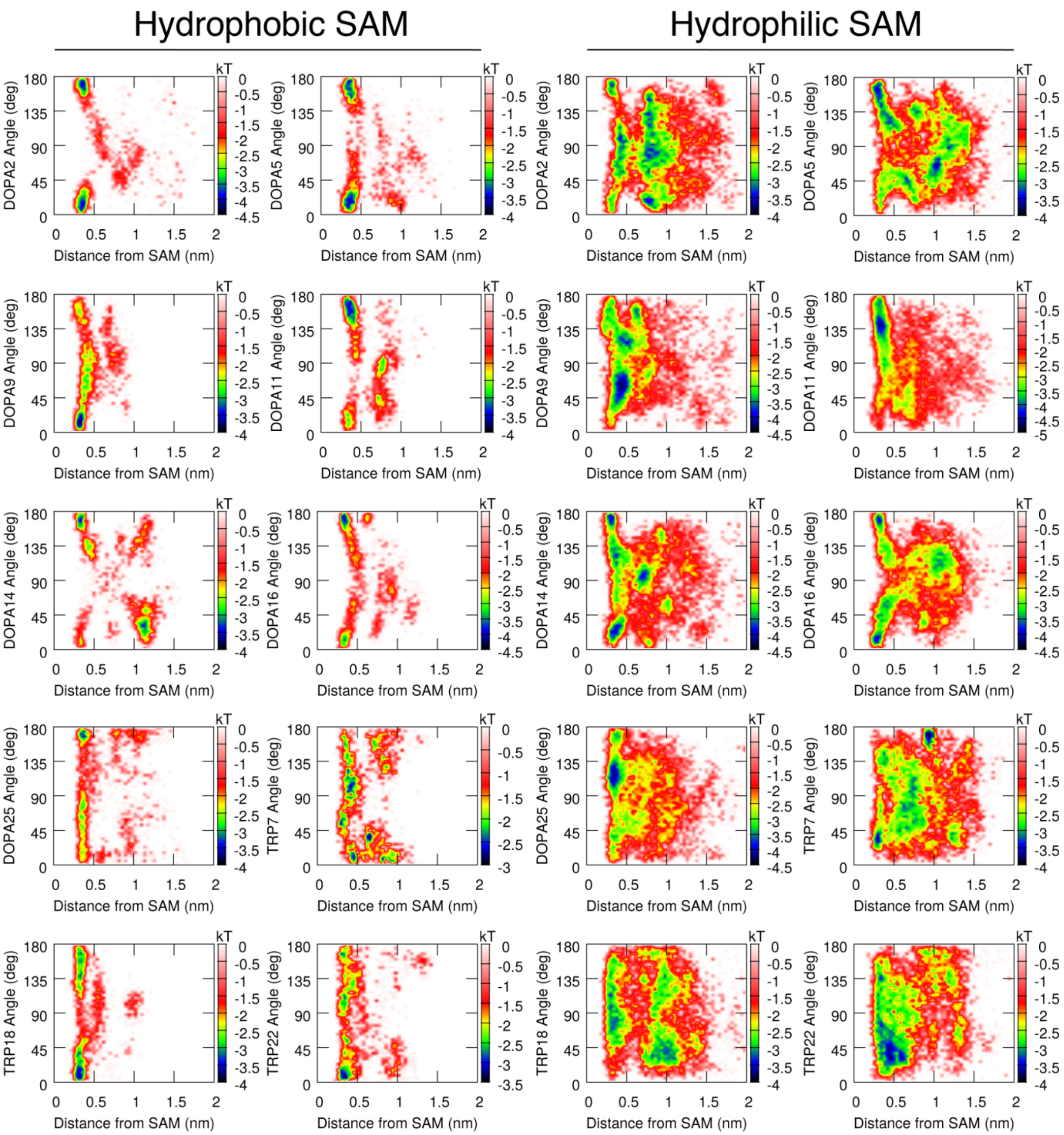

Figure 3.19: Free energy surfaces for MFP-3s peptides as a function of their aromatic residue angles (*y-axis*) and corresponding distances to the SAM surface (*x-axis*). Significant conformational and free energy differences are observed between the two surfaces, which greatly affects the hydrophobic adhesion of MFP-3s peptides. Angles near 0° or 180° represent parallel aromatic orientations on (predominantly hydrophobic) SAM surfaces, while angles between 45°-135° represent perpendicular aromatic orientations (predominantly found on hydrophilic SAM surfaces).

3.2.7 Nearby Charged Amino Acids Enhance Dopa Adhesion to Organic Surfaces

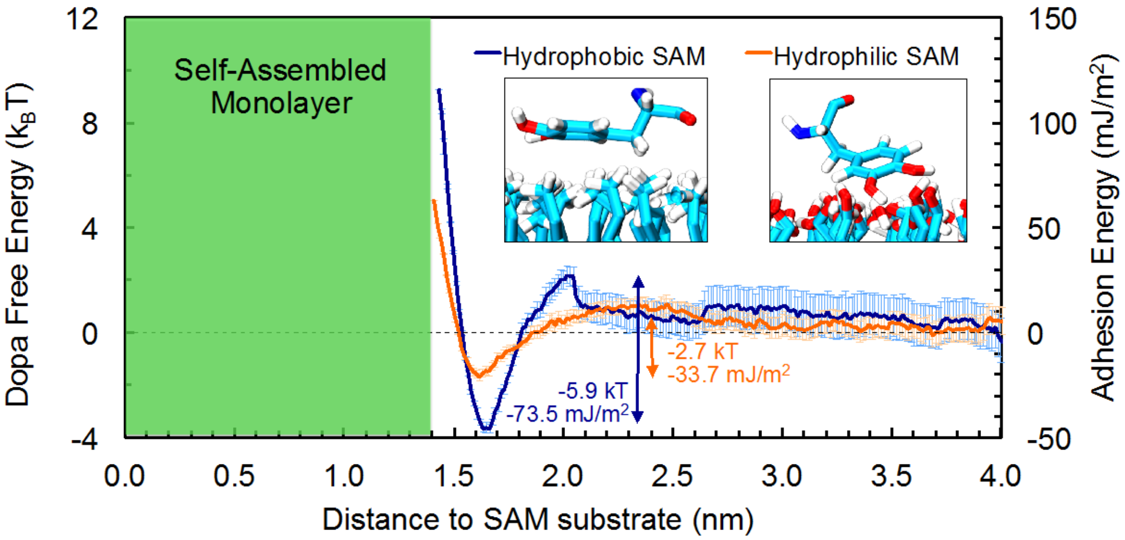

Figure 3.20: Simulated potentials of mean force for a single Dopa residue on a hydrophobic and hydrophilic SAM. Inset images show the typical conformations observed for Dopa at energy minimized locations (r_{min}).

While Dopa residues clearly contribute to robust adhesion in MFPs, there are other amino acids (such as Lys) that can perturb the conformations of Dopa. To better understand the chemical context between Dopa and adjacent charged residues, and what roles they play in binding to organic surfaces, we performed umbrella sampling simulations where we pulled either a single capped Dopa residue (Figure 3.20), a single capped Lys residue (Figure 3.21, *top*), or a combined Dopa-Gly-Lys peptide (Figure 3.21, *bottom*) off of each SAM surface. This technique allowed for the decomposition and subsequent identification of adhesive contributions from individual amino acids, while also providing information about their bound conformations. Lys was selected as a complimentary amino acid because it was recently shown to enhance Dopa adhesion,[72] but the molecular mechanisms behind this behavior are highly contested. Figure 3.20 shows the free energy profile for Dopa, where multiple interesting features stand out. When Dopa settles at hydrophilic r_{min} it binds to OH-terminated SAMs at a somewhat tilted (~ 45°) angle, where Dopa's hydroxyl and peripheral hydrogens bind to the negatively charged SAM hydroxyl oxygens. This orientation is also observed during MFP-3s peptide binding, where multiple Dopa residues were tilted on hydrophilic surfaces (Figure 3.19). Per unit area, Dopa was over 4.5 times more adhesive to hydrophobic surfaces compared to the entire MFP-3s peptide, and 11.6 times more adhesive to hydrophilic surfaces than the MFP-3s peptide. Similarly, Lys was over 10 times more adhesive per unit area on hydrophilic surfaces compared to the MFP-3s peptide (attributable primarily to Lys's positive electrostatic attraction to the surface, which extends far into bulk), and was also 1.7 times more adhesive on hydrophobic SAMs compared to the MFP-3s peptide. Near hydrophobic SAMs, the charged Lys terminus is hydrated in bulk water, however the alkyl chain remains inside the hydrophobic region near the interface. When Dopa and Lys were combined in a model tri-peptide (Figure 3.21, *bottom*), adhesion to surfaces was cooperative, where peptide free energies on both hydrophobic and hydrophilic surfaces remained attractive out to 3.5 nm (further into bulk than any of the individual amino acids). Therefore, whereas Dopa is a better adhesive (per unit area) on hydrophobic surfaces, and Lys a better adhesive (per unit area) on hydrophilic surfaces, adjacent Dopa- and Lys-containing molecules[72] are better overall adhesives on a wide-variety of organic surfaces due to their concerted binding motifs.

By using theoretical models of peptide adhesion, which highlight the nanoscale interactions between Dopa and organic surfaces, and by validating these models with SFA measurements, we have taken important first steps in revealing the atomic mechanisms behind Dopa adhesion. These results successfully bridge atomistic theories of Dopa adsorption to macro-scale material measurements of novel peptides on a wide-variety of wet organic surfaces, thereby enabling future studies to synthesize and optimize stronger, next-generation underwater adhesives.

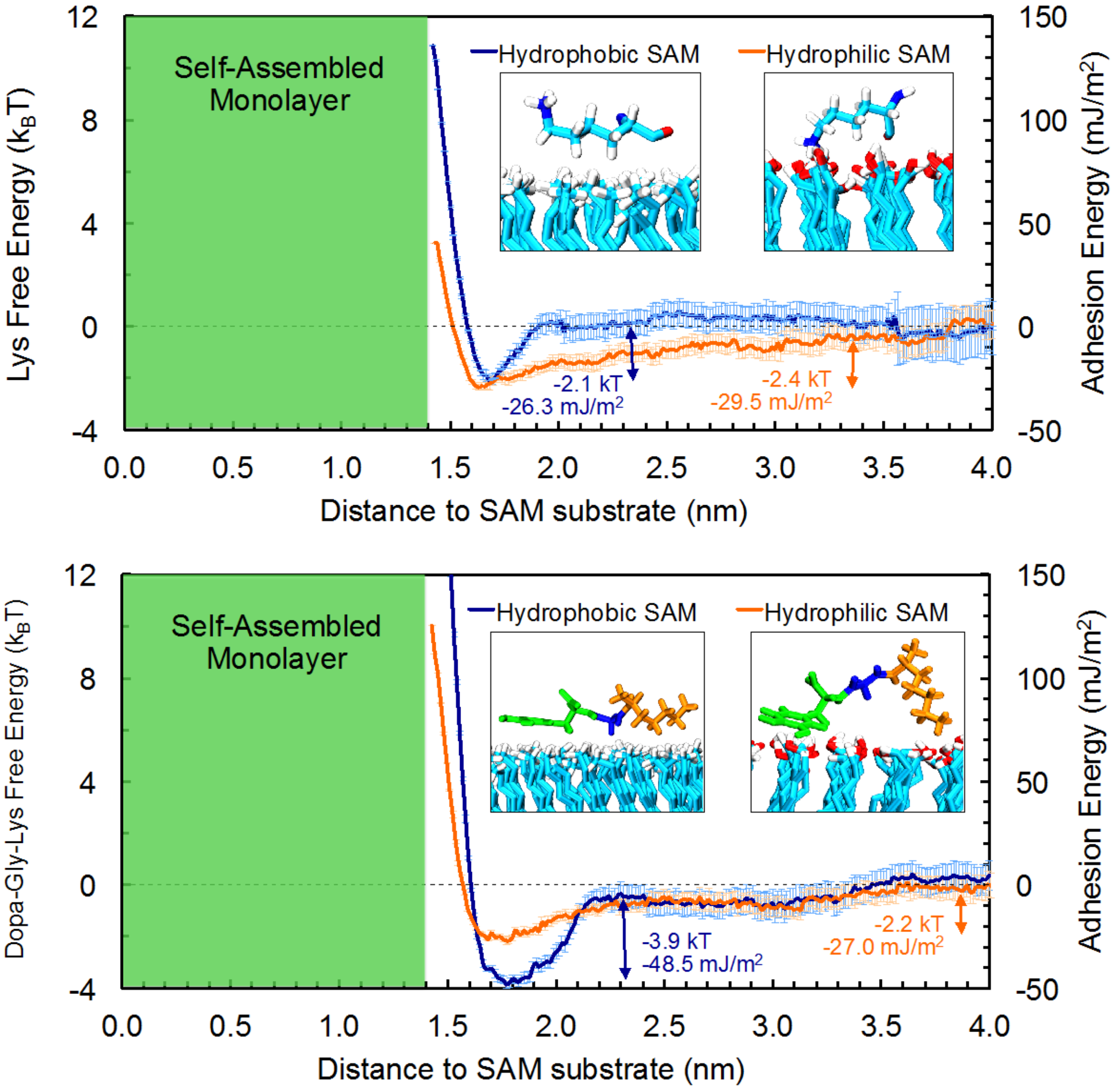

Figure 3.21: Simulated potentials of mean force for Lys and a simple tri-peptide were used to ascertain the contributions of individual residues in MFP-3s peptide binding to SAMs. Inset images show the typical conformations observed for each structure at energy minimized locations (r_{min}).

These results (highlighted in Figure 3.22) also validate earlier theoretical hypothesis[42] about the preferred orientations of Dopa on hydrophobic and hydrophilic organic surfaces, and have far-reaching implications regarding the mechanism of MFP adhesion to generalized organic surfaces, including cellular membranes. We have demonstrated that interfacial solvation is inextricably tied to the peptide's adhesive performance: at the fluctuating, vapor-like CH_3/water interface,[49] hydrophobic association mediates strong peptide adhesion, whereas at the hydrophilic OH/water interface, the competition between water and the peptide for hydrogen bonds to the surface drastically reduces the overall adhesion. By better understanding how biological surfaces stabilize or destabilize intrinsically disordered proteins,[73] and by utilizing unique amphiphilic residues that modulate adhesion to these surfaces, we have provided a template for more sophisticated studies that seek to optimize next-generation bioadhesives under a number of unique biological conditions.

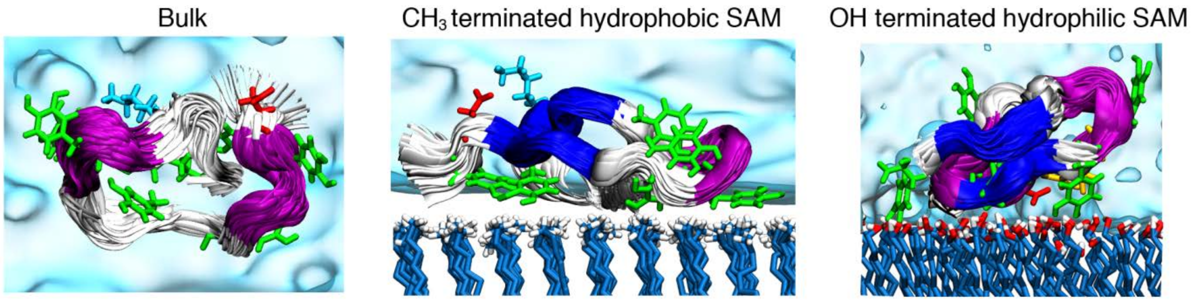

Figure 3.22: A snapshot of the most dominant peptide morphologies found in bulk and on organic surfaces. Dark blue peptide backbones indicate β-strands while purple backbones indicate turn regions. Green aromatic residues represent Dopa, red and cyan residues represent aspartic acid and arginine, and white and red interfacial atoms represent hydrogen and oxygen atoms, respectively. Water is depicted as a bright blue surface that hydrates each system uniquely.

3.3 References

(1) Lee, B. P.; Messersmith, P. B.; Israelachvili, J. N.; Waite, J. H. Mussel-Inspired Adhesives and Coatings. *Annu. Rev. Mater. Res.* **2011**, *41*, 99–132.

(2) Kastrup, C. J.; Nahrendorf, M.; Figueiredo, J. L.; Lee, H.; Kambhampati, S.; Lee, T.; Cho, S.-W.; Gorbatov, R.; Iwamoto, Y.; Dang, T. T.; et al. Painting Blood Vessels and Atherosclerotic Plaques with an Adhesive Drug Depot. *Proc. Natl. Acad. Sci. U. S. A.* **2012**, *109*, 21444–21449.

(3) Haller, C. M.; Buerzle, W.; Brubaker, C. E.; Messersmith, P. B.; Mazza, E.; Ochsenbein-Koelble, N.; Zimmermann, R.; Ehrbar, M. Mussel-Mimetic Tissue Adhesive for Fetal Membrane Repair: A Standardized Ex Vivo Evaluation Using Elastomeric Membranes. *Prenat. Diagn.* **2011**, *31*, 654–660.

(4) Yang, S. H.; Kang, S. M.; Lee, K.-B.; Chung, T. D.; Lee, H.; Choi, I. S. Mussel-Inspired Encapsulation and Functionalization of Individual Yeast Cells. *J. Am. Chem. Soc.* **2011**, *133*, 2795–2797.

(5) Winslow, B. D.; Shao, H.; Stewart, R. J.; Tresco, P. A. Biocompatibility of Adhesive Complex Coacervates Modeled after the Sandcastle Glue of Phragmatopoma Californica for Craniofacial Reconstruction. *Biomaterials* **2010**, *31*, 9373–9381.

(6) Brubaker, C. E.; Kissler, H.; Wang, L.-J.; Kaufman, D. B.; Messersmith, P. B. Biological Performance of Mussel-Inspired Adhesive in Extrahepatic Islet Transplantation. *Biomaterials* **2010**, *31*, 420–427.

(7) Sedó, J.; Saiz-Poseu, J.; Busqué, F.; Ruiz-Molina, D. Biomimetics: Catechol-Based Biomimetic Functional Materials (Adv. Mater. 5/2013). *Adv. Mater.* **2013**, *25*, 792–792.

(8) Lee, H.; Scherer, N. F.; Messersmith, P. B. Single-Molecule Mechanics of Mussel Adhesion. *Proc. Natl. Acad. Sci. U. S. A.* **2006**, *103*, 12999–13003.

(9) Yu, J.; Wei, W.; Menyo, M. S.; Masic, A.; Waite, J. H.; Israelachvili, J. N. Adhesion of Mussel Foot Protein-3 to TiO2 Surfaces: The Effect of pH. *Biomacromolecules* **2013**, *14*, 1072–1077.

(10) Lu, Q.; Danner, E.; Waite, J. H.; Israelachvili, J. N.; Zeng, H.; Hwang, D. S. Adhesion of Mussel Foot Proteins to Different Substrate Surfaces. *J. R. Soc. Interface* **2013**, *10*, 20120759.

(11) Stewart, R. J.; Ransom, T. C.; Hlady, V. Natural Underwater Adhesives. *J. Polym. Sci. B. Polym. Phys.* **2011**, *49*, 757–771.

(12) Waite, J. H.; Qin, X. Polyphosphoprotein from the Adhesive Pads of Mytilus Edulis †. *Biochemistry* **2001**, *40*, 2887–2893.

(13) Waite, J. H. *Redox-Active Amino Acids in Biology*; Methods in Enzymology; Elsevier, 1995; Vol. 258.

(14) Chai, L.; Klein, J. Large Area, Molecularly Smooth (0.2 Nm Rms) Gold Films for Surface Forces and Other Studies. *Langmuir* **2007**, *23*, 7777–7783.

(15) Strong, L.; Whitesides, G. M. Structures of Self-Assembled Monolayer Films of Organosulfur Compounds Adsorbed on Gold Single Crystals: Electron Diffraction Studies. *Langmuir* **1988**, *4*, 546–558.

(16) Valtiner, M.; Donaldson, S. H.; Gebbie, M. A.; Israelachvili, J. N. Hydrophobic Forces, Electrostatic Steering, and Acid-Base Bridging between Atomically Smooth Self-Assembled Monolayers and End-Functionalized PEGolated Lipid Bilayers. *J. Am. Chem. Soc.* **2012**, *134*, 1746–1753.

(17) Israelachvili, J.; Min, Y.; Akbulut, M.; Alig, A.; Carver, G.; Greene, W.; Kristiansen, K.; Meyer, E.; Pesika, N.; Rosenberg, K.; et al. Recent Advances in the Surface Forces Apparatus (SFA) Technique. *Reports Prog. Phys.* **2010**, *73*, 036601.

(18) Bain, C. D.; Troughton, E. B.; Tao, Y. T.; Evall, J.; Whitesides, G. M.; Nuzzo, R. G. Formation of Monolayer Films by the Spontaneous Assembly of Organic Thiols from Solution onto Gold. *J. Am. Chem. Soc.* **1989**, *111*, 321–335.

(19) Israelachvili, J. N. *Intermolecular and Surface Forces: Revised Third Edition*; Academic Press, 2011.

(20) Yang, Y.-C.; Chang, T.-Y.; Lee, Y.-L. Adsorption Behavior of 11-Mercapto-1-Undecanol on Au(111) Electrode in an Electrochemical System. *J. Phys. Chem. C* **2007**, *111*, 4014–4020.

(21) Gutman, L.; Chakraborty, A. K. Surface-Induced Ordering for Confined Random Block Copolymers. *J. Chem. Phys.* **1994**, *101*, 10074.

(22) Nozaki, Y.; Tanford, C. The Solubility of Amino Acids and Two Glycine Peptides in Aqueous Ethanol and Dioxane Solutions: Establishment of a Hydrophobicity Scale. *J. Biol. Chem.* **1971**, *246*, 2211–2217.

(23) Creighton, T. E. *Proteins: Structures and Molecular Properties*; W. H. Freeman, 1993.

(24) Hwang, D. S.; Waite, J. H. Three Intrinsically Unstructured Mussel Adhesive Proteins, Mfp-1, Mfp-2, and Mfp-3: Analysis by Circular Dichroism. *Protein Sci.* **2012**, *21*, 1689–1695.

(25) Even, M. A.; Wang, J.; Chen, Z. Structural Information of Mussel Adhesive Protein Mefp-3 Acquired at Various polymer/Mefp-3 Solution Interfaces. *Langmuir* **2008**, *24*, 5795–5801.

(26) Yu, J.; Wei, W.; Danner, E.; Ashley, R. K.; Israelachvili, J. N.; Waite, J. H. Mussel Protein Adhesion Depends on Interprotein Thiol-Mediated Redox Modulation. *Nat. Chem. Biol.* **2011**, *7*, 588–590.

(27) Frank, B. P.; Belfort, G. Adhesion of Mytilus Edulis Foot Protein 1 on Silica: Ionic Effects on Biofouling. *Biotechnol. Prog. 18*, 580–586.

(28) Bell, G. Models for the Specific Adhesion of Cells to Cells. *Science (80-.).* **1978**, *200*, 618–627.

(29) Feller, D.; Feyereisen, M. W. Ab Initio Study of Hydrogen Bonding in the Phenol-Water System. *J. Comput. Chem.* **1993**, *14*, 1027–1035.

(30) Jorgensen, W. L. Quantum and Statistical Mechanical Studies of Liquids. 10. Transferable Intermolecular Potential Functions for Water, Alcohols, and Ethers. Application to Liquid Water. *J. Am. Chem. Soc.* **1981**, *103*, 335–340.

(31) Long, M.; Rack, H. . Titanium Alloys in Total Joint Replacement—a Materials Science Perspective. *Biomaterials* **1998**, *19*, 1621–1639.

(32) Wei, W.; Yu, J.; Gebbie, M. A.; Tan, Y.; Martinez Rodriguez, N. R.; Israelachvili, J. N.; Waite, J. H. Bridging Adhesion of Mussel-Inspired Peptides: Role of Charge, Chain Length, and Surface Type. *Langmuir* **2015**, *31*, 1105–1112.

(33) Brown, C. H. Some Structural Proteins of Mytilus Edulis. *Q. J. Microsc. Sci.* **1952**, *s3-93*, 487–502.

(34) Lee, H.; Dellatore, S. M.; Miller, W. M.; Messersmith, P. B. Mussel-Inspired Surface Chemistry for Multifunctional Coatings. *Science* **2007**, *318*, 426–430.

(35) Shao, H.; Stewart, R. J. Biomimetic Underwater Adhesives with Environmentally Triggered Setting Mechanisms. *Adv. Mater.* **2010**, *22*, 729–733.

(36) Ryu, J.; Ku, S. H.; Lee, H.; Park, C. B. Mussel-Inspired Polydopamine Coating as a Universal Route to Hydroxyapatite Crystallization. *Adv. Funct. Mater.* **2010**, *20*, 2132–2139.

(37) Podsiadlo, P.; Liu, Z.; Paterson, D.; Messersmith, P. B.; Kotov, N. A. Fusion of Seashell Nacre and Marine Bioadhesive Analogs: High-Strength Nanocomposite by Layer-by-Layer Assembly of Clay andL-3,4-Dihydroxyphenylalanine Polymer. *Adv. Mater.* **2007**, *19*, 949–955.

(38) Krogsgaard, M.; Behrens, M. A.; Pedersen, J. S.; Birkedal, H. Self-Healing Mussel-Inspired Multi-pH-Responsive Hydrogels. *Biomacromolecules* **2013**, *14*, 297–301.

(39) Ahn, B. K.; Lee, D. W.; Israelachvili, J. N.; Waite, J. H. Surface-Initiated Self-Healing of Polymers in Aqueous Media. *Nat. Mater.* **2014**, *13*, 867–872.

(40) Lin, Q.; Gourdon, D.; Sun, C.; Holten-Andersen, N.; Anderson, T. H.; Waite, J. H.; Israelachvili, J. N. Adhesion Mechanisms of the Mussel Foot Proteins Mfp-1 and Mfp-3. *Proc. Natl. Acad. Sci. U. S. A.* **2007**, *104*, 3782–3786.

(41) Danner, E. W.; Kan, Y.; Hammer, M. U.; Israelachvili, J. N.; Waite, J. H. Adhesion of Mussel Foot Protein Mefp-5 to Mica: An Underwater Superglue. *Biochemistry* **2012**, *51*, 6511–6518.

(42) Yu, J.; Kan, Y.; Rapp, M.; Danner, E.; Wei, W.; Das, S.; Miller, D. R.; Chen, Y.; Waite, J. H.; Israelachvili, J. N. Adaptive Hydrophobic and Hydrophilic Interactions of Mussel Foot Proteins with Organic Thin Films. *Proc. Natl. Acad. Sci. U. S. A.* **2013**, *110*, 15680–15685.

(43) Qin, Z.; Buehler, M. Molecular Mechanics of Dihydroxyphenylalanine at a Silica Interface. *Appl. Phys. Lett.* **2012**, *101*, 083702.

(44) Qin, Z.; Buehler, M. J. Molecular Mechanics of Mussel Adhesion Proteins. *J. Mech. Phys. Solids* **2014**, *62*, 19–30.

(45) Lin, S.; Chen, C.-T.; Bdikin, I.; Ball, V.; Grácio, J.; Buehler, M. J. Tuning Heterogeneous Poly(dopamine) Structures and Mechanics: In Silico Covalent Cross-Linking and Thin Film Nanoindentation. *Soft Matter* **2014**, *10*, 457–464.

(46) Leng, C.; Liu, Y.; Jenkins, C.; Meredith, H.; Wilker, J. J.; Chen, Z. Interfacial Structure of a DOPA-Inspired Adhesive Polymer Studied by Sum Frequency Generation Vibrational Spectroscopy. *Langmuir* **2013**, *29*, 6659–6664.

(47) Qin, Z.; Buehler, M. J. Impact Tolerance in Mussel Thread Networks by Heterogeneous Material Distribution. *Nat. Commun.* **2013**, *4*, 2187.

(48) Wei, W.; Tan, Y.; Martinez Rodriguez, N. R.; Yu, J.; Israelachvili, J. N.; Waite, J. H. A Mussel-Derived One Component Adhesive Coacervate. *Acta Biomater.* **2014**, *10*, 1663–1670.

(49) Godawat, R.; Jamadagni, S. N.; Garde, S. Characterizing Hydrophobicity of Interfaces by Using Cavity Formation, Solute Binding, and Water Correlations. *Proc. Natl. Acad. Sci. U. S. A.* **2009**, *106*, 15119–15124.

(50) Hess, B.; Kutzner, C.; van der Spoel, D.; Lindahl, E. GROMACS 4: Algorithms for Highly Efficient, Load-Balanced, and Scalable Molecular Simulation. *J. Chem. Theory Comput.* **2008**, *4*, 435–447.

(51) Sugita, Y.; Okamoto, Y. Replica-Exchange Molecular Dynamics Method for Protein Folding. *Chem. Phys. Lett.* **1999**, *314*, 141–151.

(52) Beauchamp, K. A.; Lin, Y.-S.; Das, R.; Pande, V. S. Are Protein Force Fields Getting Better? A Systematic Benchmark on 524 Diverse NMR Measurements. *J. Chem. Theory Comput.* **2012**, *8*, 1409–1414.

(53) Wang, J.; Wolf, R. M.; Caldwell, J. W.; Kollman, P. A.; Case, D. A. Development and Testing of a General Amber Force Field. *J. Comput. Chem.* **2004**, *25*, 1157–1174.

(54) Bayly, C. I.; Cieplak, P.; Cornell, W.; Kollman, P. A. A Well-Behaved Electrostatic Potential Based Method Using Charge Restraints for Deriving Atomic Charges: The RESP Model. *J. Phys. Chem.* **1993**, *97*, 10269–10280.

(55) Jorgensen, W. L.; Chandrasekhar, J.; Madura, J. D.; Impey, R. W.; Klein, M. L. Comparison of Simple Potential Functions for Simulating Liquid Water. *J. Chem. Phys.* **1983**, *79*, 926.

(56) Berendsen, H. J. C.; Postma, J. P. M.; van Gunsteren, W. F.; DiNola, A.; Haak, J. R. Molecular Dynamics with Coupling to an External Bath. *J. Chem. Phys.* **1984**, *81*, 3684.

(57) Bussi, G.; Donadio, D.; Parrinello, M. Canonical Sampling through Velocity Rescaling. *J. Chem. Phys.* **2007**, *126*, 014101.

(58) Hoover, W. Canonical Dynamics: Equilibrium Phase-Space Distributions. *Phys. Rev. A* **1985**, *31*, 1695–1697.

(59) Hess, B.; Bekker, H. LINCS: A Linear Constraint Solver for Molecular Simulations. *J. Comput. Chem.* **1997**, *18*, 1463–1472.

(60) Miyamoto, S.; Kollman, P. A. Settle: An Analytical Version of the SHAKE and RATTLE Algorithm for Rigid Water Models. *J. Comput. Chem.* **1992**, *13*, 952–962.

(61) Essmann, U.; Perera, L.; Berkowitz, M. L.; Darden, T.; Lee, H.; Pedersen, L. G. A Smooth Particle Mesh Ewald Method. *J. Chem. Phys.* **1995**, *103*, 8577.

(62) Souaille, M.; Roux, B. Extension to the Weighted Histogram Analysis Method: Combining Umbrella Sampling with Free Energy Calculations. *Comput. Phys. Commun.* **2001**, *135*, 40–57.

(63) Humphrey, W.; Dalke, A.; Schulten, K. VMD: Visual Molecular Dynamics. *J. Mol. Graph.* **1996**, *14*, 33–38.

(64) Daura, X.; Gademann, K.; Schäfer, H.; Jaun, B.; Seebach, D.; van Gunsteren, W. F. The β-Peptide Hairpin in Solution: Conformational Study of a β-Hexapeptide in Methanol by NMR Spectroscopy and MD Simulation. *J. Am. Chem. Soc.* **2001**, *123*, 2393–2404.

(65) Kabsch, W.; Sander, C. Dictionary of Protein Secondary Structure: Pattern Recognition of Hydrogen-Bonded and Geometrical Features. *Biopolymers* **1983**, *22*, 2577–2637.

(66) Israelachvili, J. . Thin Film Studies Using Multiple-Beam Interferometry. *J. Colloid Interface Sci.* **1973**, *44*, 259–272.

(67) Donaldson, S. H.; Das, S.; Gebbie, M. A.; Rapp, M.; Jones, L. C.; Roiter, Y.; Koenig, P. H.; Gizaw, Y.; Israelachvili, J. N. Asymmetric Electrostatic and Hydrophobic-Hydrophilic Interaction Forces between Mica Surfaces and Silicone Polymer Thin Films. *ACS Nano* **2013**, *7*, 10094–10104.

(68) Johnson, K. L.; Kendall, K.; Roberts, A. D. Surface Energy and the Contact of Elastic Solids. *Proc. R. Soc. A Math. Phys. Eng. Sci.* **1971**, *324*, 301–313.

(69) Ye, Q.; Zhou, F.; Liu, W. Bioinspired Catecholic Chemistry for Surface Modification. *Chem. Soc. Rev.* **2011**, *40*, 4244–4258.

(70) Kristoffersen, H. H.; Shea, J.-E.; Metiu, H. Catechol and HCl Adsorption on TiO2(110) in Vacuum and at the Water-TiO2 Interface. *J. Phys. Chem. Lett.* **2015**, *6*, 2277–2281.

(71) Levine, Z. A.; Fischer, S. A.; Shea, J.-E.; Pfaendtner, J. Trp-Cage Folding on Organic Surfaces. *J. Phys. Chem. B* **2015**, *119*, 10417–10425.

(72) Maier, G. P.; Rapp, M. V; Waite, J. H.; Israelachvili, J. N.; Butler, A. Adaptive Synergy between Catechol and Lysine Promotes Wet Adhesion by Surface Salt Displacement. *Science* **2015**, *349*, 628–632.

(73) Miller, C. M.; Brown, A. C.; Mittal, J. Disorder in Cholesterol-Binding Functionality of CRAC Peptides: A Molecular Dynamics Study. *J. Phys. Chem. B* **2014**, *118*, 13169–13174.

CHAPTER 4

Synergy Between Catecholic and Cationic Functionalities in Wet Adhesion

4.1 Adaptive Synergy Between Catechol and Lysine Promotes Wet Adhesion by Surface Salt Displacement

*Maier, G. P.; *Rapp, M. V.; Waite, J. H.; Israelachvili, J. N.; Butler, A. (2015) ***Science***, 349 (6248):628–632.

4.1.1 Abstract

In physiological fluids and seawater, adhesion of synthetic polymers to solid surfaces is severely limited by high salt, pH, and hydration, yet these conditions have not deterred the evolution of effective adhesion by mussels. Mussel foot proteins provide insights about adhesive adaptations: notably, the abundance and proximity of catecholic Dopa (3,4-dihydroxyphenylalanine) and lysine residues hint at a synergistic interplay in adhesion. Certain siderophores—bacterial iron-chelators—consist of paired catechol and lysine functionalities thereby providing a convenient experimental platform to explore molecular synergies in bioadhesion. These siderophores and synthetic analogs exhibit robust adhesion ($W_{adh} \geq 15 mJ/m^2$) to mica in saline pH 3.5-7.5 and resist oxidation. The adjacent catechol-Lys placement provides a "1-2 punch", whereby Lys evicts hydrated cations from the mineral surface, allowing catechol binding to underlying oxides.

4.1.2 Introduction

Water disrupts adhesion on polar surfaces by forming hydration layers that impede intimate contact between adhesive polymers and surfaces. Sessile marine organisms, including barnacles, kelps, and mussels, routinely adhere to wet saline surfaces, suggesting that successful adaptations for removing weak boundary layers have evolved. Identifying these adaptations holds great promise for adhesion science and technology. The mussel holdfast or byssus contains ~15 adhesive mussel foot proteins (mfps), two of which, mfp-3 and mfp-5, are deposited first as a primer to condition the target surface and enable other mussel foot proteins to adhere[1] and are peculiar in containing between 20-30 mol% Dopa. Demonstration by atomic force microscopy of wet adhesion to titania by a single Dopa[2] sparked functionalization of synthetic polymeric adhesives and self-healing hydrogels with catechol,[3–8] but wet adhesion of these polymers to oxides and minerals remains controversial.[9,10] In actuality, mfp-3 and -5 are rich in Lys as well as Dopa —frequently in adjacent positions along the protein backbone.[1] The surface forces apparatus (SFA) has measured impressive wet adhesion of these proteins to mineral, oxide, and organic surfaces.[11] Dopa residues in mfp-3 and -5 form bidentate coordination and hydrogen bonds to mineral and oxide surfaces, and hydrophobic interactions on polymeric surfaces,[11] but only if protected from oxidation by low pH and anti-oxidants during deposition.[12,13] Several mimics of mussel foot proteins have been synthesized, most notably Dopa-Lys copolymers by Yamamoto[14] and Deming[15] using N-carboxyanhydride ring opening polymerization, as well as the polymer brush anchors developed by Messersmith.[6] However, the role of Lys in both the mussel surface primers and in synthetic wet adhesives remains poorly understood.

Many marine and pathogenic bacteria have evolved an adaptive iron-sequestration pathway that is based on catechol-containing siderophores, including enterobactin, the cyclic lactone of *tris*-2,3-dihydroxybenzoyl-L-Ser (2,3-DHBA-L-Ser).[16] The plant pathogen *Dickeya chrysanthemi* produces the siderophore, cyclic trichrysobactin (CTC), the lactone of *tris*-2,3-DHBA-D-Lys-L-Ser (Figure 4.1A) in which Lys is present adjacent to each catechol.[17] The prominence and proximity of catechol and Lys in CTC resemble the interfacial adhesive proteins mfp-3 and mfp-5. However, the mass of CTC (1053 g/mol) is a fraction of the mfp-3 and 5 masses (6kDa and 10kDa, respectively). As such, the siderophore has relaxed steric constraints when adsorbed to a surface, and the simpler siderophore structure allows for more straightforward interpretation of the adhesive mechanisms. In addition, the autoxidation of 2,3-DHBA is much slower than 4-methylcatechol, a proxy for the 3,4-dihydroxy substituents in the Dopa catechol, at pH 7.5 and 10 (discussed further in Section 4.1.4), reflecting intramolecular H-bonding between the ortho-OH and the carbonyl oxygen, and the electron withdrawing nature of the carboxylate substituent (Figure 4.2B), both of which stabilize CTC against oxidation compared to Dopa in mussel foot proteins. Ultimately, the subtle molecular differences make 2,3-DHBA in siderophores significantly more oxidation resistant and enlarge the pH range over which these compounds bind to target surfaces.

4.1.3 Materials and Methods

Materials: 2,3-dihydroxybenzoic acid (2,3-DHBA), catechol, 3,4-dihydroxybenzoic acid (3,4-DHBA), dicyclohexylcarbodiimide (DCC), and tris(2-aminoethyl)amine (TREN) were purchased from Aldrich. 4-methylcatechol (4-MC) was purchased from Acros Organics. Benzyl bromide, palladium on carbon, and benzoic acid were purchased from Alfa Aesar. N-hydroxysuccinimide (NHS) was purchased from Fluka. Triethylamine, sodium phosphate dibasic, potassium hydroxide, and trifluoroacetic acid (TFA) were purchased from Fisher. 3-hydroxybenzoic acid was purchased from TCI. CAPSO buffer was purchased from Research Organics. Phosphate buffer was purchased from Fisher. H-Lys(Z)-OH, H-Dab(Boc)-H, and H-Lys(Ac)-OH were purchased from Bachem. Unless otherwise stated, all chemicals were used as received without further purification or modification.

Autoxidation of Catechol Analogs: The autoxidation of 4-Methylcatechol (4-MC), catechol, 3,4-dihydroxybenzoic acid (3,4-DHBA), and 2,3-dihydroxybenzoic acid (2,3-DHBA) was tracked using the following procedure. A 5300 Biological Oxygen Monitor (Yellow Springs Instruments) equipped with a Clark electrode was used to track oxidation kinetics through the consumption of dissolved molecular oxygen. Buffer solutions were sparged with compressed air to ensure the same starting concentration of dissolved molecular oxygen for all experiments. Trace metal was removed from buffers with Chelex 100 resin (100-200 mesh, sodium form, Bio-Rad) using the batch method. 3 ml of $29.5^{\circ C}$ ± 0.01 of 50 mM buffer was introduced to the reaction chamber (also held at $29.5^{\circ C}$ ± 0.01). Phosphate buffer was used for pH 7.5 and CAPSO buffer was used for pH 10.0. The reaction chamber was sealed with the Clark electrode, removing all non-dissolved air from the system and allowed to equilibrate for 5 – 10 minutes. Kinetics experiments began upon the injection of 10 µl of a catechol analog solution with a metal free injection device and the percent oxygen remaining was recorded for ten minutes. All catechol analog solutions were prepared immediately prior to use. 4-Methylcatechol and catechol were dissolved in 0.5M HCl to prevent oxidation. 3,4-Dihydroxybenzoic acid and 2,3-dihydroxybenzoic acid were dissolved in ethanol to maximize solubility. All experiments were done in pseudo 1st order conditions with catechol analog in excess.

Siderophore Analog Synthesis: Tren-cam (TC) was synthesized according to previously published methods.[16] Tren-Lys-Cam was synthesized using well known peptide bond formation and protecting group chemistries.[18] The remaining homologs were synthesized by variations of the synthesis scheme for TLC. See Figure 4.1 for details of the synthesis procedure. See Figures 4.6-4.8 for the structures of TLC, TDC, TLP, TLB, $TL^{Ac}C$, and TC. The synthesis of TDC used H-Dab(Boc)-OH in place of H-Lys(Z)-OH in step c. An additional final step was performed in the synthesis of TDC to remove the Boc protecting group. This was done with 50% trifluoroacetic acid in DCM at room temperature for 2 hours. The synthesis of TLP was done using 3-hydroxybenzoic acid as the starting material in place of 2,3-DHBA in step a. The synthesis of TLB used benzoic acid as a starting material rather than 2,3-DHBA. The absence of hydroxyl groups obviated the need for step a. $TL^{Ac}C$ was synthesized using H-Lys(Ac)-OH in place of H-Lys(Z)-OH for step c.

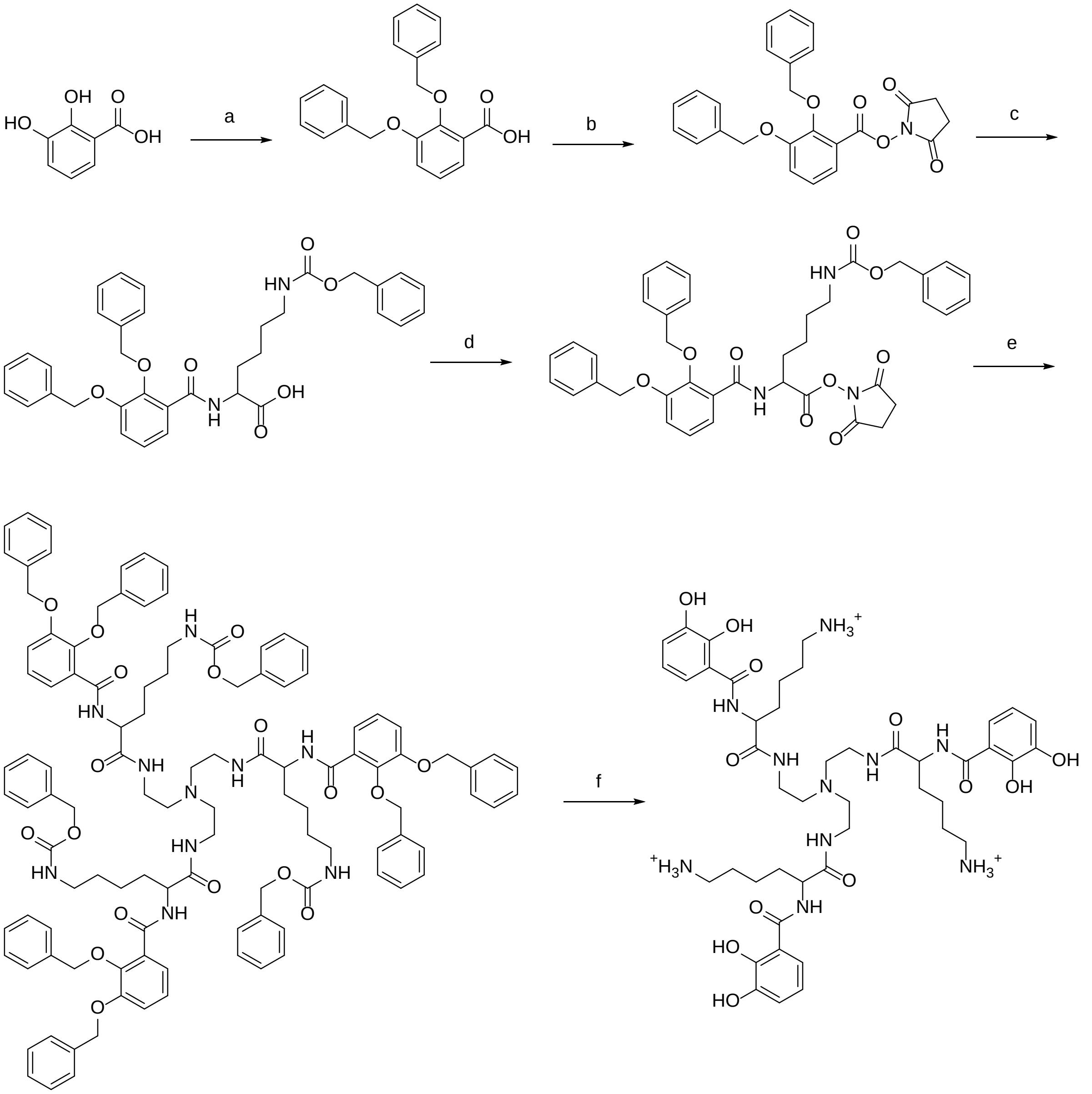

Figure 4.1: Synthesis Scheme for Tren-Lys-Cam. Reaction Conditions: (a) KOH, DMSO, Benzyl Bromide, 4 hours. (b) NHS, DCC, anhydrous THF under N_2, overnight. (c) THF, H_2O, Et_3N, H-Lys(Z)-OH, overnight. (d) NHS, DCC, anhydrous THF under N_2, overnight. (e) Et_3N, TREN, anhydrous DCM under N_2, overnight. (f) EtOH, 3% HOAc, Pd/C, overnight.

Surface Forces Apparatus (SFA): The full details of the SFA technique are elaborated elsewhere.[19] All measurements were performed with a SFA 2000, manufactured by SurForce LLC. in Santa Barbara, California. Briefly, for each experiment, two mica surfaces are prepared by gluing a piece of freshly-cleaved, back-silvered mica (~1 cm^2), of equal mica and silver thicknesses, onto cylindrical glass disks (radius ~2 cm), with the pristine mica surface facing upward. The two mica surfaces are installed into the SFA, with the pristine mica surfaces facing each other. The surfaces are brought close together and small droplets of aqueous buffer are injected between the surfaces (~50 μL total volume). Normal force-distance measurements are then performed between the two surfaces in aqueous solution. The contact area between the mica surfaces is verified as free from asperities or contaminants based on the interferometric profile of the contact zone and the measured forces, which are well documented for mica interacting in aqueous solution.[20–22] Following, a small amount (~10 μL) of siderophore, or analog, in aqueous buffer is injected into the gap solution between the surfaces, and the system is allowed to equilibrate for 20 minutes as the siderophores adsorb to the mica surfaces. While remaining at the same contact position, force-distance measurements are then performed between the mica surfaces in the siderophore solutions. The aqueous solutions used in SFA experiments were: (i) a 50 mM acetate + 150 mM KNO_3 buffer solution for pH 3.3 and 5.5, and (ii) a 50 mM phosphate + 150 mM KNO_3 buffer solution for pH 7.5. The force-distance data shown are representative of measurements performed over at least 4 separate experiments for each molecule and solution condition. The adhesion values, F_{ad}, and compressed film thicknesses, D_{T}, are reported as the sample mean and standard deviation.

4.1.4 Oxidation Resistance in 2,3-Catechols

Catechol autoxidation by dissolved molecular oxygen is a pH-dependent process that accelerates at higher pH. The reaction proceeds through a series of one electron oxidations and therefore, superoxide and semiquinone are present as intermediates. The reaction mechanism for the autoxidation of catechol is not well defined.

The rate of oxygen consumption for the series of catechol compounds correlates with the strength of electron donating or withdrawing group (see Figure 4.2). The electron donating methyl group of 4-MC promotes the fastest oxidation rate of the compounds measured. Autoxidation of unsubstituted catechol is slower. Addition of an electron withdrawing carboxylic acid, e.g., 3,4-DHBA, further slows the autoxidation rate. This correlation holds true at both pH 7.5 and pH 10.0. Increasing the concentration of the catechol compounds increases the autoxidation rate, as is expected for pseudo 1st order conditions.

The autoxidation rate of 2,3-DHBA is even slower than 3,4-DHBA; these isomeric compounds differ only in the position of the electron withdrawing substituent. Intramolecular hydrogen bonding in 2,3-DHBA, between the 2-hydroxyl group and the carbonyl oxygen atom, further protects the catechol from oxidation and raises the first catecholic hydroxyl pK_a above that of 3,4-DHBA, 10.06 and 8.82, respectively. The pH of the wet adhesion environment must be significantly lower than the first pK_a of the catechol hydroxyl groups to ensure a bidentate H-bond with the target surface. Ultimately, the subtle molecular differences make the common 2,3-DHBA catechol in siderophores significantly more oxidation resistant and enlarge the pH window over which these siderophore analogs bind to target surfaces.

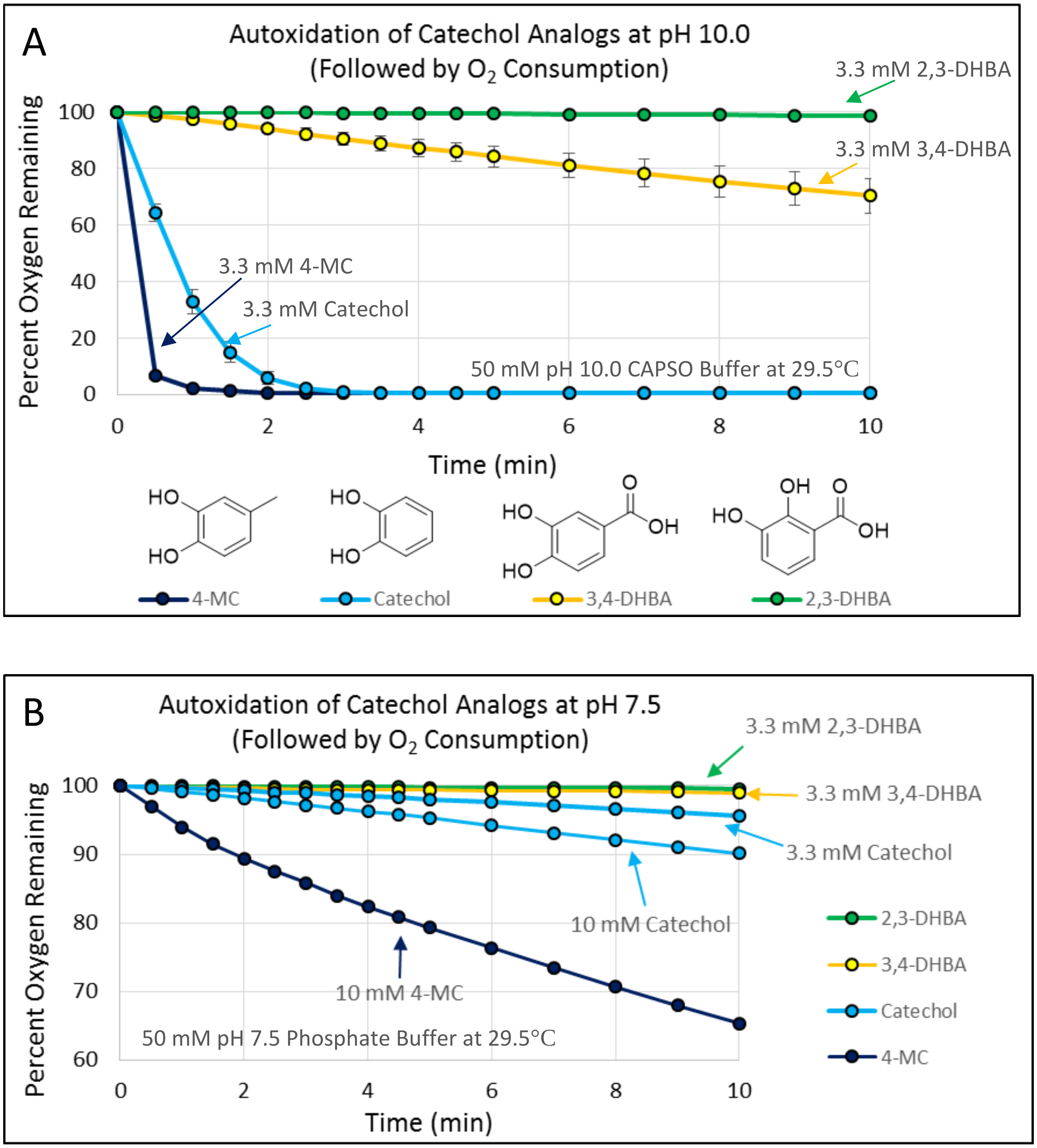

Figure 4.2: Autoxidation of 4-MC, Catechol, 2,3-DHBA and 3,4-DHBA at pH 10.0 (A.) and pH 7.5 (B.). **A.** 3.3 mM of each catechol compound, pH 10.0 in 50 mM CAPSO buffer at 29.5°C. **B.** 10.0 mM 4-MC, Catechol and 3.3mM 2,3-DHBA and 3,4-DHBA at pH 7.5 in 50 mM phosphate buffer at 29.5°C. Oxygen consumption was monitored using a Clark electrode.

4.1.5 The Siderophore CTC Mediates Wet Adhesion Between Mica Surfaces

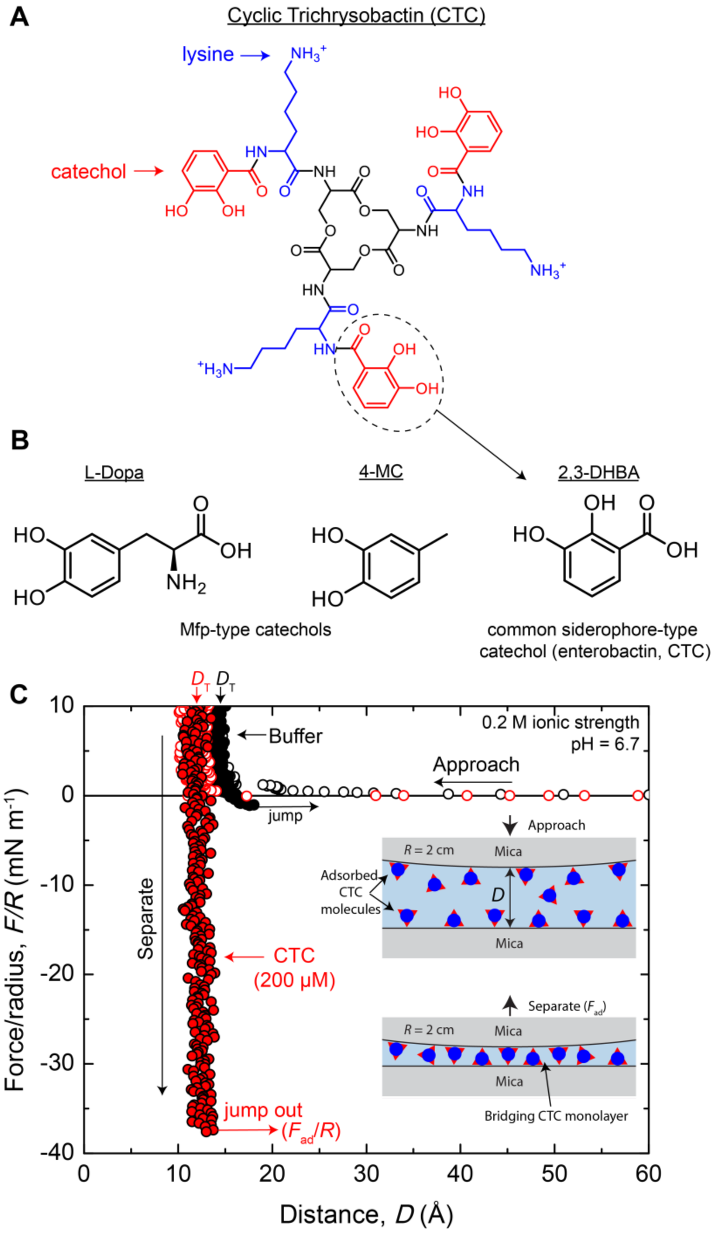

Figure 4.3: Adhesion of a natural bacterial catechol siderophore. A, Structure of cyclic trichrysobactin (CTC). B, Structures of catechols illustrating the difference between 3,4-dihydroxy catechol as in Dopa or 4-methylcatechol (4-MC), and 2,3-dihydroxy catechol, as commonly present in 2,3-dihydroxybenzoic acid (DHBA)-containing-siderophores. C, SFA force-distance interaction for CTC-mediated adhesion between two mica surfaces in buffer (50 mM phosphate buffer + 150 mM KNO3) at pH 6.7. The surfaces were left in contact for 30 min before separation. The open and solid circles are for data measured on approach and separation, respectively, of the mica surfaces. The inset displays a schematic of the interacting surfaces throughout the SFA experiments.

A surface forces apparatus (SFA) was used to measure the normalized force (F/R)-distance (D) profiles of two molecularly-smooth mica surfaces (of radius R) during their approach and separation in buffered solutions of CTC.[19] In these SFA measurements, the surfaces are first slowly brought into contact and compressed. The thickness of the intervening compressed film between the surfaces is measured as D_T. The surfaces are then slowly separated and the adhesion force (F_{ad}/R) is measured at the force minimum, at a point just before the surfaces rapidly jump apart.

Mica is an anionic and molecularly smooth aluminosilicate mineral that allows for Å-level mechanistic insight during adhesion measurements. In saline solutions, mica adsorbs cations (particularly K^+) to form a tightly bound hydration layer at the solid-liquid interface.[20,21] These hydration layers—present at virtually all marine and physiological interfaces—impose a significant molecular barrier to coatings and high-performance adhesives for wet surfaces.[22] The effects of these hydration layers between mica surfaces in buffered solution without any added siderophores (Figure 4.3C, black circles) are seen in the SFA measurements: when compressed to 10 mN m^{-1}, hydrated K^+ ions form a D_T=13 ± 1 Å thick bilayer between the mica surfaces, and only a weak adhesion force is measured on separation. However, nanomole amounts of CTC form a single monolayer "molecular bridge" that results in a large adhesion force between the micas presumably by displacing the hydrated salt ions from the mica surface (Figure 4.3C, red circles). After injecting 10 nanomoles of CTC into the buffered gap solution between the mica surfaces (~50 μL total volume, 200 μM bulk concentration), the compressed film thins to 11 ± 1 Å—indicating that the hydrated salt ions have been replaced with CTC at the surface—and the adhesion force between the surfaces increases ~30-fold to -30 ± 10 mN m^{-1}. As the surfaces are separated, the sharply vertical shape of the separation force curve does not exhibit any observable bridging (i.e., an increase in the separation distance), indicating that the physical bonds supporting adhesion are specific and short-ranged (effective only over several Å), such as a hydrogen bond or specific Coulombic interaction.[21]

4.1.6 A Synthetic Siderophore Analog also Supports Robust Adhesion

The natural 2,3-DHBA-containing CTC siderophore promotes adhesion at near-neutral pH (pH 6.7), a solution condition that rapidly oxidizes Dopa in mussel foot proteins leading to reduced adhesion.[12] Yet, the triserine lactone scaffold of CTC hydrolyses under acidic conditions, limiting its usefulness as an adhesive primer over a wide range of pH. To circumvent this limitation, we synthesized a mimic of CTC, Tren-Lys-Cam (TLC, Figure 4.4A) built on the robust tris(2-aminoethyl)amine (Tren) scaffold that retains integrity over a wide pH range (Figure 4.1).[23] TLC exhibits nearly identical adsorption and adhesion behavior to the natural CTC siderophore. In parallel SFA experiments at pH 3.3 (Figure 4.4B), TLC molecules displace hydrated salt ions at the mica surface and, after compression of the surfaces, form a 9 ± 1 Å thick monolayer that bridges between the two surfaces. The thickness of the TLC film, the shape of the force-distance profile (narrow adhesion well), and dramatically increased adhesion all indicate that the synthetic TLC performs similarly to CTC at mineral surfaces.

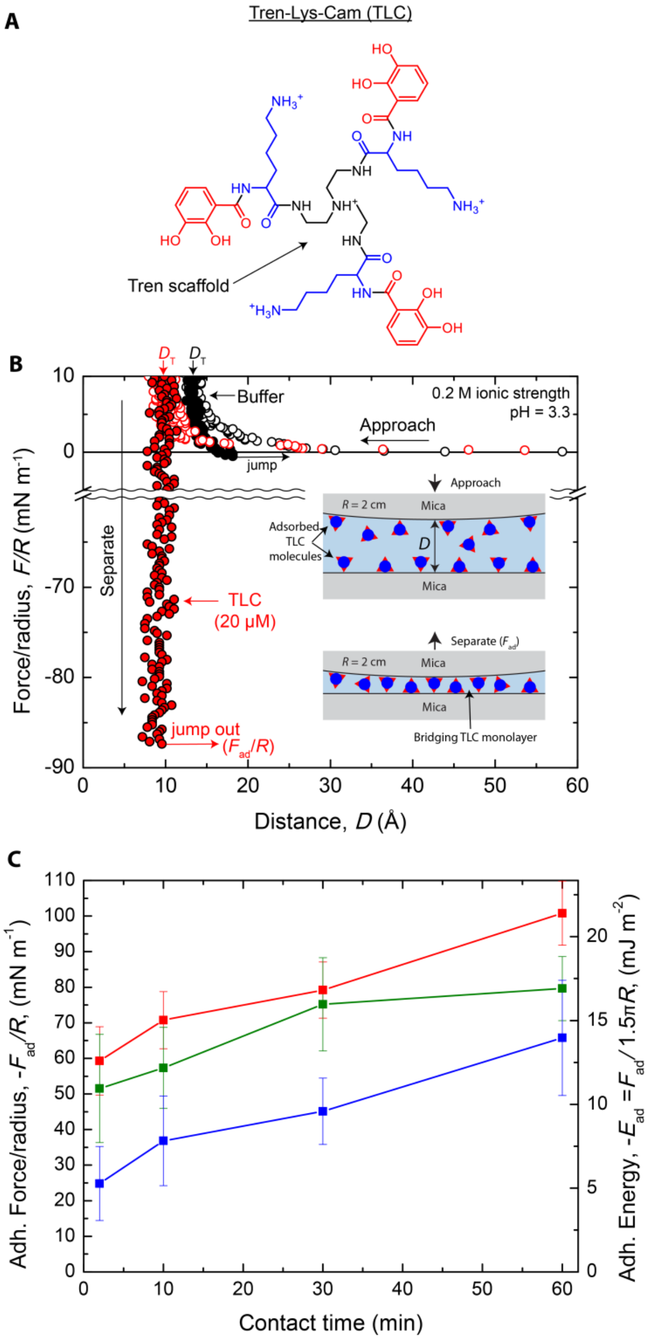

Figure 4.4: Adhesion of a synthetic siderophore mimic. A, Structure of Tren-Lys-Cam (TLC), a synthetic mimic of the natural siderophore cyclic trichrysobactin. B, SFA force-distance interaction for the TLC-mediated adhesion between two mica surfaces in buffer (50 mM acetate buffer + 150 mM KNO3) at pH 3.3. The surfaces were left in contact for 30 min before separation. The open and solid circles are for data measured on approach and separation, respectively, of the mica surfaces. The inset displays a schematic of the interacting surfaces throughout the SFA experiments. C, The adhesive force (and energy) required to separate two mica surfaces adsorbed with 1-10 nmoles (20-200 μM) of TLC, as a function of both the time the mica surfaces were left in contact and the buffer solution pH. Error bars (± 12 mN m-1) for the pH 3.3 and 5.5 measurements have been omitted for visual clarity.

TLC mediates adhesion between mineral surfaces in saline solution from pH 3.3-7.5 (Figure 4.4C). The TLC peak adhesion concentration is ~20 μM (Figure 4.5). Adhesion forces measured in SFA experiments are converted to adhesion energies through the Johnson-Kendal-Roberts theory of adhesive surfaces ($E_{ad} = F_{ad}/1.5\pi R$).[24] Adhesion is strongest at pH 3.3, and is not statistically different from pH 5.5 for a p-value ≤ 0.05 (Table 4.1). At pH 7.5, adhesion decreases ($p \leq 0.05$), yet TLC still maintains ~65% of the peak adhesion. The cause for the decrease in adhesion at pH 7.5 is under investigation; we speculate that either slow TLC oxidation or subtle interfacial pH changes reduce the number of bridging hydrogen bonds at pH 7.5. Moreover, adhesion energy increases with contact time before separation—a common trait among adhesives. As longer contact allows for better interfacial equilibration, more siderophore molecules are able to rearrange and maximize the number of bridging bonds.[21]

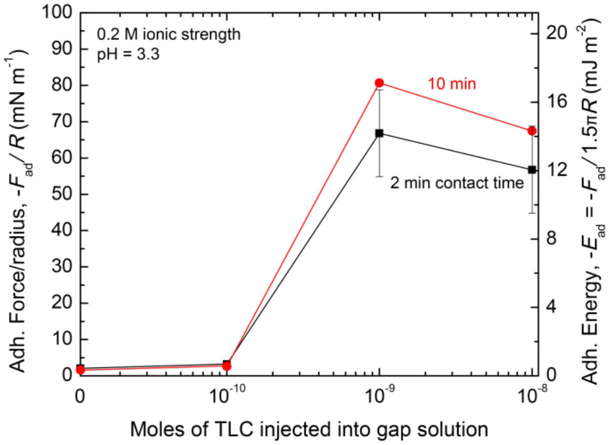

Figure 4.5: The TLC-mediated adhesion force (and energy) between two mica surfaces in buffered solution as a function of the number of moles of TLC injected into the intervening gap solution between the mica surfaces. The total volume of intervening solution between the two mica surfaces is typically ~50 μL. Error bars for the 10 min data points (±12 mN m^{-1}) have been omitted for visual clarity. The anionic mica surfaces used in these experiments are ~ 1 cm^2 and contain ~ 2.1 x 10^{14} negatively charged sites per surface. The adhesion force between mica surfaces peaks when the total number of TLC molecules injected between the surfaces (~ 6 x 10^{14} molecules) is roughly equivalent to the number of negatively charged mica sites in the system (~ 4.2 x 10^{14} total sites between the two surfaces). Increasing the number of moles of TLC injected into the system causes a slight decrease in the adhesion force, a result of over-adsorption of TLC molecules to the mica surface.

Table 4.1: P-values from the pairwise t-tests between the TLC-mediated adhesion data sets at pH 3.3, 5.5, and 7.5. P ≤ 0.05 values are highlighted in grey.

	Contact Time			
	2 min	**10 min**	**30 min**	**60 min**
pH 3.3—pH 5.5	P = 0.1274	P = 0.0952	P = 0.6216	P = 0.0158
pH 3.3—pH 7.5	P = 0.00001	P = 0.0062	P = 0.0014	P = 0.0129
pH 5.5—pH 7.5	P = 0.0002	P = 0.0492	P = 0.0135	P = 0.1954

4.1.7 Synergy between Catechol and Amines Promotes Wet Adhesion

To ascertain specific contributions made by catechol and Lys in the siderophore adhesive platform, we synthesized a suite of five additional Tren-based homologs, varying properties of the amine and the aromatic functionalities (Figure 4.6A-G). Group I homologs retain both catechol and amine functionalities (Figures 4.6B and 4.6C); Group II retains Lys but removes the catechol functionality (Figures 4.6D and 4.6E); and Group III retains catechol but removes the amine functionality (Figures 4.6F and 4.6G). Collectively, the results of the six synthetic homologs reveal a requirement for catechol and an alkylamine cation (e.g. Lys, Dab) for appreciable surface binding and adhesion.

Group I includes TLC and Tren-Dab-Cam (TDC), with the Lys chain shortened by two methylene units to diaminobutyric acid (Dab). Group I assesses whether the length or flexibility of the amine is critical to adsorption and adhesion. The length of the amine chain between 2 to 4 carbons does not alter the homolog’s behavior, as both TLC and TDC displace salt on the mica surface and promote large adhesion energies (Figures 4.6H-I, 4.7A).

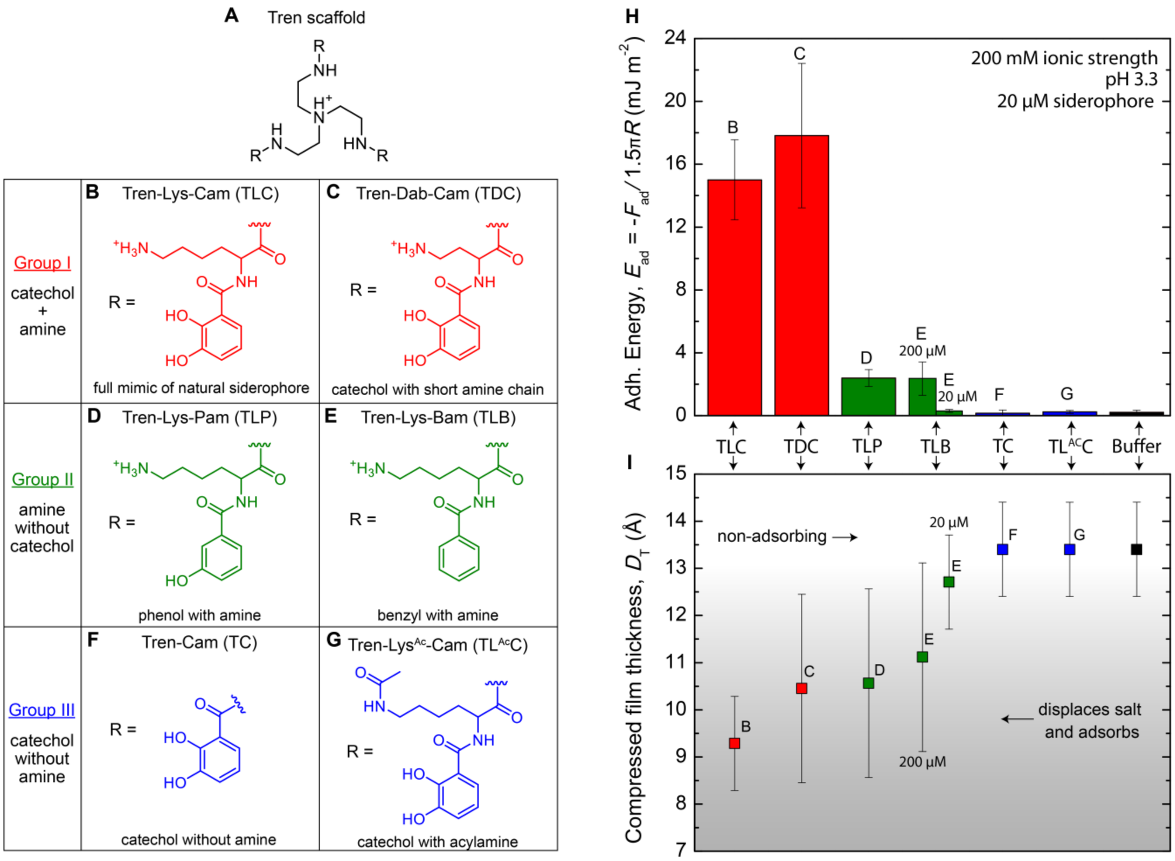

Figure 4.6: The synergy of catechol and Lys in siderophore adhesion. A, Structure of the Tren scaffold. B-G, the R groups appended to Tren. H, The average adhesion energy required to separate two mica surfaces adsorbed with 1 nmole (20 μM) of the homolog in buffer (50 mM acetate + 150 mM KNO_3) at pH 3.3 after 10 minutes of contact. I, The average film thickness, D_T, of the siderophore monolayer between two mica surfaces at 10 mN/m of compressive load. The film thicknesses correspond with the adhesion energy displayed in H, above. A decreased film thickness (<12 Å) indicates that homologs B, C, D, and E (200 μM) adsorb, displace hydrated salt at the mica surface, and mediate adhesion between two mica surfaces. SFA force-distance measurements for each molecule are shown in Figures 4.7 and 4.8.

Group II homologs test the effect of removing catechol, while maintaining the 4+ cationic charge: Tren-Lys-Pam (TLC) retains one-hydroxyl group, whereas Tren-Lys-Bam (TLB) removes both hydroxyls. Without catechol, the Group II homologs exhibit comparatively weak adhesion between mica surfaces, i.e. ~15% of the Group I homologs with both Lys and catechol. Contrary to the narrow adhesion wells of the Group I homologs, the separation force curves of Group II homologs display weak bridging (~5-10 Å) before the surfaces jump apart (Figure 4.7B-C), suggesting that the adhesion may be due to non-specific interactions between 2 or more homologs (such as hydrophobic interactions or π-cation interactions).[25] TLB is unable to donate H-bonds and has increased hydrophobicity hence has an increased energy barrier for adsorption; TLP adsorbs to the mica surface at 20 μM (the same as the TLC critical aggregation concentration), yet TLB requires an elevated bulk concentration of 200 μM before adsorption begins.

Group III homologs compromise the amine functionality, through acetylation (Tren-Lys^{Ac}-Cam, TL^{Ac}C) or by omission of Lys (Tren-Cam, TC), while maintaining the catechol presence. Over the concentration range of 2-200 μM, Group III homologs do not adsorb on the mica surface at high salt (200 mM) and provide no adhesion (Figure 4.8A-B). In pure water, TC adsorbs as a multilayer on mica and demonstrates modest cohesion (Figure 4.8C).

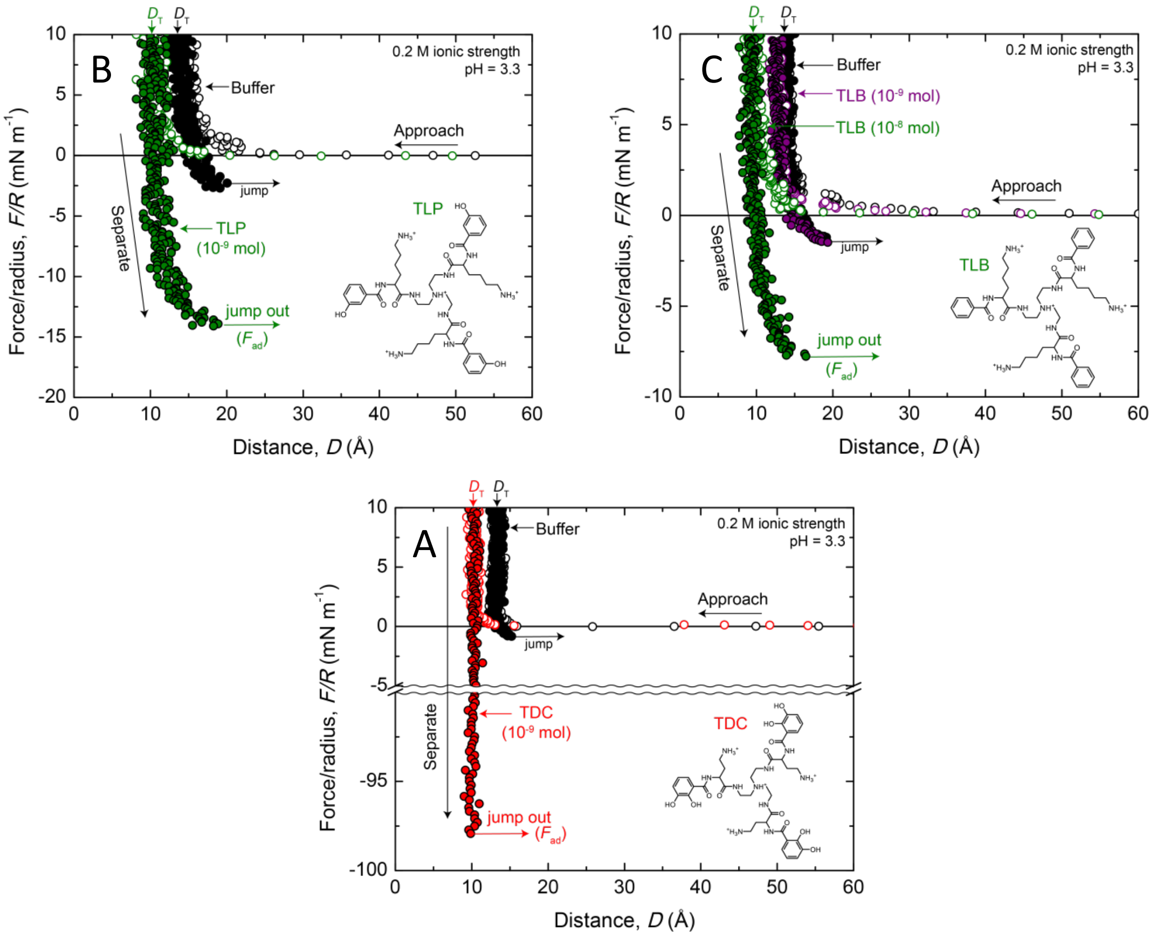

Figure 4.7: SFA force-distance interaction of tren-homologs. **A.** SFA force-distance interaction for the TDC-mediated adhesion between two mica surfaces in buffer (50 mM acetate buffer + 150 mM KNO_3) at pH 3.3. 10^{-9} moles of TDC were injected into the gap solution between the surfaces. The inset displays the molecular structure of TDC. **B.** SFA force-distance interaction for the TLP-mediated adhesion between two mica surfaces in buffer (50 mM acetate buffer + 150 mM KNO_3) at pH 3.3. 10^{-9} moles of TLP were injected into the gap solution between the surfaces. The inset displays the molecular structure of TLP. **C.** SFA force-distance interaction for the TLB-mediated adhesion between two mica surfaces in buffer (50 mM acetate buffer + 150 mM KNO_3) at pH 3.3. Measurements are shown for 10^{-9} moles and 10^{-8} moles of TLB injected into the gap solution between the surfaces. At 10^{-9} moles, TLB does not significantly adsorb onto mica, and the resulting force-distance profile appears the same as for a buffer solution in the absence of siderophore. However, at 10^{-8} moles, TLB does adsorb to the mica surface, resulting in a decrease in the compressed film thickness and an increase in the measured adhesion force. The inset displays the molecular structure of TLB.

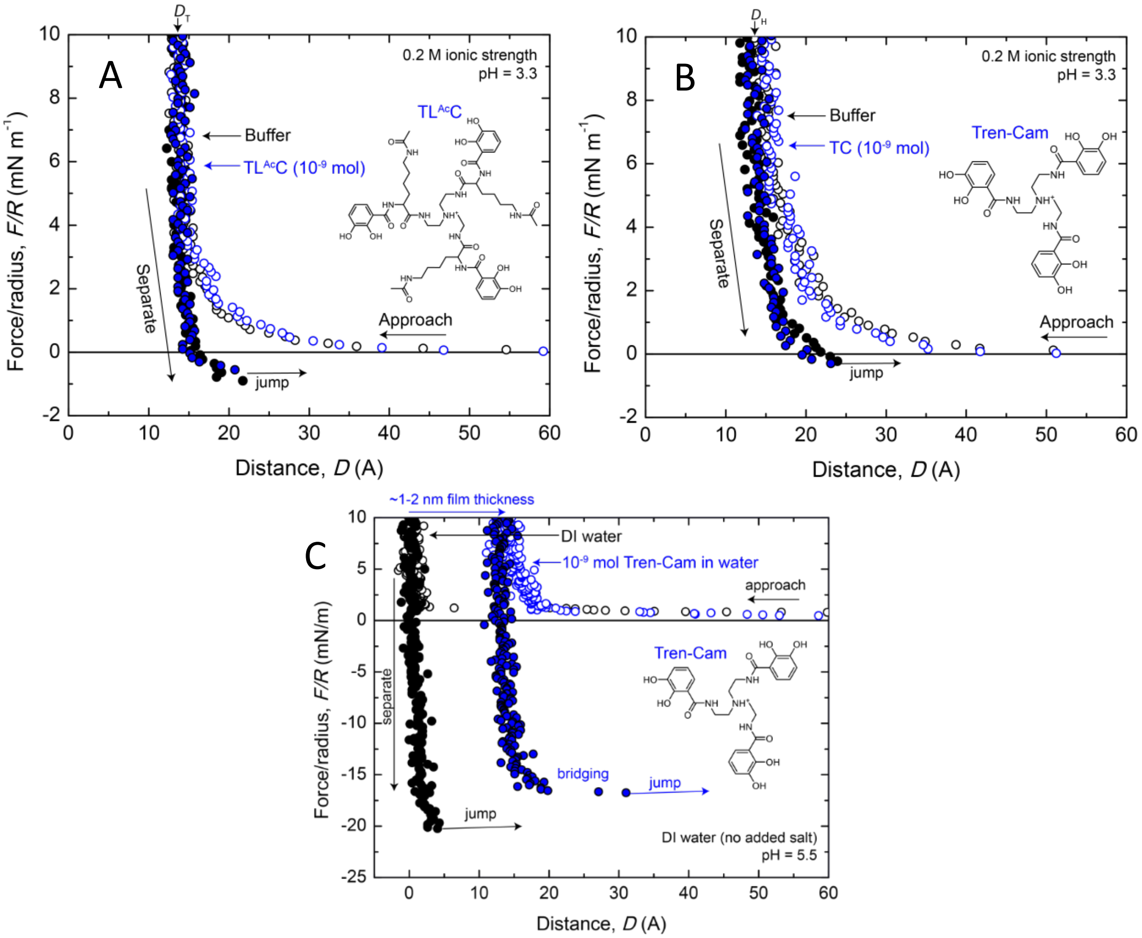

Figure 4.8: SFA force-distance interactions of modified amine tren-homologs. **A.** SFA force-distance profile for two mica surfaces interacting in a buffer at pH 3.3 (50 mM acetate buffer + 150 mM KNO_3) with an additional 10^{-9} moles of $TL^{Ac}C$ injected into the solution between the surfaces. $TL^{Ac}C$ does not significantly adsorb onto mica, and the resulting force-distance profile appears the same as for a buffer solution in the absence of siderophore. The inset displays the molecular structure of $TL^{Ac}C$. **B.** SFA force-distance profile for two mica surfaces interacting in a buffer at pH 3.3 (50 mM acetate buffer + 150 mM KNO_3) with an additional 10^{-9} moles of Tren-Cam injected into the solution between the surfaces. TC does not significantly adsorb onto mica, and the resulting force-distance profile appears the same as for a buffer solution in the absence of siderophore. The inset displays the molecular structure of TC. **C.** SFA force-distance profile for two mica surfaces interacting in de-ionized water (pH 5.5) and with an additional 10^{-9} moles of Tren-Cam injected into the water between the surfaces. In pure de-ionized water, a long-ranged electrostatic repulsion between the mica surfaces is measured on approach; upon separation of the surfaces, a moderate adhesion force is measured due to van der Waals forces between the surfaces. After injecting 10^{-9} moles of TC into the water between the surfaces, the siderophore molecules adsorb, resulting in a 1-2 nm thick TC film (multilayers). The TC film mediates a moderate adhesive force between the surfaces (that cannot be described by van der Waals forces) and notable bridging between the surfaces is observed during separation. The inset displays the molecular structure of TC.

4.1.8 Conclusions

In sum, the amine and catechol moieties interact synergistically to mediate surface priming by the catechol alkylamine compounds to mineral surfaces. Bidentate catechol-mediated interactions are necessary for robust bridging attachments between surfaces, however, catechols alone are insufficient to breach the hydrated salt layer on mica, which is typical of a wide variety of aluminosilicate minerals in its cation binding properties.[26] The amines in CTC and TLC may serve as molecular vanguards to displace hydrated salt ions and ready the surface for bidentate catechol binding.[27]

The discovery that 2,3-dihydroxycatechol and alkyl ammonium (e.g., Lys and Dab) functionalities limit oxidation and promote adhesion has relevance to other adhesive platforms in providing a compelling rationale for the >20 mole% of cationic residues in Dopa-rich mussel foot proteins[1] and establishing a set of design parameters for future bio-inspired synthetic polymers. As many synthetic adhesives are functionalized with catechols and amines[28] for improved solubility[10] or cross-linking effects,[29,30] our results highlight the need to couple catechol and cationic functionalities to displace surface salts.

4.2 Defining the Catechol-Cation Synergy for Enhanced Wet Adhesion to Mineral Surfaces

*Rapp, M. V.; *Maier, G. P.; Dobbs, H. A.; Higdon, N. J.; Waite, J. H.; Butler, A.; Israelachvili, J. N. (2016) ***Submitted to J. Am. Chem. Soc.***

4.2.1 Abstract

Mussel foot proteins (Mfps) exhibit remarkably adaptive adhesion and bridging between polar surfaces in aqueous solution, despite the strong hydration barriers at the solid-liquid interface. Recently, catechols and amines—two functionalities that account for > 50 mole % of the amino acid side chains in surface priming Mfps—were shown to cooperatively displace the interfacial hydration and mediate robust adhesion between mineral surfaces. Here, we demonstrate: (1) synergy between catecholic and guanidinium side chains similarly promotes adhesion, (2) increasing the ratio of cationic amines to catechols in a molecule reduces adhesion, and (3) the catechol-cation synergy is greatest when both functionalities are present within the same molecule.

4.2.2 Introduction

Water undermines polymer adhesion to surfaces. Water and hydrated salt ions strongly bind to hydrophilic surfaces (such as minerals, metals, oxides, fabrics, and biological interfaces) to form a thin hydration film that impedes the intimate contact between polymer and surface necessary for durable adhesion.[20–22] Moreover, the high dielectric constant of water, $\varepsilon = 80$, dramatically reduces the strength of non-covalent intermolecular interactions in solution, as compared to air ($\varepsilon = 1$), because interaction energies generally scale as $E \propto 1/\varepsilon$ (Coulomb interactions) or $E \propto 1/\varepsilon^2$ (van der Waals interactions).[21] At larger length scales, water deteriorates the bulk adhesive properties of many materials through swelling, oxidation, hydrolysis, erosion, and crazing.[1]

To surmount these obstacles, wet adhesives and coatings must displace the hydration layer, bond to the underlying surface, and resist deterioration. Marine mussels routinely accomplish this feat on intertidal rocks with a quick-curing blend of intrinsically disordered proteins, known as mussel foot proteins (Mfps).[1,31] Of the > 15 known Mfps, two vanguard proteins—Mfp-3 and Mfp-5—are deposited first to prime the wet surface, and form the interfacial bridge that couples the rest of the holdfast to the surface.[1,32] Mfp-3 and -5 both consist of unique amino acid compositions, containing 20-30 mole % of the catecholic amino acid 3,4-dihydroxyphenylalanine (Dopa), with stoichiometric levels of cationic residues that are primarily lysine (Lys) and arginine (Arg). Dopa and cationic residues commonly occur in adjacent positions along the protein backbone. Over the past decade, the multifaceted catecholic functionality of Dopa[15]—which adheres to polar surfaces through hydrogen or coordination bonds,[2] or alternatively chelates metals and covalently cross links to form cohesive glues[33,34]—has led to a surge of mussel-inspired adhesives and coatings for applications such as medical or dental adhesives,[35–37] self-healing hydrogels,[3,38] bio-polymer scaffolds,[7,28] and bio-compatible coatings.[30,39,40] However, until recently, the role of cationic residues in mussel adhesives have been poorly understood, and underutilized in bio-inspired adhesives.

We recently demonstrated that synergistic interactions between catechol and Lys groups promote adhesion to a wet mineral surface, rationalizing the high Lys composition of interfacial Mfps.[41] To reduce the complexity of studying full proteins, we measured the adhesive interactions of a bacterial siderophore—cyclic trichrysobactin,[17] an iron-chelating small molecule (1053 g/mol) comprised of catechol and Lys functionalities—and synthetic siderophore analogs assembled around the Tren scaffold (Tris[2-aminoethyl]amine), such as Tren-Lys-Cam (TLC, Figure 4.11A). Through direct force measurements with a surface forces apparatus (SFA), we determined that the siderophore and its analogs mediate robust adhesion between two mica surfaces by displacing hydrated salt ions from the surface with their cationic Lys groups, allowing catechols to form bidentate bonds to the underlying aluminosilicate surface. Removing either catechol or amine functionalities from the analogs significantly reduced or eliminated adhesion, respectively.[41]

We report herein the nanoscale adhesive properties of new siderophore analogs that further explore the synergy between catechols and cationic moieties in wet mineral surface priming. The guanidinium cation in Arg displaces surface salt and promotes adhesion, but is less effective than Lys. Doubling the number of Lys groups per molecule (from 3 to 6)—while retaining the same number of catechol groups (3)—decreases the overall adhesion between surfaces, as the ratio of catechol binding groups to total molecular area decreases. Finally, we demonstrate that co-mixtures of two separate molecules that contain only catechols (appended to a Tren core) and only amines do not recreate the same adhesion synergy as the intramolecular configuration, suggesting that the adsorbate geometry and configurational entropy contribute significantly to the adhesion. Overall, these results suggest a rationale for the molecular compositions of Mfp adhesion priming proteins, and offer design criteria for functional bioadhesives and coatings.

4.2.3 Materials and Methods

Materials: 2,3-dihydroxybenzoic acid (2,3-DHBA), dicyclohexylcarbodiimide (DCC), and tris(2-aminoethyl)amine (TREN) were purchased from Aldrich. Ethanol, THF, trimethylamine (Et_3N), potassium hydroxide, trifluoroacetic acid (TFA) and DCM were purchased from Fisher. DMSO and acetic acid were purchased from EMD. Benzyl bromide and palladium on carbon were purchased from Alfa Aesar. N-hydroxysuccinimide (NHS) was purchased from Fluka. H-Lys(Z)-OH and Boc-Arg$(Z)_2$-OSu were purchased from Bachem. Unless otherwise stated, all chemicals were used as received without further purification or modification.

Siderophore Analog Synthesis: Tren-Cam (TC) and Tren-Lys-Bam (TLB) were synthesized according to previously published methods.[16,18,41] Tren-Lys-Lys-Cam (TLLC) and Tren-Arg-Cam (TAC) were synthesized by variations of the synthesis scheme for the previous two siderophore analogs. See Figures 4.9 and 4.10 for details of the synthesis procedure.

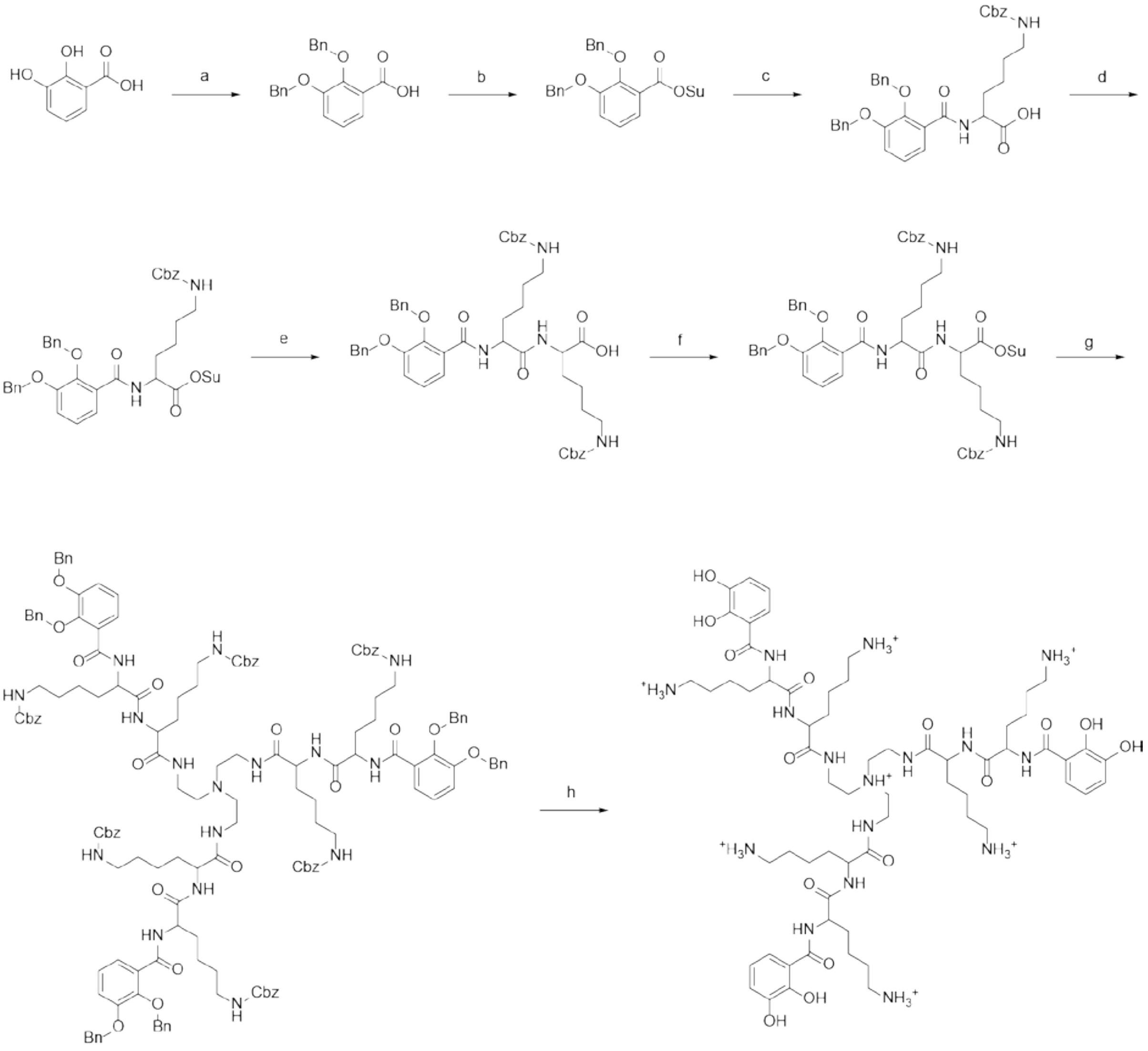

Figure 4.9: Synthesis Scheme for Tren-Lys-Lys-Cam. Reaction Conditions: (a) KOH, DMSO, benzyl bromide, stirred for 4 hours. (b) NHS, DCC, anhydrous THF under N_2, stirred overnight. (c) THF, H_2O, Et_3N, H-Lys(Z)-OH, stirred overnight. (d) NHS, DCC, anhydrous THF under N_2, stirred overnight. (e) THF, H_2O, Et_3N, H-Lys(Z)-OH, stirred overnight. (f) NHS, DCC, anhydrous THF under N_2, stirred overnight. (g) Et_3N, tris(2-aminoethyl)amine, anhydrous DCM under N_2, stirred overnight. (f) EtOH, 5% HOAc, Pd/C, stirred overnight under hydrogen atmosphere.

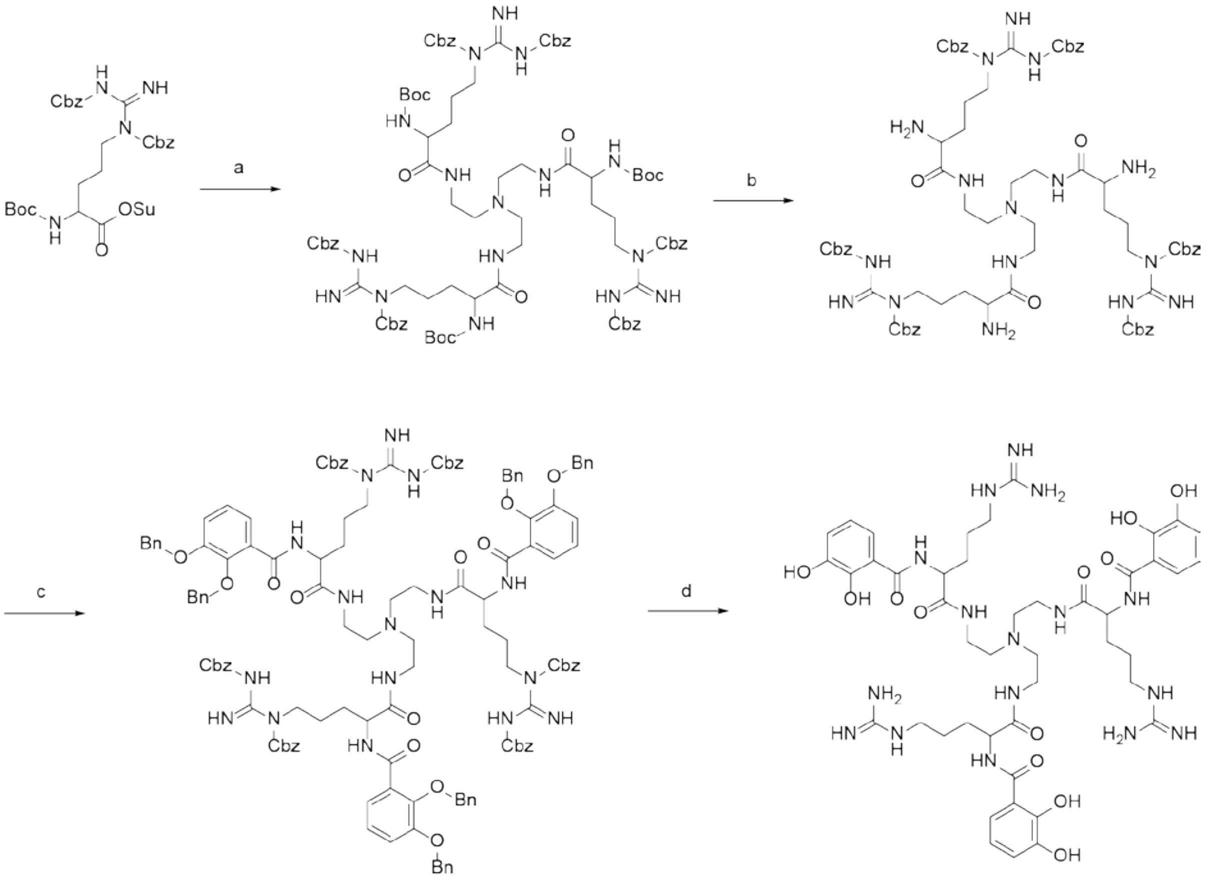

Figure 4.10: Synthesis Scheme for Tren-Arg-Cam. Reaction Conditions: (a) anhydrous THF under N_2, tris(2-aminoethyl)amine, Et_3N, stirred overnight. (b) 50% TFA in DCM added dropwise and stirred for 2 hours. (c) anhydrous THF under N_2, Et_3N, Bn-2,3-DHBA-OSu. Bn-2,3-DHBA-OSu was synthesized as described in Fig. S5 (d) 25% EtOAc in EtOH, 5% HOAc, Pd/C, stirred overnight under hydrogen atmosphere.

Surface Forces Apparatus (SFA): The full details of the SFA technique are elaborated elsewhere.[19] All measurements were performed with a SFA 2000, manufactured by SurForce LLC in Santa Barbara, California. Briefly, for each experiment, two mica surfaces are prepared by gluing a piece of freshly-cleaved, back-silvered mica (~1 cm^2), of equal mica and silver thicknesses, onto cylindrical glass disks (radius ~2 cm), with the pristine mica surface facing upward. The two mica surfaces are installed into the SFA, with the pristine mica surfaces facing each other. The surfaces are brought close together and small droplets of aqueous buffer are injected between the surfaces (~50 μL total volume). Normal force-distance measurements are then performed between the two surfaces in aqueous solution. The contact area between the mica surfaces is verified as free from asperities or contaminants based on the interferometric profile of the contact zone and the measured forces, which are well documented for mica interacting in aqueous solution.[20–22] Following, a small amount (~10 μL) of siderophore analogs in aqueous buffer is injected into the gap solution between the surfaces, and the system is allowed to equilibrate for 20 minutes as the analogs adsorb to the mica surfaces. While remaining at the same contact position, force-distance measurements are then performed between the mica surfaces in the siderophore analog solutions. The aqueous solution used in all SFA experiments was a 50 mM acetate + 150 mM KNO_3 buffer solution at pH 3.3. The force-distance data shown are representative of measurements performed over at least 4 separate experiments for each molecule and solution condition. The adhesion values, F_{ad}, and compressed film thicknesses, D_{T}, are reported as the sample mean and standard deviation.

4.2.4 Synergy Between Catechol and Arginine

Certain interfacial priming proteins secreted from mussels, such as Mfp-3f in *Mytilus edulis*,[42] contain stoichiometric compositions of Arg and Dopa, which parallels the high compositions of Lys and Dopa found in other variants, such as Mfp-5 in *Mytilus californianus*.[1] To determine if Arg is functionally similar to Lys in synergy with catechol in wet adhesion, we synthesized a siderophore analog, Tren-Arg-Cam (TAC) which replaces the Lys residues of TLC with Arg (Figure 4.11A). A SFA was used to measure the radius-normalized force (*F/R*) versus distance (*D*) profile for two cleaved mica surfaces during approach, compression, and separation in buffered solution of TAC (Figure 4.11B). Mica is a molecularly-smooth aluminosilicate mineral (Si:Al ratio of 3:1) which serves as an ideal model for the shale and clay minerals to which mussels commonly attach. The smooth and well-studied interface of mica allows for molecular-level insights into the adhesive mechanisms of adsorbates. Mica possesses a negative structural charge at surface Al sites and strongly adsorbs hydrated cations—such as K^+—and water to form a tightly-bound hydration layer that is characteristic of most polar surfaces in solution.[22,43,44] In aqueous environments, robust attachment to surfaces is contingent upon displacing this hydration layer, and binding molecules to the underlying surface.

In buffer solution (150 mM KNO_3 + 50 mM acetate, pH 3.3), a hydration layer of D_T = 13 ± 1 Å formed between mica surfaces at 10 mN/m of compression (Figure 4.11B, black circles). Upon separation of the two surfaces, only a weak van der Waals adhesion force was measured.[21] However, after nanomolar amounts of TAC were injected and equilibrated in the gap solution between the surfaces (resulting concentration of 200 μM), the thickness of the intervening layer *decreased* to 12 ± 1 Å, and a large adhesion force, $F_{ad} = -43 \pm 6$ mN m^{-1}, was measured upon separation after 10 minutes in contact, which increased slightly with additional contact time (Figure 4.11C). The measured adhesion forces between two crossed-cylinder surfaces in SFA experiments were converted into adhesion energies using the Johnson-Kendall-Roberts theory ($E_{ad} = F_{ad}/1.5\pi R$).[24] Overall, the decrease in the thickness of the intervening layer between mica surfaces, the increase in adhesion, and the sharply vertical shape of the force curve are consistent with a monolayer of TAC that bridges between the mica surfaces and mediates adhesion.

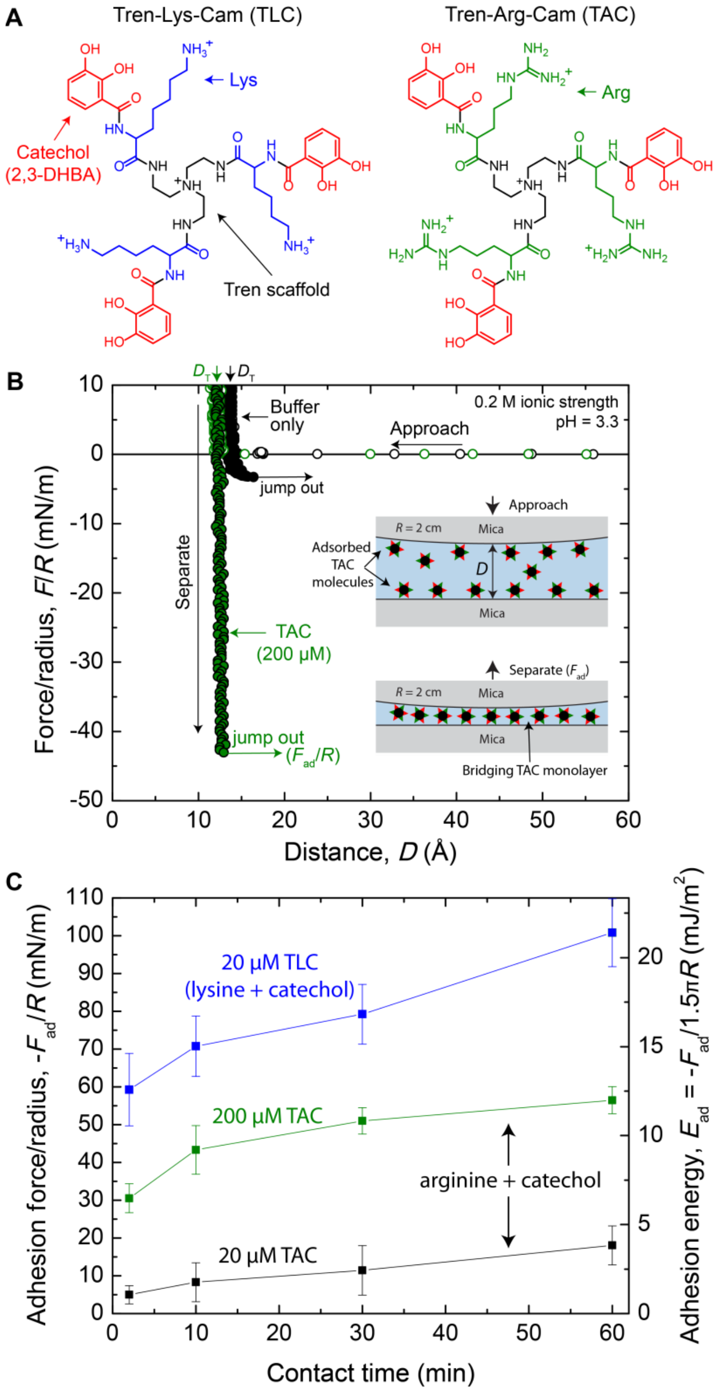

Figure 4.11: (A) Structures of siderophore analogs TLC and TAC. (B) SFA force-distance interaction for two mica surfaces in aqueous buffer (150 mM KNO_3 + 50 mM acetate, pH 3.3, black circles) and in 200 µM TAC (green circles). Open circles represent measurements during the approach of the two surfaces, while closed circles represent measurements during separation. The inset depicts the surfaces as they interact throughout the measurement. (C) TLC- and TAC-mediated adhesion force, F_{ad}, and energy, E_{ad}, required to separate two mica surfaces in aqueous solution, as a function of the time the surfaces were left in adhesive contact. Error bars represent one standard deviation.

The force-distance profiles confirm that the guanidinium cations in TAC displace hydrated salt layers and promote adhesive synergy with catechols at mineral surfaces, similar to the amine cations in TLC—yet, with subtle differences. Firstly, TAC demonstrates a critical adsorption concentration (CAC) approximately 10x higher than TLC before the molecules adsorb to the mica interface and mediate strong adhesion (Fig 4.11C), presumably an effect of guanidinium's bulkier structure,[45] delocalized charge, and lower affinity than amines for mica's negatively charged sites.[46] Additionally, the maximum adhesion mediated by TAC is only 50-60% of the maximum TLC adhesion, and the intervening TAC film thickness (12 ± 1 Å) is slightly larger than that of TLC (9 ± 1 Å). We offer two non-exclusive hypotheses for the measured differences: (1) the TAC adsorption density is lower that the TLC density, and (2) TAC's lower adhesion is due to guanidinium's weaker electrostatic interaction with mica, which also indicates that the cationic residues Lys and Arg contribute significantly to the equilibrium adhesion energy, rather than solely catechol.

4.2.5 Increasing Cation:Catechol Ratio Decreases Adhesion

To observe the effect of increasing the number of cationic groups per molecule on adhesion and surface affinity, we synthesized a siderophore analog, Tren-Lys-Lys-Cam (TLLC) that doubles the ratio of cations to catechols (Figures 4.12A). SFA force-distance measurements were performed with TLLC using the same procedure as TAC. Similar interaction profiles and adhesion forces were measured with TLLC (Figure 4.12B); the thickness of the intervening layer between mica surfaces decreased to D_T = 12 ± 1 Å and comparable adhesion forces, F_{ad} = -47 ± 9 mN/m, were measured after 10 minutes in contact.

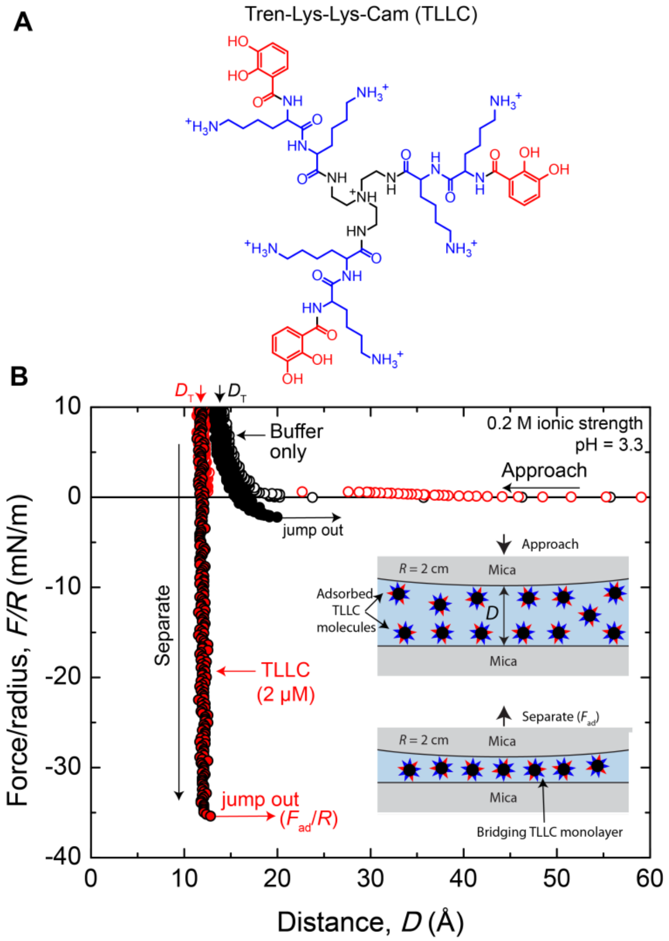

Figure 4.12: (A) Structure of siderophore analog TLLC. (B) SFA force-distance interaction for two mica surfaces in aqueous buffer (150 mM KNO$_3$ + 50 mM acetate, pH 3.3, black circles) and in 2 µM TLLC (red circles). Open circles represent measurements during the approach of the two surfaces, while closed circles represent measurements during separation. The inset depicts the surfaces as they interact throughout the measurement.

The lower adhesion energy measured with TLLC is further evidence of the importance of catechols in robust adhesion. Doubling the number of Lys groups increases the molecule's projected area at a surface, yet keeps the number of catechol groups the same, thereby decreasing the density of robust bidentate interactions per area across the surface. However, the three additional Lys groups do lower the CAC for TLLC by an order of magnitude (Figure 4.13). TLLC's adhesion performance is an interesting alternative result to

Wang *et al.*,[10] where increasing the concentration of Dopa groups in a cationic polymer had a negligible effect on the polymer's total adhesion. We ascribe these contrary results to differences in the geometries in our respective adhesive molecules; the excluded volume of random coil polymers sterically hinder high catechol-surface densities, while small molecules may assemble into more dense films.

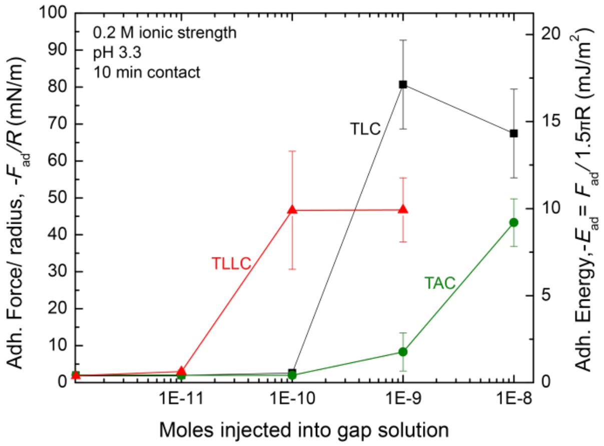

Figure 4.13: TLC-, TAC-, and TLLC-mediated adhesion force (and energy) required to separate two mica surfaces in aqueous solution, as a function of the number of moles of the siderophore analogs injected into the intervening gap solution between the mica surfaces. The total volume of intervening solution between the two mica surfaces was approximately 50 μL. Error bars represent one standard deviation.

4.2.6 Mixtures of Catechol- and Amine-Only Compounds Do Not Promote Adhesion

Do cation and catechol functionalities require intramolecular proximity to enhance adhesion? To determine if a mixture of two siderophore analogs—one without amine (Tren-Cam, TC) and the other without catechol (Tren-Lys-Bam, TLB)—promotes adhesion at aqueous mineral surfaces, we performed further SFA force-distance measurements between mica surfaces, as shown in Figure 4.14. In varying ratios of TC (0.02 mM-1 mM) and TLB

(0.02-0.2 mM), no enhanced adhesion or synergy between the siderophore analogs was detected. At a concentration of 0.2 mM, TLB preferentially adsorbed onto the mica surface over TC, displaced the hydration layer, and mediated modest adhesive forces that were identical to those measured in solutions of only TLB (Figure 4.14C-i). Additional adhesion measurements were performed in mixtures of TC and amine compounds (tetramethylamine, lysine, isopropylamine, analine, 1,3-diaminopropane, diethylentriamine, TREN, or 2,4,6-triethyl-1,3,5-benzenetrimethanamine [TEBMA]); however, no evidence of synergy or adhesion was measured in any of these mixtures. In mixtures with TC and TREN or TEBMA, the highly charged amine compounds adsorbed to the mica surface, but no influence from TC was observed (Figure 4.14C-ii and -iii). The inability to recreate the adhesive performance of TLC with mixtures of singularly-functionalized molecules suggests that molecular geometry and configurational entropy[47] upon adsorption contribute significantly to the surface phenomena of the siderophore analogs.

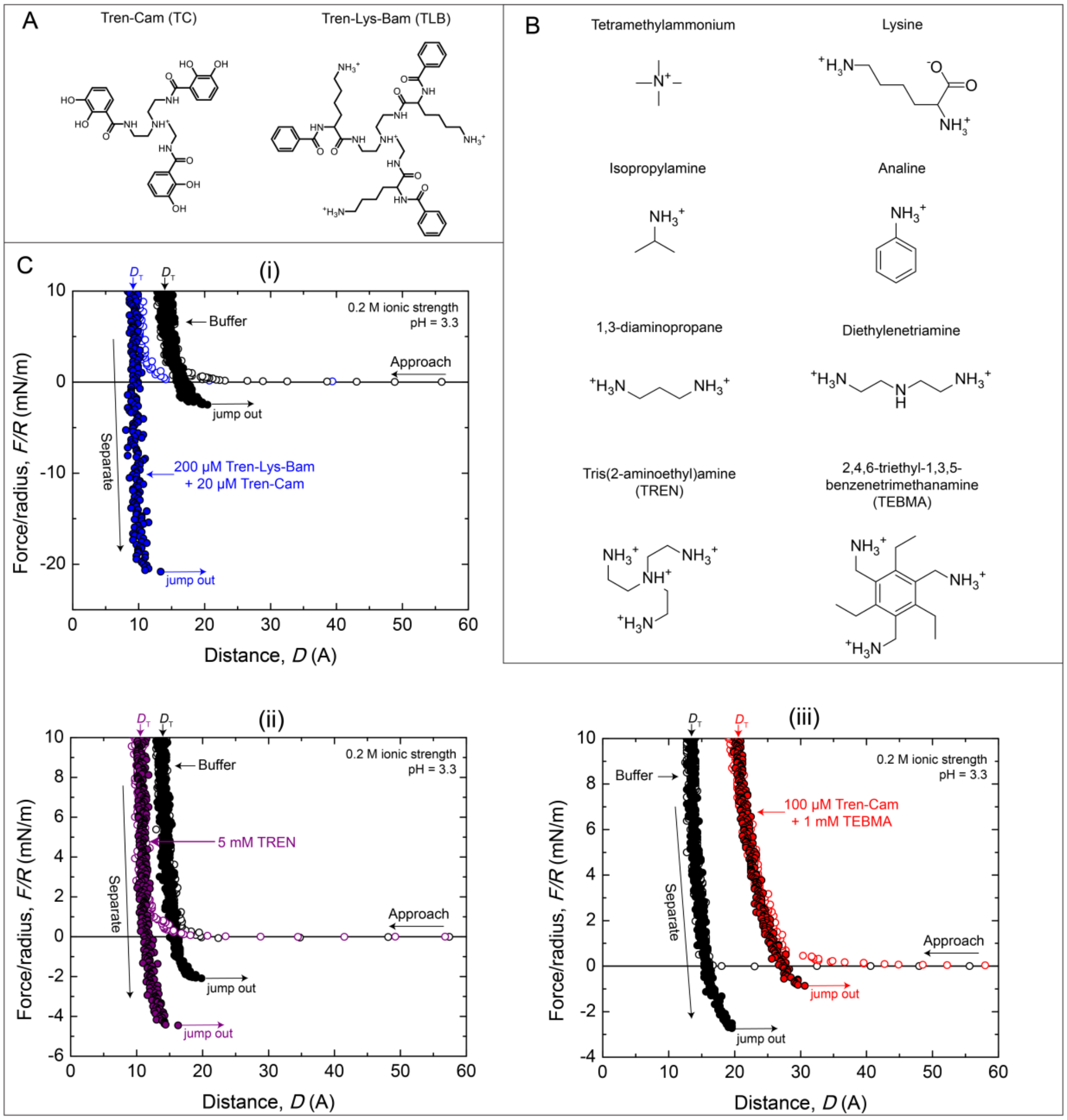

Figure 4.14: (A) Structures of siderophore analogs TC and TLB. (B) Structures of amine-containing compounds. Mixtures of varying ratios of the amine-containing compounds (0.1-5 mM) and Tren-Cam (0.02-1 mM) were prepared in buffer solution (150 mM KNO_3 + 50 mM acetate, pH 3.3) and injected into the gap solution between two mica surfaces in SFA measurements. (C) Representative SFA force-distance interaction for two mica surfaces in aqueous buffer (black circles) and various amine/catechol solutions (colored circles). Open circles represent measurements during the approach of the two surfaces, while closed circles represent measurements during separation. Mixtures of amine-containing compounds and Tren-Cam (contains no cationic functionalities) were unable to recreate the strong adhesive synergy of the siderophore analogs that contain both catechol and cationic moieties (TLC, TAC, TLLC). (i) Mixtures of the siderophore anaologs TC and TLB (contains no catechol groups) produce force-distance interactions that are identical to the interactions in pure TLB solution. Thus, TLB out-competes TC for adsorption sites and TLB mediates all adhesion between mica surfaces in mixtures with TC. (ii) 5mM solutions of TREN in buffer were able to displace some of the hydrated salt layer at the mica surfaces, and promote a minute increase in adhesion. Additions of TC into the TREN solution yielded no change to the interactions measured. (iii) In mixtures of 1 mM TEBMA and 0.1 mM TC, TEBMA adsorbs to form a thicker layer on the mica surfaces. No adhesive synergy is measured.

4.2.7 Conclusions

The specific binding mode of the 2,3-dihydroxy catechol to the surface and the resulting geometry of the siderophore analogs are not known. By virtue of single-molecule AFM force measurements, Li *et al.*[9] suggested that Dopa adsorbs to mica via bidentate hydrogen bonds. Alternatively, the catechols may form mononuclear bidentate coordination complexes to mica's alumina sites,[48–50] yet this interaction is unconfirmed at mica's crystalline surface. Similarly, a salicylate-type interaction involving the *o*-hydroxyl oxygen and carbonyl group is possible,[51] but not expected.[52] After displacing the hydrated salt layer, the role of the cationic amine group is unconfirmed; however, we strongly suspected the cationic groups to participate in adhesion to the mica surface through Coulomb interactions at the negatively charged alumina sites.

Over the first few molecular layers extending from an aqueous mineral surface, paired catechol-cationic functionalities cooperate to displace hydration layers and promote robust adhesion between the underlying surfaces. This synergy is not unique to amine cations: guanidinium groups likewise enhance aqueous adhesion, which provides a rationale for the high mole % of Arg residues in certain Mfps. In small molecule adhesives, increasing the number of cationic groups per molecule increases affinity for negatively charged surfaces, but decreases the equilibrium adhesion energy by lowering the density of bidentate binding catechol groups. Although the specific surface conformations of paired catechol-cation siderophores and analogs await characterization in future studies, it is apparent that geometry and configurational entropy significantly affect their intermolecular interactions. In analogy to the remarkably high Fe^{3+}-stability constant of tris-catechol siderophores compared to mono-catechol compounds,[53] the intramolecular adjacency of binding functionalities contributes a significant energetic gain upon adsorption to a wet surface.

4.3 References

(1) Lee, B. P.; Messersmith, P. B.; Israelachvili, J. N.; Waite, J. H. Mussel-Inspired Adhesives and Coatings. *Annu. Rev. Mater. Res.* **2011**, *41*, 99–132.

(2) Lee, H.; Scherer, N. F.; Messersmith, P. B. Single-Molecule Mechanics of Mussel Adhesion. *Proc. Natl. Acad. Sci. U. S. A.* **2006**, *103*, 12999–13003.

(3) Krogsgaard, M.; Behrens, M. A.; Pedersen, J. S.; Birkedal, H. Self-Healing Mussel-Inspired Multi-pH-Responsive Hydrogels. *Biomacromolecules* **2013**, *14,* 297–301.

(4) Shao, H.; Stewart, R. J. Biomimetic Underwater Adhesives with Environmentally Triggered Setting Mechanisms. *Adv. Mater.* **2010**, *22*, 729–733.

(5) Kastrup, C. J.; Nahrendorf, M.; Figueiredo, J. L.; Lee, H.; Kambhampati, S.; Lee, T.; Cho, S.-W.; Gorbatov, R.; Iwamoto, Y.; Dang, T. T.; et al. Painting Blood Vessels and Atherosclerotic Plaques with an Adhesive Drug Depot. *Proc. Natl. Acad. Sci. U. S. A.* **2012**, *109,* 21444–21449.

(6) Statz, A. R.; Meagher, R. J.; Barron, A. E.; Messersmith, P. B. New Peptidomimetic Polymers for Antifouling Surfaces. *J. Am. Chem. Soc.* **2005**, *127*, 7972–7973.

(7) Ryu, J.; Ku, S. H.; Lee, H.; Park, C. B. Mussel-Inspired Polydopamine Coating as a Universal Route to Hydroxyapatite Crystallization. *Adv. Funct. Mater.* **2010**, *20*, 2132–2139.

(8) White, J. D.; Wilker, J. J. Underwater Bonding with Charged Polymer Mimics of Marine Mussel Adhesive Proteins. *Macromolecules* **2011**, *44*, 5085–5088.

(9) Li, Y.; Qin, M.; Li, Y.; Cao, Y.; Wang, W. Single Molecule Evidence for the Adaptive Binding of DOPA to Different Wet Surfaces. *Langmuir* **2014**, *30,* 4358–4366.

(10) Wang, J.; Tahir, M. N.; Kappl, M.; Tremel, W.; Metz, N.; Barz, M.; Theato, P.; Butt, H.-J. Influence of Binding-Site Density in Wet Bioadhesion. *Adv. Mater.* **2008**, *20*, 3872–3876.

(11) Yu, J.; Kan, Y.; Rapp, M.; Danner, E.; Wei, W.; Das, S.; Miller, D. R.; Chen, Y.; Waite, J. H.; Israelachvili, J. N. Adaptive Hydrophobic and Hydrophilic Interactions of Mussel Foot Proteins with Organic Thin Films. *Proc. Natl. Acad. Sci. U. S. A.* **2013**, *110*, 15680–15685.

(12) Yu, J.; Wei, W.; Danner, E.; Ashley, R. K.; Israelachvili, J. N.; Waite, J. H. Mussel Protein Adhesion Depends on Interprotein Thiol-Mediated Redox Modulation. *Nat. Chem. Biol.* **2011**, *7*, 588–590.

(13) Martinez Rodriguez, N. R.; Das, S.; Kaufman, Y.; Israelachvili, J. N.; Waite, J. H. Interfacial pH during Mussel Adhesive Plaque Formation. *Biofouling* **2015**, *31*, 221–227.

(14) Yamamoto, H. Synthesis and Adhesive Studies of Marine Polypeptides. *J. Chem. Soc. Perkin Trans. 1* **1987**, 613–618.

(15) Yu, M.; Hwang, J.; Deming, T. Role of L-3, 4-Dihydroxyphenylalanine in Mussel Adhesive Proteins. *J. Am. Chem. Soc.* **1999**, *121*, 5825–5826.

(16) Raymond, K. N.; Dertz, E. A.; Kim, S. S. Enterobactin: An Archetype for Microbial Iron Transport. *Proc. Natl. Acad. Sci. U. S. A.* **2003**, *100*, 3584–3588.

(17) Sandy, M.; Butler, A. Chrysobactin Siderophores Produced by Dickeya Chrysanthemi EC16. *J. Nat. Prod.* **2011**, *74*, 1207–1212.

(18) Lu, C.; Buyer, J.; Okonya, J.; Miller, M. Synthesis of Optically Pure Chrysobactin and Immunoassay Development. *Biometals* **1996**, *9*, 377–383.

(19) Israelachvili, J.; Min, Y.; Akbulut, M.; Alig, A.; Carver, G.; Greene, W.; Kristiansen, K.; Meyer, E.; Pesika, N.; Rosenberg, K.; et al. Recent Advances in the Surface Forces Apparatus (SFA) Technique. *Reports Prog. Phys.* **2010**, *73*, 036601.

(20) Pashley, R. M. Hydration Forces between Mica Surfaces in Electrolyte Solutions. *Adv. Colloid Interface Sci.* **1982**, *16*, 57–62.

(21) Israelachvili, J. N. *Intermolecular and Surface Forces: Revised Third Edition*; Academic Press, 2011.

(22) Israelachvili, J.; Wennerström, H. Role of Hydration and Water Structure in Biological and Colloidal Interactions. *Nature* **1996**, *379*, 219–225.

(23) Rodgers, S. J.; Lee, C. W.; Ng, C. Y.; Raymond, K. N. Ferric Ion Sequestering Agents. 15. Synthesis, Solution Chemistry, and Electrochemistry of a New Cationic Analog of Enterobactin. *Inorg. Chem.* **1987**, *26*, 1622–1625.

(24) Johnson, K. L.; Kendall, K.; Roberts, A. D. Surface Energy and the Contact of Elastic Solids. *Proc. R. Soc. A Math. Phys. Eng. Sci.* **1971**, *324*, 301–313.

(25) Kim, S.; Faghihnejad, A.; Lee, Y.; Jho, Y.; Zeng, H.; Hwang, D. S. Cation–π Interaction in DOPA-Deficient Mussel Adhesive Protein Mfp-1. *J. Mater. Chem. B* **2014**, *3*, 738–743.

(26) Stumm, W.; Morgan, J. J. *Aquatic Chemistry: Chemical Equilibria and Rates in Natural Waters, 3rd Edition*; John Wiley & Sons, 1996.

(27) Akdogan, Y.; Wei, W.; Huang, K.-Y.; Kageyama, Y.; Danner, E. W.; Miller, D. R.; Martinez Rodriguez, N. R.; Waite, J. H.; Han, S. Intrinsic Surface-Drying Properties of Bioadhesive Proteins. *Angew. Chemie* **2014**, *126*, 11435–11438.

(28) Podsiadlo, P.; Liu, Z.; Paterson, D.; Messersmith, P. B.; Kotov, N. A. Fusion of Seashell Nacre and Marine Bioadhesive Analogs: High-Strength Nanocomposite by Layer-by-Layer Assembly of Clay andL-3,4-Dihydroxyphenylalanine Polymer. *Adv. Mater.* **2007**, *19*, 949–955.

(29) Zhang, F.; Liu, S.; Zhang, Y.; Wei, Y.; Xu, J. Underwater Bonding Strength of Marine Mussel-Inspired Polymers Containing DOPA-like Units with Amino Groups. *RSC Adv.* **2012**, *2*, 8919–8921.

(30) Wei, Q.; Achazi, K.; Liebe, H.; Schulz, A.; Noeske, P.-L. M.; Grunwald, I.; Haag, R. Mussel-Inspired Dendritic Polymers as Universal Multifunctional Coatings. *Angew. Chem. Int. Ed. Engl.* **2014**, *53*, 11650–11655.

(31) Waite, J. H.; Andersen, N. H.; Jewhurst, S.; Sun, C. Mussel Adhesion: Finding the Tricks Worth Mimicking. *J. Adhes.* **2005**, *81*, 297–317.

(32) Petrone, L.; Kumar, A.; Sutanto, C. N.; Patil, N. J.; Kannan, S.; Palaniappan, A.; Amini, S.; Zappone, B.; Verma, C.; Miserez, A. Mussel Adhesion Is Dictated by Time-Regulated Secretion and Molecular Conformation of Mussel Adhesive Proteins. *Nat. Commun.* **2015**, *6*, 8737.

(33) Taylor, S. W.; Chase, D. B.; Emptage, M. H.; Nelson, M. J.; Waite, J. H. Ferric Ion Complexes of a DOPA-Containing Adhesive Protein from Mytilus Edulis. *Inorg. Chem.* **1996**, *35*, 7572–7577.

(34) Wilker, J. J. The Iron-Fortified Adhesive System of Marine Mussels. *Angew. Chem. Int. Ed. Engl.* **2010**, *49*, 8076–8078.

(35) Bandara, N.; Zeng, H.; Wu, J. Marine Mussel Adhesion: Biochemistry, Mechanisms, and Biomimetics. *J. Adhes. Sci. Technol.* **2013**, *27*, 2139–2162.

(36) Haller, C. M.; Buerzle, W.; Brubaker, C. E.; Messersmith, P. B.; Mazza, E.; Ochsenbein-Koelble, N.; Zimmermann, R.; Ehrbar, M. Mussel-Mimetic Tissue Adhesive for Fetal Membrane Repair: A Standardized Ex Vivo Evaluation Using Elastomeric Membranes. *Prenat. Diagn.* **2011**, *31*, 654–660.

(37) Brubaker, C. E.; Kissler, H.; Wang, L.-J.; Kaufman, D. B.; Messersmith, P. B. Biological Performance of Mussel-Inspired Adhesive in Extrahepatic Islet Transplantation. *Biomaterials* **2010**, *31*, 420–427.

(38) Ahn, B. K.; Lee, D. W.; Israelachvili, J. N.; Waite, J. H. Surface-Initiated Self-Healing of Polymers in Aqueous Media. *Nat. Mater.* **2014**, *13*, 867–872.

(39) Lee, H.; Dellatore, S. M.; Miller, W. M.; Messersmith, P. B. Mussel-Inspired Surface Chemistry for Multifunctional Coatings. *Science* **2007**, *318*, 426–430.

(40) Lee, H.; Lee, B. P.; Messersmith, P. B. A Reversible Wet/dry Adhesive Inspired by Mussels and Geckos. *Nature* **2007**, *448*, 338–341.

(41) Maier, G. P.; Rapp, M. V; Waite, J. H.; Israelachvili, J. N.; Butler, A. Adaptive Synergy between Catechol and Lysine Promotes Wet Adhesion by Surface Salt Displacement. *Science* **2015**, *349*, 628–632.

(42) Papov, V. V.; Diamond, T. V.; Biemann, K.; Waite, J. H. Hydroxyarginine-Containing Polyphenolic Proteins in the Adhesive Plaques of the Marine Mussel Mytilus Edulis. *J. Biol. Chem.* **1995**, *270*, 20183–20192.

(43) Israelachvili, J. N.; Pashley, R. M. Molecular Layering of Water at Surfaces and Origin of Repulsive Hydration Forces. *Nature* **1983**, *306*, 249–250.

(44) Pashley, R. . DLVO and Hydration Forces between Mica Surfaces in Li+, Na+, K+, and Cs+ Electrolyte Solutions: A Correlation of Double-Layer and Hydration Forces with Surface Cation Exchange Properties. *J. Colloid Interface Sci.* **1981**, *83*, 531–546.

(45) Mason, P. E.; Neilson, G. W.; Dempsey, C. E.; Barnes, A. C.; Cruickshank, J. M. The Hydration Structure of Guanidinium and Thiocyanate Ions: Implications for Protein Stability in Aqueous Solution. *Proc. Natl. Acad. Sci. U. S. A.* **2003**, *100*, 4557–4561.

(46) Yamauchi, M.; Ishimaru, S.; Ikeda, R. Two-Dimensional Molecular Motions of Guanidinium Ions Confined in the Interlayer Space of Tetrasilicicfluormica. *Chem. Lett.* **2003**, *32*, 976–977.

(47) Baker, B. G. Configurational Entropy of Adsorption of Large Atoms. *J. Chem. Phys.* **1966**, *45*, 2694.

(48) Gulley-Stahl, H.; Hogan, P. A.; Schmidt, W. L.; Wall, S. J.; Buhrlage, A.; Bullen, H. A. Surface Complexation of Catechol to Metal Oxides: An ATR-FTIR, Adsorption, and Dissolution Study. *Environ. Sci. Technol.* **2010**, *44*, 4116–4121.

(49) McBride, M. B.; Wesselink, L. G. Chemisorption of Catechol on Gibbsite, Boehmite, and Noncrystalline Alumina Surfaces. *Environ. Sci. Technol.* **1988**, *22*, 703–708.

(50) Borah, J. M.; Sarma, J.; Mahiuddin, S. Adsorption Comparison at the α-Alumina/water Interface: 3,4-Dihydroxybenzoic Acid vs. Catechol. *Colloids Surfaces A Physicochem. Eng. Asp.* **2011**, *387*, 50–56.

(51) Cohen, S. M.; Meyer, M.; Raymond, K. N. Enterobactin Protonation and Iron Release: Hexadentate Tris-Salicylate Ligands as Models for Triprotonated Ferric Enterobactin 1. *J. Am. Chem. Soc.* **1998**, *120*, 6277–6286.

(52) Upritchard, H. G.; Yang, J.; Bremer, P. J.; Lamont, I. L.; McQuillan, A. J. Adsorption of Enterobactin to Metal Oxides and the Role of Siderophores in Bacterial Adhesion to Metals. *Langmuir* **2011**, *27*, 10587–10596.

(53) Loomis, L. D.; Raymond, K. N. Solution Equilibria of Enterobactin and Metal-Enterobactin Complexes. *Inorg. Chem.* **1991**, *30*, 906–911.